Evaluation of silicon photonic technology for the development of innovative 40 Gbps wireless link above 200 GHz

Elsa Lacombe

UNIVERSITÉ CÔTE D'AZUR

ÉCOLE DOCTORALE
SCIENCES ET TECHNOLOGIES DE L'INFORMATION ET DE LA COMMUNICATION

THÈSE DE DOCTORAT

Evaluation de la Technologie Photonique sur Silicium pour le Développement de Liens Sans Fil Innovants Visant 40 Gb/s au-delà de 200 GHz

Elsa LACOMBE

Polytech'Lab

Présentée en vue de l'obtention du grade de docteur en Electronique **d'**Université Côte d'Azur

Dirigée par : Cyril Luxey
Co-encadrée par : Frédéric Gianesello
Soutenue le : 5 Novembre 2018

Devant le jury, composé de :
Goutam Chattopadhyay, Docteur, NASA-JPL
Laurent Chusseau, Directeur de Recherche, Université de Montpellier
Carlos Del Rio Bocio, Professeur, Université publique de Navarre
Guillaume Ducournau, Professeur, Université de Lille
Frédéric Gianesello, Docteur, ST Microelectronics
Cyril Luxey, Professeur, Université Nice Sophia Antipolis
Alain Maestrini, Professeur, Observatoire de Paris
Ala Sharaiha, Professeur, Université de Rennes
Diane Titz, Docteur, Université Nice Sophia Antipolis

Evaluation de la Technologie Photonique sur Silicium pour le Développement de Liens Sans Fil Innovants Visant 40 Gb/s au-delà de 200 GHz

Jury

Président du jury :

Alain Maestrini, Professeur, Observatoire de Paris

Rapporteurs :

Laurent Chusseau, Directeur de Recherche, Université de Montpellier
Ala Sharaiha, Professeur, Université de Rennes

Examinateurs :

Goutam Chattopadhyay, Docteur, NASA-Jet Propulsion Lab
Carlos Del Rio Bocio, Professeur, Université publique de Navarre
Guillaume Ducournau, Professeur, Université de Lille
Frédéric Gianesello, Docteur, ST Microelectronics
Cyril Luxey, Professeur, Université de Nice Sophia Antipolis

Invités :

Diane Titz, Docteur, Université Nice Sophia Antipolis

Evaluation of Silicon Photonic Technology for the Development of Innovative 40 Gbps Wireless Link above 200 GHz

Abstract

With the booming of mobile data traffic, the need for higher data-rates is clearly felt. To cope with this strong demand and support the 5G roll-out, the capacity of the mobile communication network is being improved every day with many solutions, among which the development and installation of millimeter-wave (mmW) wireless systems operating at up to 10 Gb/s. However, in order to deliver such high speeds to the user, the fronthaul/backhaul network sending data back to the core network would require above 40 Gb/s data-rate wireless links. This challenge generates a growing interest for sub-mmW and THz frequencies (0.1 THz – 1 THz) at which up-to 100 GHz bandwidth (BW) is accessible. In such BW, it would be possible to achieve up to 100 Gb/s data-rates while using simple modulation schemes to reduce the wireless system's power consumption. Targeting mass-market high data-rates applications, Silicon Photonics technology seems very promising as it benefits from wide intrinsic BW and power-efficient components, as well as high integration levels and low manufacturing costs. In this context, a main aspect of this PhD project is the evaluation of an industrial Silicon Photonics technology for the development of a THz system-on-chip transmitter capable of reaching up to 100 Gb/s using a photodiode. Since THz antennas are also a hot topic for THz point-to-point transmission, a second aspect of this PhD study is the design of a low-cost and compact THz antenna-system. Hence, a planar antenna using low-loss organic packaging technology and a 3D-printed plastic lens were developed in order to assess those industrial prototyping techniques above 200 GHz.

Key words: THz transmitter, Silicon Photonics, integrated antenna, organic substrate, 3D-printing

Evaluation de la Technologie Photonique sur Silicium pour le Développement de Lien Sans Fil Innovants Visant 40 Gb/s au-delà de 200 GHz

Résumé

Avec l'explosion du trafic de données mobiles, des débits supérieurs au Gb/s deviennent nécessaires pour l'utilisateur. Ainsi, le réseau de communication est en cour d'amélioration afin de promouvoir le déploiement de la 5G, notamment grâce au développement et à l'installation de systèmes sans fil d'onde millimétrique (mmW) à 10 Gb/s. Néanmoins, pour délivrer de tels débits, les liens fronthaul/backhaul sans fil connectés au cœur de réseau devront supporter des flux de données supérieurs à 40 Gb/s. Cet enjeu suscite un intérêt croissant pour les fréquences sub-mmW et THz (0.1 THz – 1 THz) autour desquelles des bandes passantes (BPs) de 100 GHz sont accessibles. Il serait en effet possible d'atteindre un débit de 100 Gb/s, tout en utilisant des formats de modulation simples et ainsi réduire la consommation d'énergie du système. Visant le marché de masse des applications haut-débits, la technologie Photonique sur Silicium est particulièrement attractive pour générer des BPs naturellement larges et pour sa capacité à forts niveaux d'intégration et faible cout de fabrication. Dans cette thèse, une technologie Photonique sur Silicium industrielle a donc été évaluée durant le développement d'un émetteur intégré THz fonctionnant sur la base d'une photodiode et pouvant délivrer 100 Gb/s. Le développement d'une antenne THz faible cout et compacte est également un aspect majeur de cette thèse afin de permettre la transmission point-à-point du signal THz. En effet, une antenne intégrée sur substrat organique faible cout et à faibles pertes et une lentille fabriquée par impression 3D ont été développées afin d'évaluer ces technologies de prototypage industriel au-delà de 200 GHz.

Mots clés: Emetteur THz, Photonique sur Silicium, antenne intégrée, substrat organique, impression 3D

Acknowledgment

I would first like to express my sincere gratitude to Ala Sharaiha, Laurent Chusseau, Alain Maestrini, Diane Titz, Carlos Rio Del Bocio, Guillaume Ducournau and Goutam Chattopadhyay for having accepted to assume the role of members of the jury for my thesis defense. Therefore, I would like to thank them for their valuable feedbacks on the work done during my PhD thesis.

This thesis is a collaboration between STMicroelectronics, Polytech'Lab at the University of Nice Sophia-Antipolis, and the IEMN laboratory at the University of Lille. In this context, I would to express my deep appreciation to my supervisors Dr. Frederic Gianesello, Prof. Cyril Luxey, and Prof. Guillaume Ducournau for the great technical and measurement support they gave me during those three years and thanks to whom I have grown professionally.

I would like to indicate the many partnerships realized during the PhD research work which enable the realization of specific designs and measurements. Therefore, I send my thanks to Guillaume Ducournau from the University of Lille, Carlos Del Rio Bocio from the University of Navarra, Jorge R. Costa and Carlos A. Fernandes from the University of Lisbon, Thomas Zwick, Heiko Gulan and Jochen Schäfer from the Technology Institute of Karlsruhe for their contribution to this PhD research work.

I won't forget to acknowledge the valuable help, feedbacks and support given by Aimeric Bisognin, Folly Eli Ayi-Yovo, Jean-Mark Boucaud, Cybelle Belem-Goncalves, Simon Bouvot, Francesco Filice, Frédéric Devillers, Ana Arboleya, Cédric Durand, Florence Sonnerat, Vincent Gidel, Jeff Nowakowski, and Daniel Gloria during my PhD.

Table of content

Introduction

With the actual development of wireless applications, telecommunication networks are witnessing a never ending increase of the amount of data. This is further emphasized by the densification of the mobile network through the deployment of small cells led by the 5G network rollout. Indeed, to address the growing consumer demand for high data-rates, 5G will provide between 100 Mb/s and 1 Gb/s by improving the network capacity and coverage. To meet this requirement, developing high data-rate (multi-Gb/s) and low-cost point-to-point wireless links is now a main challenge of the telecommunication industry. Indeed, fronthaul/backhaul links are now largely developed with high data-rate wireless millimeter-wave (mmW) systems, since civil construction cost associated to the implementation of optical fiber cables is prohibitive.

The technologies that are being currently deployed focus on the frequency bands around 60 GHz and 80 GHz and provide the opportunity to operate at data-rate transfer ranging from 100 Mb/s to 10 Gb/s over distances up-to 20 km. However, future 5G network will require backhaul/fronthaul data-rates up to 25 Gb/s and above 40 Gb/s at longer term. Current mmW links at 60 GHz or 80 GHz will not be able to address such data rates in a cost and power-efficient manner since higher order modulation will be required. One pragmatic way to address such challenge will be to access wider bandwidths, this is why we can see a lot of transmission trails using frequency bands available beyond 100 GHz.

In this context, the development of sub-mmW (> 150 GHz) and THz (>300 GHz) integrated circuits represents a major concern. Indeed, despite the technological progress made in Silicon-based technology (for example BiCMOS Silicon-Germanium (SiGe) transistors with cut-off frequency of ~300 GHz), it becomes difficult to design power-efficient solid-state transceivers capable of generating sub-mmW signals above 250 GHz with satisfying output power and wide bandwidth simultaneously. In order to overcome this limitation, Photonics technology is an interesting alternative due to its inherent broadband nature. The main approach by which Photonics technology generates an electric THz signal is by using a photodiode exited by an optical frequency beat (coming from two lasers for example). Indeed, such a technique enables to deliver acceptable output powers while providing very large bandwidths (above 50 GHz). As a result, several laboratory demonstrations of wireless data communication above 200 GHz have already achieved up to 100 Gb/s data-rate using III-V Photonics based transmitters and Schottky barrier diode mixers as receivers. However, III-V Photonics will likely require costly fabrication processes which is not compatible with the targeted large-scale THz communication applications.

In the current context of Silicon Photonics technology development, one can therefore think about developing a THz transmitter at low fabrication cost, leveraging standard Silicon technology and using opto-electronic techniques. This is the objective of this PhD thesis, enabled thanks to the use of STMicroelectronics' existing Silicon Photonics technology platform previously developed to address high-speed optical link market. The work will mainly focus on the evaluation of achievable performance of two key building blocks: the sub-mmW/THz source achieved using available industrial SiGe photodiode and the On-Off Keying/Pulse-Amplitude-Modulation (OOK/PAM) 25 Gbaud optical

modulator. Those investigations aim to pave the way of highly integrated silicon-based THz transmitters.

To enable Silicon Photonics based high-speed wireless transmissions, ultra-broad band and low-cost antennas represent a second research topic in order to support very large RF bandwidth (> 50%) over the targeted transmission distance. Achieving both wide bandwidth and high gain is indeed very challenging at sub-mmW/THz frequencies because of the lack of antenna packaging technologies offering acceptable dielectric characteristics and design rules at THz operations. Most of the THz antennas reported in the literature are on-chip antennas (monolithically integrated in the semiconductor substrate with the transceiver circuit). However, semiconductor's dielectric characteristics are not appropriate for high performance antenna packaging since they generally exhibit high dielectric constant and significant losses occur inside the substrate. Consequently, most integrated antennas (for example achieved in Silicon technology) do not exhibit high gains or bandwidths unless non-standard micromachining is additionally implemented. Targeting mass market applications, the Antenna-in-Package (AiP) approach is an appealing strategy in order to leverage low-cost and low-loss packaging technology. This type of antenna enables an industrial assembly strategy consisting of the Silicon Photonics transceiver flip-chip mounted on an organic packaging substrate. This advanced Integrated Circuit (IC) assembly technology allows both low interconnection loss and large-scale production. This standard organic packaging substrate technology has already demonstrated its capability to integrate large bandwidth antennas (30%) up to 140 GHz. Therefore, part of this PhD thesis aimed at the evaluation of an antenna integrated in organic substrate above 200 GHz in order to assess this packaging technology at sub-mmW/THz frequencies. Due to significant free space losses of electromagnetic waves propagating in free space (for instance 140 dB for 1 km range at 300 GHz), the gain of the integrated antenna can become insufficient depending on the targeted propagation distance (since we do not consider here an antenna array approach due to the high losses associated to the antenna feeding network). To address this problem, the AiP can be associated to a lens/reflector in order to reach medium/high gains around 20/50 dBi and thus higher transmitting/receiving ranges. Leveraging low-cost additive manufacturing, such antennas can be fabricated in 3D printing in a cost-effective and timely manner. Indeed, this fast prototyping technique has already shown its potential for mmW 3D antennas and has become a good alternative to traditional subtractive manufacturing in academic and industrial research projects. For this reason, 3D printing techniques were utilized during this PhD thesis for the manufacturing of quasi-optical antenna systems in order to evaluate its potential use and performance at THz frequencies.

The **first chapter** of this thesis reviews the scientific context in which the PhD research was developed. The aim of this chapter is to evaluate the impact of emerging wireless applications on the data traffic with regards to the global telecommunication network architecture. This enables to highlight the opportunity to develop cost-effective THz wireless point-to-point links capable of achieving data-rates above 40 Gb/s. Those links could then be possibly applied to the fronthaul/backhaul mobile networks on the future.

The **second chapter** focuses on the development of a Silicon Photonics IC integrating STMicroelectronics' Silicon Germanium photodiode in order to enable THz photomixing. In a first step, a standalone photodiode IC was manufactured to retrieve its electrical characteristics and evaluate its intrinsic THz performance. In a second step, different matching networks were implemented to this Silicon Photonics IC to improve the photodiode's achievable performance (e.g. the photodiode 50Ω

matching) in three consecutive bandwidths between 130 GHz and 330 GHz. An IC integrating an electro-optic modulator in Silicon Photonics was also designed and eye diagram simulations allowed to estimate its performance in anticipation to future measurements in wireless demonstrations.

The **third chapter** presents the development of an antenna-system operating between 200 GHz and 280 GHz. The design and optimization process of the AiP is shown with a particular focus on respecting design rule constrains related to industrial fabrication. An industrial packaging technology using a low-cost and low-loss organic substrate was used for the AiP manufacturing and evaluated up to 300 GHz so as to assess its performance at THz frequencies. Dielectric lens and Cassegrain antenna designs were also realized to increase the achievable gain using the AiP as a feeding source. These quasi-optical systems were fabricated using different 3D printing techniques, among which the Fused Deposition Modeling technique was already validated up to 140 GHz using standard ABS thermo-plastic.

The **fourth chapter** deals with the achievement of data communication laboratory demonstrations of a wireless THz link at 300 GHz using the developed Silicon Photonics transmitter and a commercial Schottky barrier diode detector. The photodiode IC presented in the third chapter were used for photomixing in the transmitter side and bit error rates were measured at up to 25 Gb/s using OOK modulation over a single transmission channel.

Finally, we will provide an overall conclusion on the results obtained during this PhD thesis and propose some perspectives for future research works.

Chapter 1: Opportunities to develop high data-rate wireless links at THz frequencies

Table of Contents

Chapter 1: Opportunities to develop high data-rate wireless links at THz frequencies

This chapter aims at describing the current state and possible evolution of wireless high-speed communication applications with the major associated challenges put upon the telecommunication network's capacities. This allows to lay out important issues which led to set up this PhD project. We'll first have a look at emerging wireless applications and their impact on data traffic supported by the wireless network. This increasing data traffic imposes to rethink the telecommunication network architecture so as to improve the user-experience data-rate. This study will enable us to highlight the opportunity of THz wireless links operating above 200 GHz for very demanding applications in terms of data-rates (> 40 Gb/s). In this context, an overview of the state-of-the-art technologies employed at sub-mmW and THz frequencies will be provided in following sections in order to assess achievable performance at such high frequency.

I. Wireless applications and data traffic

1. Evolution of the number of connected mobile devices

At a time where increasingly high-performance digital technologies became widely accessible and democratized, the number of connected mobile devices is not only growing at an accelerating pace. In particular, the smartphone and tablet market is by far the most dynamic in the wireless telecommunication market. As announced in Ericsson's 2017 yearly mobility report, the number of worldwide mobile subscriptions is growing at almost 6% per year and has reached an impressive total of 7.8 billion at the end of 2017 [I.1]. A number of upgraded features such as 4K HD Resolution touch-screens and enhanced high-speed processors are also promoting better displays and high responsivity which enable to support broadband real-time applications like augmented or virtual reality, HD video streaming, location-based services or video calling.

Moreover, both public consumers and businesses are becoming less dependent on traditional hardware and software and are relying more and more on (mobile) cloud-based services to share, manage and store data anywhere at any time. According to Statista [I.2], the number of cloud consumers worldwide will have reached 3.6 billons of users at the end of year 2018 against 2.4 billion in 2013 as shown in Figure I.1 (b). Hence, even if most of the data traffic is still in download, the amount of uploads is increasing fast as information is being exchanges between users or from user to machine, followed by the growing need for lower latencies. To enable these aforementioned applications and services, wide frequency bands are required to reach high enough throughputs. In fact, according to Ericsson, the amount of data traffic per active smartphones is expected to increase by 38% from 2017 to 2023 (Figure I.1 (a)).

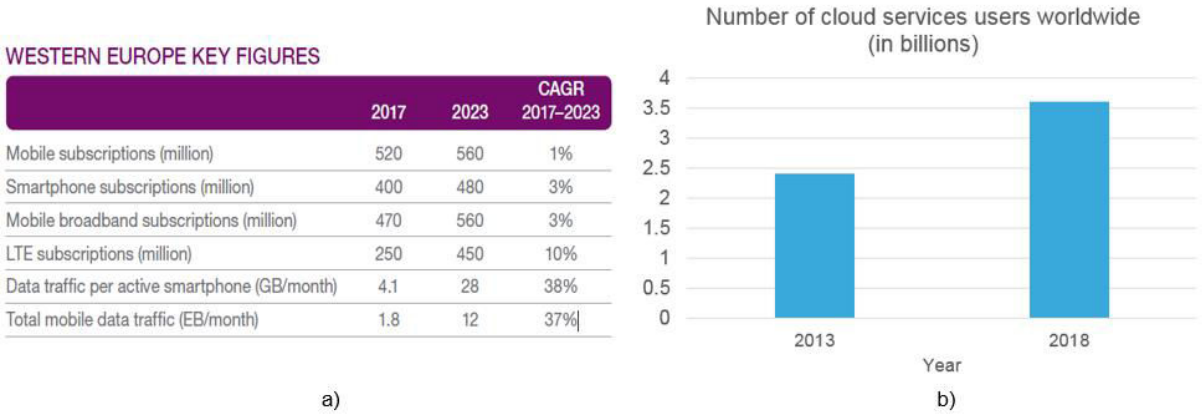

WESTERN EUROPE KEY FIGURES

	2017	2023	CAGR 2017–2023
Mobile subscriptions (million)	520	560	1%
Smartphone subscriptions (million)	400	480	3%
Mobile broadband subscriptions (million)	470	560	3%
LTE subscriptions (million)	250	450	10%
Data traffic per active smartphone (GB/month)	4.1	28	38%
Total mobile data traffic (EB/month)	1.8	12	37%

Figure I.1. (a) Number of mobile and smartphones subscriptions in 2017 and 2023 from [I.1]*, and (b) Number of cloud consumers in 2013 to 2018 from* [I.2].

As the proliferation of wireless transmissions is making our lives increasingly connected, new applications like Machine-to-Machine (M2M) communication are being established, among which the Internet of Things (IoT) is a subset. This type of application deals with real-time or near real-time communications between connected objects, devices and people, through wired or wireless communication channels. M2M communication is currently undergoing a fast development growth in the industry domain with applications like tracking device, machinery maintenance, and stocks management using RFID. IoT can be applied to the public as well as private sectors and usually offers longer transmission ranges. Smart cities, smart homes, eHealth and wearables are good examples of possible future outlooks. With the technology progress and cost reduction of connected objects, these kind of services will soon be available for mass-market. Unlike smartphones, the wireless devices that would be used for this market do not require high data-rates and can sustain on narrowband transmissions. A plethora of narrowband wireless technologies can be envisioned for this purpose, like Bluetooth or wireless Meter-Bus [I.3] for extremely short range (couple of centimeters to 100 meters) and ultra-narrowband SIGFOX, narrow-band IOT and LoRa for longer range wide-area networks. The main benefit of these connectivity solutions is low-power consumption which is very important for self-powered devices (like solar-powered or battery-fed devices).

Even though low throughputs are sufficient for this type of applications, M2M and IoT are still heavily contributing to the further increase of traffic load on communication networks, including mobile network, by the large number of connections they represent. Indeed, by 2023, M2M and IoT connections will represent 63% of the total connections on the wireless network, according to Ericsson. As shown in the forecast shown in Figure I.2 below, the number of connected M2M and IoT devices is expected to grow from 7 billion in 2017 to almost 20 billion in 2023. This market represents the most dynamic evolution in the telecommunication sector, compared to smartphones and other platforms.

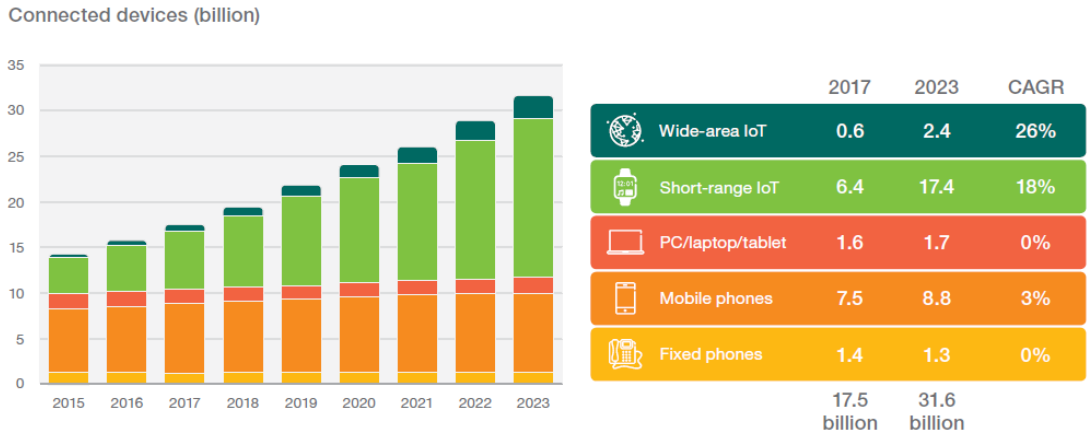

Figure I.2. Internet of Things connected devices installed base worldwide from 2015 to 2025 (in billions) from [I.1].

2. Consequence on the wireless data traffic

As shown above, the explosion of smartphone users and LTE subscriptions topped with the advent of IoT is generating and will continue to generate a tremendous amount of digital data. As a consequence, the wireless data traffic supported by the mobile communication network is expected to grow at a 42% compound annual growth rate until 2023 with a forecast global data traffic of 110 exabytes per month as shown in Figure I.3, from which 95% will come from smartphone connections only [I.1]. To a large extent, multimedia applications like augmented and virtual reality or HD broadcasting will increase the amount of data-intensive contents enabled by improved capability devices. Indeed, more than three fourth of mobile data traffic will be video in 2021, accounting for 78% of the total wireless data traffic.

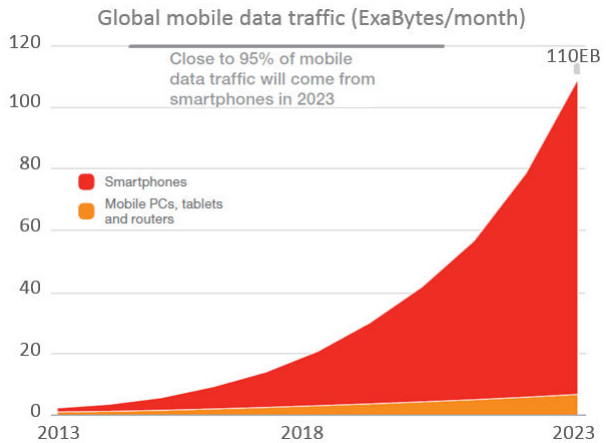

Figure I.3. Global mobile data traffic in ExaBytes per month from [I.1].

3. Advent of the 5G network

The witnessed explosion of global wireless data traffic coming from smartphones and a growing IoT industry puts a lot of pressure on the wireless network with overloaded access points. As a result, typical data-rates and latency experienced by users are degraded due to overshared bandwidths (BW). Therefore improving the capacity of wireless networks in close proximity to the user-end has become a priority for telecom operators in order to address the increasing demand for higher data-rates. A transition towards 5G networks will indeed promote ubiquitous access to Enhanced Mobile Broadband (eMBB) services and Fixed Wireless Access (targeting the last miles connection), and thus enable a

wide range of new use-case scenarios, devices, and applications. To support these applications, new air interfaces called New Radio (NR) are being developed so as to enable transmissions across a wider frequency band allocation. These NR will be built on standard technologies that ensure backward and forward network compatibility (compatibility between 4G and 5G for instance) and thus contribute to network flexibility. To do so, adequate strategies must be adopted so that operators can best build around the existing network while minimizing roll-out costs and energy consumption.

a. 5G performance goals

The telecommunication specifications for the future generation network are set through a consortium between key industrial players and organizations like the International Telecommunication Unions (ITU) and the 3rd Generation Partnership Project (3GPP). Those meetings set the major requirements of the telecommunication network (shown in Figure I.4) to tackle the current performance limitations and address the consumer's demands. The key drivers for 5G revolve around the following areas.

High capacity at low cost: Deployment of small cells combined with a reduction in cost-per-bit and lower energy-per-bit, which implies low cost/power technologies.

High data-rate: 5G mobile networks will deliver up to 10 Gb/s peak data-rates indoor or in very dense areas and at least 100 Mb/s at cell edge.

Very low latency: To support latency-critical applications, the latency will be reduced from 100 ms to 1 ms or less.

High mobility: High quality of service should be delivered by 5G for all users including users moving at a speed of up to 500 km/h. Efficient handover between different base stations is therefore required.

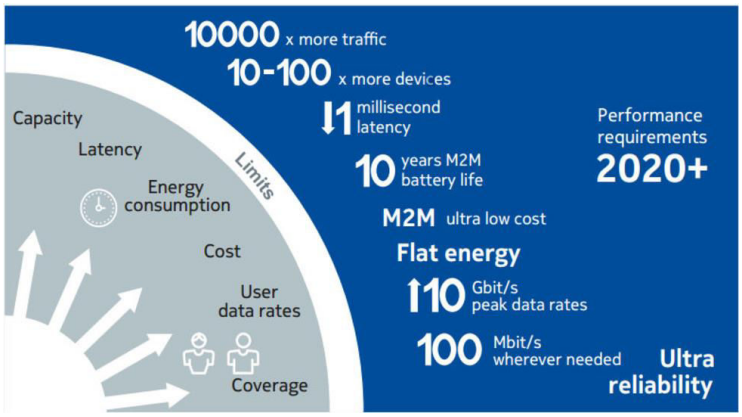

Figure I.4. 5G performance requirements for 2020 from [I.4].

b. Spectrum allocation strategy

As 5G applications call upon different technical requirements depending on the use-case scenario, bespoke optimization of the 5G link design is needed [I.5]. For instance, while virtual reality requires very low latency and ultra-high speed connections, industrial automation and connected driving will need high reliability radio links and short to long transmission range. Therefore, adequate allocation of the frequency spectrum is an important aspect of 5G technology standardization discussion in order to leverage different characteristics at different portions of the spectrum.

A short term 5G roll-out strategy consists in enhancing the existing 2G, 3G and 4G LTE infrastructure in order to offer wide coverage and higher capacity for enormous device connections like massive M2M and IoT. This enables 5G installation in a quick and cost-effective manner by mostly using the

low and mid frequency bands (below 6 GHz). In this context, the first non-standalone 5G standard (Release 15) was finalized by the 3GPP at the end of 2017, mainly targeting new frequency channels available in C band and LTE/5G NR interoperability. This means that operators can now start preparing for 5G large-scale roll-out on the basis of standardized technologies. A number of early technical trails are already being launched in order to enter the marketplace by 2019.

At a longer term, the World Radio-communication Conference 2015 (WRC-15) has initiated regulation discussions for the future International Mobile Communication on higher frequency bands. The development of new technologies would target the deployment of extreme mobile broadband networks at mmW carrier frequencies (from 20 GHz up to 100 GHz) to leverage wider frequency BWs and ensure much higher network capacity. As a result, speed, latency and reliability will be improved. The specifications of NRs for the standalone version of 5G (development of a new 5G infrastructure) have recently been signed off by the 3GPP in June 2018 and commercialization of the new 5G core network is expected by 2020. These NRs will be particularly appropriate for data offloads in very dense traffic areas, intensive-data content applications, real-time transmissions and mission-critical services.

c. Frequency spectrum below 6 GHz

Reusing LTE and existing networks, 5G can be deployed by replacing the radio head of existing base station sites in order to support NR in the C band (3.3-4.2 and 4.4-5 GHz). The C-band allocation planning that is actually under consideration for 5G is shown in Figure I.5 and has been extracted from Huawei 5G Spectrum Public Policy Position report [I.6]. This approach is incremental (and perceived less risky) since operators will first deploy existing LTE technology on wider BWs available at frequencies similar to what was used for 4G (moving to 3.5 GHz instead of 2.5 GHz). One of the main benefits of using the spectrum below 6 GHz is low free-space propagation loss compared to mmW frequencies. As a result, wide areas can be covered and long transmission ranges can be reached which makes this network particularly convenient for Non-Line-of-Sight transmissions within macro cells. In terms of network capacity, the C-band will enable to deliver at least 100 MHz contiguous frequency BWs to each 5G network in order to provide user-experience data-rates uplink and downlink of up to 1 Gb/s. Widening of contiguous spectrum also allows to move away from the carrier aggregation approach thereby reducing the cost-per-bit and improving the energy efficiency. This capacity improvement is supported by the combined use of LTE bands below 2 GHz in order to enable smart allocation of BW resources depending on the needs as well as coverage extension. Therefore, an important aspect of 5G roll-out below 6 GHz is for operators to ensure interoperability between existing LTE bands and the new C band by developing NR technologies that are compatible with LTE radio heads. In a nutshell, a smart distribution of available bands below 6 GHz between uplink and downlink transmissions allows higher spectrum efficiency and bespoke allocation of spectrum resources depending on the use-case scenario. This spectrum framework also ensures a smooth introduction of the latest technologies for long-term migration of LTE to 5G.

Supporting duplex flexibility is also a major point of 5G in order to allow more flexible use of the spectrum resources. Frequency Division Duplexing (FDD) has been widely used in previous network generations and will remain the main duplex mode for bands below 2 GHz. However, the higher C band will be mostly working on Time Division Duplexing (TDD) scheme in order to allow a more dynamic allocation of communication capacities in 5G networks. Moreover, TDD would also enable to simplify the antenna-system since frequency duplexer filters are no longer needed which would also help in

reducing equipment costs. In this approach, time slots can be dynamically allocated to different uplink or downlink transmission needs, thereby providing optimum data-rate and latency in very dense areas.

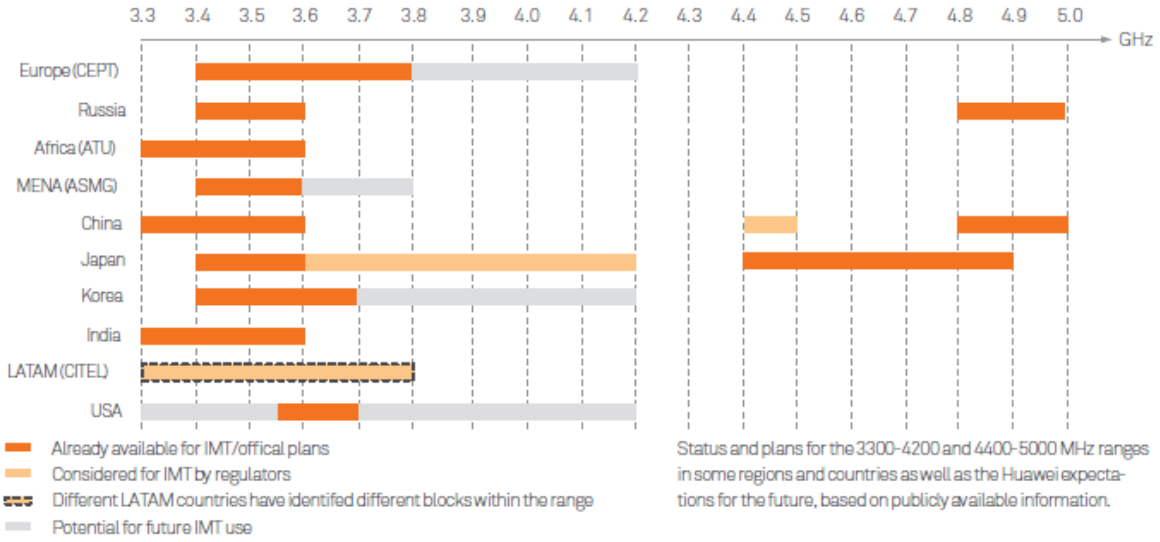

Figure I.5. Global availability and planning of the 3300-4200 MHz and 4400-5000 MHz frequency ranges (C band) for 5G from [I.6].

d. Frequency spectrum above 6 GHz

To achieve the performance promised by the 5G network in terms of data-rate and latency, several frequency bands above 6 GHz are also considered to leverage wider contiguous BWs (from 800 MHz to 10 GHz) [I.5], [I.6]. The spectrum under study is located between 24.25 and 86 GHz and promotes peak data-rates of up to 20 Gb/s in download and 10 Gb/s in upload while user-experience data-rates at cell-edge will reach 100 Mb/s. To operate on this new spectrum, the progresses made in Silicon CMOS and BiCMOS technologies led to the development of new highly integrated radio frequency circuits (RFIC) providing cost-effective, compact and low power consumption mmW transmission systems. In addition, these very dense areas will also make use of TDD to enable dynamic allocation of resources where fluctuating traffic conditions are observed. Figure I.6 represents the main frequency band candidates in scope of the World Radio-communication Conference 2019 meeting (WRC-19) for future mobiles communication [I.6] along with the 60 GHz LTE license-free band.

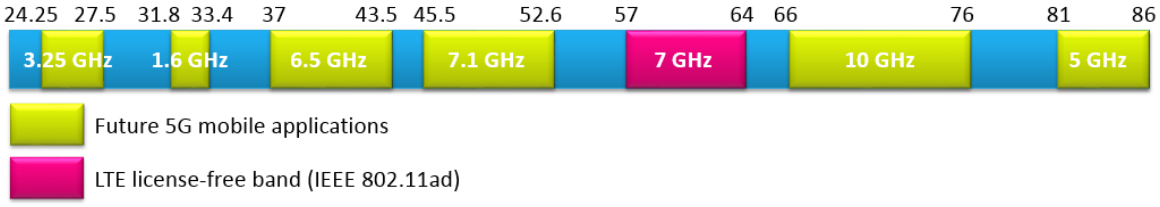

Figure I.6. Mobile communication candidate frequency bands of WRC-19 Agenda Item 1.13 from [I.6] *and 60 GHz LTE license-free band (GHz).*

II. Mobile network architecture challenges

Even though 4G and LTE-A network generations address peak theoretical data-rates in the order of 1 Gb/s, the user-experience downlink data-rates are actually a hundred times less. According to Akamai's sate of the internet report in the first quarter of 2017 [I.7], the average

peak data-rate experienced is 50 Mb/s and the typical data-rate is no higher than 4 Mb/s. In front of such a discrepancy between theoretical and real data-rates supported by the 4G network, a solution for the 4G to 5G transition consists in densifying the telecommunication network by multiplying the number of cells as well as decreasing their size (owing to small cells and pico cells) in order to guarantee high data-rate coverage promised by 5G (Figure I.7). To enable these requirements at the cell level, the implementation of specific solutions on the backbone network will play an important role towards the modification of Radio Access Network (RAN) architecture.

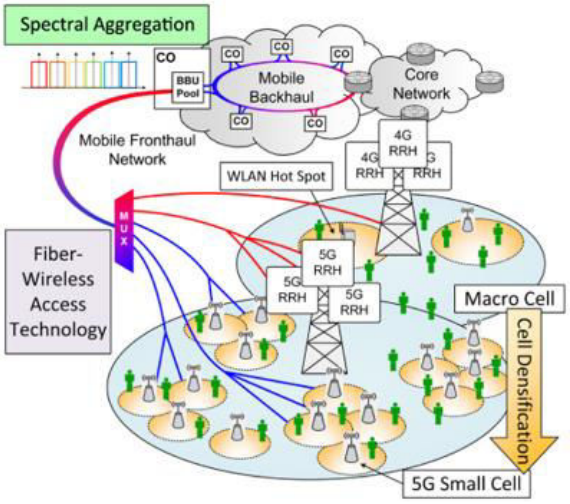

Figure I.7. 5G mobile network densification with small cells and Centralized RAN architecture from [I.8].

1. From Distributed-RAN to Cloud-RAN architecture

The RAN has been the critical asset that bolsters the mobile communication network. Therefore the telecommunication industry has made tremendous progress in mobile network performance over the past decade by optimizing the RAN architecture. Indeed, the data traffic exponential growth puts a constant pressure on fronthaul/backhaul data management. Hence it is essential to find the best way to partition the associated signal processing burden between the Remote Radio Head (RRH) and the Base Band Unit (BBU) in order to maximize the overall throughput. In a basic Distributed-RAN (D-RAN) architecture, the baseband processing is implemented at each antenna base station (BS) and interconnected to the RRH with a short Common Public Radio Interface (CPRI) link. Consequently, BS upgrades need to handle more demanding data-rate requirements which results in a drastic power consumption increase per BS as well as high technology upgrade and maintenance costs. Adopting Centralized-RAN (C-RAN) architecture enables to reduce this cost by deporting the BBU from the BS to the central office (CO). This approach greatly simplifies the RRH design and footprint at the antenna site (as shown in Figure I.7 above) and concentrates BBU servicing and maintenance operations to a unique and dedicated space. As BBUs are clustered together, the interconnections between them become much shorter (Figure I.8). This approach enables much lower latency (typically < 1 ms) between BBUs, which allows tighter coordination of the neighboring cell antennas (through Enhanced Inter-cell Interference Coordination and Coordinated Multi Point transmission/reception). However, this has to be balanced against much longer CPRI links for Digital Radio-over-Fiber (RoF) as shown in Figure I.8.

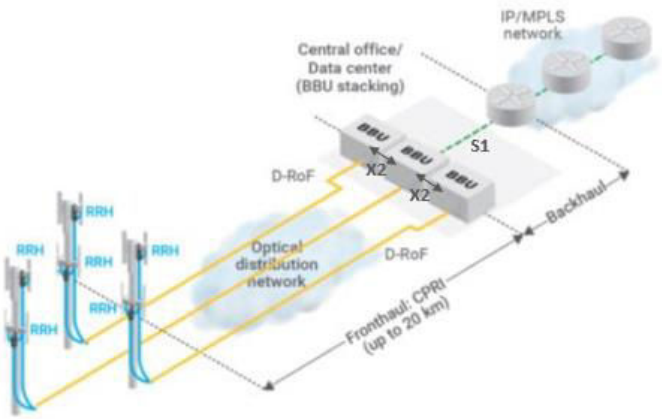

Figure I.8. Centralized-RAN architecture [I.9].

The different RAN architecture configurations presented above combined with 5G's accelerating demands pushes the CO's functions into the "Cloud" through the use of network functions virtualization techniques. In this approach, the standalone BBU devices will be virtualized (vBBU) using a common off-the-shelf server, like the x86 based platform for example, consisting of multiple virtual machines (VM) each paired to a vBBU as shown in Figure I.9. This enables great complexity reduction of the CO platform and has much more efficiency in terms of power and CPU utilization. Most importantly, replacing hardware equipment by software enables much lower cost of ownership of the network. This virtualization also allows operators to transfer several BBU functions directly to remote data-centers possibly closer to their geographical locations, taking advantage of data-center state-of-the-art IT technologies. Moreover, data-centers benefit from higher scalability than traditional BBU pooling hotels (an additional VM can be implemented in seconds) and instantaneous load balancing with dynamic allocation of VMs. Hence this approach reduces the time-to-market for new applications like IoT or M2M and allows real-time processing for high-speed applications such as virtual reality. Overall, the industry is now looking into implementing Cloud-RAN architecture, by exploiting the benefits of distribution, centralization and virtualization techniques in order to find the right balance between cost and data-rate.

We can now see how the implementation of Cloud-RAN has the potential of greatly improving the speed capacity of signal processing. However, two major aspects need to be addressed in order to take full advantage of what Cloud-RAN has to offer. Firstly, a sufficient number of CPRI links should be deployed in the fronthaul/backhaul network in order to transfer the processed signal back to each small cells. Secondly, these CPRI links should achieve high enough digital data-rate to leverage Cloud-RAN's increasing data-rate capacities. Those issues will be tackled in the following sections.

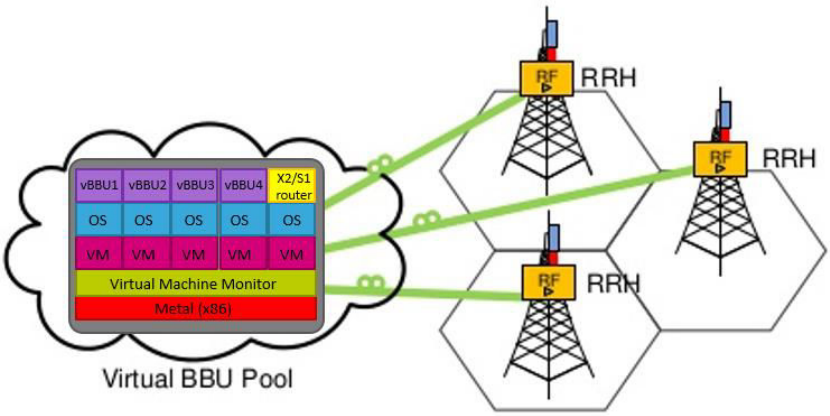

Figure I.9. Cloud-RAN with virtual BBU Pool.

2. Wireless fronthaul/backhaul opportunity

In a context where small cells are being massively deployed, the optical CPRI link distribution has to be dense enough to be able to reach each and every intra-cell sectors. Within the 5G Infrastructure Public Private Partnership (known as 5GPPP), the availability of such an optical network was identified as one of the major threats to 5G rollout, especially in dense areas. Therefore, discussions have also been set up so as to consider access-network densification strategies in a cost-effective manner. The implementation of fronthaul/backhaul optical fiber requires significant roadway construction work such as civil engineering work which is costly, slow and very disruptive. As an alternative to Fiber-To-The-Antenna, the implementation of CPRI broadband wireless links (Wireless-To-The-Antenna) shown in Figure I.10 has become an attractive solution for mobile operators as it can be directly located at the BS site and therefore installed in a cost-effective and timely manner [I.10], [I.11]. These links can be used for wireless P2P communications between BSs with directive antennas and dynamic connectivity to the backbone network can even be considered with beam steering thereby increasing resource allocation flexibility [I.12].

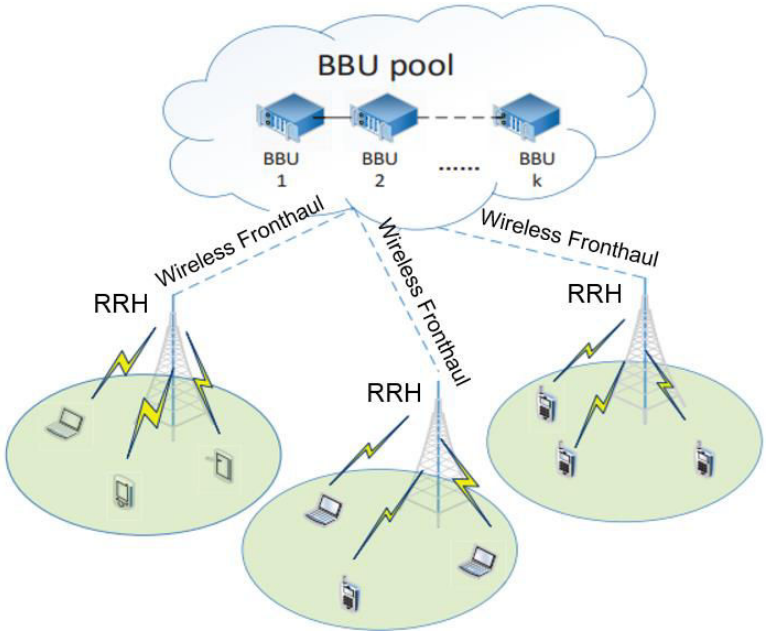

Figure I.10. System model of C-RAN architecture with wireless fronthaul from [I.11].

III. Data-rate requirements for backhaul wireless links

1. Existing wireless technologies enabling data-rates up to 10 Gbps

Wireless links have proven to be a cost-effective alternative to optical fiber deployment with mmW wireless CPRI links. In order to progressively mitigate the data-rate bottleneck actually placed upon the fronthaul/backhaul links, several wireless radio head products operating up to 10 Gb/s over several kilometers have been developed and commercialized. Amongst these products, Siklu is proposing 60 GHz and 70 GHz band radio systems in compact packages [I.13] like the one shown in Figure I.11 (a), deployed in streets or on rooftops. This system features an integrated mmW antenna and transceiver capable of delivering up to 1 Gb/s data-rates at distances as long as 2.6 km. E-link Eagle also proposes 70/80 GHz solutions for macro-cell backhaul links [I.14] with radio heads achieving from 1 to 3 Gb/s at a maximum range of 8 km (Figure I.11 (b)). In order to increase the achievable data-rate up to 10 Gb/s for longer wireless communication range, E-band wireless systems operating in the 71-76 GHz and 81-86 GHz bands in full-duplex capacity have also been developed by CableFree (Figure I.11 (c)) [I.10]. These radio heads can cover from 1.5 km up to 20 km range with 10 Gb/s Ethernet interfaces, thereby promoting a competitive solution versus optical fiber which is satisfactory for fronthaul/backhaul network densification.

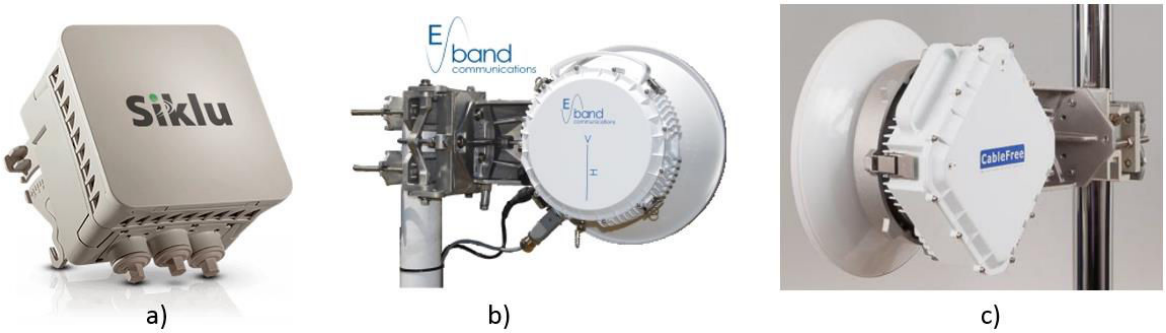

Figure I.11. (a) V-band Siklu etherhaul up to 2 km range radio head from [I.13]*, (b) E-band Eagle up to 8 km range radio head from*[I.14]*, (c) E-band CableFree up to 20 km range radio head from* [I.10]*.*

The large and still under-used frequency bands available above 100 GHz also represent a great interest for broadband high-speed wireless applications enabling higher data-rate or lower modulation complexity (and thus lower power consumption). Figure I.12 is extracted for the spectrum allocation of the FCC Table of Frequency Allocations [I.15]. As reported in [I.15], the main frequencies bands between 100 GHz and 200 GHz are basically used between wireless terminals (mobile network) and for P2P communications (fixed network). For wireless applications, the entire available BW elevates to 55 GHz, and the band around 120 GHz alone represents a 26 GHz contiguous BW for mobile applications and 18 GHz contiguous BW for fixed applications. Several transceiver systems operating above 100 GHz are reported in the literature, and in paper [I.16] specifically, a transmitter (Tx) based in InP mHEMT technology has been developed at 125 GHz. Outdoor data communication at 10 Gb/s has been successfully demonstrated over a distance of 5.8 km using a simple Amplitude Shift keying (ASK) modulation scheme. This performance is a good illustration of the major benefit that higher frequency bands are capable of offering: achieving high data-rates while operating on ASK modulation schemes and thus reducing the overall power consumption.

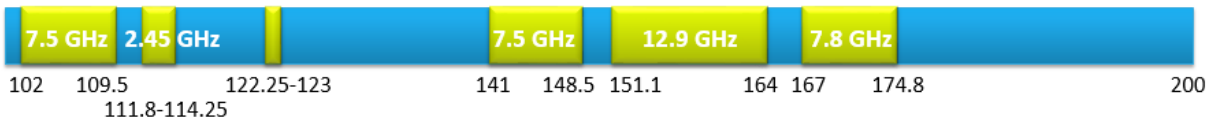

Figure I.12. Frequency spectrum allocation between 100 GHz and 200 GHz by the FCC for fixed and mobile applications from [I.15].

2. Growing need towards wireless solutions up to 40 Gbps and above

Up to a certain point, the frequency bands proposed above will however become limited, due to an accelerating consumer demand for 5G communication capacities. This enforces very heavy constraints on long-distance digital CPRI transmissions. Indeed, as digital signals are heavier than analog signals in terms of data-rate, these CPRI links require minimum latency and very large frequency BWs. For example, in an LTE scenario delivering 150 Mb/s download speed with a 2x2 Multiple-Input Multiple-Output (MIMO) antenna, each RRH will require the CPRI capacity of 2.4 Gbps [I.17]. Moving to 5G NRs (much wider BWs), a download speed of 3 Gb/s would therefore introduce 48 Gb/s data-rate requirement on the CPRI link. Therefore 10 Gb/s wireless fronthaul/backhaul links will grow to become very quickly outdated. To overcome this issue, wireless P2P systems operating from 40 Gb/s to 100 Gb/s over at least 100 m distance are a good starting point so as to considerably help in supporting the growing amount of aggregated data in the backbone network.

3. Unlicensed frequencies above 200 GHz

Aiming at wireless links delivering between 40 Gb/s and 100 Gb/s with the lowest possible DC power consumption, simple amplitude modulation schemes such as OOK or PAM4 are preferred. Indeed, less complex signal processing circuitry can be used, thereby requiring lower power supply. The resulting very low spectral efficiency (1 bit/Hz in baseband for OOK) make it necessary to operate on very wide frequency bands to sustain such high throughputs. Indeed, Shannon's formula shown in Equation (1) demonstrates that the data-rate capacity is directly proportional to the BW:

$$C = B * log_2\left(1 + \frac{S}{N}\right) \quad (1)$$

Where *C* is the capacity (bit/s), and *S/N* the signal-to-noise ratio (SNR). Because the wireless link budget strongly depends on the physical characteristics of the transmission path, it is important to identify atmospheric windows that are appropriate for wireless transmissions. Figure I.13 shows the atmospheric attenuation (in dB per km of propagation) as a function of the carrier frequency. Therefore, a first frequency recommendation would be in the THz band between 200 GHz and 320 GHz where a wide low-loss window is encountered between two absorption peeks. This very wide BW would indeed enable high data-rate wireless communication applications of up to 60 Gb/s using OOK modulation.

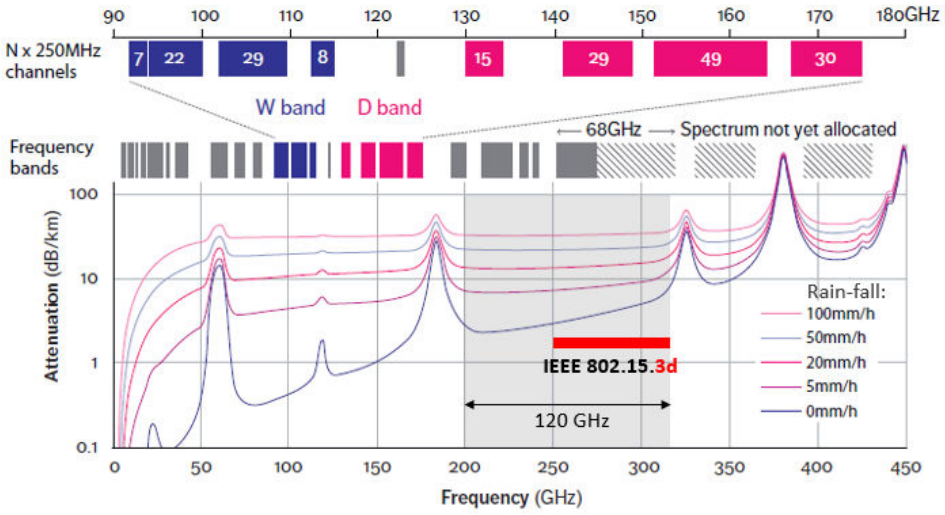

Figure I.13. Atmospheric attenuation of electro-magnetic propagation in are from DC to 450 GHz, with diagram of frequency bands.

This wide sub-mmW/THz band opportunity has triggered a strong interest amongst the academic and industrial community for the development of THz transceivers. However, the SNR remains the main limitation as mmW/THz available output power level tends to decrease when the frequency increases.

In this context, the potentiality of power-efficient THz wireless systems has opened up an even wider panel of marketable high-speed communication applications as shown in Figure I.14, such as very fast indoor internet access (similar to WiFi applications), user-experience instantaneous kiosk downloading or battery charging stations, wireless peripheral-to-computer docking stations or daisy chains and chip-to-chip interconnections.

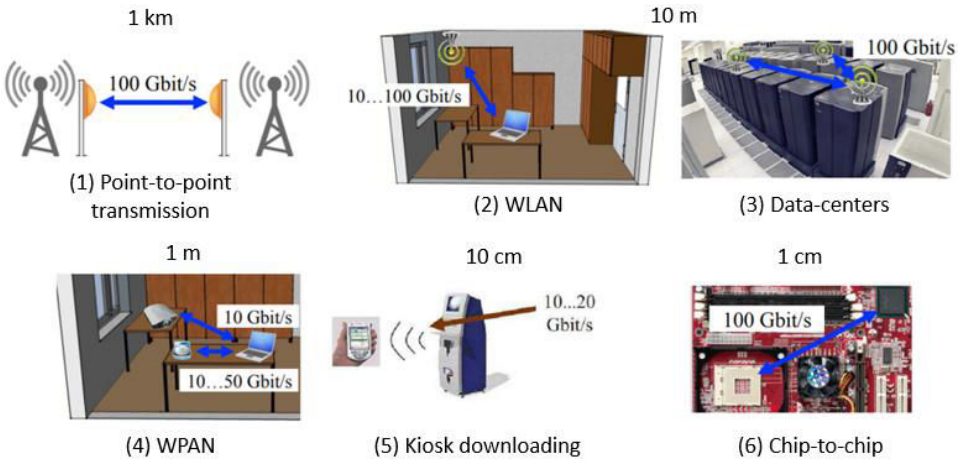

Figure I.14. Scenarios of THz power-efficient communication applications: (1) P2P transmission, (2) indoor wireless local network (WiFi type), (3) Data-centers,(4) indoor wireless personal network (peripheral-to-computer connection), (5) kiosk downloading, (6) chip-to-chip interconnections from [I.18].

To contribute to the research and development of high-speed THz links, the work presented in this PhD dissertation focuses on evaluating the THz propagation window between 200 GHz and 300 GHz for low-cost wireless links capable of operating at up to 100 Gb/s. However, it is important to note that a specific THz band was officially designated no sooner than September 2017 for the new IEEE802.15.3d standard. This IEEE standard is targeting the 100 Gb/s wireless P2P physical layer for

high data-rate wireless multi-media networks [I.19]. The frequency spectrum was allocated between 252.72 GHz and 321.84 GHz (as shown in Figure I.13 in red) which represents a contiguous BW of 69.12 GHz with the possibility to use smaller portions for multi-channel transmissions.

IV. Sub-mmW and THz all-electronics transmitter systems

1. Transmitter technology evolution from mmW to THz

Devices used in radio access points have been governed by Si-based technologies since they enable the development of low-cost and highly integrated transmission systems. Moreover, the continuous technological progress ruled by Moore's law allows for transistors to operate at ever-higher frequencies as shown in Figure I.15 (a), enabling the massive development of high-speed and low-cost wireless systems at frequencies up to 100 GHz. For this reason, they have been widely investigated for the development of communication systems up to 100 GHz in order to enable cost-effective high-speed wireless technologies. Indeed, as transistors are being scaled down in size, higher operating frequencies are becoming accessible. This is mainly realized by reducing the transistor's gate length thanks to higher lithographic process resolutions (as shown in Figure I.15 (b)) and the minimization of parasitic effects like capacitance. These improvements increase the maximum unity current gain cut-off frequency, also called transition frequency (f_T) and the oscillation frequency (f_{max}) of transistors. Indeed, in 0.13 µm SiGe BiCMOS technology, f_T and f_{max} of up to 300 GHz and 500 GHz respectively have already been reached [I.20].

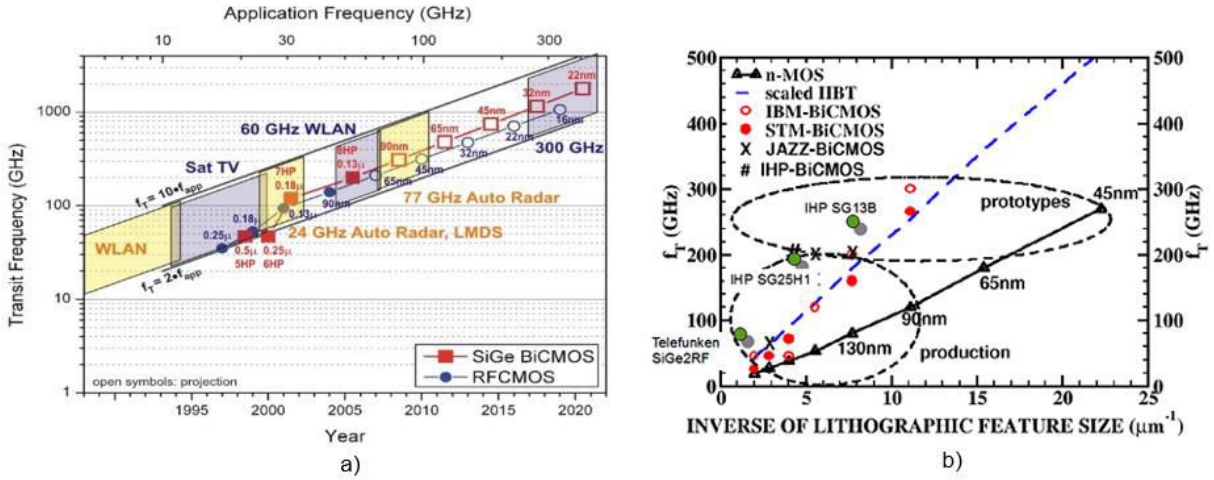

Figure I.15. (a) Projection of transit frequency for SiGe BiCMOS and RFCMOS technologies versus technology node and year from [I.21]*, (b) and Comparison of ultra-scaled CMOS and SiGe HBT technologies with respect to f_T from* [I.22].

The release of IEEE802.11ad standard providing high data-rates in the 60 GHz band led to the design and development of 60 GHz CMOS transceivers in order to support massive production of CMOS-based radio head integrated circuits (ICs). Several amplifier-based transceivers are reported in the literature in order to demonstrate the potentiality of wireless data communication in the 60 GHz frequency bands. Paper [I.23] for example presents a fully-integrated 60-GHz transceiver system, meaning Tx and receiver (Rx), in 90nm-CMOS technology with on-board low-cost patch-antenna array and is shown in Figure I.16 (a). This prototype operates on OOK modulation scheme which enables to avoid very complex baseband Digital-to-Analog Conversion (DAC) circuitry. The fabricated Tx has demonstrated low power consumption (183 mW) and achieved error-free PRBS transmission (BER < 10^{-12}) at a data-

rate of 1 Gb/s over a distance of 60 cm. Other 60 GHz wireless demonstrations have achieved up to 2.31 Gb/s (QPSK modulation) over a distance of 3.6 m and 4.62 Gb/s (QAM16 modulation) over a distance of 70 cm while consuming 980 mW DC power [I.24] (Figure I.16 (b)).

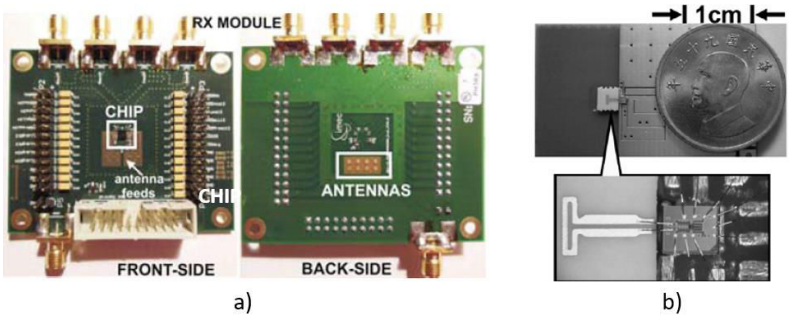

Figure I.16. (a) Board assembly of the 60 GHz transceiver from [I.23]*, and (b) board assembly (front side with flip-chip mounted die and back side with patch antennas) of the 60 GHz transceiver from* [I.24].

Operating in the 70/80 GHz band, a single-chip wireless transceiver is presented in [I.25] with its die shown in Figure I.17 (a). The Tx was fabricated in 130 nm SiGe BiCMOS technology and achieved above 10 Gb/s data-rate using QPSK modulation for a DC power consumption of 1.2 W. Another demonstration between 70 GHz and 100 GHz is presented in [I.26] with the fabrication of a Tx and Rx phased-array chipset in 180nm SiGe CMOS (Figure I.17 (b)). DC power supplies of 1 W was required and a wireless link operating at 10 Gb/s was achieved at a 1 m distance using 16-QAM modulation. Hence, based on these wireless demonstrations and in [I.27], CMOS-based transceivers seem to fit the required performance in terms of data-rate for V-band (60 GHz) and E-band (70/80 GHz) short-range transmission applications. Moreover, as shown in section II.2, long distances (> 2 km) are also achieved by several market-ready V-band and E-band CMOS-based wireless products. For example, Siklu's mmW transceivers are based on CMOS and SiGe technology.

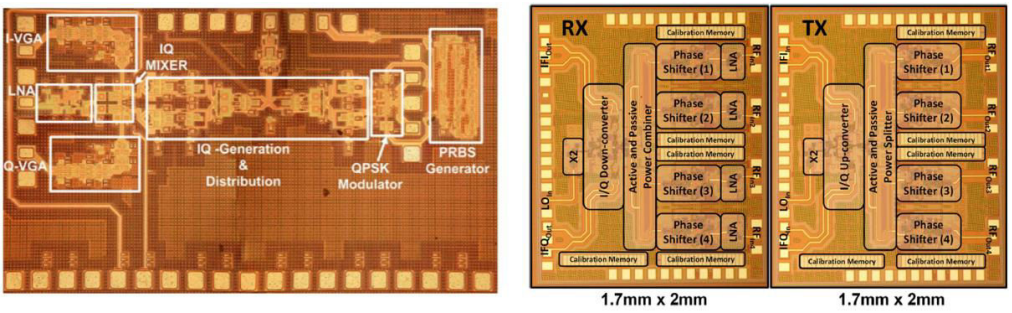

Figure I.17. (a) Die photos of the transceiver in the 70/80 GHz band from [I.25] *, and (b) the 70/100 GHz band from* [I.26].

Above 100 GHz, CMOS-based wireless solutions have also been developed. A 100 GHz fully integrated Tx with two on-chip antennas is presented in [I.28]. The Tx has been fabricated in 45nm CMOS technology and features an RF I/Q Digital-to-Analog converter architecture. A peak output power of -17 dBm and an Equivalent Isotropic Radiation Power (EIRP) of 15.7 dBm were achieved at 100 GHz with an associated DC power supply of 1.27 W. Data communication measurements at a distance of 18.9 cm have shown up to 10 Gb/s with QPSK modulation. In [I.29], a D band transceiver fabricated in 65 nm CMOS technology is described (and shown in Figure I.18 (a)). A data communication demonstration at 140 GHz was realized at a very short range (> 10 cm) with OOK modulation for direct detection. The achieved data-rate reached up to 2.5 Gb/s at a DC power

consumption of 115 mW. Another 140 GHz Tx integrated in 45nm CMOS technology is presented in [I.30] and shown in Figure I.18 (b). This wireless system achieved 2 Gb/s at a short range distance of 1 m using QPSK modulation with a power supply of 220 mW. Therefore, these examples demonstrate the possibility to develop CMOS transceivers at over 100 GHz for high-speed wireless communication applications.

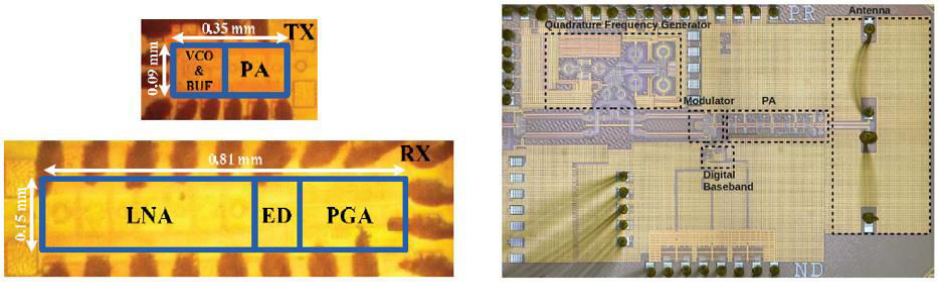

a) b)

Figure I.18. (a) Photograph of the 140 GHz Tx and Rx in [I.29]*, and (b) of the 120 GHz transmitter in* [I.30].

The successful development of wireless CMOS circuits in the V and E bands, followed by some promising wireless transceiver designs above 100 GHz opens the way for transceivers operating above 200 GHz based on Silicon technologies. Therefore, a large part of the RFIC research community has been working on the development of solid-state transceiver designs in order to evaluate achievable performance of CMOS technologies in the sub-mmW and THz frequency band. However, as the required carrier frequency is increasing beyond the transistor's f_{max}, the design of sub-mmW and THz frequency generation systems in CMOS technology is still challenging when it comes to delivering sufficient power over wide BWs while maintaining an acceptable power consumption. Indeed, the continuous size scaling of CMOS technology has also resulted in lower voltage breakdown of transistors and higher gate resistance, among other issues. This severely limits the power generation capability at sub-mmW frequencies and it significantly reduces the power efficiency of transistors when operating close or above the f_{max}. Hence, stacked amplification stages and power combining techniques are often needed to increase achievable output power, leading to higher power consumption and lower BW. Tackling these performance limitations, two system solutions are being employed: the first one consists in up-conversion from a lower Intermediate Frequency (IF) thanks to frequency multiplier chains, the second one uses oscillators to directly extract the THz frequency of higher order harmonics.

2. THz frequency CMOS-based transceivers

Designing multiplier chains operating on very low IF (generally much below one-half the f_{max} of the transistors in the design) is often used as a strategy to increase the conversion gain of the THz transceiver. Taking for example frequency multipliers fabricated in 130 nm SiGe CMOS technology offering an f_T /fmax of 300GHz/500GHz, the study presented in[I.20] and [I.31] is proposing different strategies to achieve sub-mmW signal generation above 200 GHz. In paper [I.20], a 240 GHz sixtupler was developed with a first nonlinear differential amplifier used as a tripler and a Gilbert-cell based doubler as shown in Figure I.19 (a). With an IF of 40 GHz, a peak RF output power of -4 dBm was achieved with a DC power supply of 900 mW and a -3dB gain BW of 15 GHz (6.5%). Furthermore, it should be noted that by choosing a lower IF (between 14 GHz and 17.5 GHz for example), a major advantage is the possibility to implement external commercially available low-power consumption and high performance frequency synthesizers below 20 GHz to generate the IF input, as presented in paper

[I.31]. In this paper, a wideband x16 multiplier chain combined with a 3-stage power amplifier (PA) (shown in Figure I.19 (b)) allowed to achieve a peak output power of 0 dBm at 245 GHz thanks to lower conversion losses, with a -3 dB BW of 30 GHz (12%) for a DC power consumption of 700 mW.

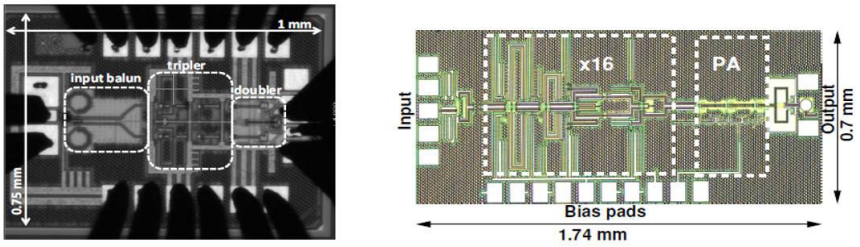

Figure I.19. (a) Chip photograph of the sixtupler from [I.20]*, and (b) the x16 multiplier from* [I.31].

However, other circuit designs, possibly using transistors with lower performance in terms cut-off frequency, can also require further signal amplification in-between multiplier chains, which can make this low IF approach inadequate in terms of power consumption, gain or BW. For example, two 325 GHz frequency multipliers produced in 130 nm SiGe CMOS technology offering a f_T/fmax of 250 GHz/380 GHz are presented in [I.32]. The first design consists of x18 multiplier chains equipped with two frequency triplers and a frequency doubler to up-convert an IF signal of 18 GHz to 325 GHz. Its chip photograph is shown in Figure I.20 (a). In order to achieve an output power of -3 dBm, a narrowband 2-stage driver amplifier was used after the first tripler and a narrowband 3-stage PA was used after the second tripler. As a result, a high DC power consumption of 1.6 W was needed and an overall narrow -3 dB gain BW of 11 GHz (3.4%) was achieved. The second design shown in Figure I.20 (b) consists of a 3-stage PA and a doubler to up-convert an input signal of 162.5 GHz to 325 GHz. This design was able to achieve an equivalent output power of -3 dBm through a wider -3dB BW of 20 GHz (6.3%) and with a lower DC power supply of 420 mW compared to the first design, at the expense however of a more complex and power-consuming external IF synthesizer at the input.

Overall, THz power generation close to the transistor's cutoff frequency f_{max} is considered as a difficult design challenge in Silicon CMOS/BiCMOS technologies where bespoke circuit design optimization and trade-offs are often required to overcome the transistors performance limitations. Moreover, as the gain and BW of transistors become limited above their cutoff frequency, there is no published THz (> 300 GHz) high gain amplifier in CMOS/BiCMOS technology.

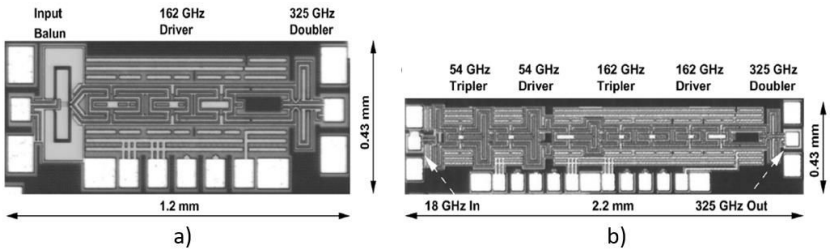

Figure I.20. Micrographs showing the (a) 325-GHz active doubler, and (b) 325 GHz x18 multiplier chip from [I.32].

Another solution consists of using Harmonic Oscillators or Voltage Controlled Oscillators (VCO) as a replacement for multi-cascaded multiplier and/or amplifier chains. Therefore, lower power consumptions have been achieved with VCOs while maintaining an output power above -2 dBm (630 mW with the amplifier-based design at 220 GHz in [I.32] compared to 167 mW with the VCO+doubler design at 290 GHz in [I.33]). Above 300 GHz, VCOs are also used inside Phase-locked loops or Injection-

Locked Oscillators so as to keep the phase match between the VCO input and output to stabilize the output frequency. This design configuration is a considerable asset for the development of CMOS transceivers above 300 GHz where phase noise needs to be minimized. Furthermore, as shown in [I.34] a majority of the reported THz power generation designs are based on fundamental and high-order oscillators rather than amplifiers due to the gain limitation of available Silicon transistors. Another popular approach is the use of passive multipliers based on Schottky diodes or III-V technology active multipliers.

3. Wireless data communication demonstrations with CMOS-based transceivers above 200 GHz

Several data communication demonstrations above 200 GHz have been reported in order to evaluate the maximum achievable data-rate of CMOS-based wireless links at sub-mmW frequencies. Paper [I.35] describes a fully integrated 240 GHz Tx based on a x16 multiplier in 0.13µm SiGe Bi-CMOS technology. An on-chip antenna topped with a 12 mm Silicon lens allows free-space radiation. The transceiver and its complete assembly system is shown in Figure I.21. The data-com measurements were realized with an output power of -14 dBm at 240 GHz, way below the saturated power of the transceiver in order to maintain the signal integrity. A Bit Error Rate (BER) below 10^{-3} was achieved at a data-rate of 24 Gbps using QPSK modulated signals at a distance of 20 cm.

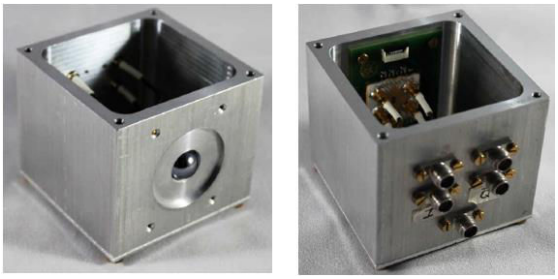

Figure I.21. Photograph of the front view and the back view of the 240 GHz multiplier-based transceiver package from [I.35].

In [I.36], fully integrated wideband 240-GHz transceiver with on-chip antenna is presented in 130 nm SiGe BiCMOS technology. The Tx, shown in Figure I.22 (a) consists of a Gilbert cell mixer driven by a x8 frequency multiplier chain. The Tx achieved a -3dB BW of 35 GHz with a peak output power of −0.8 dBm. An on-board lens was utilized to collimate the signal radiated by the on-chip antenna during wireless demonstrations. Up to 25-Gb/s data-rate was achieved at a BER of 2.2×10^{-4} using BPSK modulation, across a distance of 15 cm with a Tx and Rx consuming a DC power of 375 mW and 575 mW respectively.

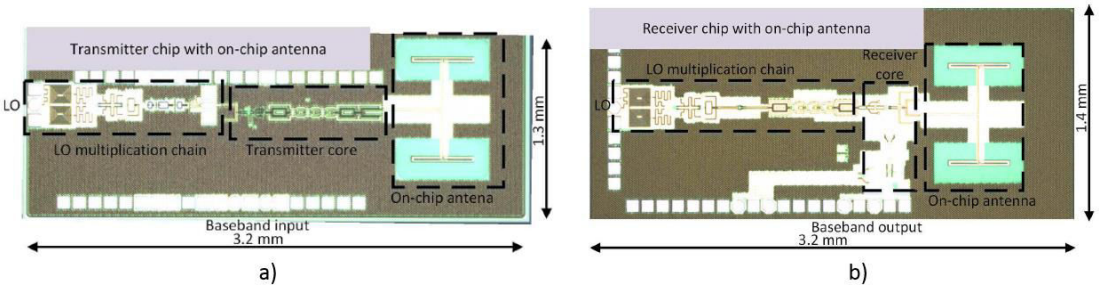

Figure I.22. Photograph of (a) the 240 GHz Tx and (b) the Rx based on LO multiplier chains and on-chip antennas from [I.36].

These successful wireless link demonstrations show that it is possible to use CMOS/BiCMOS technologies for the development of high speed (> 20 Gb/s) wireless transceivers. However, if up to 100 Gb/s data-rates are required, the limited maximum BW achieved in Silicon technology should be compensated by very complex modulation schemes, thereby increasing the DAC circuitry complexity and the DC power supply. For this reason, a more energy-efficient strategy is to achieve very wide BWs in order to enable high data-rates while using very simple ASK modulation schemes. For instance, to achieve from 25 Gb/s to 50 Gb/s using OOK modulation, 50 GHz to 100 GHz RF BWs would be necessary. Therefore, another technology supporting such BWs should be investigated.

V. Sub-mmW and THz Photonics transmitter systems

1. Photonics technologies potentiality

With the limited BW and non-negligible power consumption (often above 300 mW) of Si-based circuits at sub-mmW/THz frequency bands, it becomes difficult to target sub-mmW/THz communication applications covering very wide RF BWs (> 50 GHz) while using more energy-efficient designs. On the other hand, there has been some considerable progress in the development of THz Photonic-based transceivers in order to embrace Photonics technology's inherent broadband nature [I.37]. In this approach, transmission and processing of optical digital signal are going through high-speed optical and opto-electronic devices operating at long optical wavelengths (1.3-1.55 µm). The application of Photonics technology can be divided into two categories: optical fiber communications and wireless communications. For optical fiber communications, very long transmission distances (>10 kilometers) can be achieved, but the deployment cost prohibits the roll-out of a new cost-effective optical fiber infrastructure as mentioned in section II.2. In the meantime, Photonic-based low-cost wireless links are being widely investigated among the academic and industry community for the deployment of very short and medium range (centimeters to hundreds of meters) high-speed P2P applications.

To enable THz wireless links based on Photonics technology, the basic approach consists in photomixing two free-running optical sources. This entails down-converting to the RF frequency instead of up-converting as in solid-state-based systems. As shown in Figure I.23, the wavelengths λ_1 and λ_2 of the two optical sources are slightly shifted until the wavelength difference corresponds to the targeted output THz frequency. These optical signals are then heterodyned to create an optical frequency beat which is injected inside a photodiode. Through photomixing, this electro-optic device proceeds with an optical-to-electrical (O-E) conversion thereby generating the THz electrical signal. In this O-E conversion mechanism, electrons are indeed generated by means of photon absorption. As photomixers are usually very sensitive to electric fields, the electric field needed to control these components can be small compared to an all-electronic device, which means that the power consumption is low as well. This is a major advantage for energy efficient applications. Moreover, the photomixing process is transparent to optical modulation formats which enables to transfer a modulation from optical to electrical very easily. This aspect is very interesting for applications like RoF where wireless networks take over optical networks.

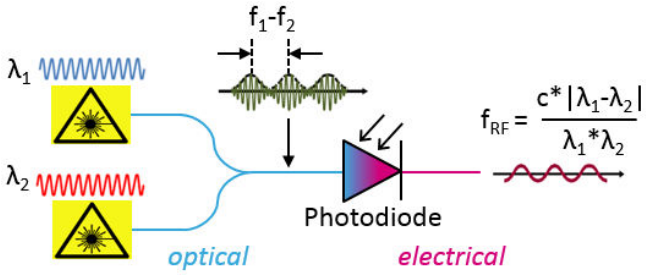

Figure I.23. Schematic of heterodyne photomixing process.

For the realization of a THz photomixer, two technologies are competing with one another in the area of telecommunication: III-V Photonics usually using Indium Gallium Arsenide (InGaAs) on Indium Phosphide (InP), and IV-IV Photonics usually using SiGe. As reported in [I.38], the IV semiconductor group shown in Table I.1 features an indirect gap whereas the III and V semiconductor groups have a direct bandgap. This property defines the quantum efficiency (or photon-absorption efficiency) of the material, which is much higher for direct bandgaps. Therefore III-V semiconductors make better optical devices than IV semiconductors. A high electron mobility is also encountered in III-V semiconductors, thereby allowing very high speed device in certain design geometries. However, Silicon technology actually allows for integrated SOI waveguides with better confinement of the optical signals compared to those in III-V semiconductors. Therefore a main asset of Silicon technology is smaller optical-circuit size and reduced manufacturing-cost. Yet, according to Table I.1, extremely poor photon absorption is achieved in Silicon at telecommunication wavelength ($4.6*10^{-10}$ at 1.55 µm). Therefore, the growth process of Germanium on Silicon has been widely studied and improved in order to reach better optical efficiency of Si-based optical devices [I.39] (Ge absorption coefficient of $4.6*10^{4}$ at 1.55 µm).

Property at 300 K	**Si**	**Ge**	**GaAs**	**InGaAs**	**InP**
Bandgap	indirect	indirect	direct	direct	direct
Energy gap (eV)	1.12	0.66	1.424	0.73	1.27/1.33
Absorption coefficient at 1.55 µm	8.32 $*10^{-10}$	4.6 $*10^{4}$	transparent	$6.8*10^{5}$	transparent
Refractive index at 1.55 µm	3.476	4.275	3.374	3.59	3.17
Electron mobility ($cm^2*(V*s)^{-1}$)	1500	3900	8500	8000	5400
Holes mobility ($cm^2*(V*s)^{-1}$)	475	1900	400/500	300	300

Table I.1. Semiconductor materials properties from [I.38].

2. State-of-the-art photodiode performance

Looking at the existing photomixers reported in the literature, the P-doped/Intrinsic/N-doped Photodiode (PIN-PD) is one of the most commonly used for its very conventional semiconductor junction structure. A -3dB BW of 70 GHz was demonstrated in [I.40] while quasi-optical photomixer module with integrated antenna and backside hemispherical Silicon lens supporting wireless transmission achieved an output power of -25.2 dBm at 200 GHz with a DC power consumption of 6.15 mW (laser power supply not included) [I.41]. It should be noted that in the photomixer designs reported in the literature and presented further, the DC power consumption doesn't take into account the optical source (laser) power consumption.

An important performance limitation in PIN-PDs is the fact that photon-absorption and electron-hole pairs separation occur in the same semiconductor region. Therefore, both photo-generated electrons and holes are drifting towards their respective electrodes. However, as the drift velocity of holes is an order of magnitude slower than that of electrons in the depletion layer, the photodiode's speed is restrained by the holes transit time. To overcome this issue, a promising approach is the Uni-Travelling-Carrier Photodiode (UTC-PD) developed III-V Photonics technology. III-V photomixers have indeed demonstrated impressive BWs and output power levels from 100 GHz to 1 THz thanks to their high optical property and the optimized architecture of UTC-PDs [I.42]–[I.44]. As explained in [I.45], the high performance of a UTC-PD can be simply illustrated by its energy band diagram compared to that of a PIN-PD. By contrast to a PIN junction structure, the photon-absorption (p-doped region) and carrier-depletion regions (intrinsic region) in a UTC-PD are physically separated. Therefore, the majority holes are quickly collected at the anode whereas the minority electrons drift down the depletion region towards the cathode. Hence, the photodiode's response is dominated by the electron's velocity only. As electrons travel much faster than holes (in GaAs for example, electron mobility is ~8500 $cm^2/(V*s)$ whereas hole mobility is ~450 $cm^2/(V*s)$), this leads to wider BWs (up to 350 GHz for UTC-PD instead of 70 GHz for PIN-PD) and higher saturation current (generally up to 20 mA for UTC-PD instead of ~10 mA for PIN-PD).

Nevertheless, in broadband designs at frequencies above 100 GHz the output power decreases significantly due to the influence of the photodiode module's RC-time constant and electron transit time. Therefore it becomes essential to implement improvement methods such as semiconductor layers optimization, resonant matching circuits and low-loss packages to compensate for these limitations around the carrier frequency. In [I.46], on-wafer measurements of the fabricated InP/InGaAs UTC-PD have shown an intrinsic -3dB O-E BW capable of achieve up to 310 GHz at a wavelength of 1.55 µm by reducing the absorption layer width – and thus the intrinsic electron transit time – without increasing the RC time constant of the junction capacitance. A short-stub matching bias-Tee circuit were also added to the UTC-PD module with a decoupling capacitor in [I.47] so as to enhance the output power around 100 GHz. On wafer characterization of this matched photodiode structure was realized and an output power of 4.8 dBm was achieved at 100 GHz with a photocurrent of 10 mA at 2V reverse DC bias (20 mW of DC power consumption). A -3dB O-E BW of 55 GHz was achieved, which is significantly lower than the UTC-PD's intrinsic BW due to the resonant effect of the matching circuit at 100 GHz. As shown in Figure I.24 (a), the development of a flip-chip bonded UTC-PD on a ceramic packaging substrate was also an interesting solution to ease the fiber-to-photodiode optical coupling and provide a heat-sink to improve the saturation power level of the photodiode [I.48], [I.49]. The resulting output power reached about -3.5 dBm at 320 GHz with a photocurrent of 10 mA at 1V (10 mW DC power consumption). Moreover, an impressive -3dB O-E BW of 330 GHz was achieved thanks to an improved UTC-PD structure and geometry as shown in Figure I.24 (b).

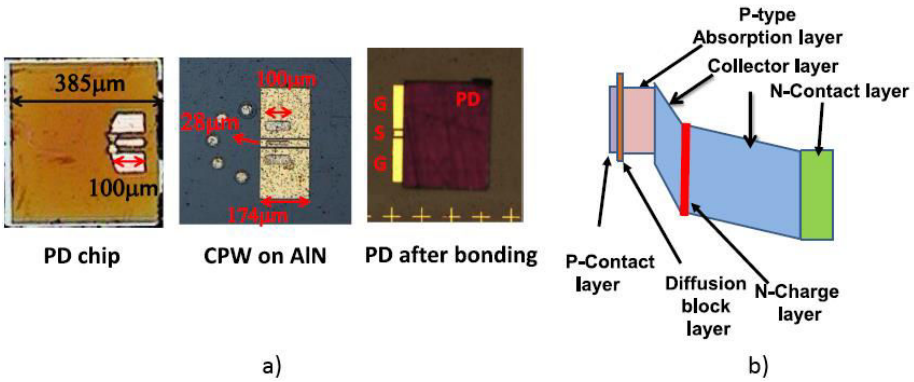

Figure I.24. (a) Top-views of the UTC- PD chip, bonding pads on Aluminum Nitride ceramic substrate, and photodiode chip after flip-chip bonding [I.48]*, and (d) band diagram of the simulated of the improved UTC-PD device* [I.49].

In order to facilitate the assembly between the photomixer and test-equipment using waveguide inputs/outputs, a waveguide-output type photomixer module was developed by NTT Electronics Corporation, incorporating a matching microstrip stub and microstrip-to-waveguide transition in quartz substrate (Figure I.25). A first design around 100 GHz was measured with an output power of 2.5 dBm, and a -3dB O-E BW of 45 GHz were obtained with a photocurrent of 10 mA and a bias DC voltage of 2V [I.50]. The implementation of such a structure eventually added about 2.3 dB loss compared to the on-wafer measurement. This waveguide-mounted design was then pushed to THz frequencies and an output power of -3 dBm at 350 GHz over a -3dB O-E BW of 120 GHz were successfully achieved with a photocurrent pushed to 20 mA at 2.5V (50 mW of DC power consumption) [I.51].

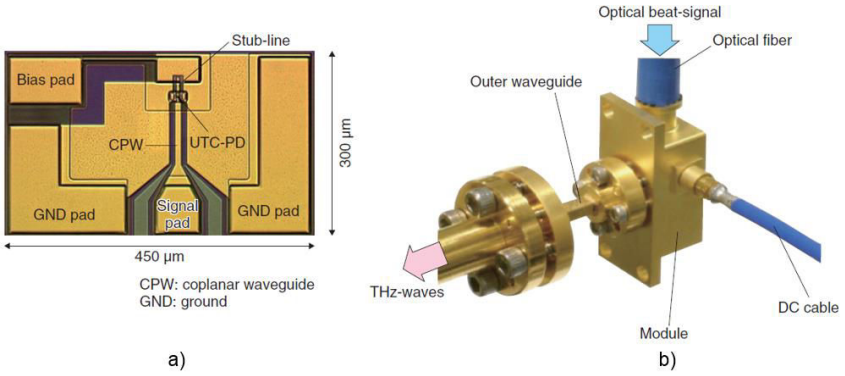

Figure I.25. Photograph of (a) the fabricated UTC-PD chip, and (b) THz-wave waveguide photomixer module [I.51].

For direct radiation into free space (without requiring waveguide assembly with the radiating system), a quasi-optical photomixer module was lastly designed with an integrated log-periodic antenna and a metal package equipped with a hemispherical Silicon lens to collimate the radiated signal [I.51] (Figure I.26). A -3dB O-E BW of 132 GHz was evaluated in [I.52] using this packaging strategy. At 350 GHz, the measured output power was estimated at about -15 dBm for a photocurrent of 10 mA at 1.5 V (15 mW DC power consumption). Finally, this wireless solution was evaluated up to 1.04 THz and has delivered a peak output power of -26.4 dBm for a photocurrent of 10 mA and at a low bias voltage of 0.75 V (or 7.5 mW DC power). According to the literature, even though this work is not very recent, these photomixer modules were not yet outperformed by other wireless photomixer modules.

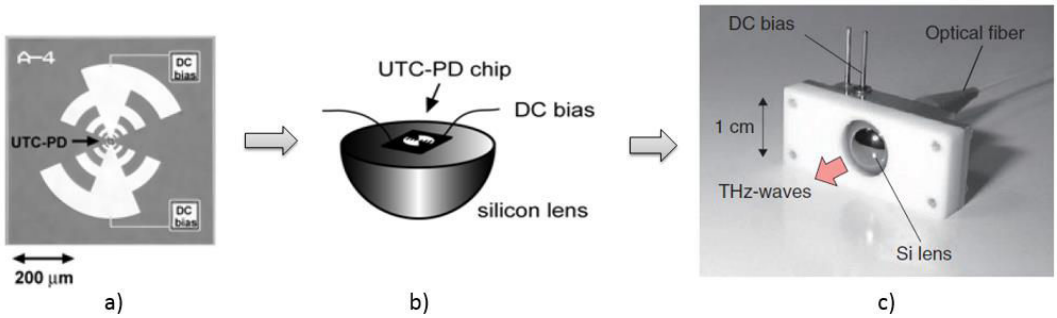

Figure I.26. (a) UTC-PD chip with integrated log-periodic planar antenna, (b) Schematic drawing of the assembly scheme in the quasi-optical UTC-PD module, (c) photograph of the final quasi-optical photomixer integrated module from [I.51], [I.52].

3. Wireless data communication demonstration with III-V Photonics-based transceivers above 200 GHz

Many wireless transmissions based on III-V Photonics technology are reported in the literature for different modulation schemes in order to assess the maximum achievable error-free data-rates and link distances. In [I.53], NTT has evaluated a wireless link based on a UTC-PD Tx at 300 GHz. The photomixer used for this experiment is the waveguide-mounted photodiode module presented in [I.51] and shown in Figure I.25 (b) and the THz link is composed of a horn and a lens on both the Tx and Rx sides. The Rx consists of a direct detection Schottky barrier diode, which enables amplitude modulation only (the phase is not retrieved). Therefore OOK modulation was used. Over a distance ranging from 0.5 m to 1 m, up to 40 Gb/s data-rate with a BER < 10^{-11} was successfully achieved in real time detection [I.53].

For longer transmission range, the work presented in [I.54] uses coherent detection to increase the Rx sensitivity. In this paper, the Tx of the wireless link consists of a waveguide-mounted UTC-PD coupled to a conical horn. As for the previous demonstrator, two lenses are used to increase the EIRP of the radiating parts. The Rx consists of a sub-harmonic mixer in order to retrieve the phase and amplitude of the received signal. The measurement was performed at the IEMN laboratory and a picture of the setup is shown in Figure I.27 (a). Real time data communication at 32 Gb/s was successfully demonstrated over a distance of 25 m using 16-QAM modulation scheme. With the same modulation scheme, up to 100 Gb/s was achieved at Karlsruhe Institute of Technology (KIT) [I.42] at 237.5 GHz, using a Rx based on an electronic I/Q mmW monolithic IC. A picture of the Tx setup is shown in Figure I.27 (b). A distance of up to 20 m was successfully covered with a BER below the Forward Error Correction (FEC) limit at ~$3*10^{-3}$, which means that the bit errors in the received signal could still be identified and corrected thanks to the use of a FEC encoder.

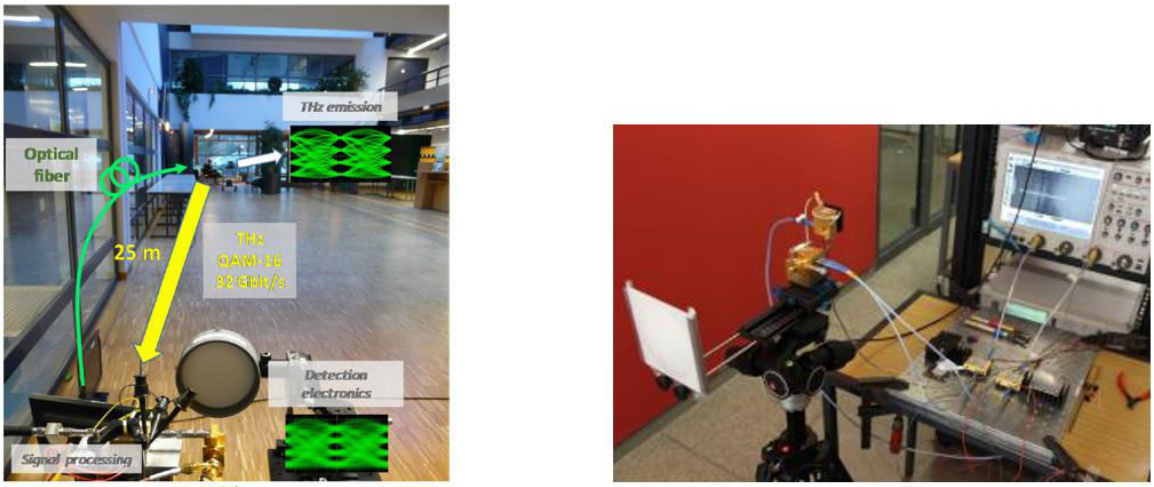

Figure I.27. III-V Photonic-based wireless link setup (a) at 300 GHz over 25m at IEMN lab, and (b) at 237.5 GHz over 20 m at KIT.

4. Silicon Photonics technology opportunity

A closer evaluation of budget links in the examples given above shows significant integrability issues. Indeed, comparing NTT's two different photomixer modules together, about 12 dB additional loss is estimated between the waveguide-mounted photomixer and the quasi-optical integrated photomixer at 350 GHz. With a Silicon lens gain estimated at about 10 dBi, this would mean that integration losses in the integrated system are probably above 20 dB. These significant losses mainly originate from the fact that III-V technologies are not easy to integrate within advanced packaging technology. Indeed, the lack of III-V Photonic industrial production platforms makes them much more difficult to access at a low price which is why III-V Photonics technologies do not benefit from available advanced fabrication and integration processes. In other words, III-V Photonics integrated devices are currently too costly and do not offer available low-loss integration capabilities. These issues are major drawbacks when targeting large-scale low-cost sub-mmW/THz applications.

As an alternative, the search for cost-effective Photonics technologies has led to consider Silicon Photonics as a very promising low-cost technology for high-speed applications. Indeed Silicon Photonics' main benefits are its inexpensive material cost and its compatibility with standard Silicon CMOS technology process, thereby offering the possibility to monolithically integrate both photonic and electronic components on a die. Therefore, the recent progress made in the past decade on the industrialization of Silicon Photonics build-in blocks is paving the way towards the development of Si-based energy-efficient THz transceivers. Most of the SiGe photomixers reported in the literature involve typical PIN-PD structures for the development of high-speed optical links requiring low power consumption while maintaining high performance in terms of O-E efficiency and BW. For example, a BW as large as 70 GHz was achieved in [I.55]. Given the growing potential of Silicon Photonics technology, STMicroelectronics has developed its own industrial platform [I.56]. This platform is using the standard 300mm SOI process flow of ST's existing CMOS processes and can therefore rely on the same high-yield and manufacturing methodology. Amongst the proposed high-speed optical components supported by this industrial platform, the SiGe PIN-PD [I.56] has shown promising performance in order to comply with high-speed wireless links. Indeed, an on-wafer measured output power of -20 dBm was achieved at 210 GHz for a 2 mW DC power consumption in [I.57]. This PIN-PD

has actually achieved a -3dB O-E BW above 20 GHz, and has already demonstrated up to 28 Gb/s data-rate with a low-cost optical packaging test vehicle [I.58].

VI. THz transceivers benchmarking and high data-rate links

1. Overall THz-wave transmitters benchmarking

A comparative study on the performance of the different technologies presented in section IV and V needs to be conducted to develop a competitive >40 Gb/s energy-efficient and low-cost wireless link. Figure I.28 (a) sums up the peak output powers of different transceiver technologies from 100 GHz to 1.25 THz. It can be seen that UTC-PD-based III-V Photonics technology is seriously competing with all-electronics transceivers between 100 GHz and 400 GHz with output powers varying more or less from 10 dBm to -10 dBm. The competitive differentiation will therefore rely on the technology's ability to deliver wide transmission BWs enabling > 40 Gb/s operation, while maintaining the lowest possible power consumption.

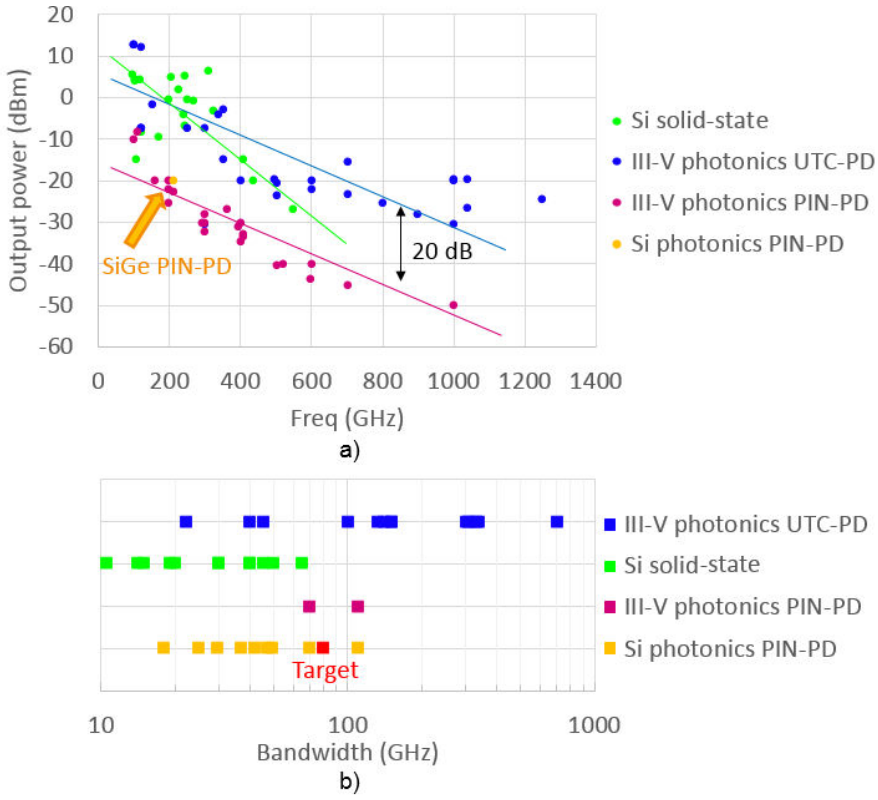

Figure I.28. (a) Peak output power for transceivers realized in different technologies from 100 GHz to 1250 GHz, and (b) achieved -3dB absolute BW of mmW to THz transceivers developed in different technologies (Si solid-sate :[I.16], [I.27], [I.28], [I.55]–[I.63]*; III-V photonics UTC-PD:* [I.49], [I.50], [I.68]–[I.71]*; III-V photonics PIN-PD:* [I.72]*; Silicon photonics PIN-PD:* [I.73]–[I.76]*).*

Hence, according to the achieved BWs reported in the literature from mmW to THz carrier frequencies and shown in Figure I.28 (b), III-V Photonics UTC-PD transceivers seem to offer the largest BWs due to their excellent intrinsic optical and electrical properties and their optimized device geometry. As a proof of concept, wireless laboratory demonstrations of data communication based on III-V Photonics Tx using UTC-PD have already achieved data-rates up to 100 Gb/s around 300 GHz with simple amplitude modulation and Schottky diode-based mixer or active monolithic microwave IC Rx

[I.42]–[I.44] (as shown in Figure I.29). However, as III-V Photonics technologies are not an option for low-cost and highly integrated THz wireless systems marketing, there is a good window of opportunity for Silicon Photonics transceivers using PIN-PDs leveraging Silicon's integration capability. Looking at Figure I.28 (b), the PIN-PD-based Silicon Photonics devices used for high-speed detectors in optical links seem to deliver competitive BW performance. The reported 110 GHz -3dB BW would indeed enable THz communications capable of achieving data-rates over 40 Gb/s with simple amplitude modulation. Nevertheless, such a device delivers a power level similar to that of III-V photonics PIN-PDs and 20 dB below the UTC-PD's output power. This considerably reduces the maximum achievable transmission distance down to 10 times shorter ranges compared to III-V UTC-PDs. Hence, to mitigate the impact of low radiated power, it is important to investigate cost-effective antenna-systems that can be implemented at high integration levels to enable compact THz system solutions with sufficient radiated power and minimized integration losses. The considered data-rate performance target for our project is shown in the red window in Figure I.29.

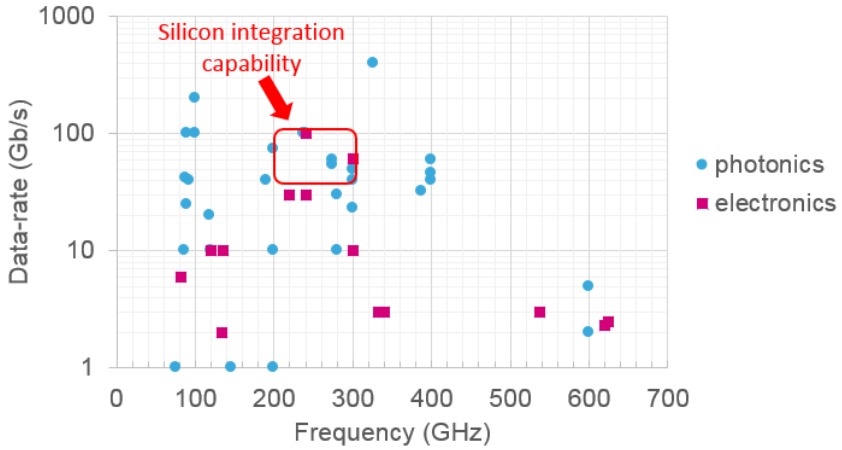

Figure I.29. R&D state-of-the-art of maximum data-rates for Photonics and electronics (solid-state) transceivers up to 630 GHz from [I.77].

2. Commercially available systems for telecommunication links

A first strategic positioning in the available high-speed communication market needs to be determined in order to assess Silicon Photonics' relevance and adequacy to the market needs, and set an outline specification of the envisioned wireless link.

Figure I.30 gives a broad insight on the data-rate performance of basic wired and wireless communication standards and their corresponding distance range. The LoRaWAN network is designed to offer wireless internet connection to battery-powered devices capable of operation on very narrow BWs in the IoT application. Therefore, very reliable and secure connection is provided with data-rates ranging from 0.3 kbps to 50 kbps and long distance coverage going from a few km to over 10 km by using low frequency bands (> 1 GHz) [I.78], [I.79]. For more demanding mobile applications in terms of throughput, the LTE-A offers higher network capacity by combining multiple network technologies (HetNet) and massive-MIMO [I.80], [I.81]. This strategy enables to deliver about 1 Gb/s peak data-rate in small cells supported by frequencies up to 6 GHz, which in the other hand reduces the coverage capacity compared to LoRa due to free space path loss at higher frequencies. Indoor wireless communication is usually governed by WiFi standards, which come in different releases offering different performance. Amongst the releases for the WiFi 802.11ac protocol, the Modulation and

Coding Scheme Index 9 (highest modulation rate) delivers from 1.5 Gb/s to 3.4 Gb/s peak data-rates in a maximum coverage of 35 m. In reality, the typical data-rate experienced by the consumers living in apartment blocks would actually be ranging from 290 Mb/s to 866 Mb/s due to many limiting factors like signal degradation, typical error rate, multipath, shadowing, etc. [I.82]. Another WiFi alternative capable of achieving up to 7 Gb/s is the recent WiGig operating in the 60 GHz frequency band. However, due to high atmospheric absorption and high signal scattering, its coverage is limiting to a few meters. In more specific situations requiring above Gigabit-per-second connections like data-centers or other intense-data services, the Ethernet protocol offers transmission standards capable of handling over 10 Gb/s data-rates. Depending on the required transmission length and data-rate, different media can be chosen to carry information such as fiber or copper cables. Even though copper's limited performances are increasingly felt as the distance and data-rate increase due to strong propagation attenuation, copper cabling is still used for switch-to-switch or switch-to-server connections in 10 Gigabit Ethernet (10GbE). Available maximum cable-length would therefore be limited to 10 m using unexpansive twinaxial 2-pair cables [I.83]. If longer distances need to be covered or for fronthaul/backhaul links, optical fiber is mostly used with the benefit of featuring lower latency, lower propagation loss and wavelength division multiplexing. Data-rates ranging from 10GbE up to 100 GbE are indeed enabled with multilane distribution (4x25 Gb/s) for a distance range capable of achieving 40 km over 100GBASE-ER4 single mode fiber [I.84]. Finally, considering very-short range device-to-device connection such as external peripherals to computers, high-performance computer-peripheral cables using Thunderbolt, USB or DOCSIS interfaces can be used. The most recent versions of these cables deliver up to 40 Gb/s peak data-rates with a length of maximum 50 cm over copper, but 20 Gb/s cables are also available for up to 3 m length allowing 4K workflows and daisy-chain networks [I.85].

As a conclusion, a very wide range of data-rate is covered by these commercially available wired and wireless links. However, it is interesting to notice the transition from wireless to wired based communication as the data-rate is progressively increasing. Indeed, wireless links from 0.3 kb/s (LoRa) to 7 Gb/s (WiGig) are giving place to wired links from 10 Gb/s (10GbE copper cable) to 100 Gb/s (100GbE optical cable). In front of this dilemma, Silicon Photonics technology could be introduced to the telecommunication market as a solution to overcome the lack of wireless links between 10 Gb/s and 100 Gb/s while providing distance ranges up to 100 m by making use of low-cost THz antenna-systems (see red target ellipse in Figure I.30).

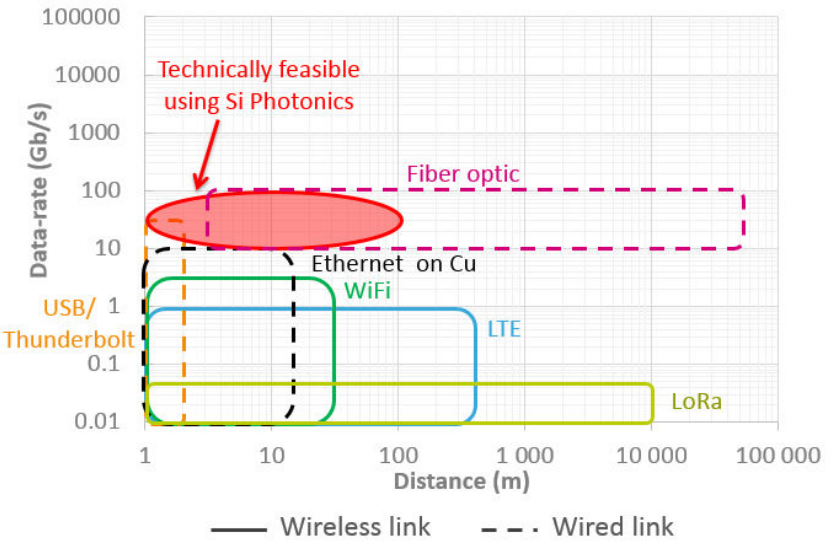

Figure I.30. Possible data-rate for different commercial wired/wireless communication standards and their corresponding distance in meters.

Global power consumption of a few Gigabit-per-second communication links are shown as a function of the link distance in Figure I.31 in order to estimate a competing positioning of the complete envisioned Silicon Photonics system-on-chip (SoC) transceiver. The E-band wireless backhaul for example is capable of delivering multi-gigabit wireless transmissions at medium distance ranging typically from 2 km to 3 km [I.86]. However E-band systems used for urban radio deployment can be very energy consuming. As an example, the E-band up/down converter proposed in [I.87] shows a total power consumption of 9.5 W, and some E-band radios can consume up to 37 W [I.88]. WiGig offering up to 7 Gb/s at short range (< 10m) also tend to require a significant level of power supply. Power consumption studies have been undertaken on devices supporting WiGig standards and have shown idle power consumption of about 2.3 W [I.89]. Furthermore, in a specific WiGig dock application proposed in [I.90], the wireless docking integrated in a notebook personal computer actually causes a significant increase in power consumption up to 6 W. As it was mentioned above, gigabit Ethernet cables often used in data-centers and backhaul networks offer a plethora of options in terms of data-rate and cable length. A short list of the proposed solutions is reported in Figure I.31. From the SFP 40GbE passive optical fiber to the Copper 10GBase-T cable, a power consumption varying between 1.5 W and 5 W for lengths ranging from 7 m (active optical cable) to 10 km (passive optical cable) is achieved [I.91]–[I.94]. Lastly, two computer-peripheral active cables are also listed: 4 W power consumption is reported for a 3 m long active copper Thunderbolt 20 Gb/s cable and a very low 0.58 W power consumption is reported for a 100 m long very expensive USB 5 Gb/s optical cable [I.95], [I.96].

Considering the low power-consumption levels reported in the literature for Silicon Photonics technologies, it seems reasonable to target a total power consumption between 0.5 W and 1 W for the envisioned global high-speed transceiver system. As a result, the deployment of extremely energy-efficient THz wireless links could be possible and very competitive.

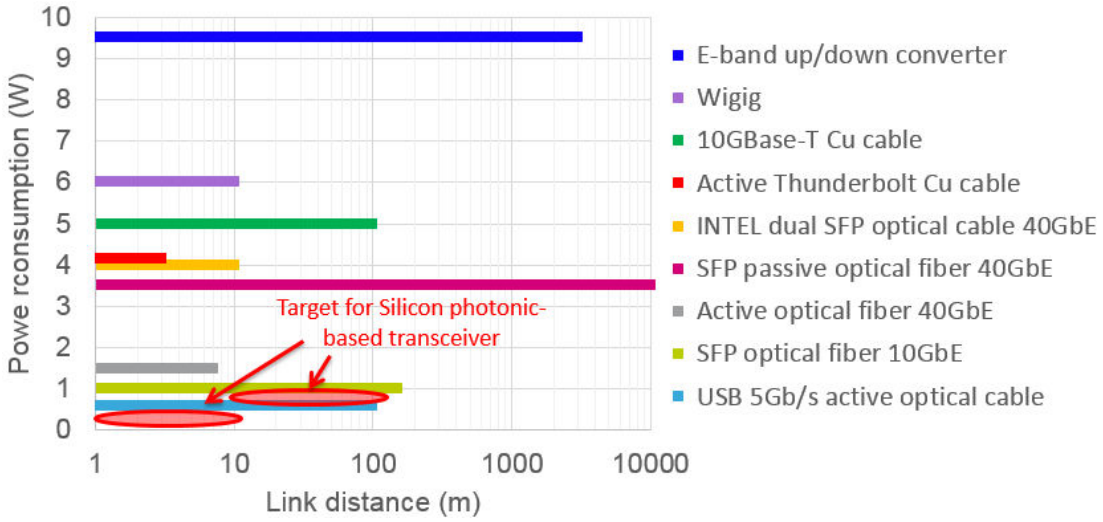

Figure I.31. Power consumption of different commercial wired/wireless links and their corresponding distance.

To conclude, according to the existing Gb/s wireless and wired systems described above, two main applications seem of interest. The first is a low-cost wireless system delivering over 20 Gb/s with 0.5 W power consumption and 1 cm to 1m range for the replacement of the following consumer products: USB, Thunderbolt, DOCSIS. The second one is a P2P wireless transmission delivering over 40 Gb/s with 1 W power consumption at a distance up to 100 m for fiber replacement to enable low-power fronthaul/backhaul links in 5G small cells.

3. Sub-mmW and THz antenna requirement

According to the previous analysis, we can resume the specification of the targeted THz telecommunication system as follow:

- Frequency band targeted at the start of this PhD : 200 GHz-300 GHz (the new IEEE802.15.3d standard signed of last year will push us to target higher frequencies in future works)
- Data-rate: from 20 Gb/s to 100 Gb/s
- Power-consumption/Range : < 0.5 W up to 10 m and < 1 W up to 100 m
- Main targeted features: level of integration better than III-V photonics, convenient and low-cost deployment.

In order to estimate the required antenna gain G_A to sustain the targeted distances, a calculation of the link budget shown in Equation (2) as a function of the Free Space Path Loss (FSPL) shown in Equation (3) is done. To do so, a wireless link operating a 240 GHz is considered, with a Silicon Photonics based Tx delivering an estimated output power of -25 dBm (according to state-of-the-art PIN-PD reported performance) and an Silicon CMOS Rx based on a commercial Schottky diode sub-harmonic mixer featuring an estimated sensitivity of -53 dBm, as shown in Figure I.32.

$$P_{out} + 2 * \boldsymbol{G_A} - FSPL > Rx.sens \quad (2)$$

$$FSPL(dB) = 20 * log\left(\frac{4\pi df}{c}\right) \quad (3)$$

With *c* being the electromagnetic propagation velocity in air and *d* the transmission distance.

Figure I.32. Schematic of a 240 GHz wireless link based on a Silicon Photonics Tx and a commercial sub-harmonic mixer Rx for link budget estimation.

The gain deduced from Equation (2) is computed in Figure I.33 as a function of the transmission range. From this calculation we can see that a transmission distance ranging from 1 cm to 100 m can be reached with an antenna gain ranging from 9 dBi to 49 dBi respectively (blue curve).

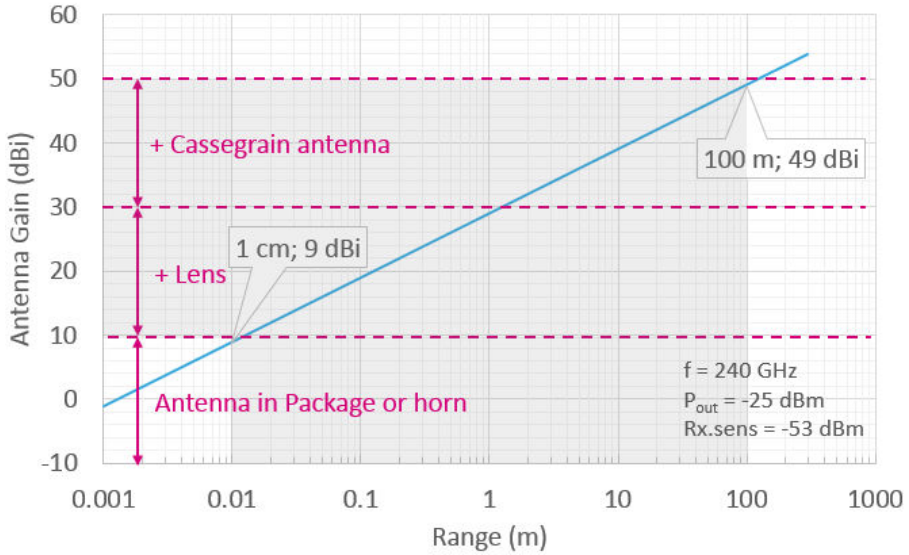

Figure I.33. Antenna gain as a function of the transmission range deduced from Equation (2), and antenna types associated to different gain levels.

Concerning fronthaul/backhaul applications, while Silicon Photonics would offer the possibility of low-cost chipset manufacturing, it won't be enough to reduce the cost of the complete wireless solution. Indeed, as it is observed for mmW frequencies, the antenna-system still represents the most expensive part of a fronthaul/backhaul link (about 300 € to 1000 €). This part generally consists of a horn, a Cassegrain antenna or a dielectric lens fabricated with CNC based conventional mechanical manufacturing methods (like turning, milling, drilling, etc.). Therefore, low-cost THz antenna solution is a key enabler in order to support the development of cost-effective THz solutions. Following this objective, a THz radiation solution based on an AiP approach was considered for this PhD research for two mains reasons. First, it enables to use a system-in-package assembly strategy where the Silicon Photonics die is flip-chip mounted onto the antenna substrate. Second, it is compatible with industrial fabrication constraints and therefore offers the possibility to target high-volume production. This integrated antenna approach was indeed successfully developed up to 140 GHz during Aimeric Bisognin's PhD thesis, using organic substrate packaging with flip-chip mounted mmW Silicon die on top of the substrate.

Another solution that was investigated during this PhD is the use of a sub-mmW/THz conical horn instead of the suggested AiP to radiate the signal coming from the photomixer. This approach enables to leverage the two orthogonal polarizations of the horn in order to realize full-duplex transmissions. However, this wireless transceiver configuration raises to issue of an assembly strategy capable of

connecting the Silicon Photonics die to the horn's waveguide input. Therefore, a microstrip-to-waveguide transition design was also under study.

Using one or the other antenna solution, an estimated gain of about 9 dBi at 240 GHz (as suggested in Figure I.33 above) seems feasible. However, it would become difficult to achieve higher antenna-gain to achieve several meters long P2P transmissions by simple using an AiP or a horn. To address this problem, a technique consists in associating the AiP or the horn with a quasi-optical antenna like a dielectric lens or a Cassegrain reflector, so as to increase the overall gain of the antenna-system. In this configuration, the AiP or horn is used as a feed source to illuminate the quasi-optical antenna. As mentioned above, cost related to the manufacturing of such antenna-systems is of primary concern and needs to be reduced in order to tackle mass-market THz applications. In this respect, Additive Manufacturing (AM), which includes the 3D-printing subset, is increasingly considered for low costs and fast prototyping, and has already shown its potential for the fabrication of mmW 3D antennas [I.97]. Hence, 3D-printing was envisioned for the manufacturing of the quasi-optical antenna and the horn, with a careful study on the fabrication performance of available 3D-printing techniques.

As shown in Figure I.33, the following antenna-system makes an interesting THz solution targeting different distance transmissions:

- AiP or horn featuring a gain of up to 9 dBi for up to 1 cm range
- AiP or horn feed source + dielectric lens featuring a gain between 19 dBi and 29 dBi for rages between 10 cm and 1 m
- AiP or horn feed source + Cassegrain antenna featuring a gain up to 49 dBi for up to 100 m range

A global architecture of the considered low-profile industrial System-in-Package antenna is shown in Figure I.34. The main challenges with the development of such a system revolve around two major points. The first one is the optimization of a design and assembly strategy that is compatible with industrial constrains while allowing satisfying antenna performance (in terms of gain and BW) above 200 GHz. The second one is the co-design between the feed source and quasi-optical antenna to maximize the radiation coupling between the two elements and thus maximize the antenna-gain.

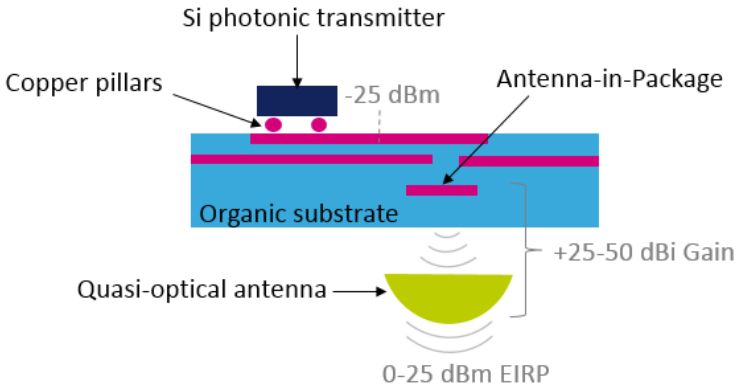

Figure I.34. Schematic of the global antenna-system architecture using the AiP/quasi-optical system solution.

VII. Conclusion

This first chapter allowed to illustrate the impact of emerging wireless applications on the global mobile data traffic transferred by the mobile telecommunication network. Supporting this increasing data traffic, fronthaul/backhaul access networks have seen their peak data-rates drastically increased. On top of this, we have seen how the upcoming 5G network will sprouts up average data-rate up to 100 Mb/s and peak data-rates up to 10 Gb/s by making use of wider BWs in the mmW frequency band. Therefore, several solutions are being deployed to enable such user-experience data-rates, like network densification through the multiplication of small cells. This involves addressing the RAN architecture and technology modification to improve its BW performance in order to connect each small cell back to the core network in a seamless and cost-effective manner. A migration towards Cloud-RAN seems promising as more and more telecommunication operators are relocating core network functions in remote data-centers. This context seems favorable for the deployment of low-cost high-speed P2P wireless links operating in higher frequency band as a way to overcome the BW limitation and very costly aspect of optical cables. Many laboratory demonstrations have already acheived data-rates up to 100 Gb/s using photonic-based transceivers, thanks to their inherent wide bandwidths (> 50 GHz). In view of this situation, the THz frequency band is being studied by telecommunication industries for extremely broadband frequency spectrum allocation enabling above 40 Gb/s data-rates (IEEE802.15.3d standard). Therefore, one of the key challenges of this PhD thesis consisted in investigating on sustainable solutions in the 200-300 GHz frequency band for the development of low-cost THz wireless links operating above 40 Gb/s by leveraging broadband and low-cost Silicon Photonics technology. The evaluation of an industrial Silicon Photonics technology was realized with the development and characterization of an integrated sub-mmW/THz photomixer used in the transmitter system. To radiate the sub-mmW/THz signal in free space, several antenna-system configurations were also studied in order to operate above 200 GHz while using low-cost antenna technologies and prototyping techniques only. In this prospect, standard organic substrate was considered for the development of an integrated antenna-in-package, and 3D-printing was considered for the fabrication of a horn, a dielectric lens, and a reflector antenna. An achieved gain between 9 dBi and 49 dBi would enable to target distance ranges from 1 cm to 100 m depending on the complete antenna-system configuration.

Reference

[I.1] "Ericsson Mobility Report," *Ericsson*, White paper, 2017.

[I.2] "Consumer cloud computing users worldwide 2018," *Statistica*. [Online]. Available: https://www.statista.com/statistics/321215/global-consumer-cloud-computing-users/.

[I.3] "Wireless M-Bus breaking new ground in metering and industrial applications," *Smart Energy International*. [Online]. Available: https://www.smart-energy.com/features-analysis/wireless-m-bus-breaking-new-ground-metering-industrial-applications/.

[I.4] "5G use cases and requirements," *Nokia*, White paper, 2014.

[I.5] "5G Spectrum Recommendations," *4G Amerimcas*, White paper, 2015.

[I.6] T. U. Kingdom, "5G spectrum Public Policy Position," *HUAWEI Technolology CO*, White paper, 2017.

[I.7] David Belson, "akamai's state of the internet Q1 2017 report," *Akamai*, White paper, 2017.

[I.8] M. Xu *et al.*, "Bidirectional Fiber-Wireless Access Technology for 5G Mobile Spectral Aggregation and Cell Densification," *IEEE Journal of Optical Communications and Networking*, vol. 8, no. 12, pp. B104–B110, 2016.

[I.9] Y.Rouault, "Fronthaul to 5G needs a strong optical network," *Inform TMForum*. [Online]. Available: https://inform.tmforum.org/sponsored-feature/2017/06/fronthaul-5g-needs-strong-optical-network/.

[I.10] "Millimeter Wave (MMW) Wireless Links 10Gbps+," *CableFree*. [Online]. Available: http://www.cablefree.net/cablefree-millimeter-wave-mmw/.

[I.11] D. Wang, Y. Wang, R. Sun, and X. Zhang, "Robust C-RAN Precoder Design for Wireless Fronthaul with Imperfect Channel State Information," *IEEE Wireless Communications and Networking Conference (WCNC)*, pp. 1–6, San Francisco, USA, 2017.

[I.12] A. De Oliva *et al.*, "Xhaul : Towards an Integrated Fronthaul / Backhaul Architecture in 5G Networks," *IEEE Wireless Communications*, vol. 22, no. 5, pp. 32-40, 2015.

[I.13] "EtherHaul™ Hundred Series Products," *Siklu*. [Online]. Available: https://www.siklu.com/product/etherhaul-hundred-series/.

[I.14] "E-Link Eagle Macro-Cell Backhaul," *E Band*. [Online]. Available: https://www.e-band.com/E-Link-Eagle-Macro-Cell-Backhaul.

[I.15] "FCC online table of frequency allocations," *Federal Communications Commission (2018)*. [Online]. Available: https://transition.fcc.gov/oet/spectrum/table/fcctable.pdf.

[I.16] A. Hirata *et al.*, "120-GHz-band wireless link technologies for outdoor 10-Gbit/s data transmission," *IEEE Transactions on Microwave Theory and Techniques*, vol. 60, no. 3, pp. 881–

895, 2012.

[I.17] S. Shin and J. S. Harrison, “Why WDM is essential in C-RAN fronthaul networks? - Ultra high CPRI link capacity,” *NETMANIAS Analyze Trendes, Technologies and Market*. [Online]. Available: https://www.netmanias.com/en/post/blog/6237/c-ran-fronthaul-cpri-lte/why-wdm-is-essential-in-c-ran-fronthaul-networks-ultra-high-cpri-link-capacity.

[I.18] S. Priebe, "MAC layer concepts for THz communications," *IEEE802 Presentation*, 2013.

[I.19] "IEEE Standard for High Data-rate Wireless Multi-Media Networks--Amendment 2: 100 Gb/s Wireless Switched P2P Physical Layer," *IEEE Standards Association (2017)*. [Online]. Available: https://ieeexplore.ieee.org/stamp/stamp.jsp?tp=&arnumber=8066476

[I.20] A. Ergintav, F. Herzel, J. Borngräber, D. Kissinger, and H. J. Ng, “An integrated 240 GHz differential frequency sixtupler in SiGe BiCMOS technology,” *IEEE Topical Meeting on Silicon Monolithic Integrated Circuits in RF Systems (SiRF)*, pp. 43–46, Phoenix, USA, 2017.

[I.21] “Background,” [Online]. Available: http://project-nanotec.com/background.html.

[I.22] “Semiconductor Technology,” [Online]. Available: http://www.tcl.tu-bs.de/research_semiconductor1.htm.

[I.23] J. Lee, Y. Chen, and Y. Huang, “A low-power low-cost fully-integrated 60-GHz transceiver system with OOK modulation and on-board antenna assembly,” *IEEE Journal of Solid-State Circuits*, vol. 45, no. 2, pp. 264–275, 2010.

[I.24] V. Vidojkovic *et al.*, “A low-power radio chipset in 40nm LP CMOS with beamforming for 60GHz high-data-rate wireless communication,” *Digest of Technical Papers - IEEE International Solid-State Circuits Conference*, vol. 56, pp. 236–237, 2013.

[I.25] E. S. Rogers, O. N. Ms, J. Monnet, and F.- Crolles, “A 12-Gb/s, Direct QPSK Modulation SiGe BiCMOS Transceiver for Last Mile Links in the 70-80 GHz Band,” *Annual IEEE Compound Semiconductor Integrated Circuit Symposium (CSICS)*, pp. 12–15, Greensboro, USA, 2009.

[I.26] S. Shahramian, Y. Baeyens, N. Kaneda, and Y. K. Chen, “A 70-100 GHz direct-conversion transmitter and receiver phased array chipset demonstrating 10 Gb/s wireless link,” *IEEE Journal of Solid-State Circuits*, vol. 48, no. 5, pp. 1113–1125, 2013.

[I.27] V. Vidojkovic, V. Szortyka, K. Khalaf, and G. Mangraviti, “CMOS Low-Power Transceivers for 60GHz Multi Gbit / s Communications,” *IEEE Custom Integrated Circuits Conference (CICC)*, pp. 1–8, San Jose, USA, 2013.

[I.28] S. Shopov, O. D. Gurbuz, G. M. Rebeiz, and S. P. Voinigescu, “A 10-Gb/s, 100-GHz RF Power-DAC Transmitter with On-Die I/Q Driven Antenna Elements and Free-Space Constellation Formation,” *Technical Digest - IEEE Compound Semiconductor Integrated Circuit Symposium, (CSIC)*, pp. 1-4, Austin, USA, 2016.

[I.29] Z. Xu *et al.*, “D-band CMOS transmitter and receiver for multi-giga-bit/sec wireless data link,” *IEEE Custom Integrated Circuits Conference (CICC)*, pp. 1–4, San Jose, USA, 2010.

[I.30] N. Deferm and P. Reynaert, "A 120 GHz fully integrated 10 Gb/s short-range star-QAM wireless transmitter with on-chip bondwire antenna in 45 nm low power CMOS," *IEEE Journal of Solid-State Circuits*, vol. 49, no. 7, pp. 1606–1616, 2014.

[I.31] N. Sarmah, B. Heinemann, and U. R. Pfeiffer, "235-275 GHz (x16) frequency multiplier chains with up to 0dBm peak output power and low DC power consumption," *IEEE Radio Frequency Integrated Circuits Symposium,* pp. 181–184, Tampa, USA, 2014.

[I.32] E. Ojefors, B. Heinemann, U. R. Pfeiffer, E. Ôjefors, and E. Öjefors, "Active 220-and 325-GHz frequency multiplier chains in an SiGe HBT technology," *IEEE Transactions on Microwave Theory and Techniques,* vol. 59, no. 5, pp. 1311–1318, 2011.

[I.33] S. P. Voinigescu *et al.*, "A study of SiGe HBT signal sources in the 220-330-GHz range," *IEEE Journal of Solid-State Circuits*, vol. 48, no. 9, pp. 2011–2021, 2013.

[I.34] T. Chi, J. Luo, S. Hu, and H. Wang, "A Multi-Phase Sub-Harmonic Injection Locking Technique for BW Extension in Silicon-Based THz Signal Generation," *IEEE Journal of Solid-State Circuits*, vol. 50, no. 8, pp. 1861–1873, 2015.

[I.35] J. Eisenbeis, F. Boes, B. Goettel, S. Malz, U. Pfeiffer, and T. Zwick, "30 Gbps wireless data transmission with fully integrated 240 GHz Silicon based transmitter," *IEEE Topical Meeting on Silicon Monolithic Integrated Circuits in RF Systems (SiRF)*, pp. 33–36, Phoenix, USA, 2017.

[I.36] M. H. Eissa, A. Malignaggi, R. Wang, M. Elkhouly, and K. Schmalz, "Wideband 240-GHz Transmitter and Receiver in BiCMOS Technology With 25-Gbit / s Data-rate," *IEEE Journal of Solid-State Circuits*, vol. 53, no. 9, pp. 1–11, 2018.

[I.37] T. Nagatsuma, G. Ducournau, C. C. Renaud, "Advances in terahertz communications accelerated by Photonics," *Nature Photonics*, vol. 10, no. 6, pp. 371–379, 2016.

[I.38] S. Klinger, "Germanium pin Photodiodes on Silicon and Photonic Integrated Circuits : Components for High-Speed Optical Data Communications," *PhD dissertation*, University of Stuttgart, 2011.

[I.39] J. Wang and S. Lee, "Ge-photodetectors for Si-based optoelectronic integration," *Sensors*, vol. 11, no. 1, pp. 696–718, 2011.

[I.40] P. G. Huggard, B. N. Ellison, P. Shen, N. J. Gomes, and J. M. Payne, "Generation of millimetre and sub-millimetre waves by photomixing in 1.55 μm wavelength photodiode," *Electronics Letters*, vol. 38, no. 7, pp. 327–328, 2002.

[I.41] D. Schoenherr *et al.*, "Characterization of THz emitter based on a high-speed pin photodiode," *Joint International Conference on Infrared and Millimeter Waves, and International Conference on Terahertz Electronics (IRMMW-THz)*, pp. 1002–1003, Cardiff, UK, 2007.

[I.42] S. Koenig *et al.*, "Wireless sub-mmW communication system with high data-rate enabled by RF Photonics and active MMIC technology," *IEEE Photonics Conference, (IPC)*, vol. 3, pp. 414–415, San Diego, USA, 2014.

[I.43] S. Jia *et al.*, "120 Gb/s multi-channel THz wireless transmission and THz receiver performance

analysis," *IEEE Photonics Technology Letters*, vol. 29, no. 3, pp. 310–313, 2017.

[I.44] T. Nagatsuma and G. Carpintero, "Recent Progress and Future Prospect of Photonics-Enabled Terahertz Communications Research," *IEICE Transaction on Electronics*, vol. E98–C, no. 12, pp. 1060–1070, 2015.

[I.45] T. Nagatsuma and H. Ito, "High-Power RF Uni-Traveling-Carrier Photodiodes (UTC-PDs) and Their Applications," *Advances in Photodiodes*, InTech, 2011.

[I.46] H. Ito, T. Furuta, S. Kodama and T. Ishibashi, "InP/lnGaAs uni-travelling-carrier photodiode with 310GHz bandwidth," *IEEE Electronics Letters*, vol. 36, no. 21, pp. 1809–1810, 2000.

[I.47] H. Ito *et al.*, "High-power Photonic millimetre wave generation at 100 GHz using matching-circuit-integrated uni-travelling-carrier photodiodes," *IEE Proceedings - Optoelectronics*, vol. 150, no. 2, pp. 138-142, 2003.

[I.48] J. M. Wun, Y. W. Wang, and J. W. Shi, "Ultrafast Uni-Traveling Carrier Photodiodes with GaAs0.5Sb0.5/In0.53Ga0.47As Type-II Hybrid Absorbers for High-Power Operation at THz Frequencies," *IEEE Journal of Selected Topics in Quantum Electronics*, vol. 24, no. 2, pp. 1-7, 2018.

[I.49] J. M. Wun *et al.*, "Photonic high-power continuous wave THz-wave generation by using flip-chip packaged uni-traveling carrier photodiodes and a femtosecond optical pulse generator," *IEEE Journal of Lightwave Technology*, vol. 34, no. 4, pp. 1387–1397, 2016.

[I.50] H. Ito *et al.*, "W-band uni-travelling-carrier photodiode module for high-power Photonic millimetre-wave generation," *IEEE Electronics Letters*, vol. 38, no. 22, p. 1376, 2002.

[I.51] A. Wakatsuki, Y. Muramoto, and T. Ishibashi, "Development of terahertz-wave photomixer module using a uni-traveling-carrier photodiode," *NTT Technical Review*, vol. 10, no. 2, 2012.

[I.52] H. Ito, T. Furuta, F. Nakajima, K. Yoshino, and T. Ishibashi, "Photonic generation of continuous THz wave using uni-traveling-carrier photodiode," *IEEE Journal of Lightwave Technology*, vol. 23, no. 12, pp. 4016–4021, 2005.

[I.53] T. Nagatsuma *et al.*, "Terahertz wireless communications based on Photonics technologies," *Optics Express*, vol. 21, no. 20, p. 23736, 2013.

[I.54] P. Latzel *et al.*, "THz transmission using QAM-16 and 32 Gbit/s on 25m," *IEEE International Conference on Infrared, Millimeter, and Terahertz waves (IRMMW-THz)*, pp. 1-2, Copenhagen, Denmark, 2016.

[I.55] S. Lischke *et al.*, "High BW, high responsivity waveguide-coupled germanium p-i-n photodiode," *Optics Express*, vol. 23, no. 21, pp. 27213–27220, 2015.

[I.56] F. Boeuf *et al.*, "Silicon Photonics R&D and Manufacturing on 300-mm Wafer Platform," *IEEE Journal of Lightwave Technology*, vol. 34, no. 2, pp. 4–6, 2015.

[I.57] O. Sandrine, "Caractérisation d'une photodiode Germanium sur Silicium en vue d'une utilization source de bruit intégrée Térahertz," *PhD dissertation*, University of Lille, 2014.

[I.58] F. Boeuf *et al.*, "Recent Progress in Silicon Photonics R&D and Manufacturing on 300mm Wafer Platform," *IEEE Optical Fiber Communication Conference (OFC)*, Los Angeles, USA, 2015.

[I.59] F. Ahmed, M. Furqan, and A. Stelzer, "A 0.3-THz SiGe-based frequency doubler chip with 3-dB 50 GHz BW and 17 dB peak conversion gain," *IEEE European Microwave Integrated Circuits Conference (EuMIC)*, pp. 134–137, Nuremberg, Germany, 2017.

[I.60] O. Momeni, S. Member, and E. Afshari, "A Broadband mm-Wave and Terahertz Traveling-Wave Frequency Multiplier on CMOS," *IEEE Journal of Solid-State Circuits*, vol. 46, no. 12, pp. 2966–2976, 2011.

[I.61] N. Sarmah, P. R. Vazquez, J. Grzyb, W. Foerster, B. Heinemann, and U. R. Pfeiffer, "A wideband fully integrated SiGe chipset for high data-rate communication at 240 GHz," *IEEE European Microwave Integrated Circuits Conference (EuMIC)*, pp. 181–184, London, UK, 2016.

[I.62] S. Shopov *et al.*, "A 234 – 261-GHz 55-nm SiGe BiCMOS Signal 1-GHz Divided-Down Output," *IEEE Journal of Solid-State Circuits*, vol. 51, no. 9, pp. 2054–2065, 2016.

[I.63] H. Lin, G. M. Rebeiz, and I. Terms, "A 200-245 GHz Balanced Frequency Doubler with Peak Output Power of + 2 dBm," *IEEE Compound Semiconductor Integrated Circuit Symposium (CSICS)*, pp. 4–7, Monterey, USA, 2013.

[I.64] A. S. A. Chain and W. Peak, "A 165-230GHz SiGe Amplifier-Doubler Chain With 5dBm Peak Output Power," *IEEE Radio Frequency Integrated Circuits Symposium (RFIC)*, pp. 302–305, San Francisco, USA, 2016.

[I.65] A. S. I. Oscillator, O. Power, S. Li, D. Fritsche, C. Carta, and F. Ellinger, "A 200-GHz Sub-Harmonic Injection-Locked Oscillator with 0-dBm Output Power and 3.5% DC-to-RF-Efficiency," *IEEE Radio Frequency Integrated Circuits Symposium (RFIC)*, pp. 212–215, Philadelphia, USA, 2018.

[I.66] S. Hu *et al.*, "A SiGe BiCMOS transmitter/receiver chipset with on-chip SIW antennas for terahertz applications," *IEEE Journal of Solid-State Circuits*, vol. 47, no. 11, pp. 2654–2664, 2012.

[I.67] C. J. Lee *et al.*, "A 120 GHz I / Q Transmitter Front-end in a 40 nm CMOS for Wireless Chip to Chip Communication," *IEEE Radio Frequency Integrated Circuits Symposium (RFIC)*, pp. 192–195, Philadelphia, USA, 2018.

[I.68] H. Ito, S. Member, and T. Ishibashi, "Photonic Terahertz-Wave Generation Using Slot-Antenna-Integrated Uni-Traveling-Carrier Photodiodes," *IEEE Journal of Selected Topics in Quantum Electronics*, vol. 23, no. 4, 2017.

[I.69] H. Ito *et al.*, "Pre-amplifier-integrated uni-traveling-carrier photodiode module with a rectangular waveguide output port for operation in the 120-GHz band," *Annual Meeting of the IEEELasers and Electro-Optics Society (LEOS)*, vol. 1, pp. 128–129, Rio Grande, Puerto Rico, 2004.

[I.70] A. Wakatsuki, T. Furuta, Y. Muramoto, T. Yoshimatsu, H. Ito, and M. Wakamiya, "High-power and Broadband Sub-terahertz Wave Generation Using a J-band Photomixer Module with Rectangular-waveguide Output Port," *IEEE International Conference on Infrared, Millimeter and Terahertz Waves (IRMMW-THz),* vol. 3, pp. 1-2, Pasadena, USA, 2008.

[I.71] T. Nagatsuma, H. Song, Y. Fujimoto, K. Miyake, and A. Hirata, "Giga-bit Wireless Link Using 300-400 GHz Band," *IEEE International Topical Meeting on Microwave Photonics (MWP)*, pp. 1-4, Valencia, Spain, 2009.

[I.72] P. G. Huggard, B. N. Ellison, P. Shen, N. J. Gomes, and J. M. Payne, "Generation of millimetre and sub-millimetre waves by photomixing in 1.55μm wavelength photodiode," *Electronics Letters*,vol. 38, no. 7, pp. 327–328, 2002.

[I.73] E. Fondamentale, C. Umr, U. P. Xi, and F.- Orsay, "42 GHz waveguide Germanium-on-Silicon vertical PIN photodetector," *IEEE International Conference on Group IV Photonics (GFP)*, pp. 185–187, 2008.

[I.74] D. Suh, J. Joo, S. Kim, and G. Kim, "High-Speed RPCVD Ge Waveguide Photodetector," *IEEE International Conference on Group IV Photonics (OFP)*, pp. 16–18, San Francisco, USA, 2009.

[I.75] L. Colace, G. Masini, and G. Assanto, "Ge-on-Si approaches to the detection of near-infrared light," *IEEE Journal of Quantum Electronics*, vol. 35, no. 12, pp. 1843–1852, 1999.

[I.76] S. Klinger, M. Berroth, M. Kaschel, M. Oehme, and E. Kasper, "Ge-on-Si p-i-n photodiodes with a 3-dB BW of 49 GHz," *IEEE Photonics Technology Letters*, vol. 21, no. 13, pp. 920–922, 2009.

[I.77] X. Yu *et al.*, "400-GHz Wireless Transmission of 60-Gb/s Nyquist-QPSK Signals Using UTC-PD and Heterodyne Mixer," *IEEE Transactions on Terahertz Science and Technology*, vol. 6, no. 6, pp. 765–770, 2016.

[I.78] "LoRaWAN," *LoRa Alliance*. [Online]. Available: https://www.lora-alliance.org/about-lorawan.

[I.79] "LoRa Network Protocol and Long Range Wireless IoT," *Postscapes*. [Online]. Available: https://www.postscapes.com/long-range-wireless-iot-protocol-lora/.

[I.80] "LTE-Advanced," *3GPP*, 2013. [Online]. Available: http://www.3gpp.org/technologies/keywords-acronyms/97-lte-advanced.

[I.81] "LTE and LTE advanced," Universtiy of Cyprus, [Online]. Available: https://www.cs.ucy.ac.cy/courses/EPL657/slides_2014/EPL%20657%20LTE%20and%20LTE%20advanced%202014.pdf.

[I.82] C. Links, "Wi-Fi Data-rates: Channels and Capacity," *Qorvo*, White paper, 2017.

[I.83] "Fiber Transceiver Solution: Copper Cabling Choices for 10G Ethernet," [Online]. Available: http://www.fiber-optic-transceiver-module.com/copper-cabling-choices-for-10g-ethernet.html.

[I.84] A. Gui, "Tutorials Of Optical fiber Products: Understand 100G Ethernet Standards," [Online]. Available: http://www.fiber-optic-tutorial.com/understand-100g-ethernet-standards.html.

[I.85] "OWC Thunderbolt 2 Cables," [Online]. Available: https://eshop.macsales.com/shop/Thunderbolt/OWC/Thunderbolt-Cables/.

[I.86] E. Johnson, "Mobile Data Backhaul : The Need For E - Band," *Sky Light Research, Mobile World Congress*, White paper, 2013.

[I.87] "E-band Converter with LO E-band Converter with LO," *SiversIMA data-sheet.* [Online]. Available: https://siversima.com/wp-content/uploads/FC1003E02-Data-Sheet.pdf.

[I.88] "WTM 3300 70-80 GHz Eband radio," *Aviat Network*. [Online]. Available: https://aviatnetworks.com/products/all-outdoor-radio/wtm-3300-high-capacity/.

[I.89] S. K. Saha, T. Siddiqui, D. Koutsonikolas, A. Loch, J. Widmer, and R. Sridhar, "A Detailed Look into Power Consumption of Commodity 60 GHz Devices," *IEEE International Symposium on A World of Wireless, Mobile and Multimedia Networks (WoWMoM)*, pp. 12 - 15, Macau, China, 2017.

[I.90] "Lenovo ThinkPad T460s Long-Term Review: Part 2 - Wireless Docks and Terabyte SSDs," *NotebookCheck*. [Online]. Available: https://www.notebookcheck.net/Lenovo-ThinkPad-T460s-Long-Term-Review-Part-2-Wireless-Docks-and-Terabyte-SSDs.168208.0.html.

[I.91] "Cisco 40GBASE QSFP Modules Data Sheet," *Cisco*. [Online]. Available: https://www.cisco.com/c/en/us/products/collateral/interfaces-modules/transceiver-modules/data_sheet_c78-660083.html.

[I.92] "10GBASE-T Cabling Vs. 10G SFP+ Cabling in 2017," *Optical fiberal Networking*. [Online]. Available: http://www.fiber-optical-networking.com/10gbase-t-cabling-vs-10g-sfp-cabling-in-2017.html.

[I.93] "QSFP+ v. SFP+ v. 10Gbase-T – Testing power consumption differences," *STH*. [Online]. Available: https://www.servethehome.com/qsfp-v-sfp-v-10gbase-t-testing-power-consumption-differences/.

[I.94] "Confused by 10GbE optics modules," *NetworkWorld*. [Online]. Available: https://www.networkworld.com/article/2231028/cisco-subnet/confused-by-10gbe-optics-modules-.html.

[I.95] "USB3.0 Active Optical Cable (U3C)," *Yangtze optical fibre and cable joint stock limited company.* [Online]. Available: http://en.yofc.com/wcs/Upload/201610/5811664bba3f1.pdf.

[I.96] B. Schweber, "Active Thunderbolt cables get transceiver, power management IC support," *EETimes*. [Online]. Available: https://www.eetimes.com/document.asp?doc_id=1317215.

[I.97] M. Liang, J. Wu, and X. Yu, "3D printing technology for RF and THz antennas," *IEEE International Symposium on Antennas and Propagation (ISAP)*, pp. 536–537, Okinawa, Japan, 2016.

Chapter 2: High data-rate Tx integrated in Silicon Photonics targeting the 200-300 GHz frequency band

Table of Contents

Chapter 2: High data-rate Tx integrated in Silicon Photonics targeting the 200-300 GHz frequency band

In order to maximize the antenna system's performance and maintain the signal integrity, the signal power should be optimized at each building blocks of the wireless system, from the generation of the sub-mmW/THz optical signal in the Photonic Tx to the radiation of the electrical signal at the antenna. In this chapter, we will focus on the maximization of the Silicon Photonics IC's output power. The design and conception of an IC using STMicroelectronics' industrial photodiode is presented, with the integration of a matching network to optimize the delivered 50Ω-matching and a bias Tee for DC polarization. A sub-mmW/THz source design was realized targeting three different frequency bands in order to evaluate a very large frequency spectrum: 130-220 GHz, 200-280 GH, and 220-330 GHz.

Towards the development of a complete system-on-chip (SoC) Tx, the integration of an optical modulator was also considered in the second part of this chapter. Two types of modulators were investigated in order to reach different data-rates. A modulator dedicated to OOK modulation schemes is aimed at reaching maximum 25 Gb/s, while another modulator design is able to withstand PAM4 modulation schemes in order to reach 50 Gb/s.

Several Photonic integrated circuits (PICs) were manufactured in order to realize sub-mmW and THz electrical characterizations of these Silicon Photonics components. Data-communication wireless link demonstrations using these PICs will be presented in Chapter 5.

I. STMicroelectronics' Silicon Photonic platform

One of the major benefits offered by Silicon Photonics technology is its capability to enable monolithically integrated optical and electrical components on one Silicon wafer using standard Silicon manufacturing process. Its compatibility with Silicon technology is indeed a key enabler for Silicon-based cost-effective Txs at sub-mmW or THz frequencies. In the context of data-center optical module business, STMicroelectronics has developed an industrial Silicon Photonics platform referred to as Photonic Integrated Circuit targeting data rate of 25 Gb/s (PIC25G). This platform offers the main Silicon Photonics building blocks required for the development of low-cost high-speed optical links operating on the main wavelengths used for telecommunication applications (1310 nm, 1490 nm, 1550 nm) [II.1], and is supported by standard fabrication plants using 300 mm wafers. The wafers consist of 300 nm thick Semiconductor-Oxide Insulator substrates (SOI) with a 720 nm thick buried oxide (BOX). On these wafers dedicated to PIC25G, the front end of line (FEOL) integrates all the processed active and passive Photonic and electrical components whereas the back end of line (BEOL) integrates four stacked metallic layers and a top aluminum layer used for the design of passive devices (Figure II.1).

The key optical components available in technology PIC25G are the single-mode waveguide, the single polarization grating coupler, the high-speed phase modulator and the SiGe PIN photodiode. A description of these devices is given in the following sections.

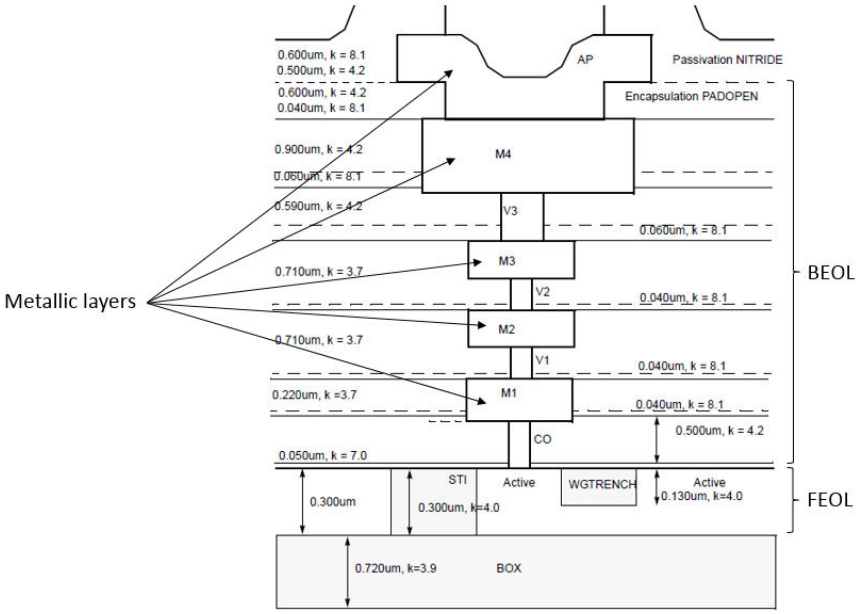

Figure II.1. PIC25G technology cross section (FEOL and BEOL).

1. Single-mode waveguide

The optical waveguide is used for the transmission of optical signals inside the PIC. It is formed on SOI wafer by etching the Si layer located on top of the buried Silicon dioxide (SiO_2). By doing so, we can leverage the high refraction index contrast between Si and SiO_2 (n_{Si} ~3.5 and n_{SiO2} ~1.45) in order to confine the optical signal. The integrated waveguides provided by STMicroelectronics' PIC25G technology are rib waveguides. The structure of such a waveguide consists of a Si slab with a Si strip waveguide superimposed onto it, and SiO_2 claddings on the top and bottom. This structure is illustrated in Figure II.2.

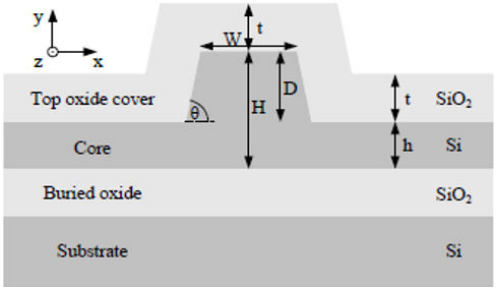

Figure II.2. Cross-section schematic of a rib waveguide in PIC25G technology.

In order to achieve a single-mode waveguide, the ratio D/H needs to be contained between 0.5 and 1. Consequently, if we consider a standard 300 µm thick Si substrate, we would choose D = 200 µm and H = 300 µm (D/H = 0.67). Even those rib waveguides are more complex than strip waveguides, they offer a more flexible design and higher performance. Finally, this single-mode waveguide exhibits losses lower than 1.2 dB/cm.

2. Grating coupler

The grating coupler (also call holographic lens) takes care of the coupling between the optical signal coming from a single-monde optical fiber (SMF) and the Si PIC (and vis-versa), which is necessary considering the high mismatch between the two modes. Indeed, waveguides integrated on SOI are

about 50 times more compact than the typical core diameter of a SMF due to a very strong refractive index gradient between the Si core and SiO_2 claddings of the rib waveguide. As a result, it is very difficult to directly couple a SMF to the rib waveguide.

This holographic lens allows coupling perpendicular to the PIC, which is quite practical for on wafer testing (using fiber arrays for example) as well as for integrated optical assembly (signal transfer from an optical interposer to a flip-chipped PIC). Indeed, it is a passive reciprocal component and thus operates both in transmission and reception. Single-polarization grating couplers are used in PIC25G, thereby coupling effectively under one optical polarization. The grating patterns are implemented through a partial Si etching process as shown in Figure II.3. Insertion losses are typically in the order of 2 dB.

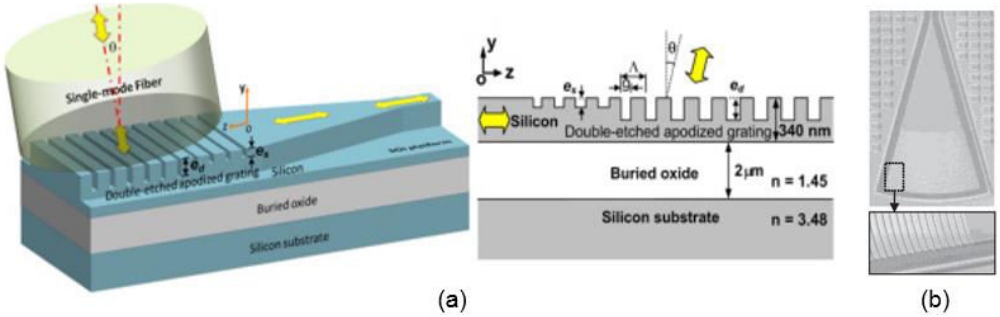

Figure II.3. (a) Schematic of grating coupler and its functioning principle, (b) microscope photo of the fabrication grating coupling integrated in PIC25G.

3. High-speed phase modulator

The high-speed phase modulator (HSPM) is used to overlap an electric data flow onto an optical carrier signal through phase modulation. This technique relies upon the change of Silicon refractive index in order to induce phase shifts on the optical signal. However, Silicon is not an ideal material in which to integrate an optical modulator due to its very low intrinsic linear electro-optic effect compared to more traditional materials like Lithium Niobate. As an alternative, an efficient way to change the refractive index is through plasma dispersion effect which relies upon free carrier dispersion [II.2]. An example of an industrial Mach-Zehnder modulator (MZM) based on HSPMs is represented in Figure II.4 (a) and the topology of an HSPM is shown in Figure II.4 (b) as well.

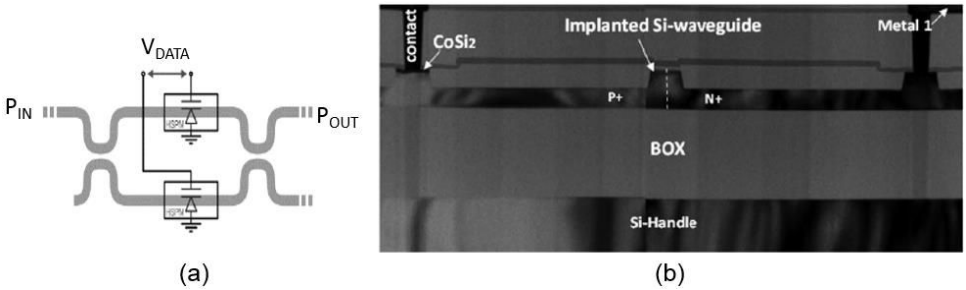

Figure II.4. Schematic (a) and SEM cross-section of integrated PN junction depletion mode (b) of PIC25G high-speed phase modulator.

As we can see, a lateral PN junction is created by doping the Silicon waveguide with negative (N+) and positive (P+) free charge carriers. This diode junction is direct and reverse biased in order to modify the charge carrier density in the depletion zone overlapping the optical waveguides of the HSPM. In order to lower down the equivalent resistance of the junction, a strong doping is necessary. However,

losses inside the waveguide are increasing with the increasing density of free carriers. Therefore, a compromise between those two aspects is found while insuring a sufficient phase shift along the modulator's waveguides. At the output of the MZM, these phase shifts induce either constructive or destructive interferences between two optical signals, resulting in high and low optical intensity. The phase shift difference between the two arms of the HSPM is a function of the PN junction's length. Therefore, the MZM's arm should be long enough to reach the maximum phase shift, which corresponds to a maximum extinction ratio.

4. Silicon-Germanium PIN photodiode

The photodiode is a semiconductor device that converts a flow of photons into an electrical current. This quantum detector device generates free charge carriers only when the right photon energy level (corresponding to the semiconductor's bandgap) is reached. As Silicon has an indirect bandgap, it features a rather poor optical absorption efficiency compared to III-V semiconductors. To bypass this issue, hetero-epitaxy of Germanium on Silicon has proven to be a successful solution offering low-cost integration process and compatibility with Silicon technology. This process has now reached a high level of maturity for the fabrication of industrial SiGe photodiodes.

Among the different types of photodetectors junctions, the P-doped/Intrinsic/N-doped (PIN) junction was selected for Silicon Photonics technologies rather than a PN junction, in order to increase the speed of response. This junction consists of an intrinsic semiconductor zone between a positively doped and negatively doped zone. The intrinsic zone is generally very large in order to generate a maximum of free carriers and benefit from a strong reverse electric field for the generated holes and electrons to drift towards the P and N regions respectively. Structure optimization strategies have been employed in order to significantly increase the responsivity and therefore the O-E efficiency of this type of photodiodes. The first one is the waveguide integrated PIN-PD (WG PIN-PD) structure shown in Figure II.5. In this configuration, optical input is coupled to an integrated waveguide on top of which the Ge absorption layer is processed. By increasing the length of the waveguide and Ge layer, the optical coupling inside the latter is increased thereby improving the optical efficiency. Indeed, from a responsivity of 0.2 A/W at -1 V achieved in [II.3], this method enabled to reach a responsivity of 1 A/W at -1 V with a waveguide length of 20 µm under the active layer in [II.4].

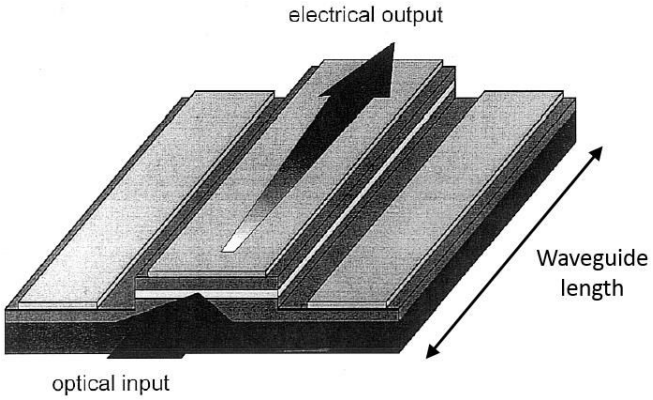

Figure II.5. Concept of a travelling wave PIN-PD with an optical rib waveguide and a coplanar transmission line.

Tow WG PIN-PD topologies have been investigated for further performance improvement: the vertical photodiode (VPD) and the lateral photodiode (LPD) shown in Figure II.6 (a) and (b) respectively

[II.5]. Both topologies have delivered similar results according to [II.6]. However, they behave differently when optimizing the -3dB BW due to their different geometries. In the VPD, modifying the Ge layer thickness ($t_{i\text{-}Ge}$) to optimize the RC time constant and carrier transit-time trade-off also modifies the absorption efficiency. By contrast, in the LPD, the RC and transit-time BW and the absorption efficiency can be independently optimized through the Ge layer width ($w_{i\text{-}Ge}$) and height (t_{Ge}) respectively.

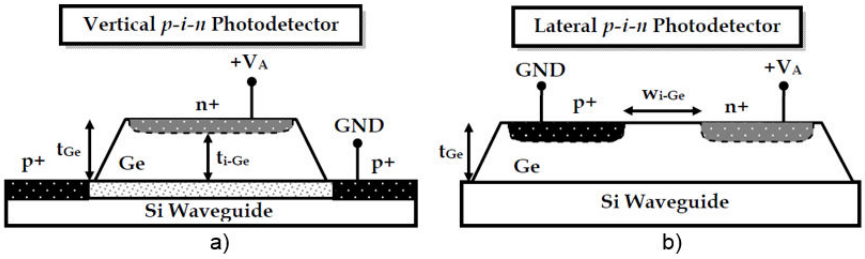

Figure II.6. Design of an evanescent butt-coupled SiGe photodetector featuring (a) vertical PIN configuration and (b) lateral PIN configuration [II.5].

The implementation of a waveguide-coupled vertical PIN-PD structure has allowed to improve the -3dB BW from 10 GHz at -1 V in [II.7] to 49 GHz at -2 V in [II.8]. Moreover, a BW of up to 70 GHz was achieved at -1 V in [II.4] with the development of a waveguide-coupled lateral PIN-PD structure. As a conclusion, the waveguide-coupled lateral PIN-PD structure has been considered to be the most promising photomixer candidate to deal with BW-efficiency trade-off.

The up-to-date PIN-PD (shown in Figure II.7) developed in PIC25G consists of a waveguide-coupled lateral PIN-PD structure featuring a responsivity close to 1 A/W at -1 V. Even though these detectors exhibit relatively low obscurity current levels, their major drawback is their inability to exhibit high cut-off frequencies and high quantum efficiency simultaneously. Nevertheless, this photodiode has achieved a -3dB O-E BW above 20 GHz, and has already demonstrated up to 28 Gb/s data-rate with a low-cost optical packaging test vehicle [II.9]. According to previous work led by former STMicroelectronics PhD student S. Oeuvrard, a PIC25G test structure with integrated PIN-PD and matching circuit was developed and an on-wafer measured output power of -20 dBm was achieved at 210 GHz for a photocurrent of 2 mA at 1 V reverse bias (2 mW DC power consumption) [II.10].

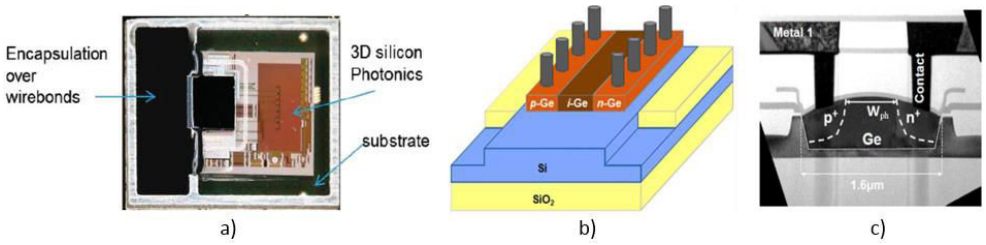

Figure II.7.(a) 28 Gb/s Land-Grid-Array packaging for Silicon Photonics with flip-chipped Si chip [II.9]*, (b) 3D schematic, and (c) TEM cross section of the PIC25G PIN photodiode* [II.10].

II. Complete Silicon Photonics THz system overview

Towards the development of a complete SoC sub-mmW Tx integrated in Silicon Photonics, a schematic of the envisioned wireless link based on a Silicon Photonics in shown in Figure II.8. Three main blocks are necessary: the Photonic-based sub-mmW frequency comb (blue box), the 40 Gb/s sub-

mmW optical-based signal generation (green box), and the Schottky diode Rx using direct detection (black box). A short description of the working principle for each build-in blocks is given in this section. However, the objectives of this PhD project were focused on the study and development of the 40 Gb/s sub-mmW optical and electrical signal generation exclusively (green box).

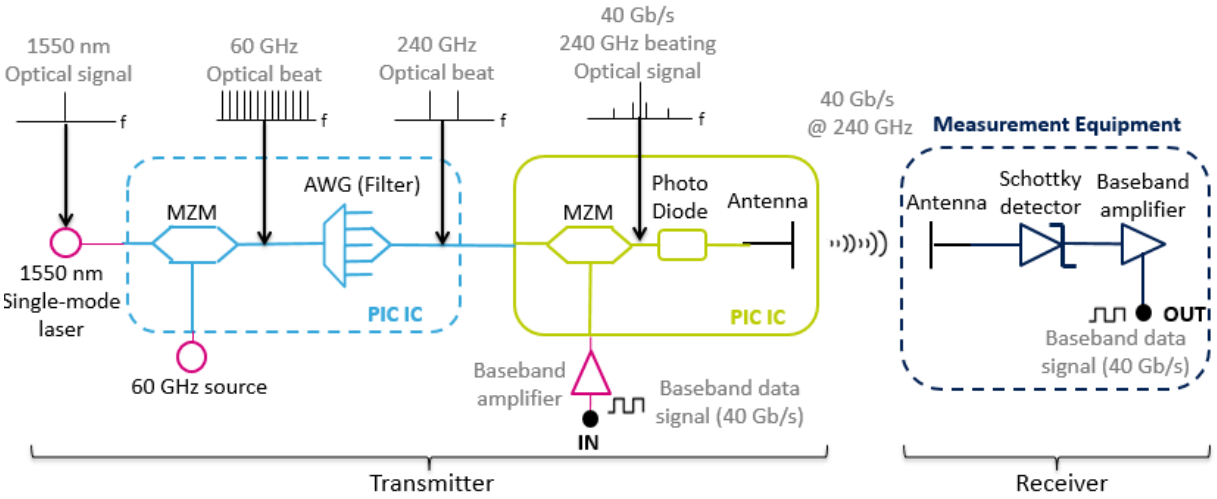

Figure II.8. Schematic of a sub-mmW wireless link based on a complete system on chip Silicon-Photonic Tx.

1. Photonic sub-mmW frequency comb

The first build-in block in blue on Figure II.8 is dedicated to the integration of a Photonic frequency comb used for the generation of an optical mmW frequency beat. This frequency comb first consists of an integrated Continuous-Wave (CW) laser diode at 1550 nm that doesn't need any phase locking. This optical signal with a corresponding frequency $f_0 = v/\lambda_0$ is frequency (or phase) modulated through a plasma dispersion phase modulator like the MZM presented in the above section. Both arms of the MZM are driven by a sine wave with a modulation frequency f_m of 60 GHz. This induces a frequency modulation of the optical field at the output of the MZM with a final signal spectrum containing the centre frequency f_0, and the harmonic side-bands $f_0 \pm n*f_m$. These multiple side-bands with even spectral spacing of 60 GHz represent the desired frequency comb, which could as well be seen as a wavelength comb (Figure II.9).

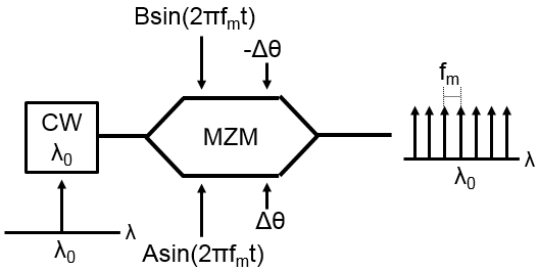

Figure II.9. Electro-optic phase modulation frequency comb principle.

The frequency comb is then injected inside a planar Arrayed Waveguide Grating (AWG). This device is usually used for wavelength division multiplexing/demultiplexing in multiple-channel optical signal transmissions. Its functioning principle is shown on the schematic in Figure II.10. The incoming large wavelength-spectrum beam is diffracted from an integrated waveguide to an array of integrated waveguides, also called a phased array. Each waveguide of the phased has a constant path difference from one waveguide to the next. Therefore, at the phased array's output, each wavelength of the light

beam is spectrally separated and focused into a single waveguide at the output of the AWG. This happens when the total phase-shift of a specific wavelength between two arrayed-waveguides equals a multiple of 2π. Under this condition, constrictive interferences occur at a specific focusing point which corresponds to the dedicated output waveguide as shown in Figure II.10. As the frequency separation of the AWG between two adjacent ports is 60 GHz, two optical signals λ_1 and λ_2 separated by a frequency of 240 GHz can be retrieved by selecting the 1st and the 4th output waveguide ports.

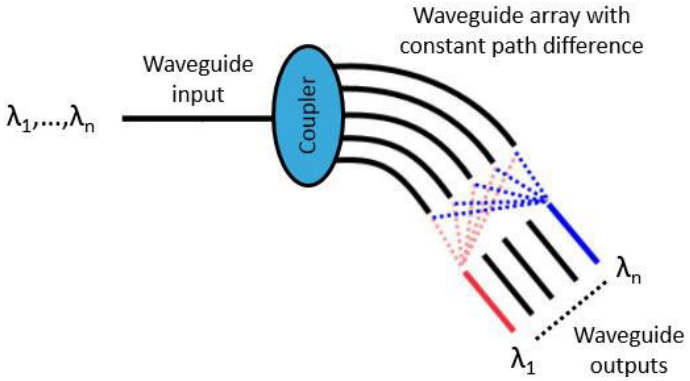

Figure II.10. Arrayed waveguide grating working principle.

2. 40 Gb/s sub-mmW optical and electrical signal generation

The second build-in block in green on Figure II.8 is dedicated to the integration of a 40 Gb/s sub-mmW/THz signal modulator. Its functioning principle is shown in Figure II.11. The first step is to modulate the optical signal with a 40 Gb/s OOK modulation scheme through a MZM. Modulating the two optical signals λ_1 and λ_2 is not necessary, therefore only λ_1 can be modulated with the same approach as the generation of the frequency comb described earlier. In this approach, a 40 Gb/s baseband signal is generated by a PRBS electrical generator in a baseband BW of 40 GHz. This baseband signal drives the arms of the MZM in order to transfer this modulation onto the optical carrier. Sidebands are therefore produced around the centre frequency $f_1 = v/\lambda_1$ with a deviation frequency equal to the rate frequency $f_R = 40$ GHz, resulting in a total optical BW of $2*f_R = 80$ GHz.

The modulated optical carrier λ_1 is then combined with λ_2 through a 3dB coupler to create the 40 Gb/s 240 GHz optical frequency beat. This optical beat is finally transmitted to the photodiode for photomixing, after which a 240 GHz electrical signal modulated at 40 Gb/s is generated. This signal transits towards the antenna system which finally radiates it into free space.

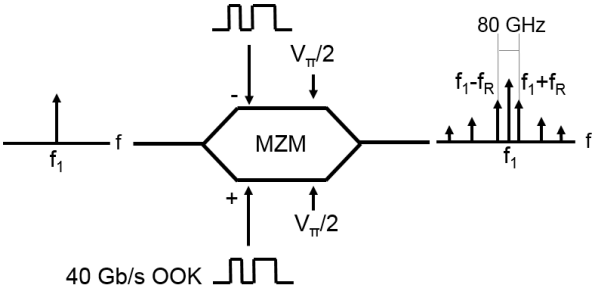

Figure II.11. 40 Gb/s Photonic modulation through an electro-optic phase modulator.

3. Schottky diode direct detection

A direct detector based on a Schottky diode is used for the sub-mmW Rx in black in Figure II.8. Indeed, the Schottky diode provides a low forward voltage, low capacitance and high frequency capability, which makes it well suited for RF detection. It operates by producing a baseband output signal that is proportional to the magnitude of the RF input power, thereby retrieving the envelope of the RF input signal. For the detection of small signals (very low incoming power), the Schottky diode is used in its square law region (as opposed to its linear region) where the output voltage is proportional to the square of the input voltage and thus proportional to the input power as shown in Figure II.12 (a). The simplest design of a direct detector based on a Schottky diode is shown in Figure II.12 (b) and includes a capacitor, which removes the unwanted RF carrier. The baseband signal is finally amplified before data measurement. A global description of the Tx/Rx set-up used in data communication demonstrations will be given in Chapter 4.

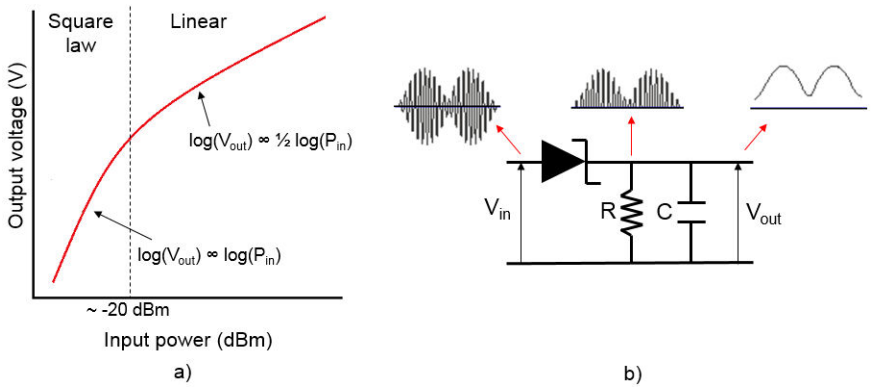

Figure II.12. (a) Square law and linear detection regions of a Schottky diode and (b) detector circuit.

III. THz source integrated in PIC25G

This section focuses on the design of a preliminary Tx integrated in PIC25G in order to evaluate achievable performance at sub-mmW frequencies using this industrial technology. A test structure integrating the SiGe PIN-PD alone was first realized so as to evaluate the intrinsic performance of this component. Several other test structures were then designed with the addition of 50 ohm matching circuits and DC bias targeting three different BWs: 120-220 GHz, 200-280 GHz and 220-330 GHz. A MZM was also considered in the design of new test structures. Theses PICs were finally prototyped and performance such as the S parameters, output power, and achievable data-rates were measured.

1. Equivalent circuit of the SiGe photodiode integrated in PIC25G

In order to evaluate the frequency response and electrical characteristics of the PIN-PD, S parameter measurements have been performed at STMicroelectronics during former PhD studies led by Dr. Sandrine Oeuvrard [II.10]. This enabled to retrieve the equivalent electrical circuit of the PIN-PD. However, the GSG pads that were used for probing were exhibiting significant capacitive effect of about 30 fF (value that can be minimized by optimizing the RF PAD layout). We can visualize the impact of the pads' capacitance by comparing the real and de-embedded S_{11} shown in Figure II.13.

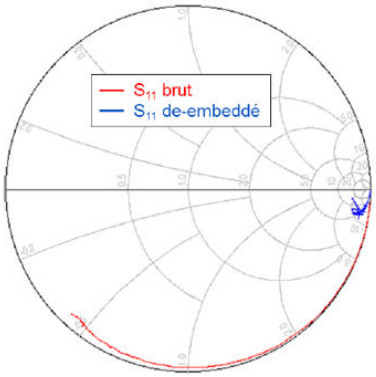

Figure II.13. S_{11} measurement of the PIN-PD before (red) and after (blue) de-embedding of the pads between 1 GHz and 67 GHz for a reverse bias of -2V and in the dark from S. Oeuvrard's PhD.

Taking into account this pad capacitance, the equivalent circuit shown below was retrieved from measurements above 40 GHz with an equivalent resistance R_{eq} = 271 Ω, inductance L_{eq} = 100 pH and capacitance C_{eq} = 4.4 fF. Those values seemed constant above 40 GHz and were therefore used to simulate the PIN-PD's insertion loss and matching up to 330 GHz (Figure II.14). Without any matching network, the PIN-PD shows the following performance under a 50 ohm load:

- -4 dB insertion loss over 130-330 GHz
- -2 dB matching BW over 130-330 GHz

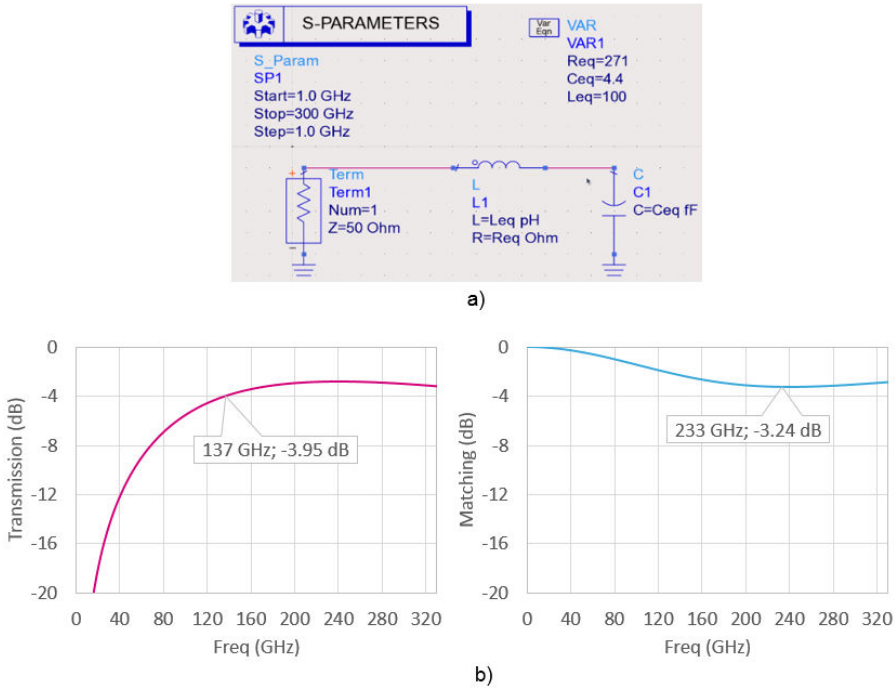

Figure II.14. (a) Equivalent circuit of the PIN-PD from S. Oeuvrard's PhD study, and (b) resulting matching under 50 ohms and insertion loss of the PIN-PD from 0 to 330 GHz.

We can note that half of the available energy at the PIN-PD's output would be lost due to mismatch between the photodiode and a 50 ohm load. In order to minimize this effect and improve the transmission, the integration of a matching circuit between the photodiode and the load seems necessary. The design and simulation of such a circuit was realized and simulated between 130 GHz and 330 GHz using Keysight ADS Design software, and is presented in the following section.

In parallel, a first test structure was designed with the integration of the PIN-PD in order to evaluate its intrinsic performance. In previous works [II.3], the achievable output power using PIC25G technology was investigated at W band but the performance at higher frequencies (G band) was limited by the RF pads parasitic capacitance (~50 fF). In this new design, the photodiode is physically connected to an optimized RF pad (parasitic capacitance < 10 fF) and an open-circuit pad was added for pad parasitic de-embedding. A circuit layout was designed using Cadence Virtuoso software (Figure II.15), in which each metal level of the IC can be represented, from the FEOL (grating coupler, waveguide, photodiode) up to the BEOL (metallic layers of the electrical circuit). This drawing allows to take into account the minimum distances between the pads and the GC to ensure that assembly rule constraints and probe measurement constraints are respected (distance between the optical fiber and the RF probe).

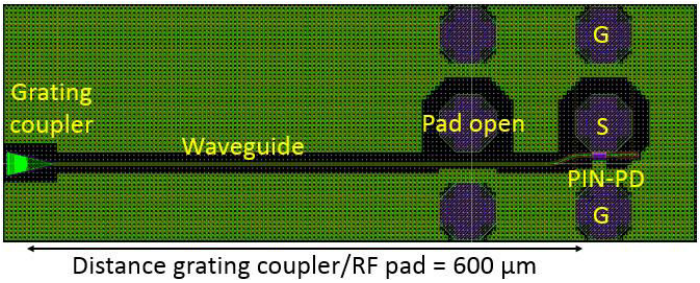

Figure II.15. Layout of the PIC25G test structure integrating the PIN-PD alone.

2. Design of a THz source with matched SiGe PIN-PD integrated in PIC25G

As mentioned above, matching circuits were designed in new test structures to optimize the photodiode's performance as an RF power source. Three BWs were targeted: 130-220 GHz (51%), 200-280 GHz (33%), 220-330 GHz (40%). However, for sake of clarity, only the design process of the 220-330 GHz matched test structure will be detailed.

The microstrip line model used in ADS for the design of the integrated matching circuit is part of the PIC25G design kit and is realized on the AP metallic layer of the PIC25G BEOL. Its electrical characteristics were implemented in ADS. To do so, the PIC25G BEOL's layers thickness and dielectric characteristics were used as well as experimental coefficients retrieved from measurements, in order to fit the microstrip line's simulated frequency behavior through polynomial regressions of several parameters (like the equivalent resistance, capacitance and inductance of the line). The transmission matrix of the microstrip line model was then calculated and imported inside of a transmission line model dedicated to PIC25G technology, as shown in Figure II.16.

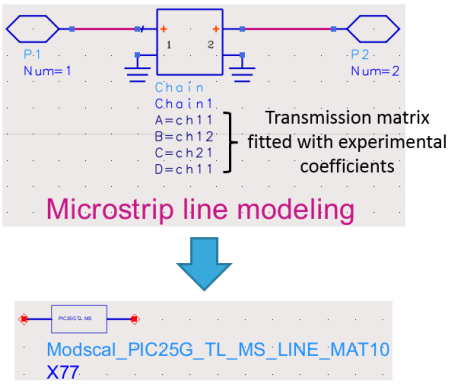

Figure II.16. PIC25G microstrip transmission line model on ADS.

a. Electrical matching network and DC bias

Assuming that the photodiode's impedance remains constant up-to THz frequencies, a matching circuit is needed in the prospect of connecting the sub-mmW/THz source to a 50ohm-antenna. What's more, considering a fully integrated sub-mmW/THz source SoC, the integration of a DC biasing circuit is also mandatory in order to bias the photodiode within the PIC25G module.

The circuit's first element consists of a quarter-wavelength (λ/4) microstrip line, commonly used for real impedance matching according to the formula $Z_C = \sqrt{(Z_{IN} * Z_{OUT})}$, where Z_C, Z_{IN} and Z_{OUT} are the characteristic, input, and output impedances. With a characteristic impedance of 80 Ω, this line transforms the photodiode's impedance of 271 Ω into 25 Ω. The line's width was adjusted as such.

A bias Tee was then added in order to both transform the 25 Ω impedance into 50 Ω and allow direct DC bias of the photodiode while decoupling the DC and RF signals. This bias Tee was arranged with a simple high Z_C λ/4 line and low Z_C λ/4 stub. This configuration transforms the open-circuit of the stub into a short-circuit inside the DC circuit, and finally brings an open-circuit to the RF circuit in order to avoid RF signal leakage towards the DC port as explained in the schematic on Figure II.17.

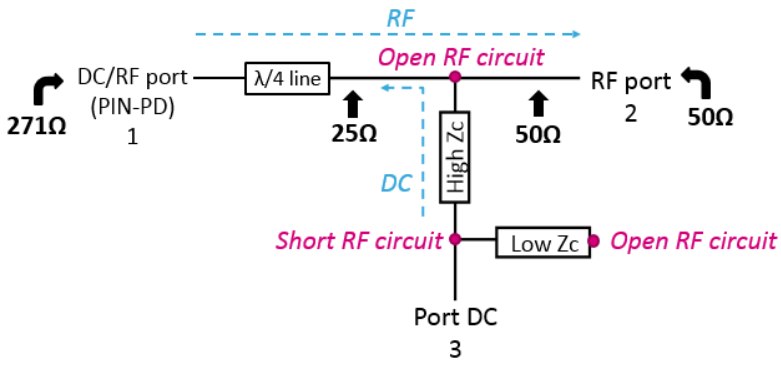

Figure II.17. Photodiode matching circuit and bias Tee schematic.

The simulated insertion loss and matching between 220 GHz and 330 GHz are the following:

- 1.9 dB < insertion loss < 2.12 dB
- Matching BW over 220-330 GHz: -11.3 dB.

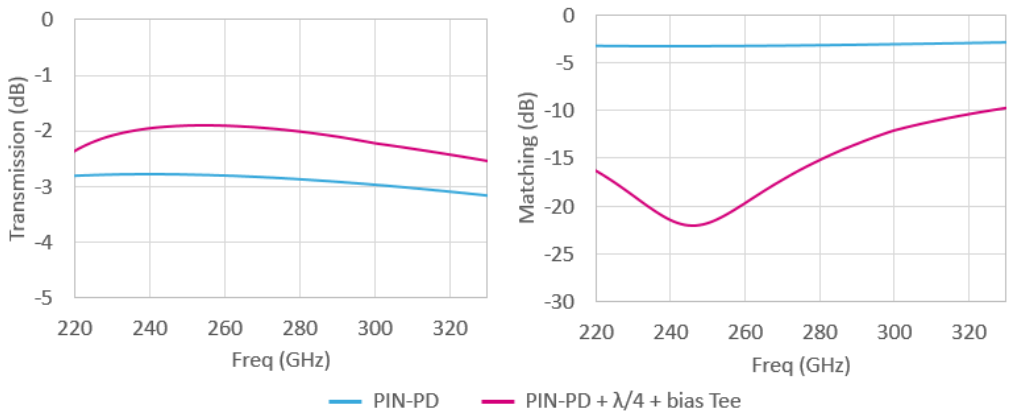

Figure II.18. Simulated transmission coefficient and matching comparison between unmatched and match PIN-PD integrated circuit between 220 GHz and 330 GHz.

In order to take into account the implementation constraints related to the integration of the proposed circuit, a first layout of the electrical circuit schematic shown in Figure II.17 was designed using Cadence Virtuoso. The resulting drawing shown in Figure II.19 allows to estimate the interconnection line length that is needed between the DC input of the bias Tee and the DC pad of the chip. A simulation of this missing line enables to estimate the impact on the matching and insertion loss.

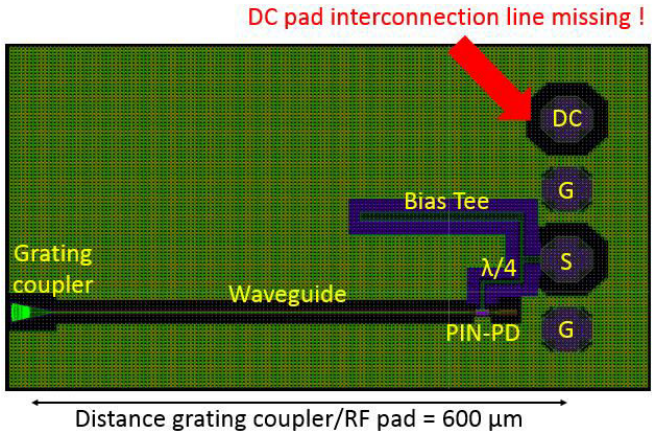

Figure II.19. Layout of the PIC25G test structure with integrated PIN-PD, matching circuit and bias Tee.

b. Improvement of the RF/DC decoupling capacity of the bias Tee

The modified electrical schematic of the IC is shown in Figure II.20 (a). As explained in the previous section, the lines 1 and 2 bring a short-circuit impedance in the bias Tee node in order to effectively block the RF signal and maximize the coefficient transmission. However the impact analysis of the interconnection line 3 added at the DC port revealed a non-negligible effect on the transmission coefficient $|S_{21}|$ close to the operating BW ($|S_{21}|$ = -18 dB at 140 GHz) as shown in Figure II.20 (b). This can eventually disturb the source's performance when moving from simulation to experimental measurement. Indeed, the DC interconnection line's impact at 140 GHz modifies the impedance shown by the bias Tee, which creates a non-ideal open-circuit inside the RF circuit.

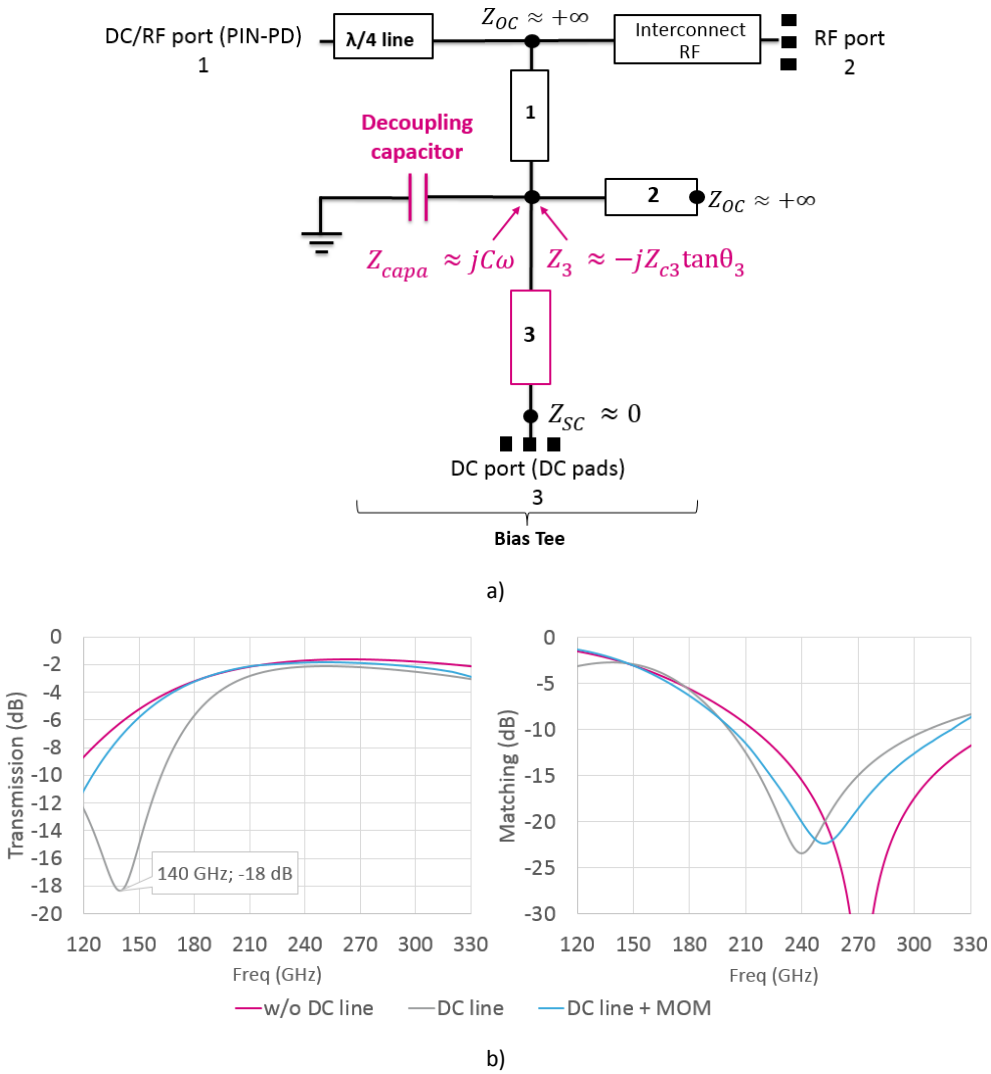

Figure II.20. (a) Photodiode matching circuit and bias Tee schematic with interconnection lines and decoupling capacitor, (b) simulated transmission coefficient and matching comparison between different circuit configurations from 120 GHz to 330 GHz.

In order to recover the bias Tee's decoupling capacity, a shunt DC/RF decoupling Metal-Oxide-Metal capacitor of about 30 fF was added so as to counterbalance the impedance shown by the line 3 and improve the transmission coefficient (Figure II.20). The main challenge relied on the design of a capacitor in PIC25G featuring a sufficiently high resonant frequency so as to avoid circuit dysfunctions in the BW of interest. A "Woven" capacitor architecture was therefore considered [II.11] because its "crossed fingers" structure enables capacitive effect maximization and inductive effect minimization simultaneously. An electromagnetic simulation of the capacitor's final design using 3D full-wave HFSS software showed a resonant frequency above 300 GHz as shown in Figure II.21.

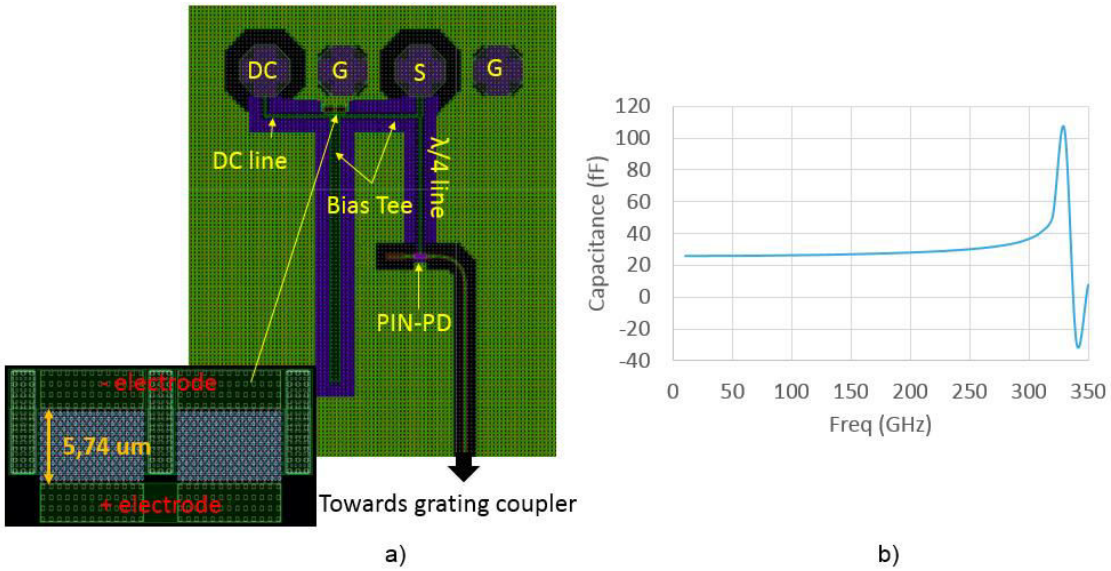

Figure II.21. (a) Final PIC25G test structure integrating a decoupling capacitor, (b) HFSS decoupling capacitance simulation from 0 GHz to 350 GHz.

c. *Assembly strategy impact on the PIC25G integrated circuit's performance*

The assembly strategy of the sub-mmW/THz IC chip on top of a substrate needs now to be considered in order to connect it to the antenna. To do so, two major solutions can be considered (Figure II.22) and a simple impact analysis of each solution on the IC's performance was undertaken. Those solutions consist of *(a)* wire-bonding mounting strategy using wire bonds, and *(b)* flip-chip mounting strategy using copper pillars.

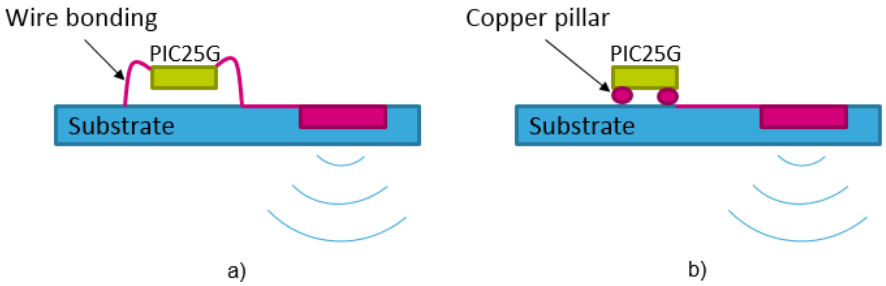

Figure II.22. (a) Schematic of a chip mounted on substrate using wire-bonding, and (b) flip-chip copper pillars.

The majority of the available chips operating below 40 GHz are interconnected using wire-bonding which offers the following main benefits: mature, low-cost and high yield fabrication process, high degree of flexibility for different chips and package designs and form factors. However, wire-bonded interconnections exhibit severe low-pass frequency characteristics at mmW, owing to electrically long wires at these frequencies. Indeed, this leads to significant inductance effects which degrade the circuit's mmW performance. As an illustration, a wire bond with a typical diameter of 25 µm and length of 500 µm suffers from a parasitic inductance of about 500 pH at 50 GHz which seems extremely high at sub-mmW frequencies. This assembly model, represented in Figure II.23 (a), was simulated on ADS with the PIC25G IC's impedance at the input and a 50ohm load at the output. From Figure II.24 (in grey), it appears very clearly that it is not appropriate for the targeted sub-mmW/THz frequency band. Indeed the transmission coefficient is at least 15 dB below that of the final circuit design and an important mismatch occurs over the entire frequency band.

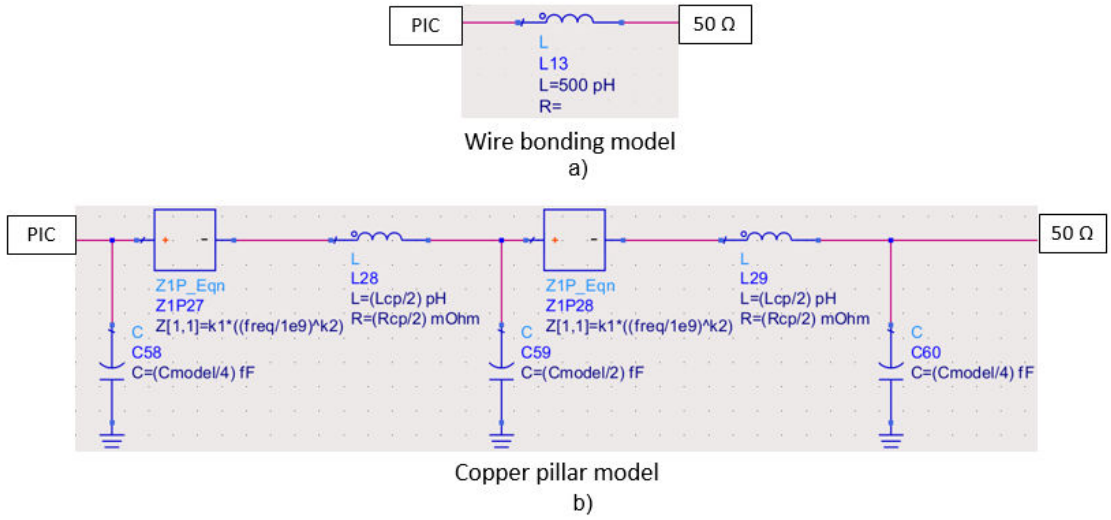

Figure II.23. (a) Wire-bonding electrical model, and (b) copper pillar electrical model.

Flip-chip bonding is also considered and has gained considerable attention in mmW high density packaging for industrial applications. In this approach, the IC is mounted onto a packaging substrate with copper pillars exhibiting much smaller electrical lengths than wirebonds (40 µm to 60 µm). From this point of view, the parasitics associated to a single copper bump are much smaller. Therefore this assembly strategy can be applied to a wide range of frequency applications from mmW to THz, and enables to achieve high-speed electrical performance. Studies on copper pillar modelling up to 50 GHz have been undertaken in previous work lead by STMicroelectronics and have enabled to establish the equivalent circuit (frequency dependant) shown above in Figure II.23 (b). In this respect, the parasitics associated to a copper pillar assembly can be modelled by a series resistance of 4 mΩ, a series inductance of 36 pH, and a shunt capacitance of 2.6 fF. With such low values compared to the wirebond's parasitics, the use of flip-chip mounting seems relevant for our targeted application. Indeed, as shown in Figure II.24 (in pink), the simulated transmission coefficient is hardly affected by the copper pillar model with an $|S_{21}|$ between -2.6 dB and -2 dB over 220-300 GHz, and a simulated -10 matching BW is achieved from 204 GHz to 320 GHz. As a conclusion, flip-chip assembly using this type of copper pillars should have a negligible impact on the sub-mmW/THz power source's performance so as to achieve the targeted specifications.

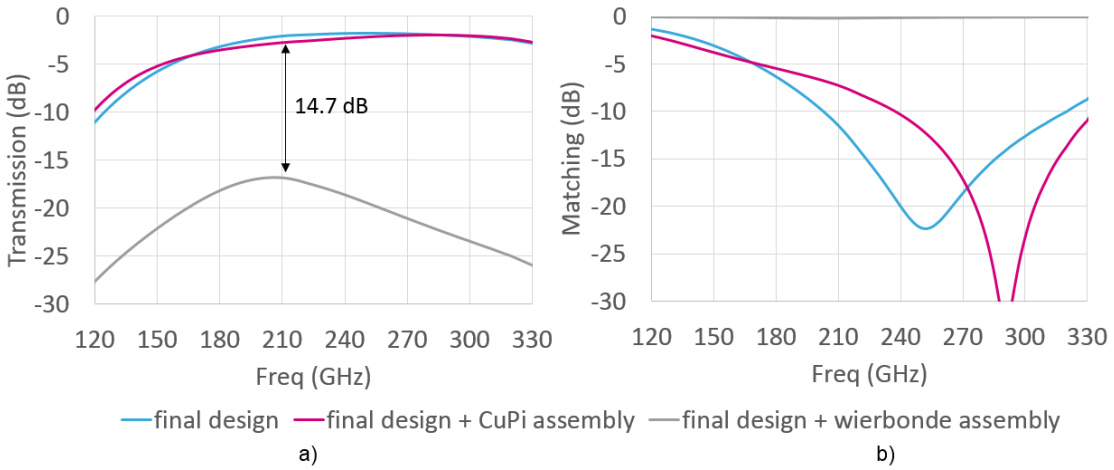

Figure II.24. (a) Simulated transmission coefficient and (b) matching comparison between PIC modules mounted with wire-bonding and with copper pillars from 120 GHz to 330 GHz.

d. Final Silicon Photonics IC layouts and performance for different frequency bands

The final test structure schematic for a photodiode matched in the 130-220 GHz, 200-280 GHz and 220-330 GHz frequency bands is shown in Figure II.25.

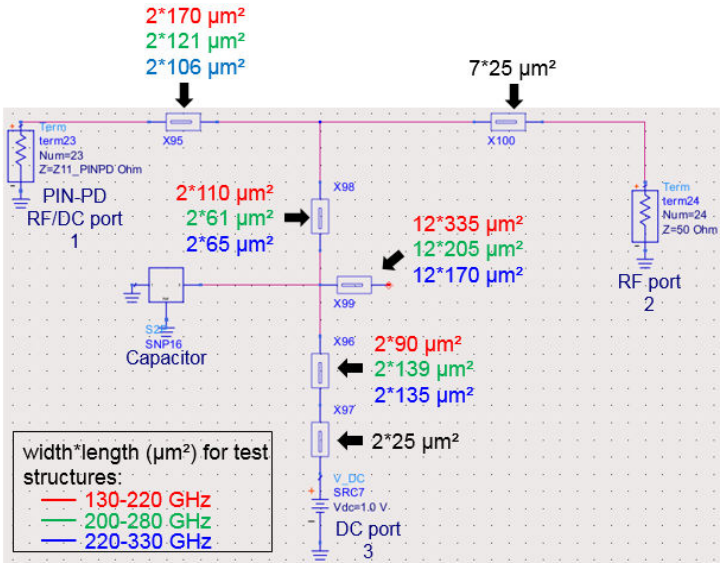

Figure II.25. Final ADS schematic and dimensions of the three PIC25G test structures targeting the BWs 130-220 GHz, 200-280 GHz and 220-330 GHz.

The corresponding final S parameters are shown in the Figure II.26 with summarized performance available in Table II.1 below. Structures #2, #3, and #4 represent the matched test structures initially targeting the bands 130-220 GHz, 200-280 GHz, and 220-330 GHz respectively.

	2.5 dB insertion loss BW	-10 matching BW
Structure #2	140 GHz to 234 GHz (50%)	113 GHz to 201 GHz (56%)
Structure #3	190 GHz to 307 GHz (47%)	188 GHz to 304 GHz (47%)
Structure #4	194 GHz to 322 GHz (50%)	201 GHz to 323 GHz (47%)

Table II.1. Summarized final performance of the PIC25G integrated sub-mmW source for different BWs.

We can notice that the S parameters for the test structure #2 are not as satisfying at the beginning and the end of the targeted frequency band as for the 2 other structures. Indeed, the achieved transmission coefficient $|S_{21}|$ at 130 GHz is -5 dB. However, from 140 GHz upward, a good insertion loss level is still achieved.

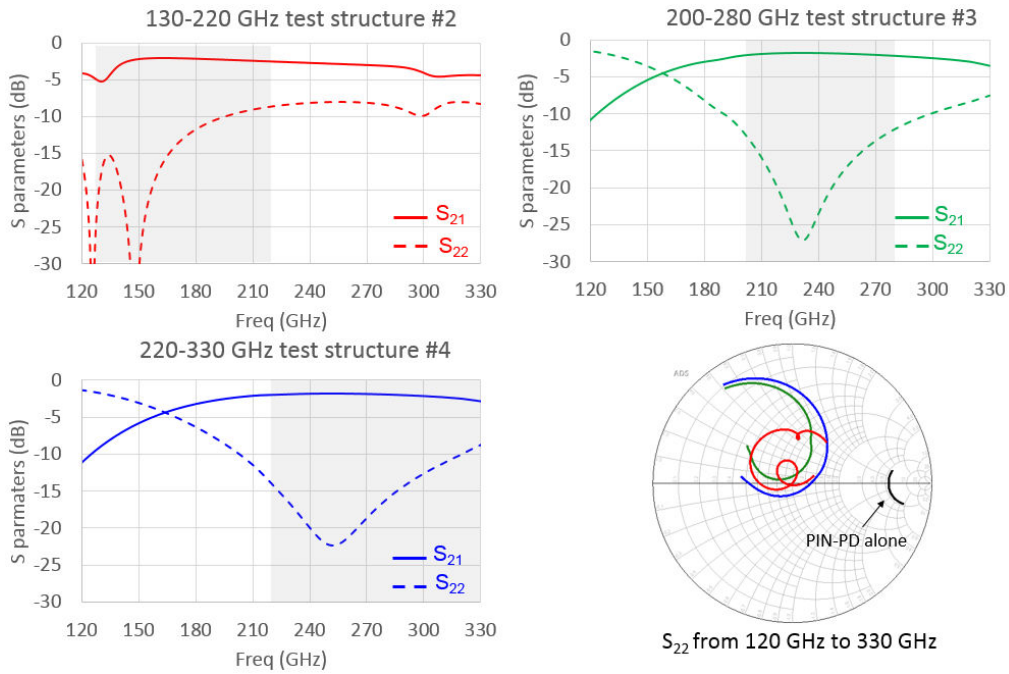

Figure II.26. Final simulated transmission coefficient and matching of the three PIC25G test structures targeting the BWs 130-220 GHz, 200-280 GHz and 220-330 GHz.

Unfortunate, the ICs of the prototyped test structures were actually designed and processed on the M4 metal layer instead of AP, which is 1 level lower on the PIC25G's BEOL and therefore closer to the M1 ground plane as explained in Figure II.27. This thinner dielectric between the line and the ground increases the microstrip line's equivalent capacitance which would decrease its resonant frequency and would eventually impact on the S parameters of the ICs presented above.

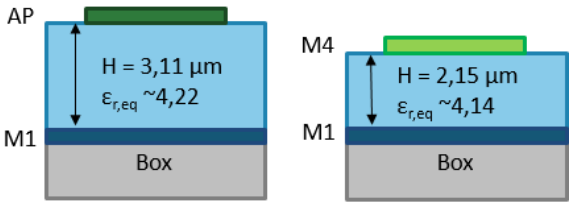

Figure II.27. Schematic of an AP microstrip line and M4 microstrip line retrieved for the PIC25G BEOL build-up.

Therefore the real integrated matching circuits (on layer M4) were simulated with the PIN-PD to visualize the impact on the matching S_{11}. First, an HFSS simulation of the matching network was realized on the M4 metal level. The S parameters of this design were then imported to ADS inside a SnP component as shown in Figure II.28. Connected to the PIN-PD's equivalent circuit terminal at port 2 and to the decoupling capacitor at port 3, the S_{11} was simulated with a 50ohm terminal at port 1. The Figure II.28 shown below represents the matching network of the structure #4.

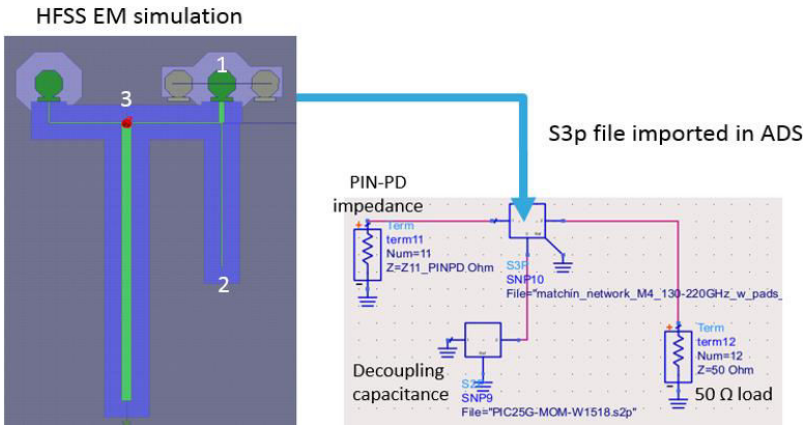

Figure II.28. Simulation strategy of the matched PIN-PD test structure #4 with microstrip lines at the M4 metallic layer.

As we were expecting, the ADS simulation results given in Figure II.29 show a resonant frequency shift of the bias Tee towards the lower frequencies. This relative shift varies from 8% to 15% between the structure #2 and the structure #4. The measured matchings of the prototyped test structures will therefore be compared to the simulated matching networks on M4 metal level.

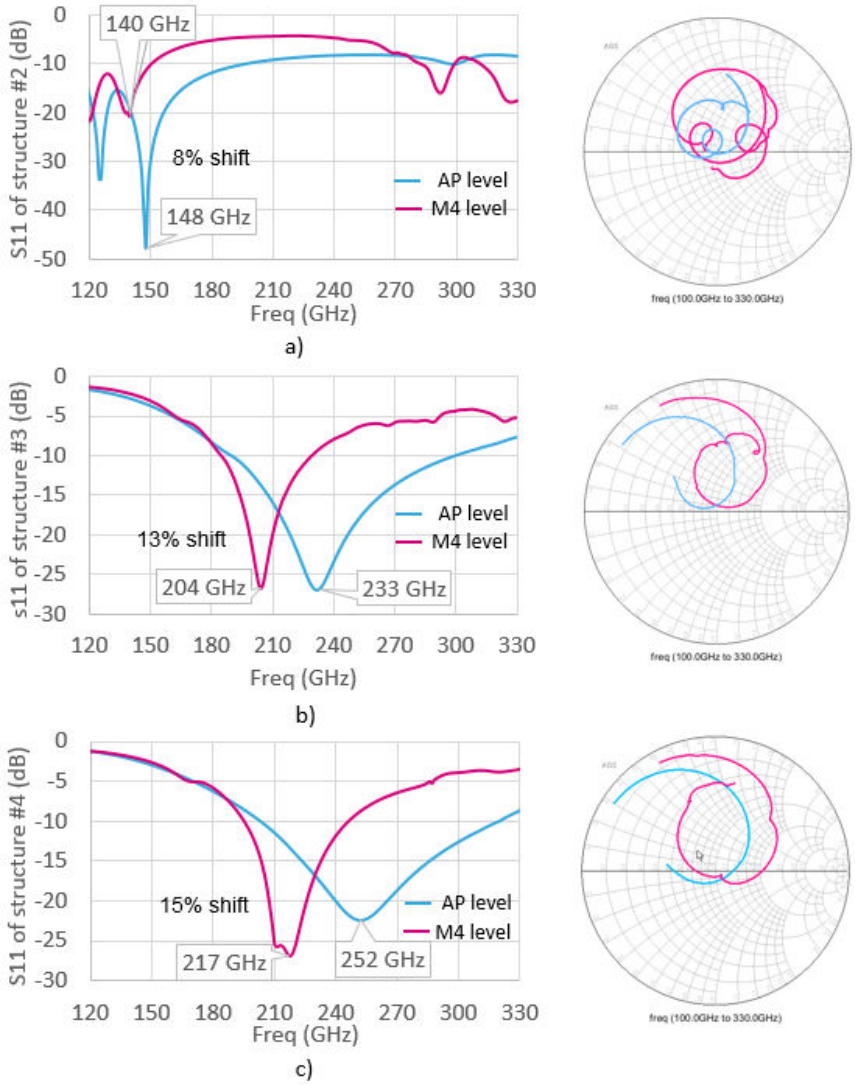

Figure II.29. ADS simulation results of the matching S_{11} in rectangular plot and Smith chart for (a) the structure #2, (b) the structure #3, (c) the structure #4.

3. Measurement of the prototyped PIC25G test structures

a. Experimental set-up

The sub-mmW/THz source was measured on an opto-mmW test bench at the IEMN laboratory. In the measurement setup, two laser spectral lines from tunable lasers were set around 1.55 µm wavelength to generate a tunable beat frequency between 100 and 350 GHz. This beat signal is injected into an erbium doped fiber amplifier (EDFA) in order to control the optical power injected in the grating coupler and also to ensure an operation below the saturation level of the photodiode. The resulting optical signal is coupled into the photodiode by using a grating coupler, illuminated with a standard single-mode optical fiber. A GSG probe then collects the generated sub-mmW or THz signal. This probe enables to apply the required DC bias and couple the signal into a rectangular waveguide (WR5.1 in 140-220 GHz and WR3.4 in 220-325 GHz). At the waveguide's output, the signal is finally injected inside a Vector Network Analyzer (VNA) for S parameters measurement or a THz PM5 power-meter (± 0.25 dB accuracy) for power measurement. A schematic and a photo of the bench are shown in Figure II.30.

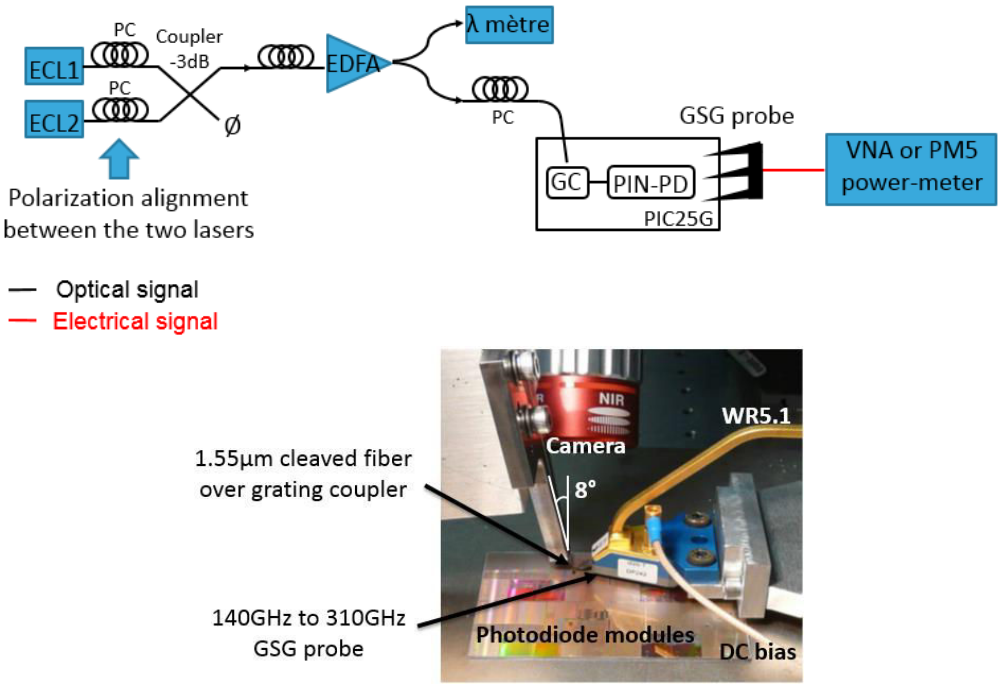

Figure II.30. Schematic of the opto-mmW bench used for the electrical characterisation of the PIC25G modules and photo of the bench.

A photo of the prototyped test structures is shown in Figure II.31 below and fits into a space of 1790 µm by 930 µm.

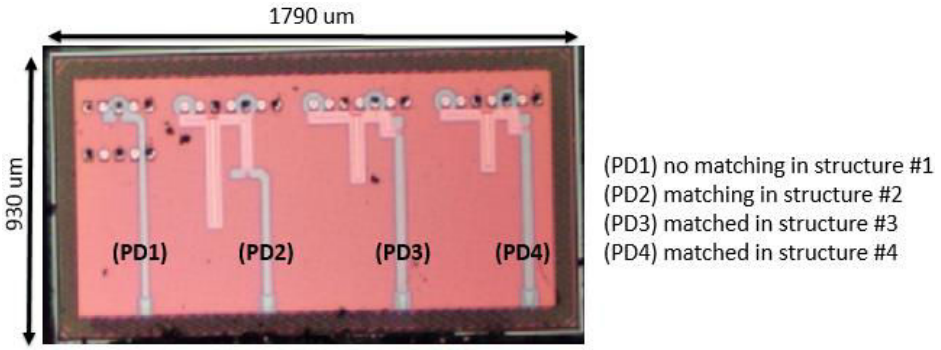

Figure II.31. Photo of the four prototyped PIC25G test structures integrating the PIN-PD and matching networks targeting the BWs 130-220 GHz, 200-280 GHz and 220-330 GHz.

These test structures were produced several times on a dedicated Silicon wafer according to the matrix shown in Figure II.32. Each cell of this matrix groups together the four different test structures and will be referred to as a reticule. The measured reticules are shown in green (Ret12, Ret21, Ret22 and Ret32) and measurements were realized from 0 GHz to 110 GHz and in the G band from 130 GHz to 220 GHz using two different GSG probes.

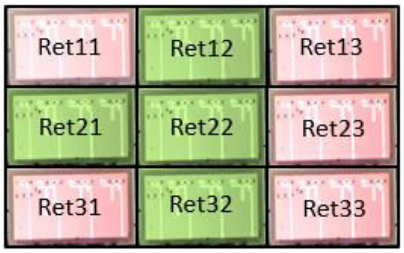

Figure II.32. Matrix of reticules composed of the four PIN-PD test structures in PIC25G technology.

b. Measurements and analysis of the PIN-PD's equivalent circuit

As explained in the previous section and shown in Figure II.33, the 1st hypothesis made on the PIN-PD's equivalent circuit was retrieved from studies made by Sandrine Oeuvrard during her PhD thesis [II.10] and consists of an equivalent resistance R_{eq}, capacitance C_{eq} and inductance L_{eq} connected in series.

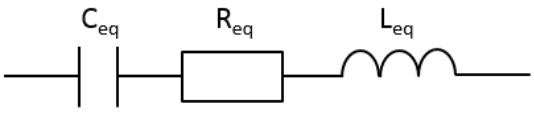

Figure II.33 PIN-PD's equivalent circuit.

Therefore, from the measured normalized S_{11} of the PD1, we were able to estimate the values of each equivalent elements as follow. The real and imaginary parts of the impedance Z_{11} (in Ohm) are first calculated through Equation (4), (5) and (6):

$$S_{11} = a + jb \tag{4}$$

$$Re(Z_{11}) = Z_0\left(\frac{1-a^2-b^2}{(1-a)^2+b^2}\right) \tag{5}$$

$$Im(Z_{11}) = jZ_0\left(\frac{2b}{(1-a)^2+b^2}\right) \tag{6}$$

With Z_0 the reference impedance taken at 50 Ohm.

From the obtained $Re(Z_{11})$ and $Im(Z_{11})$, each elements of the equivalent circuit are calculated following Equation (7), (8) and (9) and are traced in Figure II.34 bellow.

$$R_{eq} = Re(Z_{11}) \tag{7}$$

$$C_{eq} = \frac{-1}{Im(Z_{11}) * 2\pi f} \tag{8}$$

$$L_{eq} = \frac{Im(Z_{11})}{2\pi f} \tag{9}$$

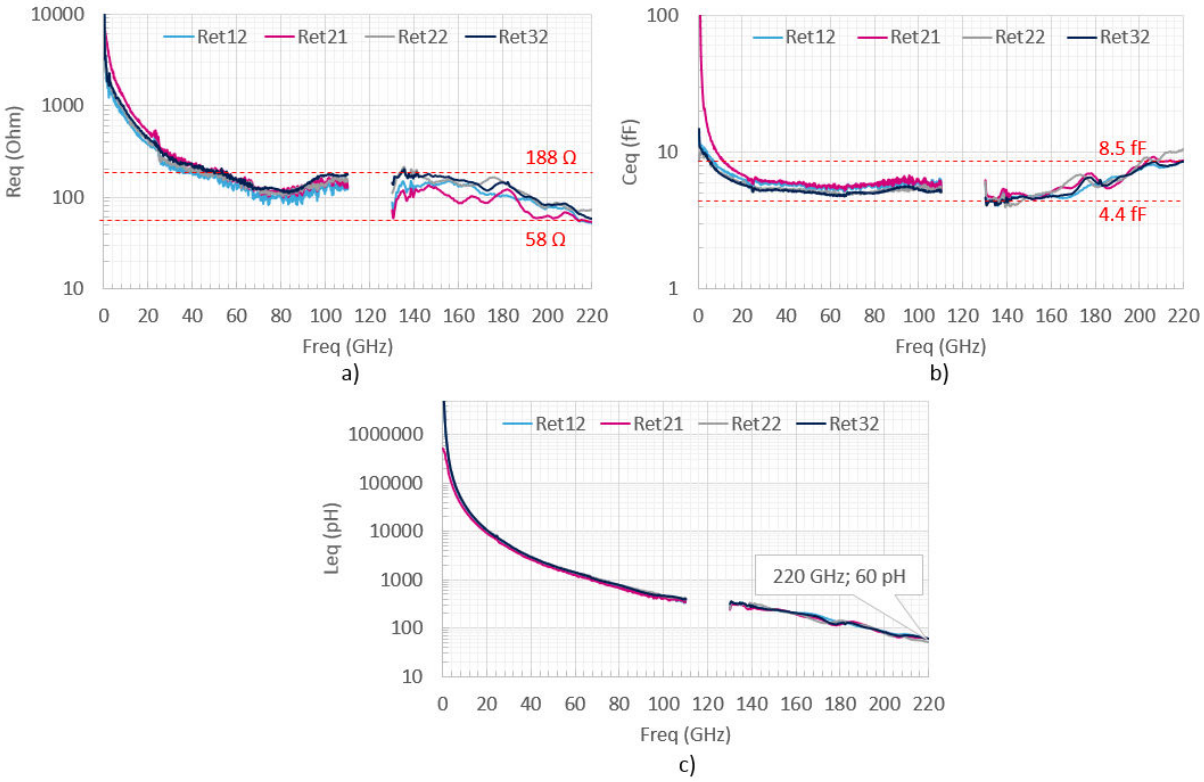

Figure II.34. Retrieved elements of the PIN-PD equivalent circuit from the measured S_{11} of PD1: (a) R_{eq}, (b) C_{eq}, (c) L_{eq}.

The new calculated values of each elements in the PIN-PD's equivalent circuit (2nd hypothesis) are compared to the 1st equivalent circuit hypothesis [II.10] in the Table II.2 below. A significant difference between the two hypothesises is the equivalent resistance and inductance value which is much lower than in the 2nd hypothesis. This can be accounted for the use of optimized GSG pad access inside the IC prototypes which helped in reducing the parasitic resistive and inductive impact on the measurement.

Equivalent element	1st hypothesis	2nd hypothesis
R_{eq} (Ohm)	200 (75 GHz) to 271 (40 GHz)	58 (220 GHz) to 188 (135 GHz)
C_{eq} (fF)	4.4 (40 GHz) to 7.5 (60 GHz)	4.4 (130 GHz) to 8.5 (220 GHz)
L_{eq} (pH)	100 (at 45 GHz)	60 (at 220 GHz)

Table II.2. Comparison of the 1st and 2nd hypothesis made on the equivalent circuit of the PIN-PD.

The measured S_{11} of PD1 is compared to the simulated S_{11} from both 1st and 2nd hypothesis in Figure II.35 with the following parameters:

- 1st hypothesis: 271 Ω, 4.4 fF, 100 pH
- 2nd hypothesis: 120 Ω, 4.4 fF, 60 pH.

We first notice a better fit between the measured and the simulated S_{11} (especially on the Smith chart) when taking the equivalent circuit parameters of the 2nd hypothesis. Furthermore, an increased capacitive effect of the measured S_{11} compared to the simulation can be noticed on the Smith chart from about 170 GHz upward. This is reflected in the calculated C_{eq} shown in Figure II.34 (b); above 170 GHz the capacitance actually increases for 5 fF to 8.5 fF. This behaviour may come from an increasing parasitic capacitance effect at the GSG probe level for very high frequencies. Indeed, above 140 GHz, the lumped element configuration do not apply anymore and the GSG probe should be visualized as a distributed element. In this configuration, electromagnetic interactions between the probe and its environment (PIC25G IC, GSG pads, etc.) should be taken into account in order to add the appropriate parasitic elements to the simulation.

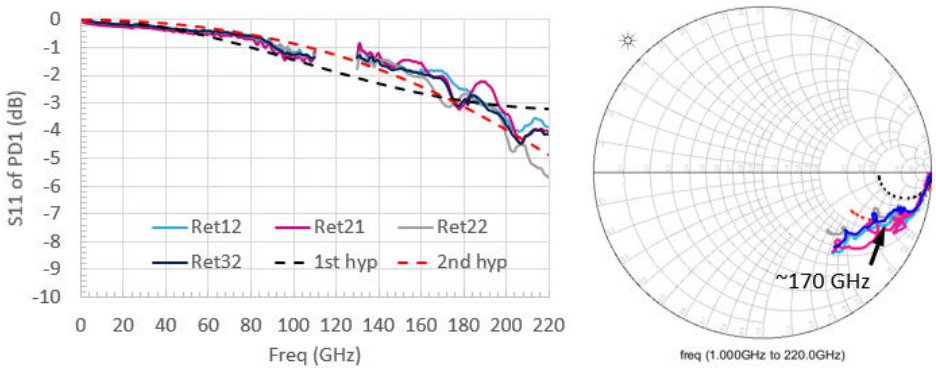

Figure II.35. Measured S_{11} in rectangular plot and Smith chart of PD1.

For further insight on this retrieved equivalent circuit study, measurement results concerning the matched test structures (PD2, PD3, PD4) have also been analysed on ADS together with the PD1 connected to a simulated matching network. An example of the ADS schematics for the test structure #4 is represented in Figure II.36: *(a)* in green the measured data of the PD4 is imported inside a SnP component, whereas *(b)* in red the measured data of the PD1 is imported and connected to the simulated HFSS matching network (shown in Figure II.28) of the test structure #4.

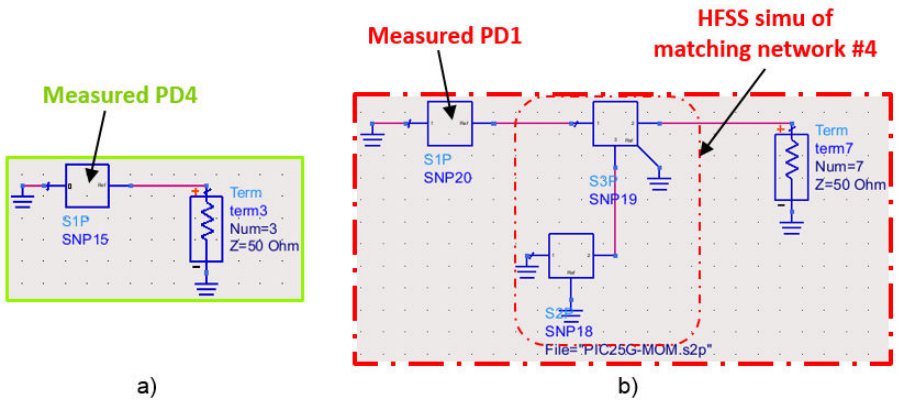

Figure II.36. ADS schematics of (a) the measured PD4, and (b) measured PD1+HFSS matching network #4 simulation.

The matching S_{11} is shown in Figure II.37 below for the four measured reticules, with a very good repeatability between the different reticule measurements. We first notice a significant resonant frequency shift of about 13% between the simulated test structure (in dashed grey) and the measured PD1+simulated matching (in dashed red). Moreover, this shift becomes even further pronounced (about 17%) towards the lower frequencies when looking at the measured PD3 and PD4 (Figure II.37 (b) and (c)). In the Smith charts, a shift of the S_{11} loop to the upper left side is also noticed, which could be understood in theory as a lower resistive effect. Actually, from the PD1+simulated matching to the PD2, 3 and 4, the electromagnetic environment of the experimental measurement is significantly different: an integrated matching circuit has been added and could be coupled to the GSG probe. Therefore, retrieving the values of R_{eq}, C_{eq} and L_{eq} from the measured matched structures is difficult because it would require to take into account the GSG probe body in the HFSS simulation in order to retrieve the additional parasitic elements and adapt the equivalent circuit configuration. For this reason, in order to improve the matching network designs in future PIC25G test-chip prototypes, a post-simulation based on the dashed red curve was done.

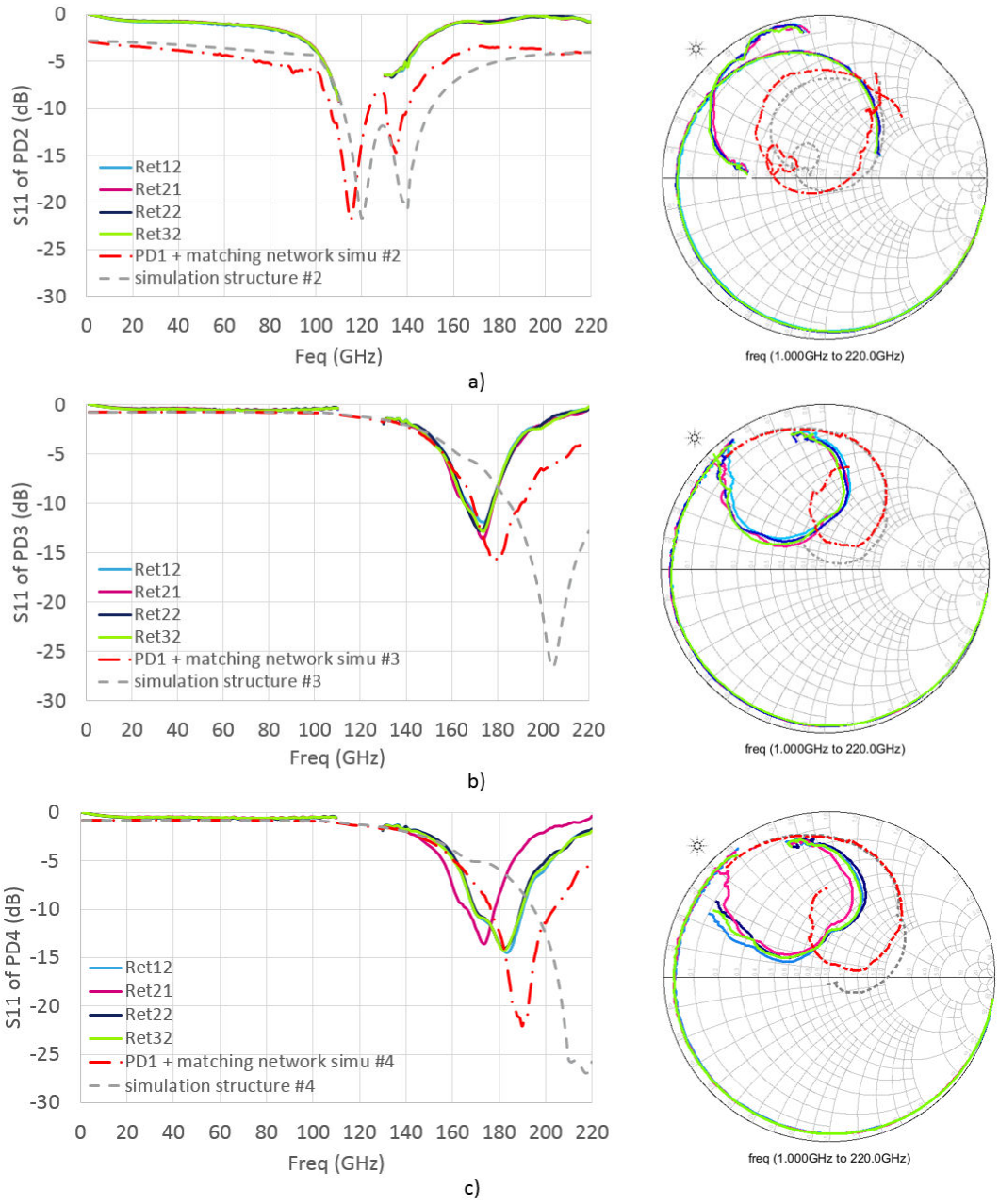

Figure II.37. Comparison between measured and simulated S_{11} in rectangular plot and Smith chart for structure a) PD2, b) PD3 and c) PD4.

In a set of post-simulations, the PD1 was replaced by the PIN-PD's equivalent circuit and the RCL values were tuned until a fit it reached between the two S_{11} parameters, as shown in Figure II.38. The retrieved values of the elements composing the equivalent circuit are:

- R_{eq} = [93 ; 120] Ω
- C_{eq} = [4 ; 5] fF
- L_{eq} = 60 pH.

As a conclusion, those new values should be used for future matched PIN-PD designs in order to correctly dimension the microstrip integrated circuits of the developed PICs to target the BWs 130-220

GHz, 200-280 GHz and 220-330 GHz. However, several limits to the deduced equivalent circuit values are to be remembered for future improvements. First, the RLC series equivalent circuit configuration in [II.10] was determined at around 45 GHz, and may be different above 200 GHz. Second, the reference impedance Z_0 is not necessarily exactly 50 ohm and should be retrieved during the VNA calibration using an Alumina substrate calibration kit before starting the measurements. Finally, at such high frequency a distributed element analysis of the GSG probe's behaviour should be realized with a consideration of its interactions with the environment, in order to appropriately establish the equivalent circuit of the PIN-PD.

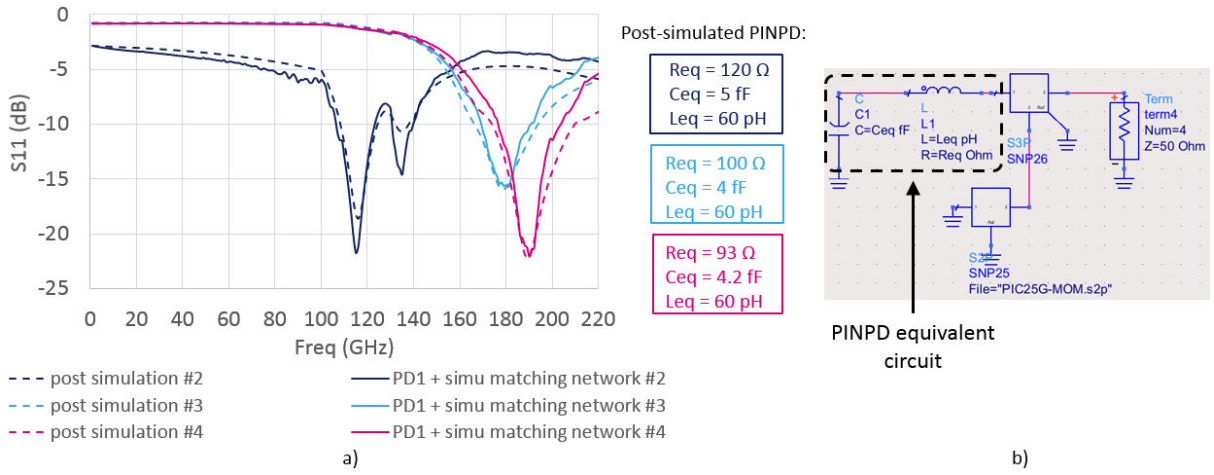

Figure II.38. (a) $|S_{11}|$ post-simulation of the matched PIN-PDs, (b) ADS schematic of the PIN-PD's equivalent circuit connected to the HFSS matching network structure for the post-simulation.

c. Photocurrent and output power measurements

DC characterization of the photocurrent was first realized on the PD1 integrating the unmatched photodiode with a 1.55 µm optical signal and a growing optical power level (up to 7.1 mW). The bias varied from a forward bias (-0.5 V) to a reverse bias (2 V). As shown in Figure II.39, a darkness current below 10 nA is achieved at 1 V, while maximum photocurrent of 4.2 mA is achieved for an optical power of 12.6 dBm. The overall graph shows an I(V) characteristic that is typical of a revere-biased photodiode's behaviour, as found in [II.3].

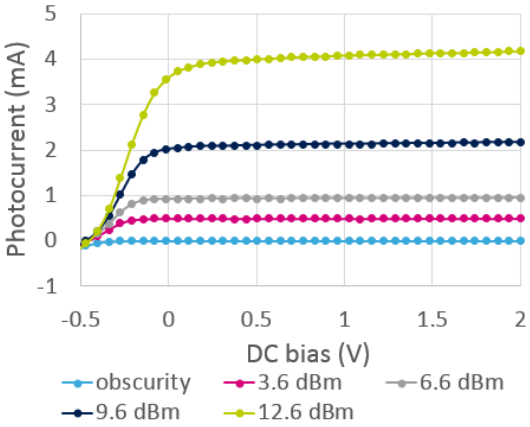

Figure II.39. Measured photocurrent as a function of the DC bias voltage for different optical input powers.

The photodiode DC linearity was also studied with a reverse bias of 1 V. A sweep on the optical input power is done from 0.9 mW to 28 mW. As we can see in Figure II.40 (a), a very good linearity of

the photocurrent is measured as a response to the increasing input power. RF measurements were then undertaken using a PM5 waveguide power-meter. First, the photodiode's linearity was measured at a beating frequency of 140 GHz as shown in Figure II.40 (b), on the PD2 test structure. The input/output power proportionality is maintained up to an optical input power of 11.3 mW corresponding to the 1dB compression point, above which the photodiode RF saturation is reached. At this point, the generated charge carriers accumulate inside the intrinsic space. This substantially screens the bias electric field in the space charge zone and the carrier transit-speed becomes slower than the carrier photo-generation process. An applied DC bias higher than 1 V should help to push up the saturation threshold. The photodiode's linearity was also measured at 240 GHz on the PD4 test structure, for an input power ranging from 6 mW to 22 mW. The noise floor of the power-meter was evaluated to be -40 dBm, so the detected power cannot be measured below this value. As a result, only the transient state between the photodiode's linear mode and saturation mode can be shown. The photodiode saturation threshold at the 1dB compression point is reached for an input power of ~10 mW which is similar to the saturation threshold at 140 GHz. This shows a good saturation threshold stability of the photodiode at RF frequencies.

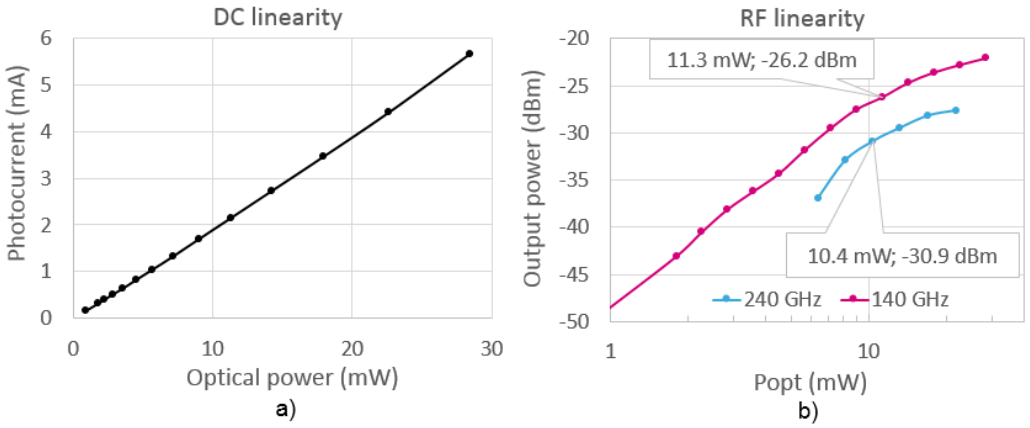

Figure II.40. (a) Measured DC photocurrent with increasing input power for a reverse bias of 1V, (b) and measured output power at 140 GHz with increasing input power and biasing of 1V.

The RF output power of the three pre-matched photodiode test structures were then measured between 125 GHz and 310 GHz and compared with the measured output power of the unmatched photodiode in Figure II.41. The measured power slopes are globally monotone as a function of the frequency throughout 125-310 GHz and roughly follow the unmatched photodiode's negative slope of -12 dB/octave. This is a good indicator of the stability and well-functioning of the matching and bias Tee circuits. Indeed, the addition of such a circuit did not disturb the power source's behaviour. Depending on the test structure's matching BW, an output power between -21.5 dBm and -19.6 dBm is reached at 150 GHz and between -33.1 dBm and -31 dBm at 300 GHz, which is comparable to the

reported output power levels of state-of-the-art PIN-PDs and is about 20 dB below the average output power level of state-of-the-art UTC-PDs ([II.12], [II.13]).

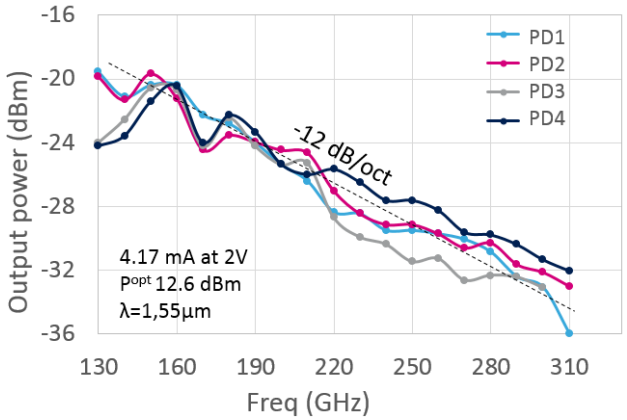

Figure II.41. Measured output power of the four different test structures from 130 GHz to 310 GHz with a reverse bias of 2V and an input optical power of 12.6 dBm.

IV. High data-rate optical modulator integrated in PIC25G

As explained in section II, a MZM should be integrated in the PIC25C chip in order to modulate the optical signal before it reaches the integrated photodiode for photomixing. In order to achieve a maximum optical modulation amplitude, the phase shift between the two arms should be maximized. Usually, a maximum phase shift of 180° requires quite a long HSPM junction length (several millimeters), resulting in a very large equivalent capacitance (typically > 300 fF/mm). This large parasitic limits the operating speed of the modulator due its high time constant. To lower down the time constant and target data-rates up to 50 Gb/s, a solution consists in dividing the modulator's PN junction into several elementary cells. A schematic of the traveling wave MZM modulator used in PIC25G is shown in Figure II.42. As long electrodes are required to drive the several millimeter length MZM, lumped electrode circuit models are no longer valid considering high operating speed and significant optical propagation delay. Therefore, traveling-wave electrodes are implemented with respect to a distributed element circuit model in order to appropriately design and optimize the modulator.

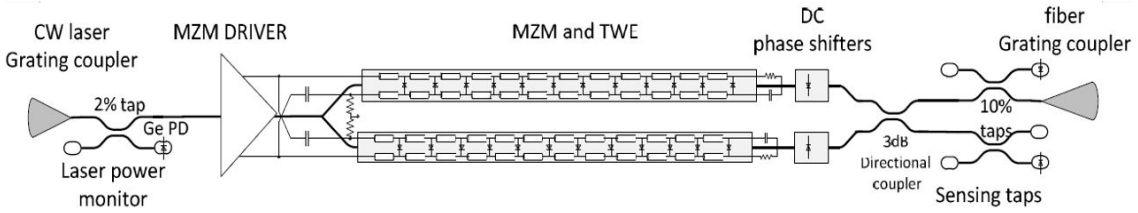

Figure II.42. Global schematic of a Mach-Zehnder modulator based on STMicroelectronics' HSPMs.

In this design, each section of line connected to a PN junction can be represented by a RLCG transmission line model, a diode and its equivalent capacitance as shown in Figure II.43. As the capacitance acts like a low-pass filter, it narrows down the achievable BW and operating speed of the modulator. To minimize this issue, a previous study led by Jean-Marc Boucaud, a PhD student at STMicroelectronics, consisted in implementing an optimized inductance to each segments of the MZM to increase the matching BW with respect to the 50 ohm MZM driver as shown in Figure II.43 (b). By

doing so, the linear inductance of the traveling wave electrodes is indeed increased. However, a limit on the inductance length (directly proportional to its value) is fixed in order to limit the increase of RF propagation attenuation along the electrodes. As the inductance value also modifies the phase velocity of the electric signal with respect to the optical signal, a compromise between impedance matching and phase velocity matching is done in order to maximize the modulator's performance. The electrodes were finally ended with a 35 ohm load in order to further improve the matching BW of the modulator without having to further increase the size of the inductances.

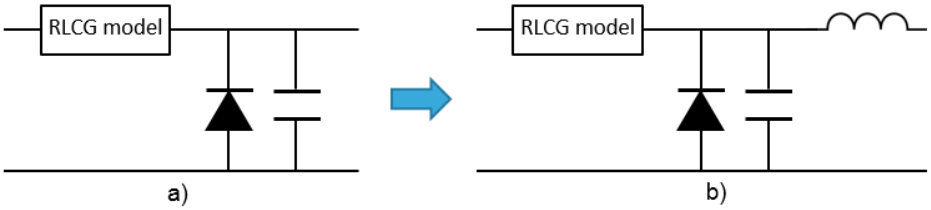

Figure II.43. Equivalent circuit model of (a) an elementary cell of the Mach-Zehnder modulator with capacitive parasitic, and (b) with capacitive parasitic and matching inductance.

The final MZM layout is shown in Figure II.44, for an electrode length of 2.1 mm. A modulated voltage signal is injected in the MZM to drive the HSPM through differential signal GSGSG pads and a phase shifter was implemented at the end for the design to set the operating point of the modulator. This phase shifter consists of a PIN phase modulator (PINPM) based on a PIN junction driven thought the DC biasing input.

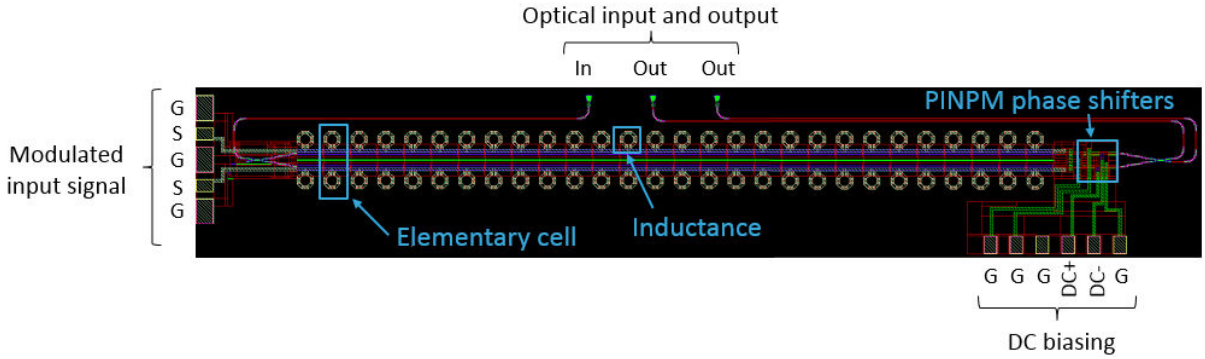

Figure II.44. Layout of the Mach-Zehnder modulator with matching inductances in PIC25G technology.

The typical transfer function of a 2.1 mm long MZM is shown in Figure II.45. To reach a maximum phase shift of 180° with a specific MZM length L_π, an input voltage V_π is necessary. This value represents a figure of merit of the MZM's performance and is referred to as $V_\pi L_\pi$ (V.mm). In a previous study on HSPM-based MZM, HSPMs featuring a 17.2°/mm phase shift at $V_\pi L_\pi$ = 25 V.mm were succesfully evaluated at 25 Gb/s and 50 Gb/s [II.14], giving a good insigth on ST's HSPM performance.

To set the operating point of the MZM to the appropriate value, the DC voltage value used to drive the phase modulator is positioned at the maximum slope of the transfer function. By doing so, we benefit from a maximum optical amplitude difference between the two different states P_{on} and P_{off} of a PRBS signal. This value corresponds to a quadrature phase shift ($\pi/2$) and is refered to as $V_{\pi/2}$ or $V_\pi/2$. For a MZM length of 2.1 mm, this quadrature point is reached for a theoretical DC voltage input of 6V. However, when considering the manufactured modulator, multiple design variations with respect to the actual model should be taken into account during measurements, and often result in a different $V_{\pi/2}$ so as to compensate the intrinsic phase shift difference between the two arms. A modulated input

voltage $V_m(t)$ is then superimposed on the DC voltage in order to actually modulate the output optical signal.

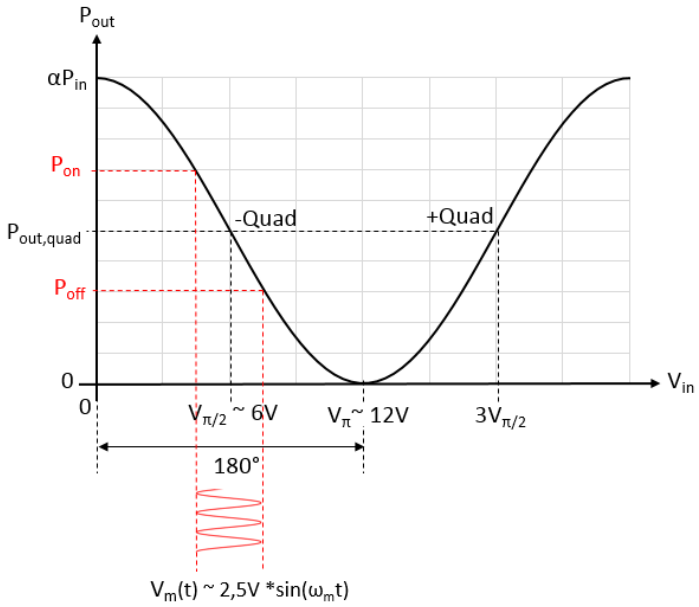

Figure II.45. Transfer function of the Mach-Zehnder modulator.

1. 25 Gbps On-Off keying modulator design with a 1550 nm wavelength optical carrier

A quick study on the modulator's length impact was undertaken with the simulation and evaluation of eye diagrams. These simulations were realized using the Cadence Virtuoso software to implement the schematics of the MZM layouts for a length of 2.1 mm and 2.8 mm. As we look at Figure II.46, we see that for a PRBS signal of 25 Gb/s, the eye opening is bigger with lower distortions and jitters for the shorter MZM. The eye diagram degradation at 2.8 mm is mainly due to an increase of losses in the transmission lines (~0.6 dB/mm) and a larger mismatch between the electric and phase velocity. In fact, up to a certain length, the modulator no longer induces additional phase-shift and the efficiency decreases due to increasing losses. As the data-rate is increased up to 50 Gb/s, the eye of the 2.8 mm MZM is completely closed, due to a very low SNR. Therefore, the 2.1 mm length MZM was selected for the development of the sub-mmW/THz Tx integrated in PIC25G.

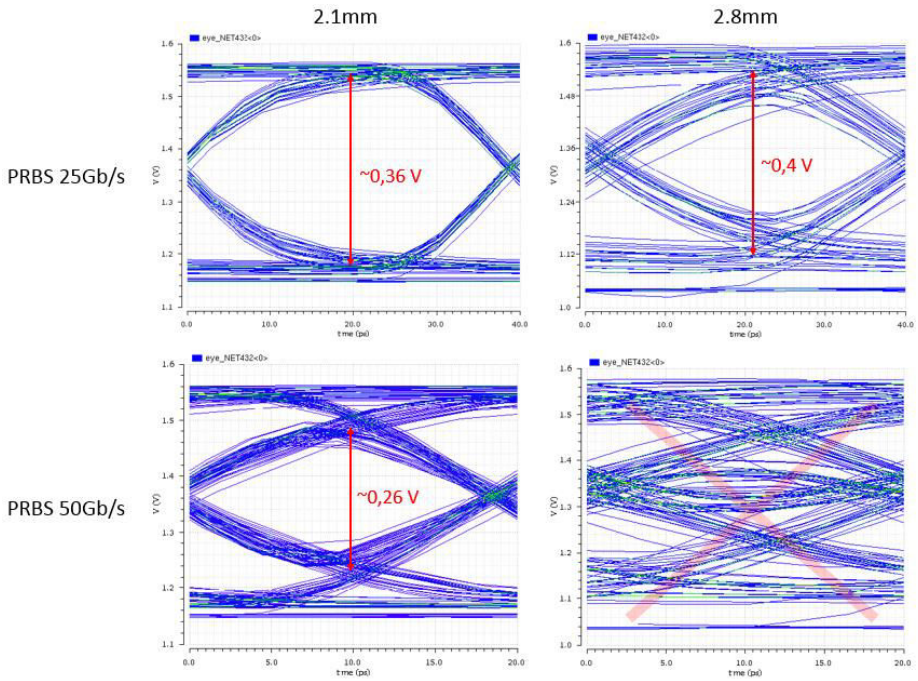

Figure II.46. Simulated eye diagrams for a PIC25G 2.1 mm and 2.8 mm long Mach-Zehnder modulator at 25 Gb/s and 50 Gb/s PRBS.

The final layout is shown in Figure II.47. The matched PIN-PD test structure #4 is connected to the MZM's output to produce the photomixing of the optical modulated signal. The optical accesses implemented in the design include the λ_1 optical signal input for the MZM, an optical output at the end of the MZM to allow optical characterization and the λ_2 optical input at the end of the MZM, which is then 3dB-coupled to the λ_1 optical signal to generate the modulated sub-mmW/THz frequency beat. This optical input can also be used to measure and evaluate the PIN-PD IC in "stand-alone" configuration where microstrip lines are actually at the correct metallic level (AP metal layer).

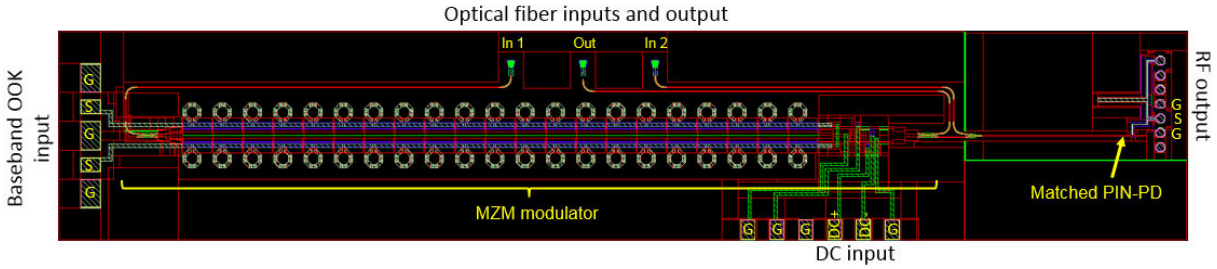

Figure II.47. Layout of the final 2.1 mm Mach-Zehnder modulator with integrated matched PIN-PD targeting the 220-330 GHz in PIC25G technology.

2. 50 Gbps PAM4 optical modulator design with a 1550 nm wavelength optical carrier

To double the data-rate payload without increasing the BW, 4-level pulse amplitude modulation (PAM4) was considered. This type of modulation is particularly attractive because it enables to double-up the bit spectral density (bit/s/Hz) compared to non-return to zero (NRZ) modulations like OOK, while requiring only direct detection. To produce 4 amplitude levels, the modulator's electrode in each arm is divided into a first transmission line with a length L and a second transmission line twice as long (2*L) as shown in Figure II.48 (a). These two sections are controlled by two different PRBS drivers. By doing so, one phase delay "unit" can be applied on the first section which gives access to the two

higher states of the PAM4 signal, and two phase delay "units" can be applied on the second section to produce the two lower states. A representation of those four power levels with their corresponding bits combination is shown in Figure II.48 (b). The challenge in designing a PAM4 modulator is to achieve a big enough amplitude modulation depth P_3-P_0 in order to be able to distinguish the 4 amplitude levels.

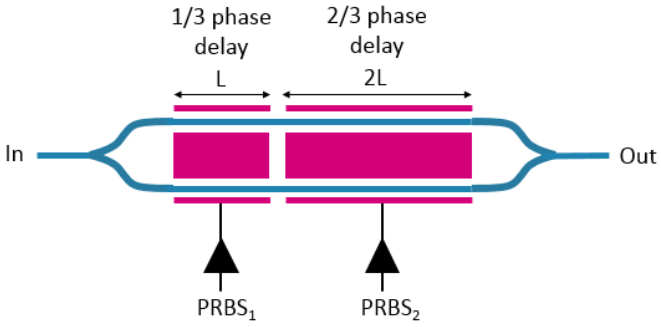

a)

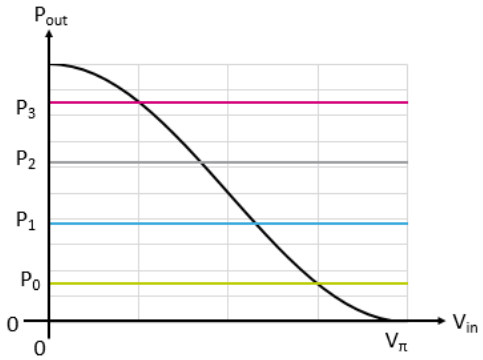

PRBS$_1$ 1/3φ	PRBS$_2$ 2/3φ	Optical output
0	0	0
0	1	1
1	0	2
1	1	3

b)

Figure II.48. (a) PAM4 modulator architecture schematic, and (b) PAM4's 4 power levels and associated bits combination.

A PAM4 modulator schematic was realized with a first arm of 1 mm and a second arm of 2 mm, and was simulated on Cadence Virtuoso with a 25 Gbaud PRBS signals to reach 50 Gb/s and a 50 Gbaud PRBS signal to reach 100 Gb/s (Figure II.49). Similar eye diagrams were obtained, with three visible eye openings and a significant amount of jitters leading to important inter-symbol effects. Even though narrow eye-widths are achieved, if the detection time is set correctly during the measurements, the 4 amplitude levels could still be detected.

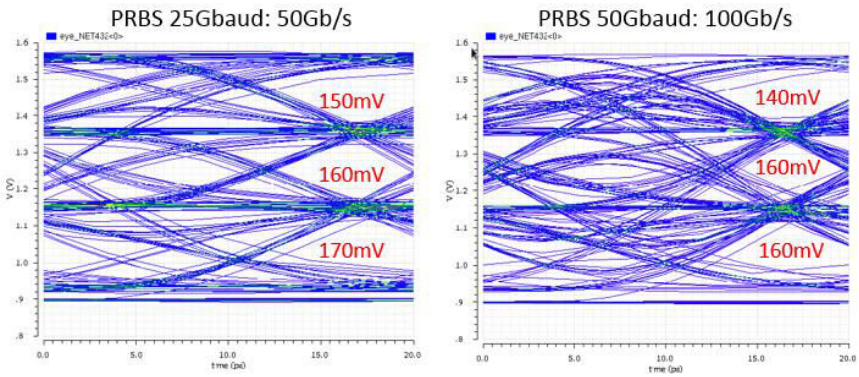

Figure II.49. Simulated eye diagrams of a PIC25G PAM4 Mach-Zehnder modulator at 50 Gb/s and 100 Gb/s PRBS.

The final PAM4 modulator layout is shown in Figure II.50. The differential signals of the two PRBS generators are not injected through the same GSGSG pads but separated in opposite pads in order to facilitate the design structure and characterization setup. An optical output will enable optical characterisation of this PAM4 MZM.

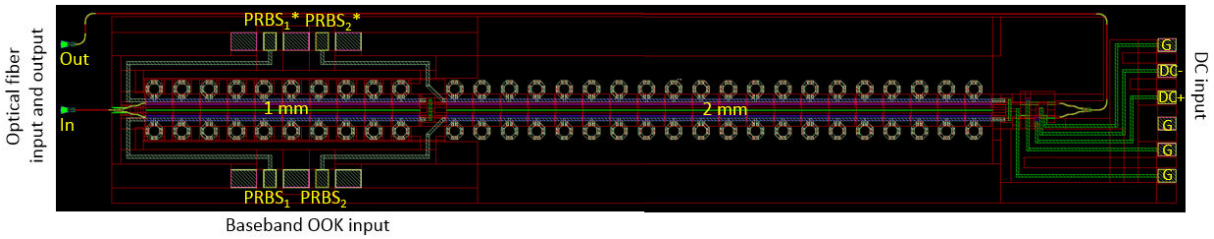

Figure II.50. Final layout of the PAM4 Mach-Zehnder modulator integrated in PIC25G.

V. Conclusion

This chapter gives a good insight on the feasibility and achievable performance of a preliminary sub-mmW/THz Tx integrated in industrial Silicon Photonics technology. The first part of this chapter deals with the development and evaluation of an integrated photomixer based on the industrial PIN photodiode available in STMicroelectronics' Silicon Photonic technology platform. The intrinsic electrical characteristics of the photodiode were first measured on a prototyped 1st test structure integrating this device. The generated photocurrent was measured as a function of the DC bias voltage and the achieved I(V) curves at different optical powers were typical of a photodiode's behaviour in reverse and forward bias mode. At 1 V, a darkness current below 10 nA was achieved, while maximum photocurrent of 4.2 mA was achieved for an optical power of 12.6 dBm. Finally, a very good DC linearity was also achieved as a function of the optical power.

A very simple matching circuit and a DC bias Tee were then integrated in the BEOL of the Silicon Photonic die to match the photodiode's characteristic impedance of 271 Ω to 50 Ω and allow DC polarisation within the Tx. Three structures targeting different matching BWs from 130 GHz to 330 GHz were designed. After optimisation of the integrated circuits, a -10 dB matching BW was achieved from 113 GHz to 234 GHz, 188 GHz to 304 GHz and 201 GHz to 323 GHz for the 2nd, 3rd and 4th test structure respectively, compared to a -3 dB matching for the unmatched photodiode. RF characterisation of these test structures were realized, starting with an evaluation of the RF linearity on the 2nd structure (PD2) at 140 GHz and on the 4th structure (PD4) at 240 GHz. Similar saturation levels of ~10 dBm were obtained at the 1dB compression point, showing the device's RF response stability. Finally the output power of the four test structures was measured between 135 GHz and 310 GHz and very similar curve tendencies were obtained for each structure. A decreasing power slope of -12 dB/octave was achieved for the unmatched photodiode while -8dB/octave was achieved for the 4th test structure matched from 194 GHz to 322 GHz. A state-of-the-art output power of about -29 dBm was reached at 240 GHz, which validates the proposed integrated circuit design.

Lastly, the matching S_{11} was measured for each test structure. A significant matching shift of about 17% was noticed for each chips. This is firstly attributed to the fact that the integrated circuits were designed on a metal layer than the one in the initial designs. Therefore the prototyped transmission-line circuits exhibit a higher capacitance, which results in a decreasing matching frequency. Furthermore, an incorrect hypothesis made on the photodiode's equivalent circuit was also made. The

appropriate equivalent circuit of the photodiode was retrieved from these measurements and post-simulations. The main difference being a much lower equivalent resistance, mainly due to optimized access GSG pads (from 271 Ω to about 100 Ω).

The second part of the chapter deals with the integration of a Mach-Zehnder modulator in the Silicon Photonics die placed before the photodiode. The design of the available modulator was optimized in previous work with traveling-wave electrodes matched with series inductances in order to achieve up to 50 GHz BWs. This enables to target at least 25 Gb/s data transmissions with PRBS modulation schemes. The modulator was integrated in the 4th test structure and prototyped in order to evaluate its performance throughout a future measurement campaign. To target data-rates up to 50 Gb/s without increasing the need for a wider BW, an integrated PAM4 modulator was designed and prototyped in Silicon Photonic technology as well. Therefore, we can consider reaching up to 100 Gb/s by using PAM4 25 Gbaud/s transmission on a double-channel wireless setup. Future measurements are also planned so as to evaluate its performance.

Towards the development of a complete SoC Tx in Silicon Photonics, the development of a mmW frequency comb is also considered and will be the subject matter of future works. In this block, a 60 GHz frequency comb is envisioned with a single CW optical source and a phase modulator. Two lines of this frequency comb separated by 240 GHz will then be selected thanks to an arrayed waveguide grating in order to generate the 240 GHz optical frequency beat that will be modulated by the Mach-Zehnder modulator.

To our knowledge, this is the first study of industrial Silicon Photonics technology in the literature aiming at the development of a sub-mmW/THz integrated Tx. With promising achieved performance, this study-case paves the way towards Silicon-based low-cost sub-mmW and THz high-speed and low-consumption wireless link applications.

Reference

[II.1] F. Boeuf *et al.*, "Silicon Photonics R&D and Manufacturing on 300-mm Wafer Platform," *IEEE Journal of lightwave technology*, vol. 34, no. 2, pp. 4–6, 2015.

[II.2] J. Basak *et al.*, "Developments in Gigascale Silicon Optical Modulators Using Free Carrier Dispersion Mechanisms," *Advances in Optical Technologies*, vol. 2008, p. 10, 2008.

[II.3] S. Oeuvrard *et al.*, "Optical high frequency test structure and test bench definition for on wafer Silicon integrated noise source characterization up to 110 GHz based on Germanium-on-Silicon photodiode," *IEEE International Conference on Microelectronic Test Structures (ICMTS)*, pp. 73–76, Osaka, Japan, 2013.

[II.4] S. Lischke *et al.*, "High BW, high responsivity waveguide-coupled germanium p-i-n photodiode," *Optics Express*, vol. 23, no. 21, p. 27213, 2015.

[II.5] K.-W. Ang, G.-Q. Lo, and D.-L. Kwong, "Germanium Photodetector Technologies for Optical Communication Applications," *Semiconductor Technologies,* InTech, pp. 373–407, 2010.

[II.6] J. M. Fédéli *et al.*, "High-performance waveguide-integrated germanium PIN photodiodes for optical communication applications," *IEEE International Silicon-Germanium Technology and Device Meeting (ISTDM)*, vol. 1, no. 3, pp. 131–132, Singapore, Singapore, 2014.

[II.7] L. Colace, M. Balbi, G. Masini, and G. Assanto, "Ge on Si p-i-n photodiodes operating at 10Gbit⁄s," *Applied Physics Letters*, vol. 88, no. 10, p. 101111, 2006.

[II.8] S. Klinger, M. Berroth, M. Kaschel, M. Oehme, and E. Kasper, "Ge-on-Si p-i-n photodiodes with a 3-dB BW of 49 GHz," *IEEE Photonics Technology Letters*, vol. 21, no. 13, pp. 920–922, 2009.

[II.9] F. Boeuf *et al.*, "Recent Progress in Silicon Photonics R & D and Manufacturing on 300mm Wafer Platform," *IEEE Optical Fiber Communications Conference and Exhibition (OFC)*, Workshop W3A-1, Los Angeles, USA, 2015.

[II.10] O. Sandrine, "Caractérisation d'une photodiode Germanium sur Silicium en vue d'une utilization source de bruit intégrée Térahertz," *University of Lille*, PhD dissertation, 2014.

[II.11] A. M. Elshurafa and K. N. Salama, "Two-layer radio frequency MEMS fractal capacitors in PolyMUMPS for S-band applications," *IET Micro & Nano Letters*, vol. 7, no. 5, pp. 419–421, 2012.

[II.12] Z. Li *et al.*, "High-power high-linearity flip-chip bonded modified uni-traveling carrier photodiode," *Optical Express*, vol. 19, no. 26, pp. 385–390, 2011.

[II.13] H.-J. Song, K. Ajito, Y. Muramoto, A. Wakatsuki, T. Nagatsuma, and N. Kukutsu, "24 Gbit/s data transmission in 300 GHz band for future terahertz communications," *Electronics Letters*, vol. 48, no. 15, p. 953, 2012.

[II.14] E. Temporiti *et al.*, "Insights into Silicon Photonics Mach-Zehnder-Based Optical Transmitter Architectures," *IEEE Journal of Solid-State Circuits*, vol. 51, no. 12, pp. 3178–3191, 2016.

Chapter 3: 200-300 GHz innovative antenna-systems using organic packaging module and 3D-printing

Table of Contents

Chapter 3: 200-300 GHz innovative antenna-systems using organic packaging module and 3D-printing

In the sub-mmW/THz spectrum, available unlicensed BWs as large as 100 GHz currently represent a great opportunity for the high-speed wireless telecommunication market. Indeed, data-rates up to 100 Gb/s could be achieved with low-complexity modulation scheme which would enable to mitigate the actual fronthaul/backhaul data-traffic bottleneck and facilitate the deployment of 5G. A lot of sub-mmW and THz antenna-system demonstrations have already been reported in the literature showing impressive data-rates. However, keeping in mind the expected low-cost infrastructure from the telecommunication operators, development of innovative antenna-systems combining sufficient performance and cost-effective technologies is probably the most important challenge to be addressed. Indeed, the cost of the antenna-system alone constitutes by far the main part of the total wireless system's cost. Therefore, low-cost and low-loss packaging strategies for sub-mmW and THz antennas are of great interest among researchers and industrial players.

In this chapter, after reviewing the most important state-of-the-art mmW to THz antenna-systems and packaging techniques, we propose different innovative antenna-solutions and assembly strategies compliant with industrial constraints. An evaluation of low-cost Ball Grid Array (BGA) organic packaging technology is first given above 200 GHz for integrated antenna designs. Then, we will demonstrate how low-cost additive manufacturing technologies can be used for fast and cheap prototyping of antennas and quasi-optical parts aiming at increasing the overall gain of the antenna-system.

I. State-of-the-art of sub-mmW and THz antennas

Over the past 10 years, antennas operating at sub-mmW and THz frequencies have attracted much attention to address the growing demand for higher speed wireless links and lower transmission latency. The key features that are considered by the antenna designer are gain, BW and radiation efficiency – which are specified depending on the targeted application in order to meet the customer's requirements over specific deployment distances, data-rates, power consumption, etc.

On-chip antenna designs have been widely considered by researchers for sub-mmW and THz transmissions. In this approach, the antenna is monolithically integrated with the radio IC in a single-chip semiconductor leveraging minimum RF interconnection loss. Several transceivers in III-V technology with integrated antennas have demonstrated high output power levels at sub-mmW and THz frequencies [III.1]. From an industrial point-of-view however, standard Silicon technologies are more likely considered as they benefit from low fabrication cost and therefore apply well to high-volume production, with a trade-off on electrical intrinsic performance. Regarding dielectric characteristics, these semiconductors usually exhibit a high dielectric constant (11.9 for Silicon, 9.6 for InP and 10.9 for GaAs). This high dielectric constant brings losses due to power trapped in the form of surface-waves modes in the substrate. Additionally, the low resistivity of Silicon semiconductor brings more losses due to heating in the presences of an electric field in the substrate. Furthermore, thick Silicon substrates (200 µm to 300 µm) are often used as standard wafer sizes in order to ensure

mechanical robustness with respect to assembly constraints. As a result, higher dielectric and conductive losses are obtained leading to a lower antenna gain, and more substrate modes are excited inside the semiconductor itself leading to a chaotic radiation diagram [III.2] [1]. Several techniques have been reported in order to improve the performance of those on-chip antenna solutions.

The first one is substrate thinning. As presented in [III.3] and illustrated in Figure III.1, only the metal stack at the BEOL dielectric layer is used by the on-chip antenna. In typical Silicon ICs, this dielectric consists of a thin SiO_2 slab with a thickness below 10 µm. A metal ground separating the SiO_2 layer from the lossy Silicon bulk is used as a shield for the antenna to prevent electromagnetic (EM) waves from propagating through the bulk. Though the propagation of surface waves decreases as the substrate thickness is reduced, the BW decreases as well. Therefore, as reported in [III.3], the main drawbacks of this thinning technique are very limited simulated gain (-1.6 dBi) and low radiation efficiency (21%) over a narrow -10dB matching BW (7% at 280 GHz).

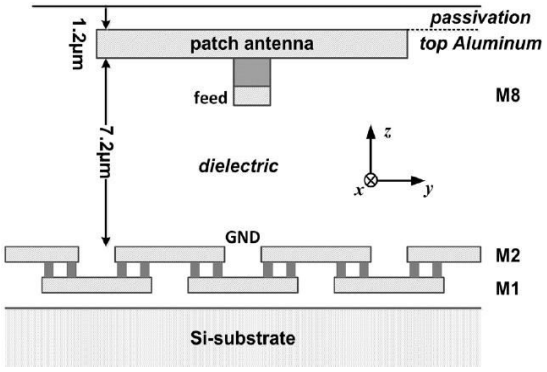

Figure III.1. Cross section of the 280 GHz on-chip antenna from [III.3].

Another solution to overcome dielectric losses in on-chip antennas is to foster electromagnetic wave propagation through-the-air instead of through-the-substrate. In [III.4], two different techniques are proposed at 130 GHz to implement this method (Figure III.2). The first one (a) consists in creating an air separation between the antenna and the SiO_2 by elevating the antenna with via-supports. By doing so, this design has achieved a measured gain of 5.5 dBi, a measured -10dB matching BW of 30% and a radiation efficiency of 78%. The second design (b) consists of a Si-BCB layer stack with a backed-cavity below the antenna. The air cavity improves the radiation efficiency up to 88%, with a simulated gain higher than 4.5 dBi over 15% fractional BW and a -10dB matching BW of 13%. However, those two options assume additional micromachining steps based on wet or dry etching to selectively remove parts of the Silicon substrate, which can lead to non-standard costly processes and fragile antenna structures.

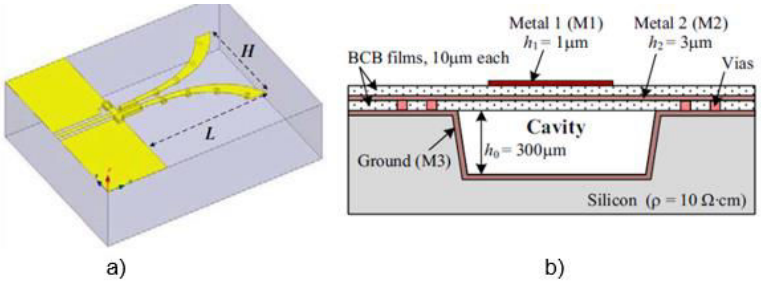

Figure III.2. (a) 3D view of the suspended Vivaldi antenna, and (b) cross-section of the monopole antenna in micro-machined Si-BCB from [III.4].

To further improve the radiation efficiency, a dielectric resonator with high dielectric constant (as opposed to SiO_2) can be placed on top of the on-chip antenna like suggested in [III.5]. In this paper, the power radiated by an E-shaped patch antenna is coupled to this dielectric resonator which increases

the radiation efficiency. This antenna-structure (Figure III.3) achieved a measured peak gain of 10 dBi at 340 GHz with a simulated gain above 9 dBi over 11.8% fractional BW. This design provides a good radiation efficiency of 80%. However, special care on the design optimization and assembly should be taken in order to avoid trapping energy inside the resonator for this kind of antenna-structure. This has an impact on the overall fabrication cost as this architecture requires additional fabrication steps.

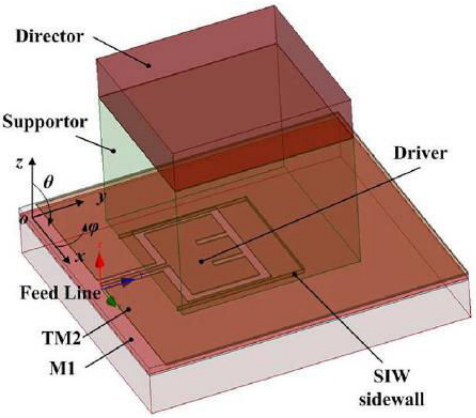

Figure III.3. 3D view of the on-chip 3-D antenna with dielectric resonator on top from [III.5].

A similar approach is the use of an "artificial" dielectric layer (ADL) on top of an on-chip antenna to increase the radiation efficiency [III.6], [III.7] as shown in Figure III.4. This ADL is obtained by embedding a cascade of metal patches within the metal layers of this superstrate. By doing so, an equivalent anisotropic medium is achieved; the dielectric slab exhibits an extremely high dielectric constant (ε_r > 30) in the normal propagation direction to the antenna and a low dielectric constant in the longitudinal direction supported by the surface waves. As a result, a gain improvement of 2 dB was measured using the ADL presented in [III.6]. In [III.7], a high radiation efficiency of 87% is predicted with a simulated peak gain of 6.8 dBi at 280 GHz and -10dB matching fractional BW of 10% around 280 GHz.

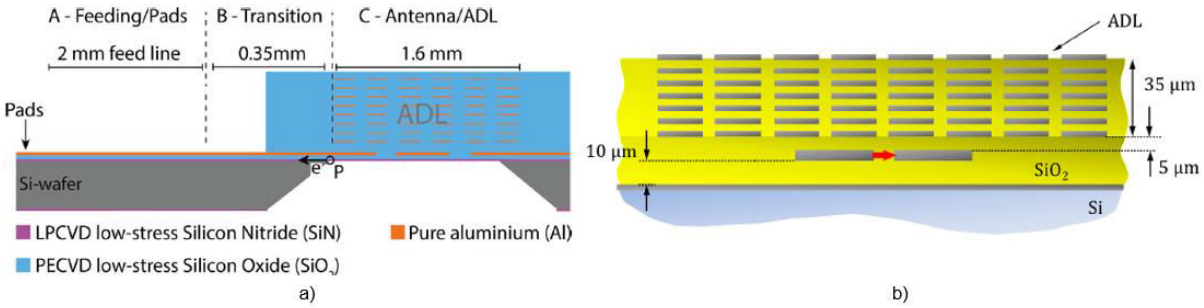

Figure III.4. Cross-section of the antenna/artificial-dielectric-layer structure (a) from [III.6]*, and (b) from* [III.7].

A well-known solution to increase the gain level and radiation efficiency of on-chip antennas is to use a Silicon lens. In order to reduce the negative impact of substrate modes, the lens should have a higher dielectric constant than the one of the substrate [III.8] integrating the antenna and possibly a matching layer-stack [III.9]. Indeed, the substrate waves are being confined in the medium with the highest dielectric constant which here is the lens. Then it is finally collimated and radiated by the lens towards the broadside direction thereby increasing the gain of the on-chip antenna. In [III.8], an antenna integrated within a Tx in SiGe HBT technology is directly mounted on the back-side of a hemispherical Silicon lens featuring a 26.4 dBi directivity, as represented in Figure III.5. Both Silicon bulk and Silicon lens exhibit a high resistivity as a way to reduce the usual conductive losses in the substrate. Evaluating the output power of the Tx, a 3dB fractional BW of 16.6% is achieved at 240 GHz

with a radiation efficiency of 80%. Considering a total efficiency of 75% [III.10], an antenna gain of ~19.8 dBi is assumed.

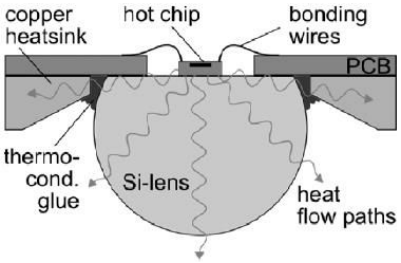

Figure III.5. Lens-packaged Tx/Rx module from [III.8].

Despite some obvious performance enhancement of these on-chip antenna designs compared to Si-bulk integrated-antennas, it seems difficult for the gain fractional BW to exceed ~15% which is mainly due to intrinsic poor dielectric properties of the considered semiconductors, and the fractional matching BW seems to remain limited below 15% as well.

Therefore, other types of antenna designs are also investigated in order to combine high radiation efficiency and wide gain and matching BW. Horn antennas are one type of antenna providing high radiation efficiency (~80%) and wider gain and matching BW than on-chip antennas presented here-above. However, milling fabricated metal horns are very expensive and therefore not compatible with mass production. To tackle this issue, different techniques have been reported in the literature in order to integrate horn antennas within the substrate. In [III.11], a micro-machined dielectric planar H-plane horn antenna is etched on a high resistivity Silicon wafer and fed by a dielectric ridge waveguide. The measured end-fire gain is larger than 8 dBi over 28.6% fractional BW centered at 875 GHz, with a radiation efficiency of 80%.

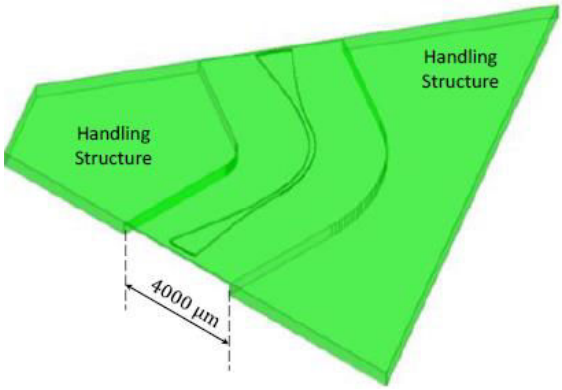

Figure III.6. 3D view of the fabricated back-to-back dielectric horn from [III.11].

Moving towards standard multi-layer Low-Temperature Co-fired Ceramics (LTCC) technology, a sub-mmW Antenna-In-Package (AiP) is also considered for structuring an integrated 3D horn antenna, leveraging substrate integrated waveguide (SIW) technology [III.12],[III.13]. The hollow structure of the corrugated horn is etched through multiple layers of LTCC. Therefore, a very high radiation efficiency of 90% is obtained in [III.12] with a measured peak gain of 18 dBi and a gain higher than 13 dBi over 40% fractional BW around 275 GHz. The System-In-Package assembly shown in Figure III.7 is envisioned, with the radio IC die flip-chip mounted onto the package and connected to a microstrip-to-waveguide transition integrated in the LTCC substrate so as to couple the signal to the horn [III.13].

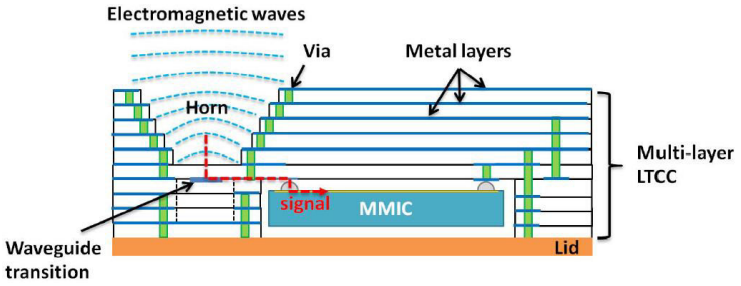

Figure III.7. Cross section of 3D horn integrated in standard LTCC package from [III.13].

As a conclusion, lots of different strategies have been reviewed in order to improve the performance of integrated antennas at sub-mmW and THz frequencies. However, these methods often call upon high-precision micro-machining and/or complex assembly to achieve sophisticated structures which is not always appropriate for high-volume production.

At lower frequency bands like V and D-bands, the microstrip AiP solution has been recognized as the most promising integrated antenna solution for mmW high-speed wireless transmissions. In this approach, a microstrip antenna is integrated in a packaging substrate and the radio chip is surface-mounted on top of the substrate. This type of antenna is well appreciated amongst industrial players for mass-market applications like mobile telecommunication. Indeed, the main benefits of this AiP strategy are moderate to low manufacturing cost, ease-of-assembly, low-profile and readiness for mass production.

MmW AiP designs based on conventional Flame-Retardant-4 (commonly referred to as FR4) PCB material have demonstrated acceptable performance at 60 GHz with appropriate assembly strategies. Indeed, when considering the global antenna-system assembly, suitable chip-to-package interconnect schemes should be addressed in order to achieve the targeted performance. At frequencies below 40 GHz, wirebond interconnects can be used between the IC and the packaging substrate. However, wirebonds suffer from non-negligible parasitic inductance at 60 GHz and above, leading to matching deterioration (see Chapter 2). Indeed, a typical 500 µm-long wire exhibits a significant parasitic inductance of about 500 pH around 50 GHz. Therefore, flip-chip assembly is preferred due to its much smaller dimensions (about 25 µm diameter) and thus smaller parasitic inductance (36 pH evaluated around 50 GHz). As a result, minimum impact on the matching is ensured, leading to wider achievable BWs and higher signal speeds. Paper [III.14] proposes a FR4 AiP which offers an extremely low-cost manufacturing process while exhibiting a measured matching fractional BW of 15% at 60 GHz, a measured gain above 11 dBi and a simulated radiation efficiency of 74%. A schematic of the aforementioned FR4 AiP with flip-chipped mounted IC is shown in Figure III.8.

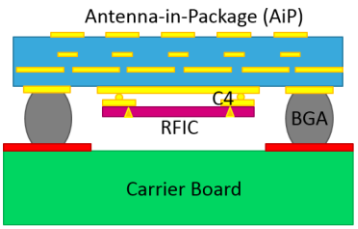

Figure III.8. 60 GHz antenna array integrated in FR4 PCB packaging with flip-chipped IC from [III.14].

High-performance packaging materials like High-Temperature Co-fired Ceramics (HTCC), LTCC and Integrated Passive Device (IPD) technology have also demonstrated high-antenna performance at mmW frequencies [III.15]–[III.16]. In [III.17], a microstrip antenna integrated within LTCC package (Figure III.9) exhibiting an 85% radiation efficiency is designed to work with a 60 GHz CMOS transceiver chip. A measured gain above 10 dBi has been achieved over 13% fractional BW while the antenna is matched over a fractional BW of 11.5%.

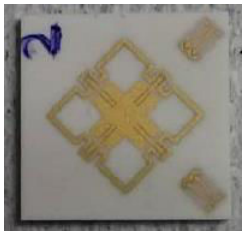

Figure III.9. Picture of the fabricated LTCC integrated antenna at 60 GHz from [III.17].

As mentioned earlier, the next generation of high-speed wireless networks is targeting BWs as large as 100 GHz (40% fractional BW at 250 GHz) in order to increase the data-rates up to 100 Gb/s. In this context, adjusting the existing antenna packaging techniques at V and D-band up to J-band has proven to be extremely challenging in terms of both design and fabrication. Indeed, aiming at sub-mmW/THz frequency bands leads to more aggressive antenna dimensions. Design rules' limitations of standard mmW packaging tend to limit the achievable antenna footprint miniaturization and therefore its sub-mmW/THz performance. As an example, reference [III.18] presents a simple design of a 270 GHz LTCC-integrated slot antenna-array which exhibits low fabrication-tolerance susceptibility. This multi-layer LTCC design shown in Figure III.10 has demonstrated a peak gain of 27.6 dBi at 275.2 GHz and a gain higher than 25 dBi over a fractional BW of 3.5% and a radiation efficiency of 40%. If radiation efficiency and peak gain are definitely fair and competitive results, the small fractional BW indeed illustrates the need for better packaging technologies enabling higher achievable BW performance. What's more, associated high-volume production of HTCC and LTCC technology makes this technology too expensive to be economically profitable for mass market applications.

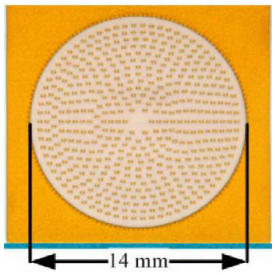

Figure III.10. Picture of the LTCC-integrated 270 GHz antenna from [III.18].

Leveraging low-cost antenna packaging technology, High Density Interconnect (HDI) organic substrate has proven to be a good solution for integrated microstrip antenna designs requiring higher integration levels. Indeed, HDI packaging technology has already demonstrated satisfying performance at 60 GHz [III.19] and 140 GHz [III.20].

The work presented in this chapter aims at evaluating the potentiality of HDI organic substrate packaging above 200 GHz by leveraging its aggressive integration level capability. Two different antenna-system solutions integrated in HDI organic substrate will be investigated: an Aperture Coupled Patch AiP, and a microstrip-to-WR3 transition that would be coupled to a low-cost 3D printed THz horn. The targeted gain of both systems was about 10 dBi over 33% fractional BW from 200 GHz to 280 GHz. Those antenna systems are actually meant to be used as feeds to illuminate quasi-optical antennas such as a dielectric lens or a Cassegrain reflector in order to reach gains ranging from 20 to 50 dBi.

II. Aperture coupled-patch antenna integrated in organic substrate

Among the different types of mmW antennas, microstrip patch antennas are largely used due to their low profile, light weight, robustness, simple fabrication process, and are easy to integrate. These structures are usually considered for wide BW and high directivity mmW wireless applications such as P2P wireless transmissions [III.21]–[III.23]. However, very little microstrip patch antennas reported in the literature achieve sufficient matching/gain BW and radiation efficiency above the Ka frequency band without implementing specific techniques to enhance the performance. A significant amount of energy is indeed launched into surface waves propagating in the substrate [III.2], thus degrading the overall antenna performance and shape of radiation pattern. Aside from the typical antenna array strategy, a technique to increase the gain and matching BW is the use of parasitic radiating elements, either stacked in multiple dielectric layers to trigger multiple frequency resonances or added in series with the line-fed patches in a single dielectric layer to radiate in phase [III.24], [III.25]. Another reported strategy to increase the antenna's performance is to add slots inside the patch. This method is based on a specific disposition of the slots to reshape the distribution of surface electric currents on the patch so as to reduce side lobes and adjust the radiation pattern of the antenna [III.26]. Overall, the strategies that are used to improve the antenna's performance generally call upon standard and thus low-cost fabrication process compared to on-chip antenna ICs.

In this context, reaching the desired performance above 200 GHz with a microstrip patch antenna seems challenging and our strategy to enhance the antenna's performance is to harness the energy of surface waves in a constructive way. The Aperture Coupled-Patch Antenna (ACPA) design that we propose in the following section tackles this issue by the integration of a metal cavity around the patch. This structure has indeed achieved promising results at 60 GHz [III.19]. Designs at 140 GHz have also shown promising results [III.27] which makes the development of ACPA between 200 GHz and 280 GHz all the more encouraging.

1. Aperture coupled-patch antenna

a. Design description

A patch antenna is usually described as a simple rectangular metal patch with a ground plane both separated by a dielectric. This structure is usually manufactured using a planar process like PCB process for instance. A convenient way to explain the functioning of a patch antenna is to assimilate the structure to a capacitor, with its two electrode plates consisting of the patch and the ground plane. When the capacitor is loaded by energy, opposite charges accumulate in the upper plate (the patch) and lower plate (the ground plane). These moving charges establish an electric field inside the dielectric and create corresponding surface electric currents on the patch and ground plane as shown in Figure III.11. In these conditions, if the patch length corresponds to its resonating length, radiation occurs. The fundamental resonance mode corresponds to a length of about λ/2 and can be easily recovered if the electric current is of the form a sinusoidal wave:

$$I(y) = I_0 \sin\left(\frac{2\pi}{\lambda} y\right) \tag{10}$$

$$I\left(0; \frac{\lambda}{2}\right) = 0 \tag{11}$$

$$I\left(\frac{\lambda}{4}\right) = I_0 \tag{12}$$

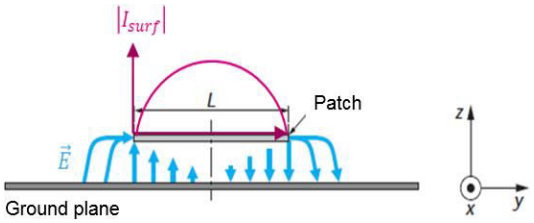

Figure III.11. E-field and Surface current amplitude distribution of the fundamental radiating mode of a rectangular microstrip patch antenna.

b. Aperture Coupled-Patch Antenna structure

A common way to excite a patch is known as aperture coupling: it consists of two dielectric layers separated by a ground plane. As shown in Figure III.12 (a), the rectangular patch is located at the top of the upper dielectric layer whereas the feed line is located at the bottom of the lower dielectric layer. A slot located on the ground plane between the patch and the line allows electromagnetic coupling between the two elements. Therefore, energy is transferred from the line to the slot and then from the slot to the patch. A benefit of this type of structure is the isolation of the feed line from the patch by the common ground plane which minimizes interferences between the spurious radiation coming from the feeding line and the patch radiation. This plays an important role on the back-side radiation. Moreover, this structure contributes to the widening of the BW thanks to the resonances of the slot and the patch. This is manifested by a loop of the S_{11} parameter crossing the $Im[S_{11}] = 0$ axis twice on the Smith chart (Figure III.12 (b)). The elongated line going beyond the slot correspond to a stub, and a fine tuning of its length allows better matching of the antenna on the entire BW.

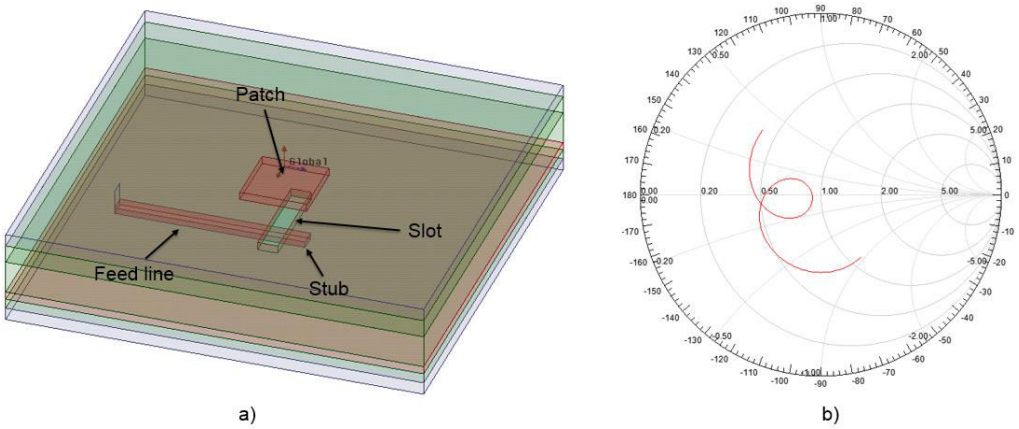

Figure III.12. (a) Aperture Coupled-Patch structure, and (b) double resonance input impedance locus on Smith Chart.

2. HDI organic technology and BGA packaging

a. Technology introduction

Low dielectric loss organic BGA packaging substrates are commonly used at lower frequencies using low-cost materials. Applied to mmW frequencies, preliminary evaluation of HDI materials at 60 GHz has also allowed to identify proper dielectric materials [III.19]. This HDI technology is based on semi-additive fabrication which makes it possible to access more aggressive Design Rule Constraints (DRC). As a result, metallic tracks width/spacing of 40/40 µm can be reached. Moreover, flip-chip mounting technology is compatible with the existing automated equipment used in BGA packaging technology and thus requires no additional or special process steps.

b. *Example of BGA technology used at 60 GHz and 140 GHz by STMicroelectronics*

In the context of Aimeric Bisognin's PhD, state-of-the-art antennas have been designed and fabricated at 60 GHz in HDI organic technology [III.19], [III.28]. A schematic of the proposed antenna assembly strategy is shown in Figure III.13. Low losses, and high electrical performance provided by this technology have allowed to reach the antenna specifications required by WiGig standards while offering a cost-effective solution.

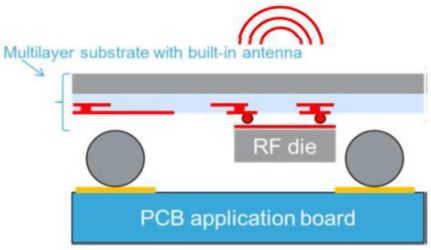

Figure III.13. 60 GHz system-in-package with antenna integrated is BGA technology.

The integration of mmW antennas in BGA technology has also been evaluated at frequencies above 100 GHz. BWs of up to 20 GHz around 120 GHz were targeted in order to achieve data rates in the order of 10 Gb/s with very simple signal modulation schemes [III.20]. An excellent agreement between simulations and measurements was achieved for antennas working at 120 GHz using HDI organic substrate. Hence, demonstrated performance is competing with state-of-the-art at such high frequency. In view of these results, it seems legitimate to think about the evaluation of BGA technology for the integration of antennas operating in the 200 to 280 GHz frequency band.

3. Design process and simulation results

c. *Substrate thickness estimation*

The considered dielectric build-up of the HDI packaging substrate is a standard 1+2+1 build-up with a core substrate stacked between 2 prepreg and solder-mask layers as can be seen in Figure III.14. The feeding microstrip line is designed on M1 below the P2 ground plane and the patch is designed on P1 metal layer.

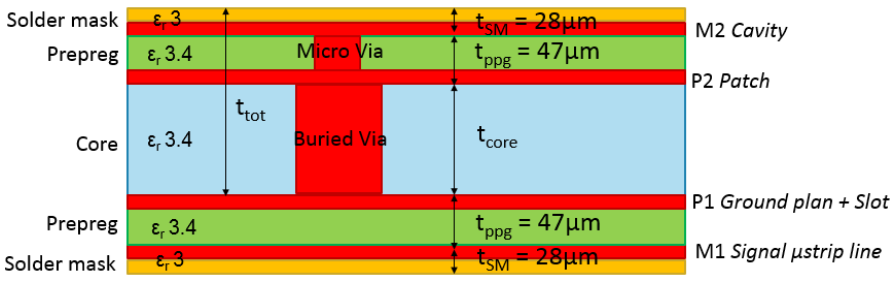

Figure III.14. Cross-section of the chosen HDI 1+2+1 build-up.

The build-up of substrate packaging can be seen as a dielectric slab waveguide consisting of three layers of dielectrics: the core also referred to as the guiding layer (with a refractive index of n_1) and the prepregs at the top and bottom (with a refractive index of n_2 for a symmetric waveguide). To support wave propagation inside this dielectric waveguide, the following conditions must be verified:

- The refractive indexes validate the inequality $n_1 > n_2$
- The wave angle of incidence corresponds to a partial or total reflection angle

- The core thickness is bigger than the thickness corresponding to the fundamental propagation mode cut-off frequency.

Under these conditions, the incident power is however not completely transmitted to the patch, but rather partially leaking into the substrate by means of multiple reflections on the core interfaces. These waves are mostly known as surface waves. The amount of surface wave modes allowed inside the substrate can be analytically determined. Each electric and magnetic field components can be found in order to evaluate their propagation constant based on the Maxwell's wave equation and the appropriate boundary conditions. This procedure is explained in detail in Aimeric Bisognin's PhD work [III.27]. Discrete solutions of the normalized propagation constant can then be found as a function of the substrate thickness. These correspond to propagating modes which can be seen in Figure III.15.

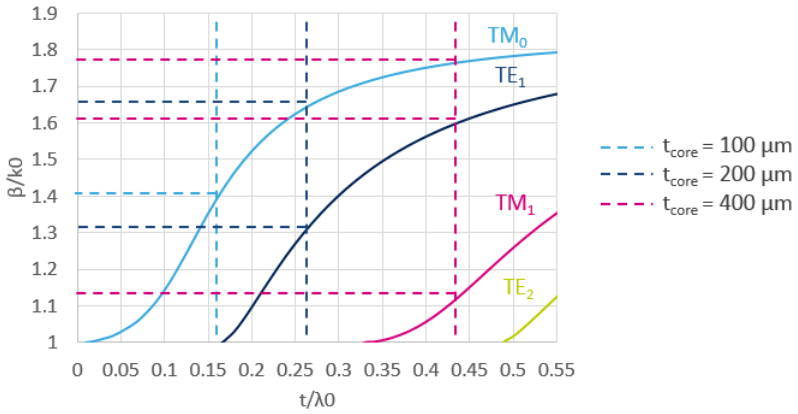

Figure III.15. Propagation constant of surface wave modes at 280 GHz in a substrate (ε_r = 3.4) with ground plane.

Having performed this analysis, we can see how the substrate thickness is a key parameter for the performance optimization of the antenna. Indeed the substrate should be thick enough to enable sufficient BW but thin enough to prevent too many surface wave modes from degrading the performance. Applying this line of reasoning to the HDI substrate build-up shown in Figure III.14, the proper core thickness can be chosen. The prepreg and solder mask layer are already fixed by the maximum resolution of HDI technology and a core thickness from 100 µm to 400 µm is authorized. A core thickness of 400 µm and 200 µm would support three modes (TM_0, TE_1, TM_1) and two modes (TM_0, TE_1) respectively, which would significantly reduce the performance. At the minimum thickness of 100 µm, the energy inside the substrate would only couple to the fundamental TM_0 mode (β/k_0 ~ 1.4 at 240 GHz). Therefore, the core thickness of the antenna design was fixed at 100 µm.

d. Benefits of a metal cavity

As the TM_0 surface wave mode is still excited inside the 100 µm substrate, it is well advised to minimize its impact on the antenna performance. According to studies realized in Aimeric Bisognin's PhD work [III.27], a solution consists in the implementation of a metallic cavity around the patch. In this approach, the cavity not only stops the surface waves from further propagating, but also collects and radiates them in the broadside direction of the BGA through surface currents excited on the top ring of the cavity (as illustrated in Figure III.16). A smart dimensioning of this cavity enables a radiation in phase with the patch radiation, thereby producing constructive interferences. Hence, the power transmitted through the slot contributes completely to the antenna radiation thereby increasing the broadside gain.

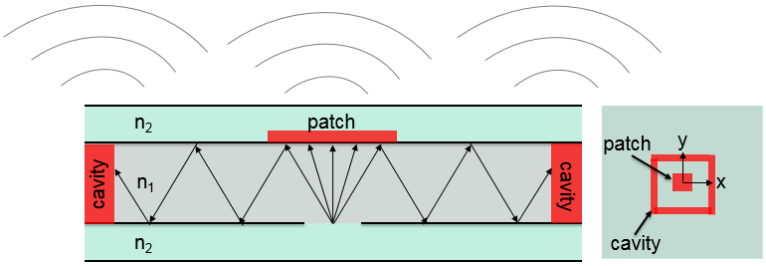

Figure III.16. Operating principle of the metallic cavity.

e. Canonical design simulations

The ACPA's main goal is to be used as a feed source for a dielectric lens. A full description of this lens is detailed in section III.5. In order to maximize the final gain, an appropriate feed source must be designed to optimize the illumination of the lens. This is achieved by validating the following ACPA specifications: the radiated beam should have a Gaussian-like shape and the power at the subtended angle of the feed (80° to 100°) should be 10 dB below the maximum power level at the broadside direction to reduce spillover losses by over-illuminating the lens.

i. Cavity influence on the radiation diagram

After having optimized the ACPA's dimensions and matching, a series of simulations were performed in a 5*5 mm² substrate to highlight the cavity's impact on surface wave propagations. These simulations were achieved using the 3D full-wave electromagnetic solver HFSS from Ansys, based on the finite element method. Figure III.17 (a) shows a quantification of surface waves propagating inside the 100µm thick substrate, and their strong impact on the resulting radiation diagram. These surface waves come from the TM_0 mode excited by the slot and propagating towards the substrate edges where they are diffracted. This diffraction is responsible for the radiation diagram degradation. The addition of a cavity around the patch greatly improves the radiation diagram as it can be seen in Figure III.17 (b). Indeed, the surface waves are "collected" by the cavity and radiated in phase with the radiation of the patch, thereby focusing the energy into the main lobe of the diagram with a maximum gain in the broadside direction (10.6 dB). As TM_0 surface waves mainly propagate parallel to the E-plane of the patch, the cavity radiation arises mostly from the walls excited lengthwise. Indeed, as shown in Figure III.17 the electric field density is higher along these walls. This configuration creates an equivalent 3 by 1 radiating element array (wall/patch/wall) in the E-plane.

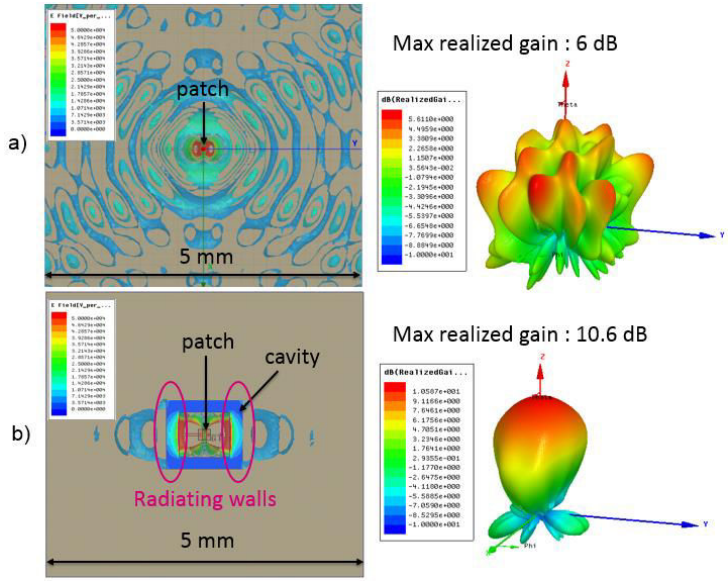

Figure III.17. E-field propagation inside the substrate and corresponding radiation pattern at 240 GHz (a) without any cavity and (b) with cavity.

The addition of the cavity also impacts the achievable BW with the addition of a third frequency resonance to the previous existing ones. Indeed, the -15dB fractional BW has been increased from 30% to 44%. As illustrated in Figure III.18 (a), the slot, patch and cavity sizing respectively affect the matching at the beginning, middle and end of the considered BW. The simulated broadside gain is also clearly improved thanks to the grounded metal cavity as shown in Figure III.18 (b). It may be noted here that this solution provides an extremely large simulated BW around 240 GHz and therefore represents state-of-the-art performance for planar sub-mmW antennas compared to antenna performance found in the literature and summarized in Table III.1.

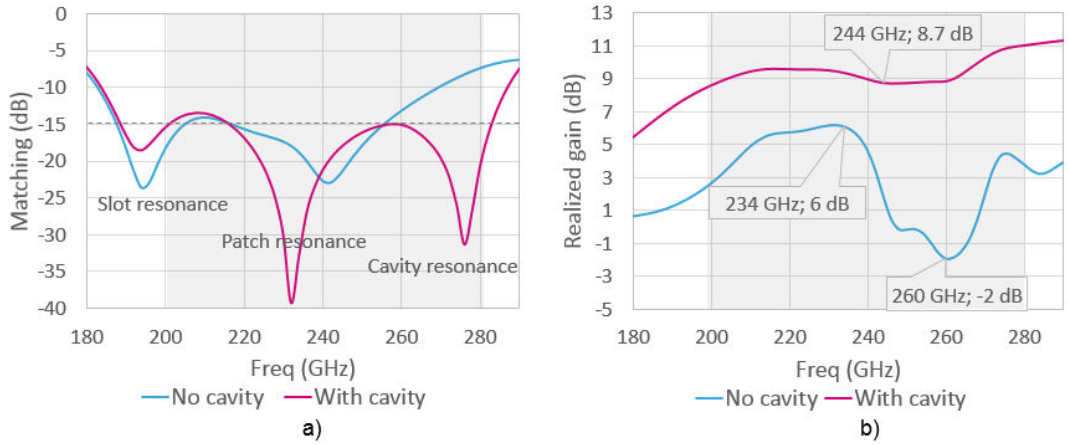

Figure III.18. (a)|S_{11}| with and without cavity, (b) broadside realized gain with and without cavity.

ii. E-plane and H-plane radiation pattern optimization

The radiation patterns of the ACPA in the E-plane (containing the feeding line) and H-plane (perpendicular to the feeding line) were simulated so as to evaluate the main lobe width agreement with the feed source specifications previously defined. Targeting a radiation diagram with an ideal Gaussian shape, the E-plane and H-plane radiation patterns should overlap one-another on a half-width radiation angle of 40/50°. However, the actual H-plane is much larger than the E-plane shown in Figure III.19 (a). Consequently, a practical solution consists in taking advantage of an array effect by

adding a second patch in the H-plane, thereby reducing the main lobe's width in the H-plane. Moving to a 2 by 1 patch array with a spacing of 500 µm center-to-center, we clearly improve the E-plane/H-plane symmetry so as to validate the targeted specifications: the E and H plane main lobes are overlapping and the side lobes remain 10 dB below the maximum for a corresponding theta of 40° (Figure III.19 (b)).

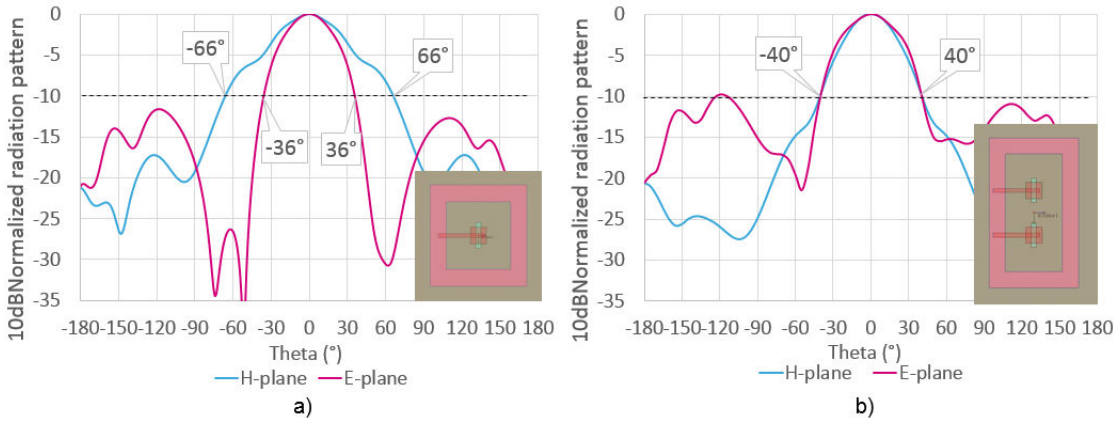

Figure III.19. (a) E-plane and H-plane normalized radiation patterns at 240 GHz with one patch, and (b) with two patches in the E-plane at 280 GHz.

iii. ACPA design with feeding network

A microstrip power divider distributing the signal equally to the two patches was designed in a 50Ω environment. The simulated insertion loss for each lines lies between -0.7 dB and -1.5 dB from 200 GHz to 280 GHz and a matching better than -15 dB is achieved at the input port.

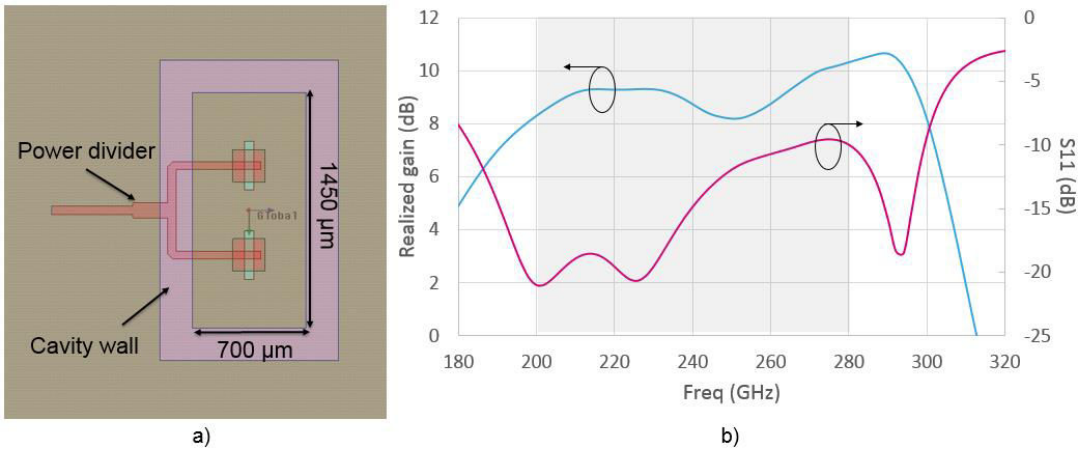

Figure III.20. (a) Final design of the divider, and (b) corresponding $|S_{11}|$ and simulated broadside gain of the 2x1 array of patches fed by the divider.

f. Fabrication constraints implementation

i. Design rule constraints

At this stage, design rules related to HDI organic BGA technology should be taken into account in the initial design in order to remain compatible with the chosen manufacturing process. The main design change consisted in replacing the walls of the cavity by laser-drilled micro-vias connecting the top layer with the inner layer and buried-vias connecting the inner layers together. A cross-sectional

view of the core and build-up showing the vias dimensions is shown in Figure III.21. The vias dimensions available in this kind of technology are:

- Buried-via diameter : 75 µm
- Micro-via diameter: 65 µm
- Minimum buried-via pitch (center to center): 175 µm.

Metal caps called “land-plate” have to be placed within the metal layer M1, P1, P2 and M2 above and under each vias. According to the DRC, the following land-plates dimensions must be respected:

- Land-plate diameter on P1 and P2: 175 µm
- Land-plate diameter on M1 and M2: top side 120 µm / bottom side 130 µm.

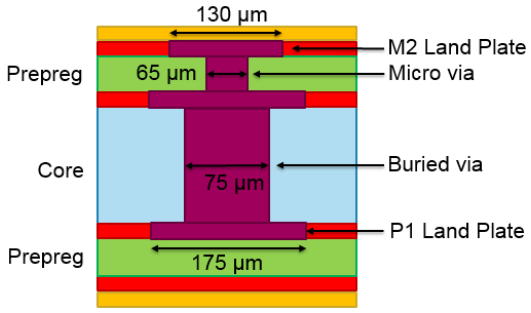

Figure III.21. Cross sectional view of the core and the build-up with vias and land-plates dimensions.

ii. Implementation of vias

As shown in Figure III.22 (a), the walls of the cavity were replaced by micro-vias and buried-vias. The vias were put at the inner edge of the cavity ring with a pitch of 175 µm. This design modification had a negative impact on the performance of the antenna. As a result, the broadside realized gain that was obtained is less flat throughout the BW of interest and is much lower in the 200-300 GHz band, with a 2dB notch at 226 GHz and a narrower BW (Figure III.22 (b)).

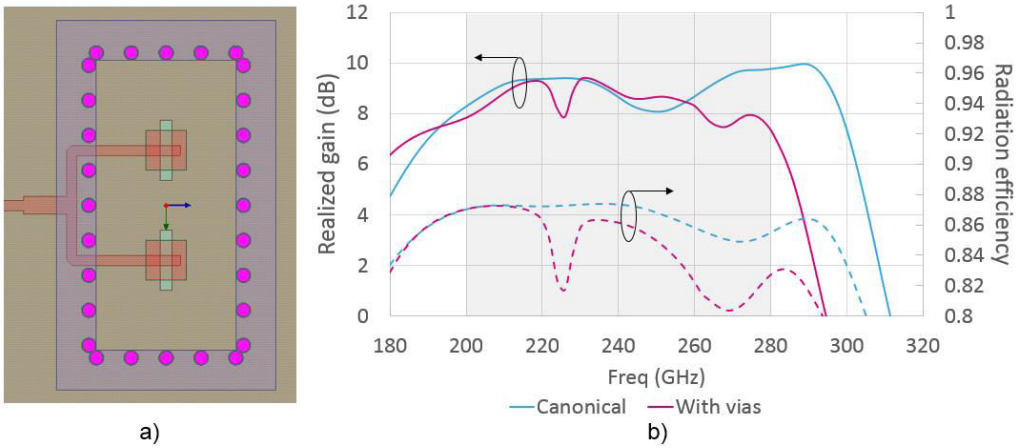

Figure III.22. (a) Top-view of the design with vias, (b) broadside realized gain and radiation efficiency comparison between initial design and design with realistic vias.

In the following steps, we investigated the root-cause of this performance degradation in order to propose an antenna design compliant with manufacturing constraints while still ensuring acceptable performance.

iii. Cavity height impact

As shown in Figure III.23 (a), it was noticed that the upper cavity (from P2 to M2) in the prepreg dielectric layer was trapping a lot of energy at 226 GHz, which eventually doesn't contribute to the antenna radiation. Therefore, this cavity was removed from P2 to M2 (micro-vias and metallic ring at M2) in the initial design. An image of the E-field distribution inside the upper prepreg is shown in Figure III.23 (a) for the new BGA design with a lower cavity ranging from P1 to P2, along with a performance comparison between those two designs in Figure III.23 (b). A more stable gain and flat radiation efficiency were achieved throughout the BW of interest without this upper-cavity. Consequently, the upper-cavity was definitively removed from the antenna design.

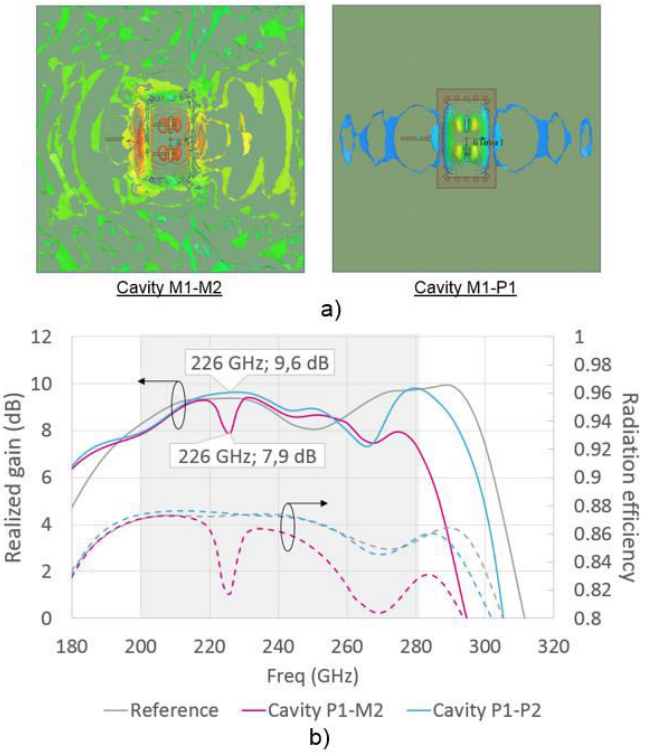

Figure III.23. (a) E-field propagation comparison in prepreg dielectric layer at 226 GHz, (b) broadside Realized gain and radiation efficiency comparison.

As explained earlier, the cavity radiation mainly comes from the two walls perpendicular to the E-plane of the patch. Therefore, the next simulations were mostly oriented towards the optimization of the cavity width along the E-plane.

iv. Cavity width impact

An optimization of the cavity width was achieved (vias and ring moving together) with the vias positioned at the center of the cavity ring. It is important to notice that the effective cavity width is no longer the distance between two opposite walls but the distance between two opposite vias as shown in Figure III.24 (a).

To assess the impact on the higher cut-off frequency of the antenna gain, we performed a sweep on the width of the cavity. This cut-off frequency corresponds to two complementary phenomenon: a resonant cavity mode triggered for a specific cavity dimension producing standing waves inside the cavity, and the generation of surface currents on the cavity ring that are no longer in phase with the surface currents on the patches. As the width was reduced, the standing wave resonant frequency of

the cavity increased and the surface current goes out of phase. This simulation highlights the design sensitivity towards the cavity size; at such high frequency a couple of 10µm difference greatly impacts the antenna's frequency response. An optimum gain level and flatness was found with a cavity width of 575 µm (Figure III.24 (b)).

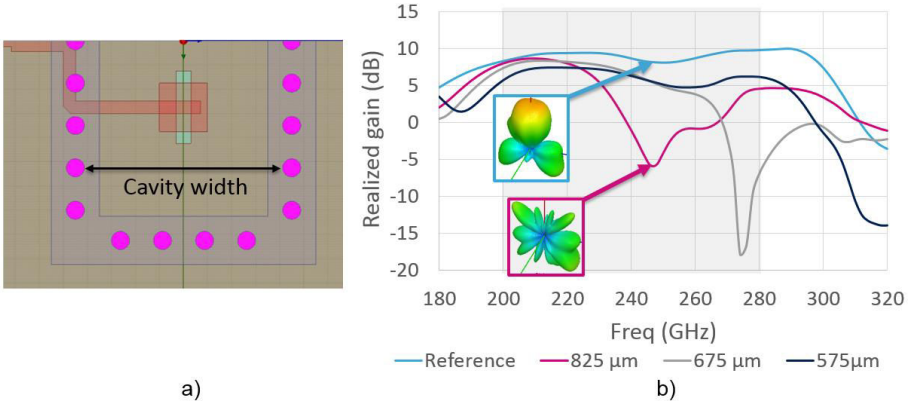

Figure III.24. (a) Cavity width parameter, (b) broadside Realized gain as a function of frequency versus several cavity width.

v. Land-plates and vias pitch optimization

To comply with the DRC, land-plates were added on the metal layer P1 and P2. First, the land-plate pitch was increased from 175 µm to 220 µm to create a design that is compatible with the resolution of the actual semi-additive fabrication process (Figure III.25). Indeed, touching land-plates would be difficult to fabricate. Then in order to ensure a proper radiation of the cavity ring, the vias should be placed as close as possible to the inner edge of the ring. This configuration allows to force the surface current propagation in one privileged direction along the width of the ring thereby reinforcing a coherent phase distribution along the cavity ring. Therefore, the goal was to minimize the ring overrun towards the patch by exposing the land-plates as shown in Figure III.25 (c). By doing so, a gain increase of 2 to 3 dB was achieved (Figure III.25 (d)).

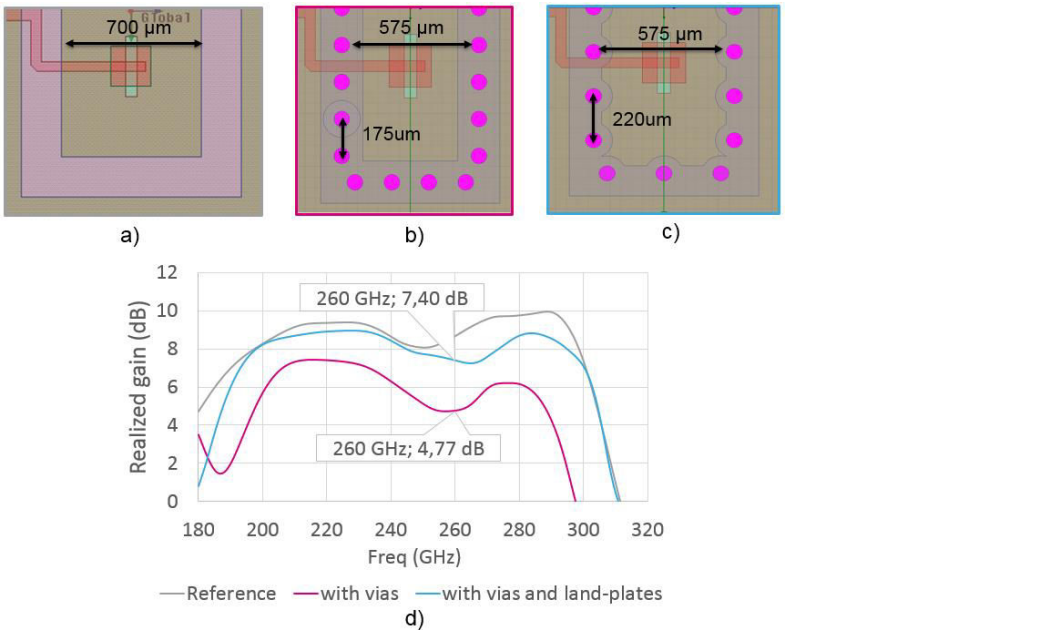

Figure III.25. Design top views of (a) the canonical design, (b) the design with a via-cavity, (c) the optimized design with exposed land-plates in the cavity, and (d) broadside realized gain after width and via pitch optimization.

vi. Final design with GSG pad access

Lastly, GSG pads were incorporated to the design to enable the antenna performance measurement as well as electrical connection with a flip-chipped IC. Along with the pads, a feeding line with an optimized characteristic impedance was implemented to ensure optimized matching and gain. The final design of the ACPA is shown in Figure III.26 (a). A simple design was finally achieved, which applies well to mass-market applications where standard processes and robust low-profile antennas are required. This design exhibits a stable simulated broadside realized gain of about 8 dB between 200 GHz and 296 GHz (Figure III.26 (b)), which corresponds to a large fractional BW of 38.7 %, with an achieved radiation efficiency above 75 %. A trade-off on the S_{11} is however noticed, as it has been increased from -10 dB to -5 dB at the end of the targeted BW (Figure III.26 (c)). Indeed, such a simple design does not allow a matching below -10 dB over a BW as large as 38.7 %.

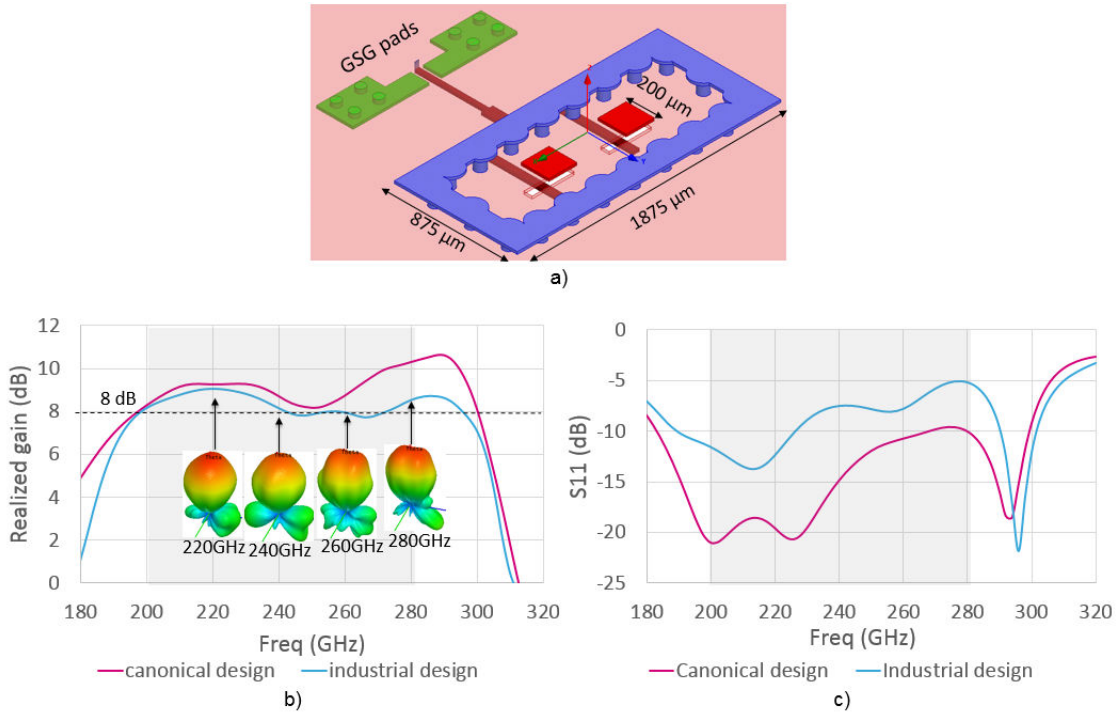

Figure III.26. (a) 3D view of the final AiP design, (b) simulated broadside realized gain, and (c) $|S_{11}|$ comparison between canonical and final design from 180 GHz to 320 GHz.

As a conclusion, from the obtained simulation results, the HDI organic technology seems appropriate for sub-mmW AiPs working above 200 GHz. However, this optimization process has shown that DRC limitations of this technology were reached at 280 GHz (with a struggle on the via-cavity design) and antenna designs at higher frequency would eventually require a technology with more aggressive design rules. Some innovative packaging technologies like thin-glass technology already enables more aggressive drawing rules with minimum features in the order of 5 µm [III.29].

4. Measurement results

The AiP prototypes were measured in collaboration with the Institute of Radio Frequency Engineering and Electronics (IHE) at Karlsruhe Institute of Technology in Germany.

a. Experimental setup

The antennas were measured on IHE's probe-based measurement setup, operating in the 220 GHz – 325 GHz Band [III.30]. In the set-up, an Agilent PNA-X vector network-analyser (VNA) controls a sub-mmW/THz frequency extension module to generate a sub-mmW/THz signal. This signal is fed to the Antenna Under Test (AUT) through a coplanar GGB Picoprobe with an 80 µm pitch. This configuration allows measurement of the AUT reflection coefficient $|S_{11}|$. The AUT is positioned onto an electromagnetically transparent holder. The main radiation of the AUT is opposite to the probing side. Thus, spurious reflections on the probe or waveguide have a minimum impact on the antenna radiation in the lower hemisphere of the measurable zone. The Rx consists of a horn antenna rotating around the AUT thanks to two arms and two steps motors. This configuration allows measurement of the radiation pattern in the E and H planes. However, the maximum theta range in the E-plane is 255° (and not 360°) due to blockage from the table supporting the equipment and the probe. Since cable losses are high at sub-mmW and THz frequencies, a sub-harmonic mixer is directly connected to the horn antenna in order to down-convert the signal to the IF frequency (404 MHz) thanks to an LO signal. Both LO and IF signals are respectively transmitted to the mixer and the VNA through rotary joints using a coaxial cable and two diplexers. The measurement of the transmission coefficient $|S_{21}|$ by the VNA enable the computation of the antenna gain in the recorded position. A picture of the Tx system setup and a schematic of the complete measurement setup are shown in Figure III.27 along with a picture of the AUT.

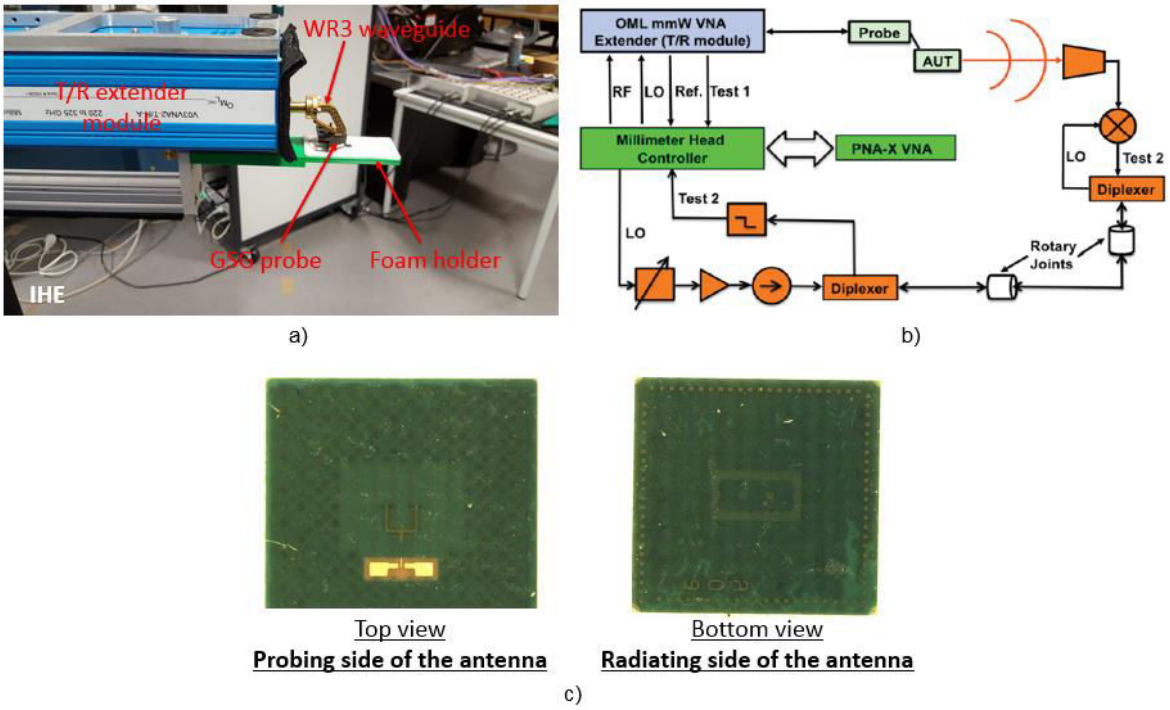

Figure III.27. (a) Sub-mmW/THz signal generator part of the set-up, (b) block diagram of the set-up from [III.30]*, and (c) top and bottom view of the fabricated BGA AUT.*

b. Measurement of the 1st BGA antenna batch

A schematic of the different metal layers of the 1st batch of BGA antennas are shown in Figure III.28. Hollow dummies were integrated in the ground plane to respect the copper balance on this very large copper area. Standard semi-additive BGA process fabrication for HDI technology delivers an average

fabrication tolerance of ±20 µm which can be lowered down to ± 12 µm if specified. Thus a specific process control on layers M1 and P1 was required with a fabrication tolerance of ± 12 µm, in order to respect the GSG pads pitch, the lines width, and the slots dimensions.

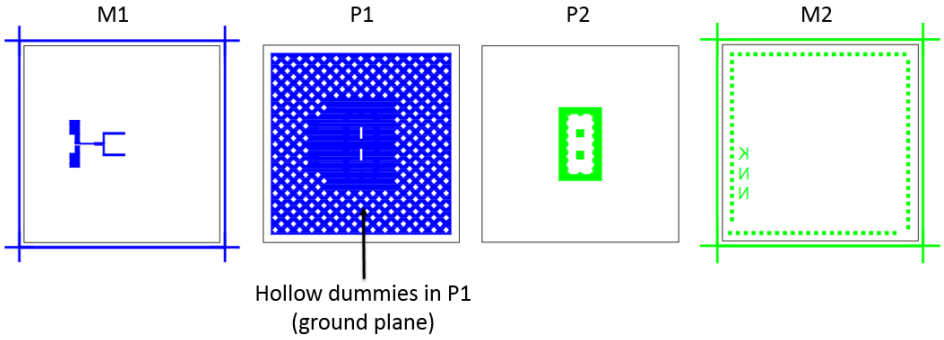

Figure III.28. Different Metal layers of the 1st BGA batch.

Three antenna samples (#1, #2, #3) were measured in order to have an insight on the antenna performance reproducibility. As shown in Figure III.29, a good measurement reproducibility was obtained, with a noticeable difference between the simulation and measurement results due to a significant gain notch around 270 GHz. This notch divides the frequency band into two dual bands: 220-240 GHz where the gain reaches 5 dBi and 280-300 GHz where the gain is higher than 2 dBi.

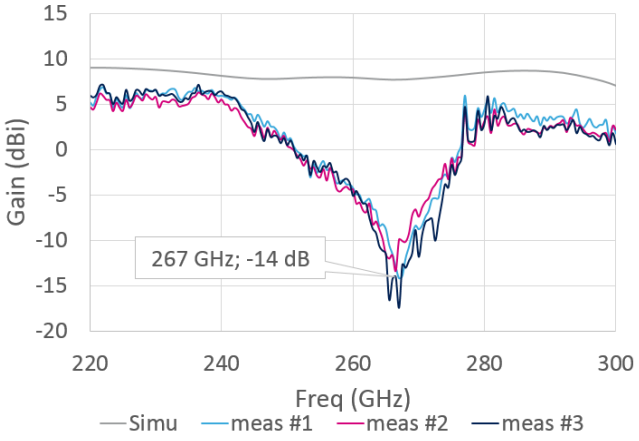

Figure III.29. Broadside gain measured between 220 GHz and 300 GHz.

Looking at the radiation pattern in Figure III.30, the main lobes in H-plane (a) are satisfactory for the first dual band, however the E-plane patterns (b) are greatly disturbed and the main lobe is hardly distinguished from the side lobes. Since the grounded cavity is supposed to control the surface waves in the E-plane, a first assumption is that the observed gain and radiation pattern distortion might be related to unexpected defects in the E-plane of the fabricated cavity. Indeed, when comparing the simulated and measured normalized gain pattern in Figure III.30, a fair agreement is obtained for the H-plane main lobe (c), whereas significant differences are observed in the E-plane main lobe (d).

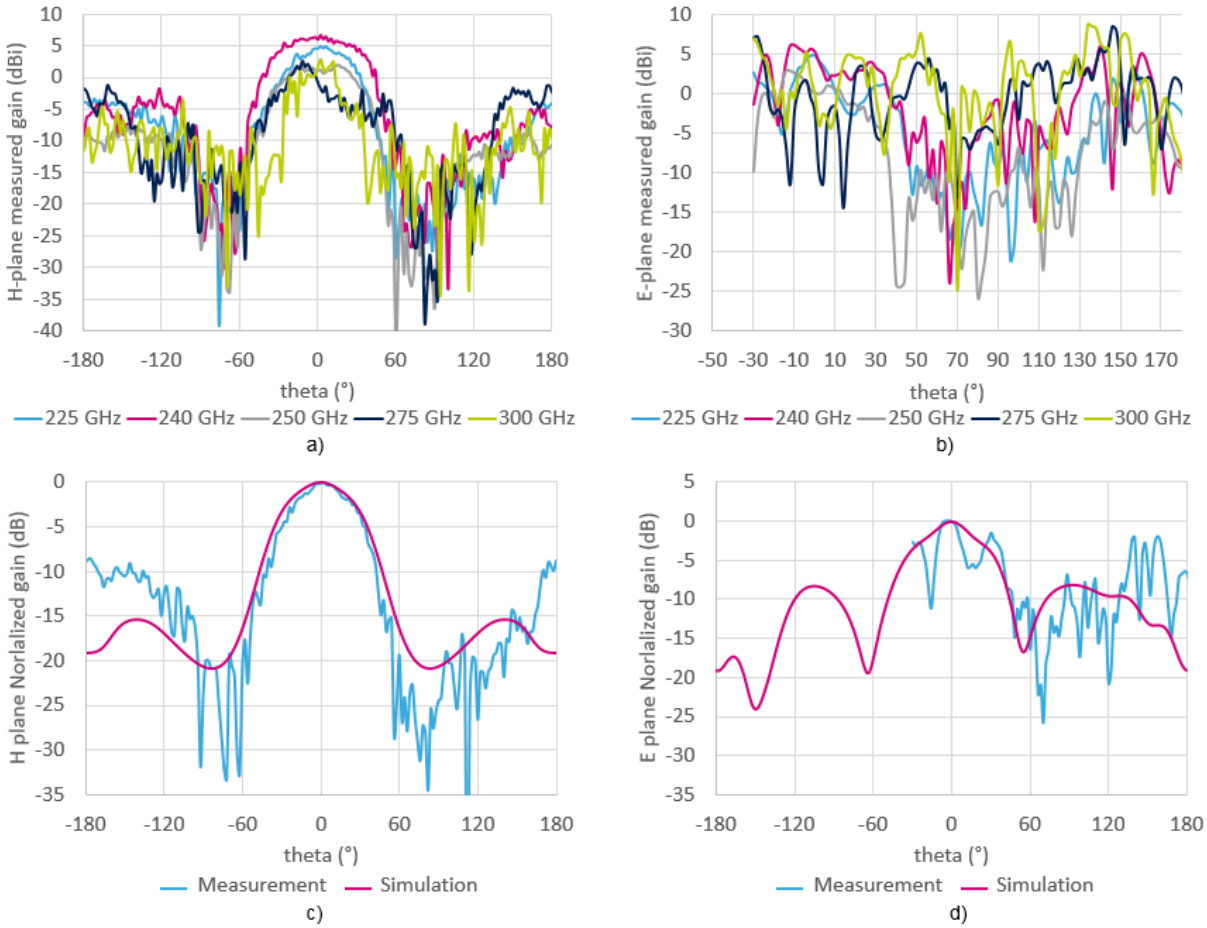

Figure III.30. Measured (a) H-plane gain and (b) E-plane gain, and simulation/measurement comparison of the normalized gain at 230 GHz in (c) the H-plane and (d) E-plane.

Similarly, a strong discrepancy between the measured and simulated reflection coefficient $|S_{11}|$ is observed, and a shift to the right side of the Smith chart reveals an additional resistive and inductive effect during the measurement as shown in Figure III.31.

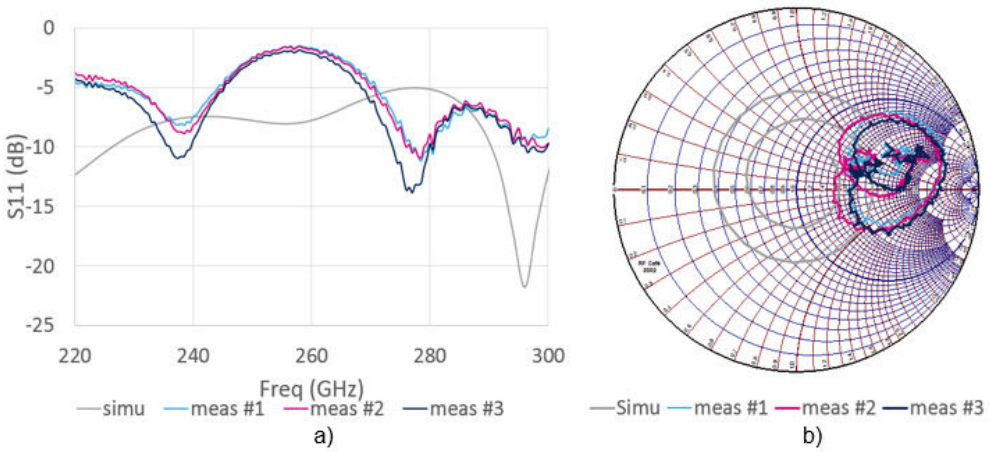

Figure III.31. (a) $|S_{11}|$ rectangular plot, and (b) input impedance on the Smith chart simulation and measurement of the first batch of antennas between 220 GHz and 300 GHz.

Given the significant discrepancy between these simulated and measured results and the important radiation pattern distortion in the E-plane, a dimensional analyses of the prototyped antenna was realized and the actual dimensions were imported in HFSS for a post-simulation of the antenna design.

c. Post-simulations

An X-ray scanning of the BGA prototype was realized for dimensional analyses of the fabricated design (Figure III.32). As a result, a significant amount of inaccuracies were uncovered on several parts of the antenna probably playing a role on the radiation and the matching: an average error above 16% was made on the dimension of the patches, the ring and cavity width. Knowing the antenna's performance sensitivity to the cavity parameters, these fabrication defects might be responsible for the measured gain notch and radiation pattern distortion in the E-plane. A significant misalignment between the M1 and P1 layers was also observed and an average error of 54% was made on the power divider's dimensions, thereby showing a higher impedance to the probe. The GSG pitch is also wider by 24 µm which could lead to a bad contact quality loaded with parasitic effects. This could explain the $|S_{11}|$ mismatch observed in the rectangular plot and the shift of the measured S_{11} towards the right side of the Smith chart.

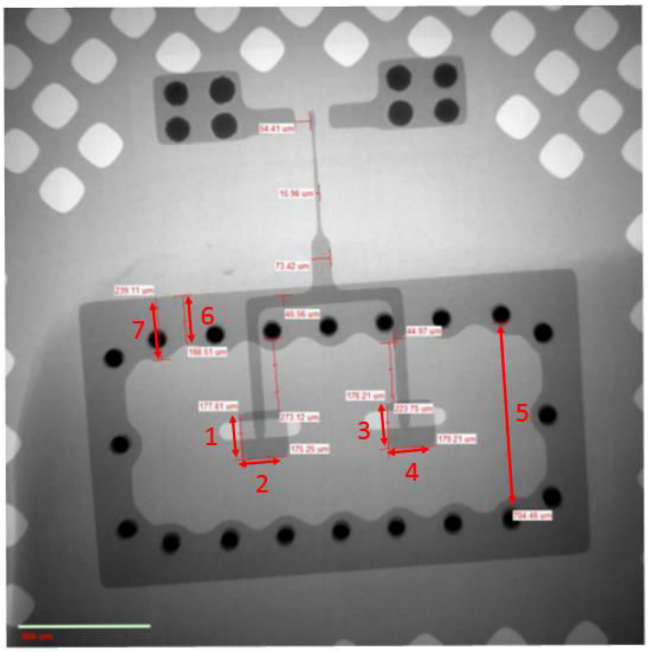

		Real value	Initial value	delta (%)
1	Patch width 1 (µm)	177.61	200	11.20
2	Patch width 2 (µm)	176.21	200	11.90
3	Patch width 3 (µm)	175.25	200	12.38
4	Patch width 4 (µm)	179.21	200	10.40
5	Cavity width (µm)	704.45	575	22.51
6	Ring width 1 (µm)	239.11	200	19.56
7	Ring width 2 (µm)	188.51	150	25.67
			Average	16.23

Figure III.32. X-ray imaging of the prototyped antenna and dimensional analysis.

The post-simulation analysis realized with the measured dimensions retrieved from the X-ray image showed a similar gain signature with a deep notch around 270 GHz. As expected, this emphasizes the antenna's susceptibility to the fabrication tolerance of semi-additive HDI organic technology process at 240 GHz, which was not an issue at 60 GHz and 140 GHz. As a conclusion, if a better process control is mastered, better antenna performance should be achieved, namely the 6 dBi flat gain within 33% BW if some losses are expected versus simulation results (8 dBi).

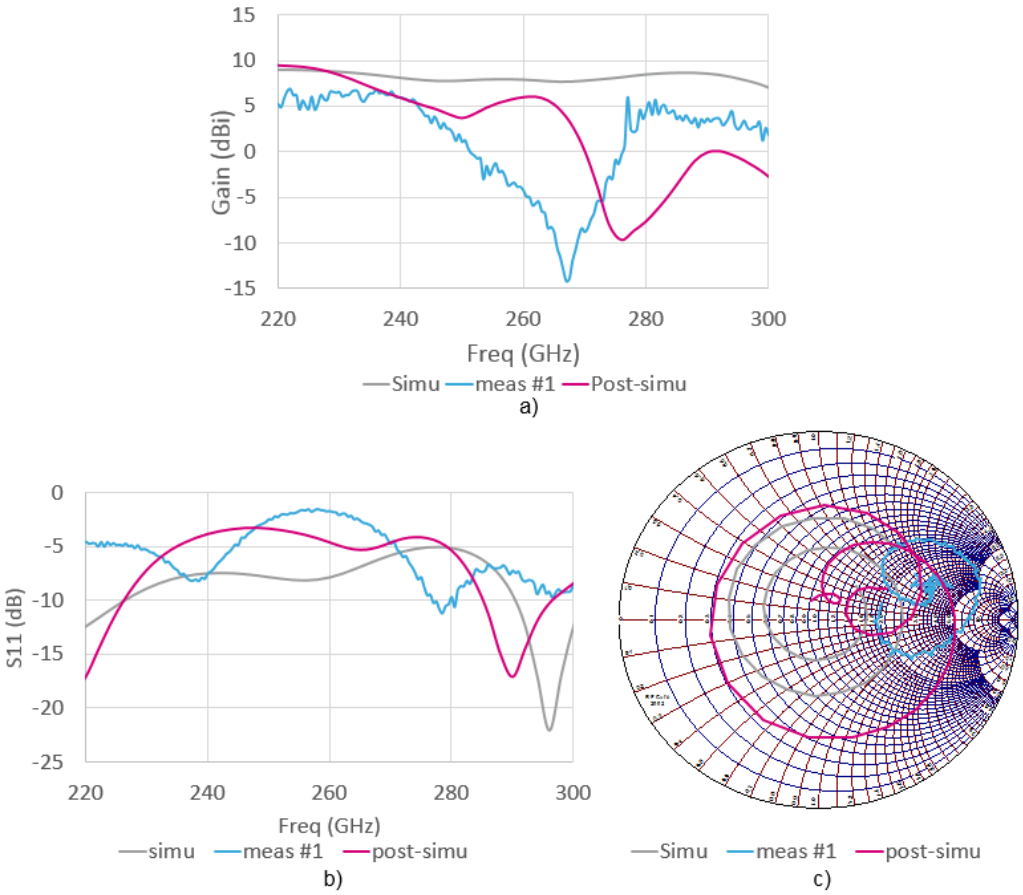

Figure III.33. Post-simulation and measurement comparison of the gain (top), S_{11} rectangular plot (bottom left) and Smith chart (bottom right) post-simulation.

The design of a 2nd batch of BGA antennas was achieved with respect to better copper balance on each metal layers with the addition of copper filling on M1, P2 and M2 to minimize fabrication errors within the metal traces and the alignment of the dielectric build-up during the fabrication process as shown in Figure III.34. Indeed, metal traces should be distributed as uniformly as possible on each layer and across the build-up. A specific process control was also requested on M1, P1 as well as P2 with a fabrication tolerance of ± 15 µm in order to replicate as accurately as possible the ring dimensions and alignment with the vias. Future measurements of this batch will allow to better estimate the capacity of HDI organic substrate technology above 200 GHz.

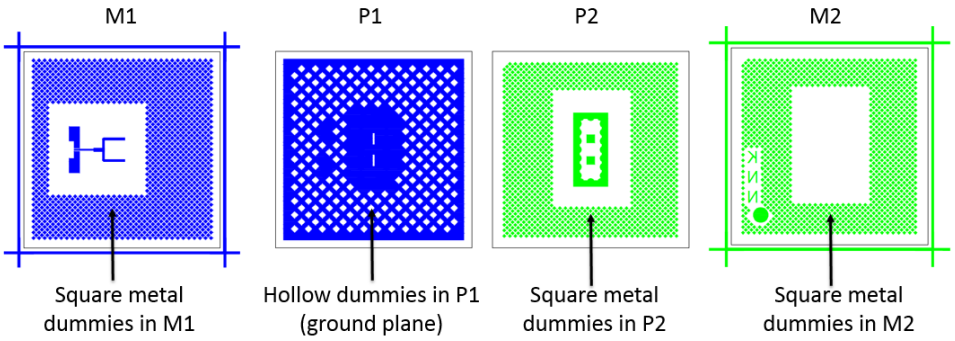

Figure III.34. Metal layers of the 2nd BGA batch.

d. *Integrated sub-mmW and THz antenna benchmarking*

Ref.	Techno.	Type of antenna	Carrier Freq.	Simu. gain	Meas. gain	Gain BW	-10dB S_{11} BW	Radia-tion eff.	Dimen-sions
[III.14]	FR4 PCB	Stacked coupled patch	60 GHz		>11 dBi		15%	74%	20x20x0.838 mm^3
[III.17]	LTCC	Dual polarized aperture antenna	60 GHz	~12 dB	>10 dBi	11.50% at 10 dBi	11.50%	85%	12x12x1.128 mm^3
[III.18]	LTCC	Slot antenna array	270 GHz	>25 dB	>25 dBi	3.50% at 25 dBi	5%	40%	36x16x0.49 mm^3
[III.3]	130nm CMOS	Patch antenna	280 GHz	-1.6 dBi max			7%	21%	1.5x0.8 mm^2
[III.4]	Si-based	Modified vivaldi antenna	130 GHz		5.5 dBi max		30%	78%	1.21x1.6 mm^2
[III.4]	Si-BCB	Monopol antenna with backed cavity	130 GHz	>4.5 dBi		15% at 4.5 dBi	13%	88%	1x0.6 mm^2
[III.5]	0.13µm SiGe BiCMOS	3D Yagi-like antenna with dielectric resonator	340 GHz	>9 dBi	10 dBi max	11.80% at 9 dBi	12%	80%	0.7x0.7x0.58 mm^3
[III.7]	CMOS	Dipole antenna with artificial dielectric superstrate	280 GHz	6.8 dBi max			10%	87%	
[III.18]	Si-based	H-plane dielectric planar horn antenna	875 GHz	>8 dBi	>8 dBi	28.60% at 8 dBi		80%	3.13x4x0.1 mm^3
[III.12]	LTCC	Integrated SIW horn	275 GHz		>13 dBi	40% at 13 dBi	>36%	90%	5x5x2.8 mm^3
This work	HDI organic	Aperture coupled patch	250 GHz	~8 dBi		40% at 8 dBi	18%	75%	0.875x1.875x0.250 mm^3

Table III.1. Sub-mmW and THz state of the art integrated antennas benchmarking (ref. = reference, techno. = technology, freq. = frequency, simu. = simulation, meas. = measurement, eff. = efficiency).

III. Microstrip/WR3 transition embedded in BGA substrate

A second sub-mmW antenna-system solution that was investigated through this work uses a corrugated horn antenna instead of an integrated antenna as a feed source of a quasi-optical larger antenna. The advantages of using a corrugated horn are well known among the microwave community [III.31]. Here, the corrugated horn antenna is particularly attractive for its very wide matching BW and radiation efficiency (> 80%), its high polarization purity between its two orthogonal polarizations. This

last characteristic would allow the possibility to either double the achievable data rate of the transmitted signal or work as a Tx and Rx simultaneously for full-duplex communication. The considered horn's input corresponds to a standard WR3 rectangular waveguide and is therefore easily assembled with a waveguide-fed system configuration. However, an integrated solution requires to connect the Silicon Photonic IC back to the horn through a PCB-to-waveguide transition. In this matter, a microstrip-to-waveguide transition has been selected and its design integrated in HDI organic substrate is investigated in this section. A very simple assembly strategy with the horn is proposed, with however a trade-off dealing with the insertion loss.

1. Overview of microstrip-to-WR waveguide transitions

Various transition structures can be found in the literature. One example of a high performance transition is the fin-line antipodal transition [III.32]. Its structure consists in antipodal fin-lines overlapping one another and positioned on opposite sides of a common substrate. These lines are gradually tapered to rotate the E-field by 90° so as to transform the fundamental TE_{01} mode of the rectangular waveguide into the quasi-TEM mode of the microstrip line as shown in Figure III.35.

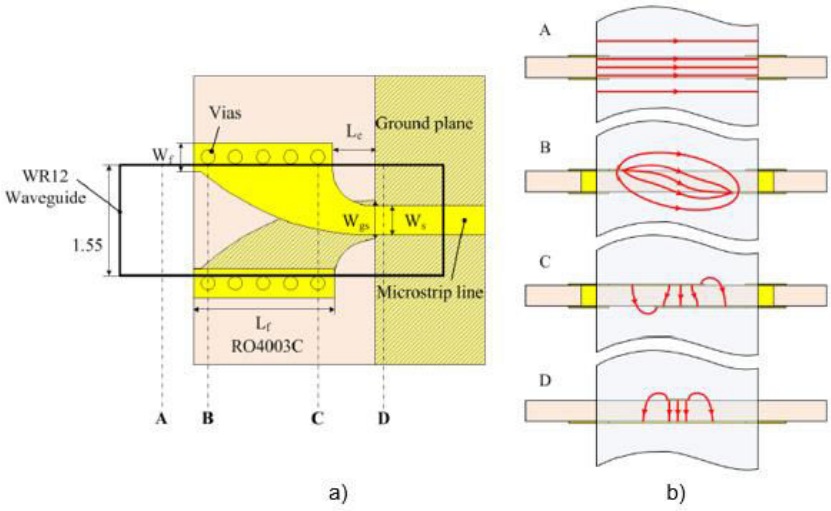

Figure III.35. (a) Waveguide-to-microstrip transition structure, and (b) E field transformation in designed antipodal fin-line waveguide-to-microstrip transition [III.32].

For example, this transition was simulated on HFSS between 200 GHz and 280 GHz and a transmission of -1 dB was achieved with a microstrip port matching $|S_{11}|$ of -15 dB (Figure III.36).

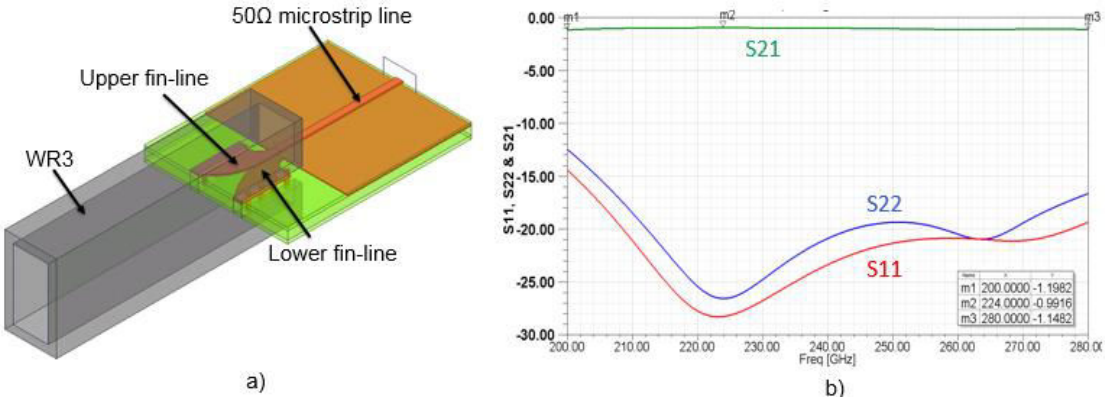

Figure III.36. (a) Fin-line antipodal transition design, and (b) simulated S parameters at 240 GHz.

However, the longitudinal assembly of the organic substrate with the waveguide and its very thin thickness make the overall packaging system very fragile and inconvenient for mass production. Indeed, this type of transition hardly applies to the targeted robustness of antenna-systems that is required for mass market sub-mmW/THz applications. Therefore, our interest pointed toward the design and evaluation of a vertical transition which seemed more appropriate for ease of assembly and system robustness.

Among the state-of-the-art integrated vertical microstrip-to-waveguide transitions, NTT's transition integrated in LTCC substrate has achieved a minimum insertion loss of 1.2 dB and a transmission fractional BW of 12% at 300 GHz [III.33]. Leveraging a multi-layer process (seven LTCC layers in total), this transition is based on SIW technology. Combined with air cavities etched inside the design, these techniques enable to achieve a high mode-conversion efficiency of the transition which leads to the low insertion loss of 1.2 dB.

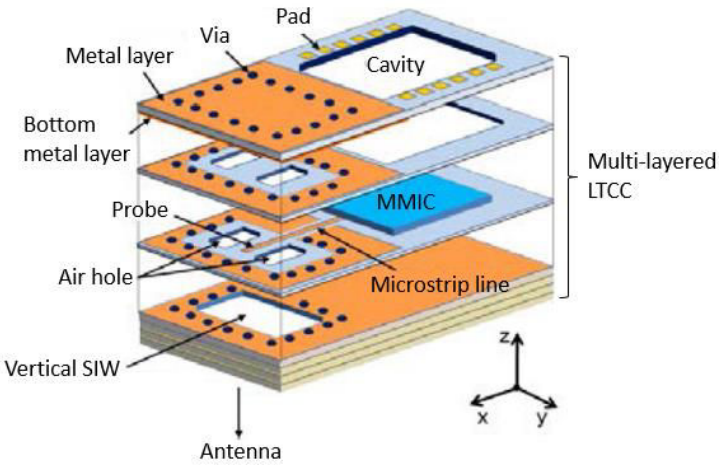

Figure III.37. Concept of the multi-layered LTCC packaging with integrated probe-type microstrip-to-waveguide transition at 300 GHz [III.33].

Another approach consists in applying the gap waveguide method to the transition design as shown in Figure III.38 and presented in [III.34]. In this design, an inverted microstrip gap waveguide is connected to a WR15 rectangular waveguide through an inverted microstrip probe. In this type of line, the E-field is mainly confined in an air gap which greatly reduces dielectric and conductive losses. On the other side of the inverted line, a metal bed of nails ensures the suppression of parallel plate modes that are usually propagating between the packaging substrate and the rectangular waveguide module. A simulated insertion loss of 0.7 dB was achieved over a fractional BW of 32% around 62 GHz.

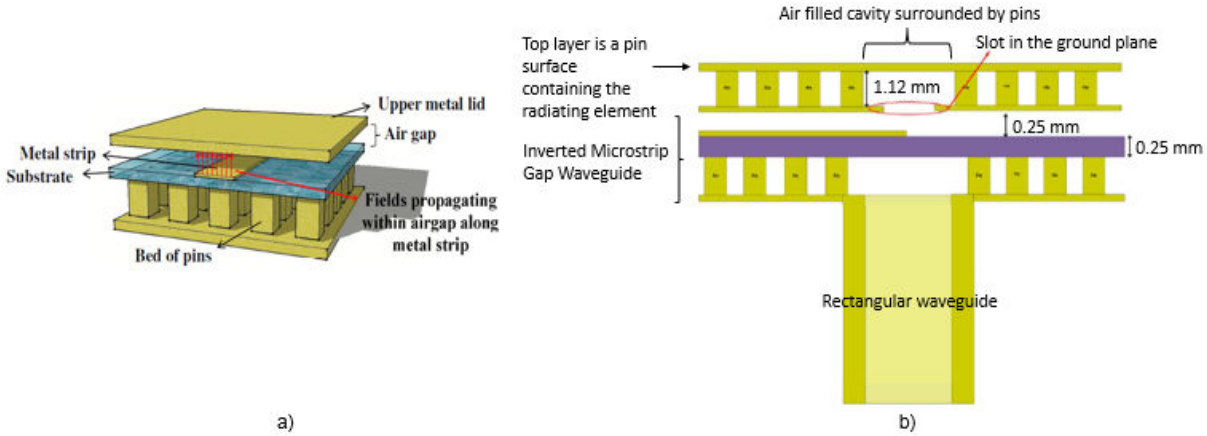

Figure III.38. (a) Inverted microstrip gap waveguide geometry, and (b) cross section of the transition geometry integrated into the antenna layer at 62 GHz [III.34].

Overall, satisfying insertion losses were reported around 1 dB thanks to the use of techniques such as the ones presented here-above. However, most of the designs based on SIW technology require a large amount of vias and very accurate control of via holes placements thereby increasing the manufacturing process complexity. Concerning gap waveguides, as efficient as this technology goes for potential E band applications, the actual dimensions at sub-mmW and THz frequencies would involve very precise micromachining processes which are not yet compatible with high-volume production targeting the consumer market.

An extremely simple design was reported in [III.35], [III.36] and consists of a planar proximity coupled transition with a two-metal layer build-up. This structure can be implemented in a single dielectric layer. As shown in Figure III.39 (a), the top metal layer consists of a microstrip line ended by a probe which is surrounded by a grounded waveguide short-circuit. A patch is located at the bottom metal layer and surrounded by the ground plane. An electromagnetic coupling between the probe and the patch allows a power transfer from one element to another. As it was explained for the ACPA, the patch radiates when the appropriated resonant dimensions are chosen. The waveguide short surrounding the probe reduces backside radiations, thereby constraining the patch to radiate inside the waveguide. The Figure III.39 (b) shows the E-field lines of the planar proximity coupled transition in the E-plane of the design. The quasi-TEM mode of the microstrip line transforms into the fundamental TM_{01} mode of the patch which finally rotates the E field by 90° in order to fit to the fundamental TE_{01} mode of the waveguide. Paper [3] presents a simulated insertion loss below 3 dB over more than 31% BW around 76 GHz.

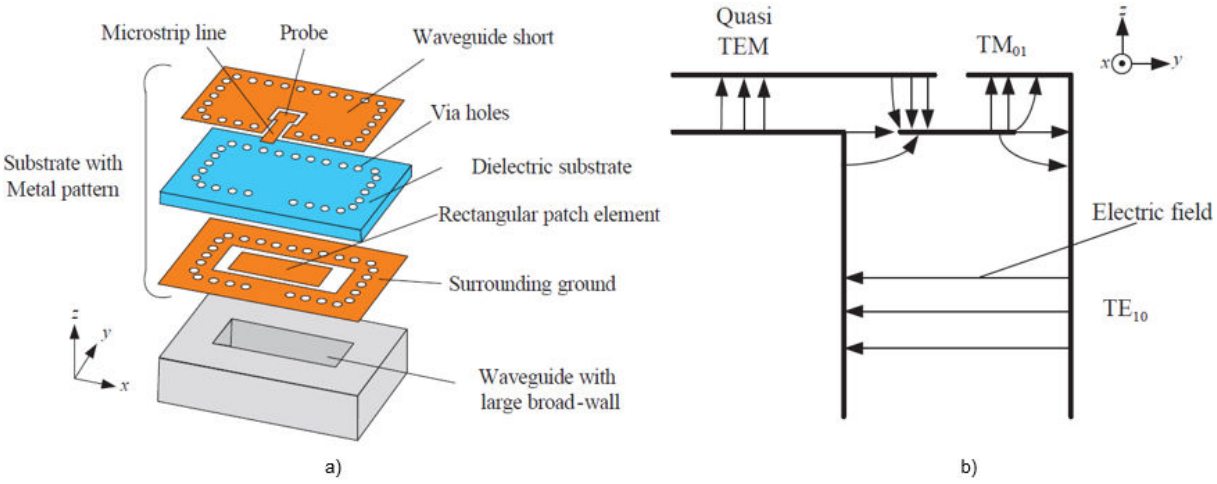

Figure III.39. (a) Schematic of a single dielectric layer transition configuration, (b) E-field lines of the different modes occurring in a single dielectric layer vertical transition [III.36].

Therefore, the design simplicity and acceptable achieved insertion loss and BW make this type of transition a good candidate for mass-market mmW applications, and was therefore investigated in the context of our work above 200 GHz using a low-loss and low-cost HDI organic BGA packaging technology.

2. Design of the transition and simulation results

a. Integration strategy

Figure III.40 presents a non-proportional simplified cross-section view of the proposed antenna-system assembly strategy with the vertical transition integrated in HDI organic BGA substrate. The benefits of such a system are a compact transition profile and a robust BGA substrate-on-PCB assembly.

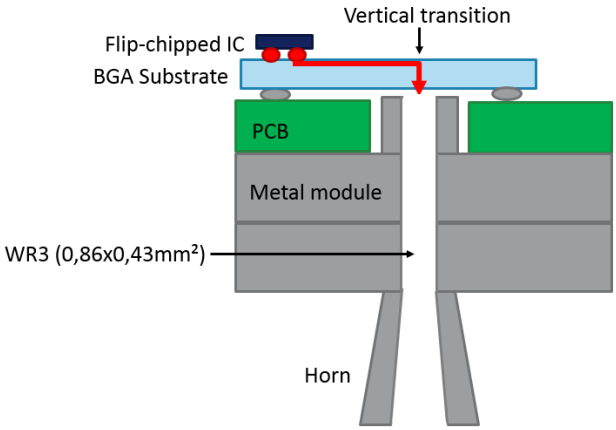

Figure III.40. Non-proportional schematic cross-section view of the proposed antenna-system assembly with vertical transition.

The measurement of the transition's performance will be done in a back-to-back (B2B) transition configuration, which consists in connecting two transitions together with a microstrip line. The assembly strategy of the B2B with the measurement set-up also needs to be considered. In the proposed measurement set-up shown in Figure III.41, a metallic block integrating two WR3 waveguides brings the input power to the first transition and collects the output power from the second transition. The substrate would be assembled with LGA lands on top of a PCB inside which a hole is cut. This PCB

is screwed on the waveguide metallic block to secure the integrated transitions on top of the two waveguide openings.

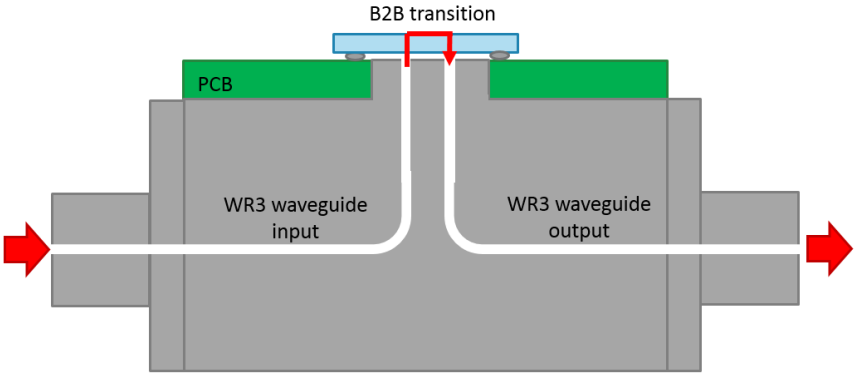

Figure III.41. Cross-sectional view of the Measurement set-up assembly for B2B transition configuration.

b. Design simulations

A preliminary dimensioning of the design shown in Figure III.42 (a) was realized on a single dielectric layer substrate. Different parameters were optimized such as the probe and patch size and the waveguide-short dimensions. The resulting design and associated S_{ij} parameters are shown in Figure III.42 (b). A maximum insertion loss of 0.8 dB was achieved between 200 GHz and 260 GHz which represents a fractional BW of 26%.

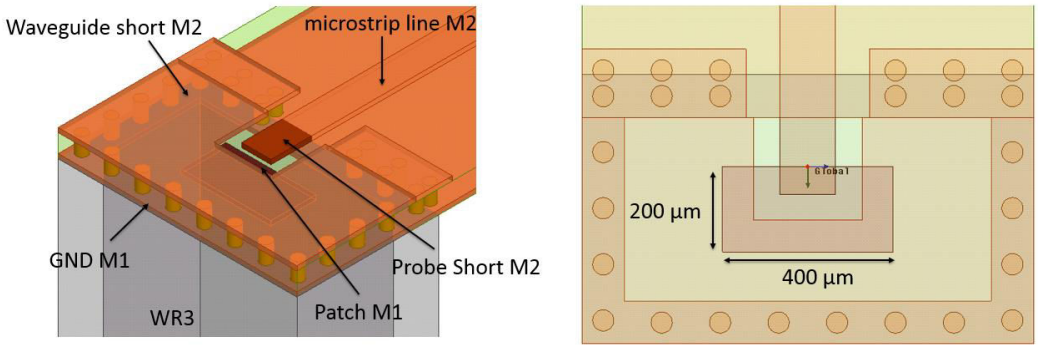

a)

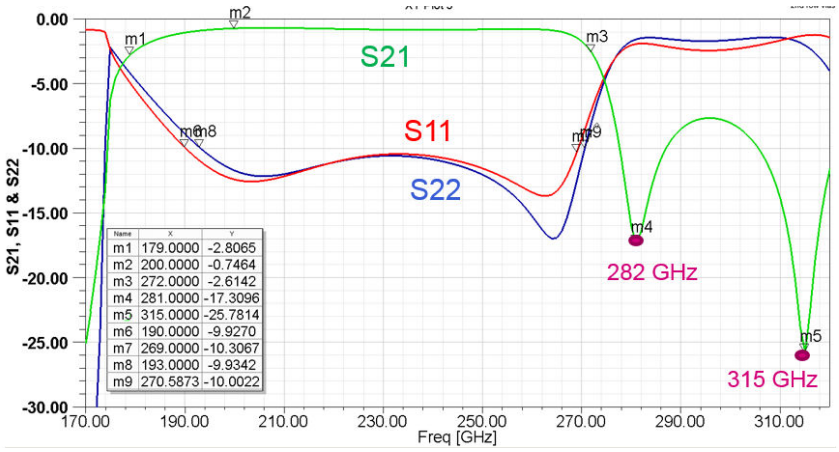

b)

Figure III.42. (a) 3D view of the initial design, and (b) associated simulated Sij parameters.

Solder-masks were then added for the claddings as shown in Figure III.43 (a) in order to obtain a standard dielectric build-up and protect all the metal lines. This action leaded to increased dielectric losses and in turn, modified the frequency response of the design. Indeed, it impacted the $|S_{21}|$ by narrowing its BW down to 19% with an insertion loss of 2 dB as we can see in Figure III.43 (b).

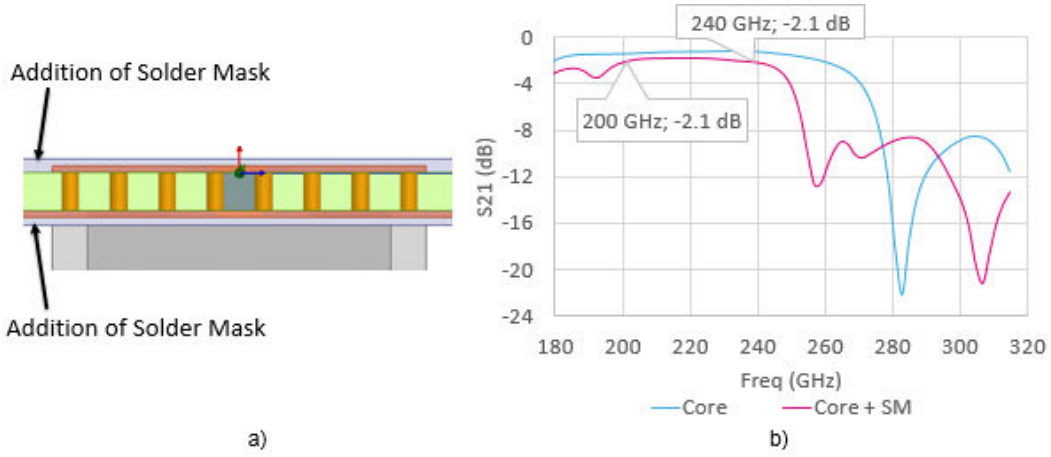

Figure III.43. (a) Cross sectional view of the transition layers with the addition of solder-masks, (b) and solder-masks impact on the transmission coefficient $|S_{21}|$ between 180 GHz and 320 GHz.

To recover the initial $|S_{21}|$ values, another optimization on the dimensions of the design was performed. In addition to that, land plates were added to the design to comply with the DRC of the HDI organic technology. Removing the solder mask around the probe and the patch as shown in the pink zones from Figure III.44 (a) greatly improved the insertion loss BW of the transition. Moreover, this operation is compatible with standard semi-additive fabrication process. The resulting insertion loss shown in Figure III.44 (b) is 4 dB over 34% factional BW with a minimum insertion loss of 2 dB at 240 GHz, and the -10 dB matching covers a fractional BW of 31% from 220 GHz to 302 GHz.

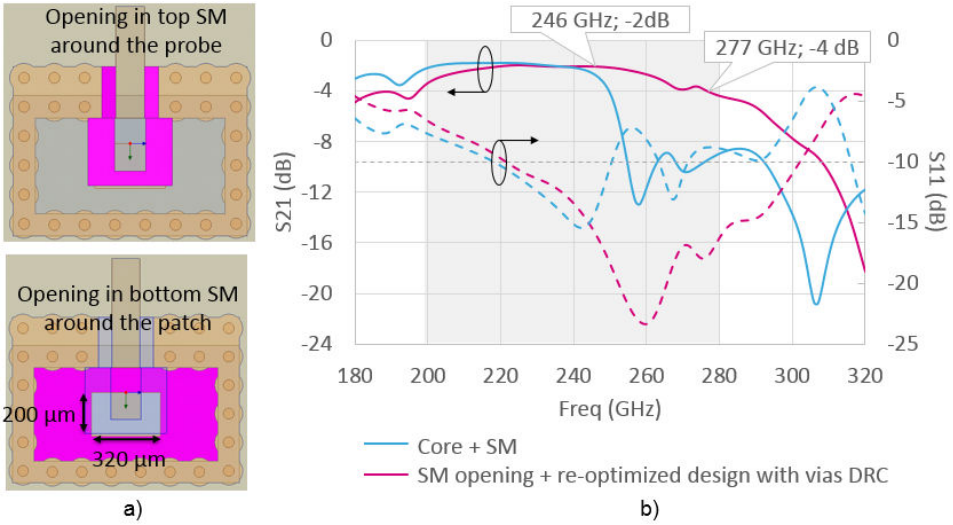

Figure III.44. (a) Top view of the optimized design with respect to the DRC, (b) resulting simulated $|S_{21}|$ and $|S_{11}|$.

An epoxy thermoset material is usually used as a molding to encapsulate the entire substrate and flip-chipped ICs to form an electrical enclosure which also serves as a protection from the outside environment. For our design to be compatible with such standard process, a molding layer was added on top of the substrate. This material features a high tanδ of 0.05 and a slightly higher permittivity ε_r=

3.6 (measured at low frequency), thus leading to a significant amount of energy confined inside this layer and an important increase of dielectric loss. As we can see in Figure III.45 (b), a 2dB increase of the insertion loss is noticed when the molding thickness is set to 100 µm on top of the transition. However, laser-etching a cavity inside the molding on top of the transition would help to reduce these losses and thus recover the initial $|S_{21}|$. This laser ablation process is actually used for standard Package-on-Package assembly processes and is therefore adequate for the targeted standard transition manufacturing.

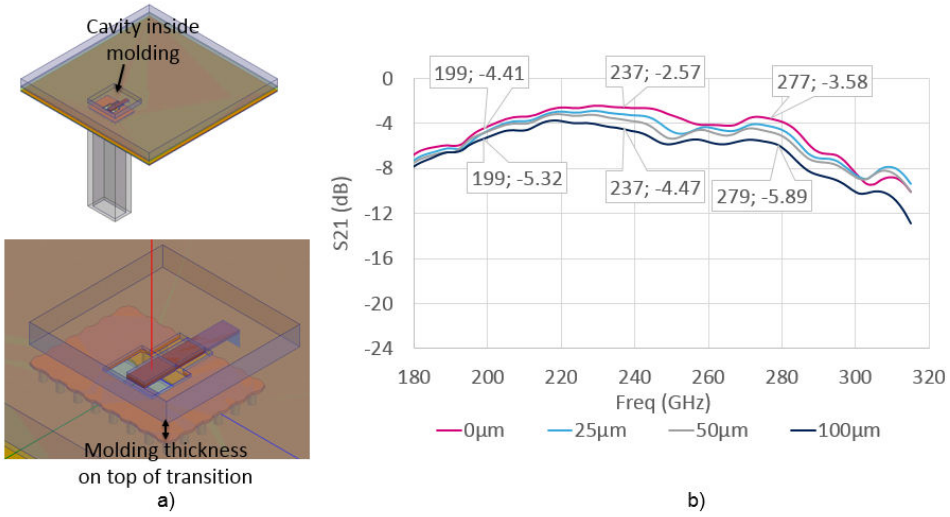

Figure III.45. (a) 3D view of the final transition design, and (b) $|S_{21}|$ as a function of the molding thickness on top of the transition versus frequency.

A first transition batch was prototyped in back-to-back configuration to proceed with measurements. The following Figure III.46 shows the metal traces at the top and bottom metal layers the prototype structure in HDI organic technology. In this configuration, the transitions are connected together with a microstrip line on M1 and dummies were added to M1 and M2 for copper balance.

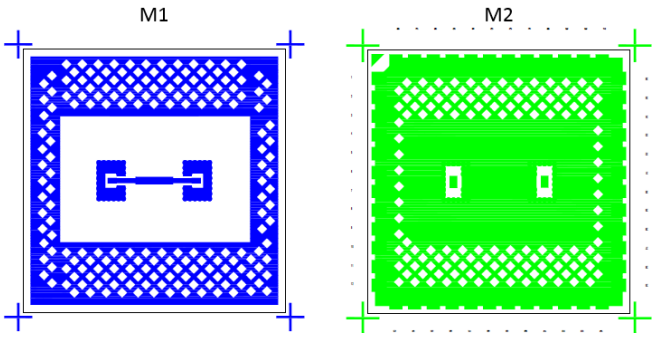

Figure III.46. Top view of Metal layers of the transition in back-to-back configuration.

A measurement campaign will be undertaken at the IEMN laboratory in Villeneuve d'Ascq in order to evaluate the performance of this transition in back-to-back configuration. Before proceeding with the transition measurement, a 3D printed calibration module integrating a unique WR3 waveguide was prototyped with the aim of calibrating the 3D-printed WR3 module that will be used in the back-to-back measurement set-up. The HFSS design of this structure is shown in Figure III.47 (a) and was fabricated using the Stereolithographic 3D-printed technique described in the next section. A photo of

the prototyped WR3 module is shown Figure III.47 (b) and will have to be copper-plated and measured first in order to assess the performance of this 3D-printing technology 200 GHz.

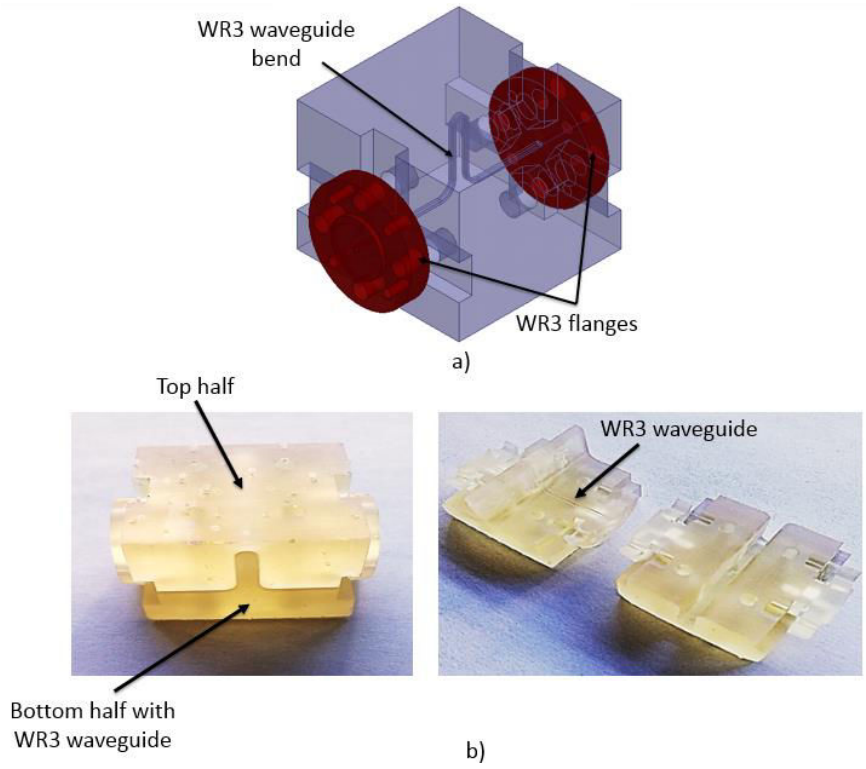

Figure III.47. (a) 3D View of the WR3 bend calibration module, (b) photos of the SLA 3D-printed module.

c. *Benchmark of vertical microstrip-to-waveguide transitions*

Table III.2 compares the transition simulated performance achieved in our work with the vertical transitions presented earlier. As we can see, the developed transition has the lowest simulated $|S_{21}|$ (-4 dB), even though it still addresses the 33% fractional BW mentioned in the specifications of the antenna system for the insertion loss. This limited transmission coefficient is mainly due to the poor coupling efficiency between the probe and the waveguide provided by this type of planar proximity coupled design when very large BWs are targeted. Similar performance was obtained with this type of transition at 76 GHz in [III.36]. However, this transition has one major advantage over the others, which is that it calls upon standard and simple fabrication processes.

Ref.	**Technology**	**Technique**	**Center frequency**	**Fractional BW**	**Minimum simulated $\|S_{21}\|$**
[III.33]	LTCC	Multi-layer hollow SIW	300 GHz	12%	-1.2 dB
[III.34]	Roger PCB	Gap waveguide	62 GHz	32%	-0.7 dB
[III.36]	PCB	Planar proximity coupling	76 GHz	31%	-3 dB
This work	HDI organic	Planar proximity coupling	240 GHz	33%	-4 dB

Table III.2. Vertical microstrip-to-waveguide transitions benchmarking.

IV. WR3.4 horn antenna fabricated in metal coated plastic 3D printing technology

A horn antenna was designed for the targeted frequency band of 200-300 GHz. This horn is meant to be assembled with the microstrip-to-waveguide transition according to the global system architecture shown in Figure III.40. The design of the horn was performed by Prof. Carlos Del Rio from the Institute of Smart Cities (at the University of Navarra in Spain). The prototyping of this antenna was realized using an additive manufacturing (AM) techniques which consists in 3D-printing. Indeed AM has become a good alternative to traditional manufacturing (usually subtractive), due to fast and low-cost prototyping services. Moreover, the continuously improving resolution of 3D-printing techniques makes it possible to manufacture designs with very low profiles or high complexity aimed for sub-mmW and THz applications, usually impossible to manufacture using conventional tooling.

1. WR3.4 horn design and simulation results

The horn shown in Figure III.48 was design so as to be compatible with low-cost 3D-printing fabrication process. For example, the minimum achievable wall thickness was 300 µm. With respect to this design rule constraints, careful attention was paid on the design of the corrugations in order to enable its feasibility in 3D printing while optimizing the BW of the horn and minimizing the side-lobes. A standard WR3.4 UG387-UM flange was integrated to the final design to attach the horn to a WR3.4 waveguide in the measurement set-up.

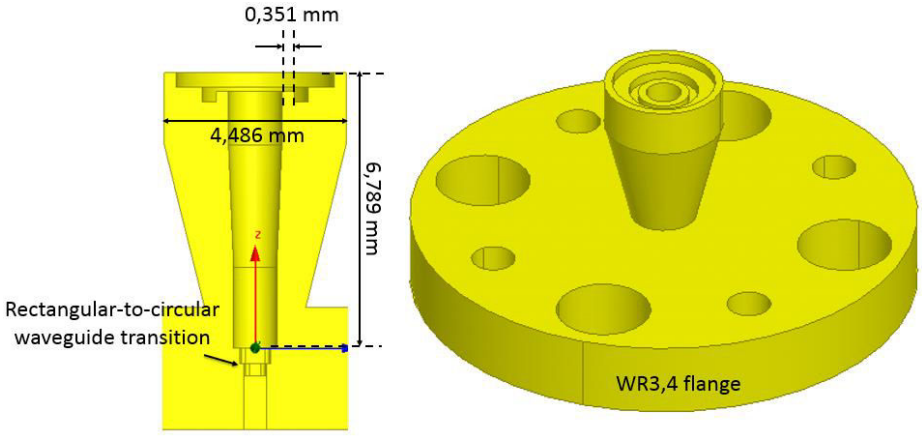

Figure III.48. Cross-sectional view of the 300 GHz horn antenna, and 3D view of the complete design.

The simulated E-plane and H-plane of the radiation patterns in Figure III.49 are fully stable across the 200-300 GHz BW with side-lobes below the -10 dB criteria and a main-lobe with a -10dB radiation taper of 50°.

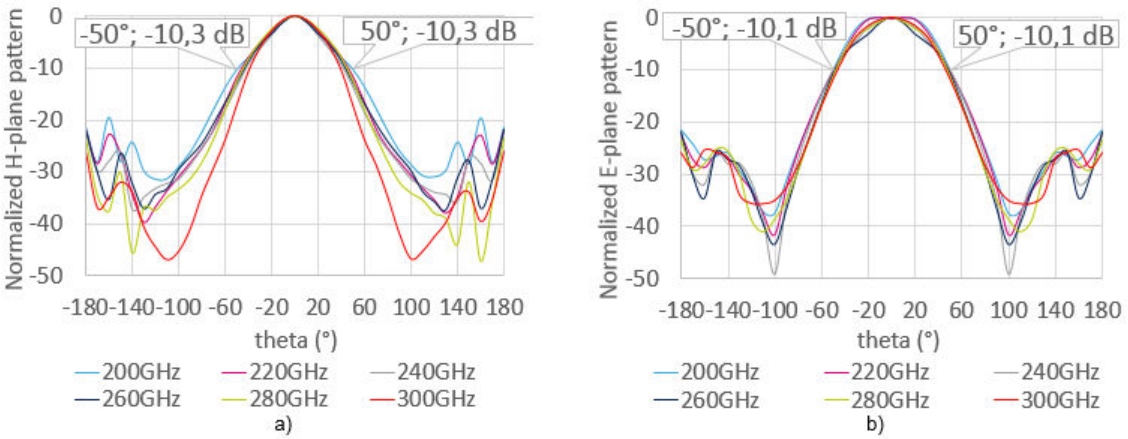

Figure III.49. Simulated radiation patterns between 200 GHz and 300 GHz on (a) the H plane and (b) the E plane of the corrugated horn.

In Figure III.50, we can see that a simulated broadside realized gain of at least 10.8 dB over a fractional BW of 40% is achieved with a gain peak of 12.7 dB at 250 GHz. Moreover, a $|S_{11}|$ below -20 dB is obtained between 200 GHz and 280 GHz (33% fractional BW).

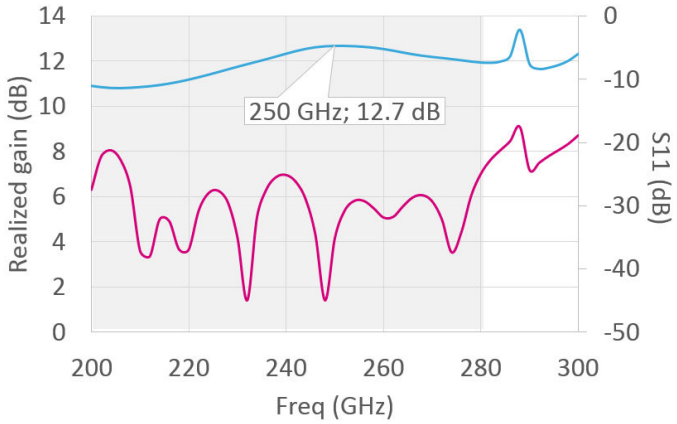

Figure III.50. Simulated broadside realized gain and $|S_{11}|$ of the corrugated horn from 200 GHz to 300 GHz.

2. Metal-coated 3D-printed plastic prototyping

AM consists in building an object by adding some material layer by layer. In order to do so, 3D-printers are reading computer-aided-design (CAD) files, in which the 3D-shape of the object is described. With the advent of affordable AM, different 3D-printing techniques have been developed and have already shown their potential for the fabrication of mmW 3D antennas [III.37], [III.38]. Indeed, equivalent antenna performance in terms of gain, radiation pattern and BW can be achieved, compared to traditional manufacturing like micromachining [III.38]. Furthermore, compactness, lightweight and design flexibility provided by AM are major benefits in the telecommunication market, which makes these fabrication processes very competitive for prototyping and medium volume production.

These AM techniques provide different levels of cost, design accuracy, surface roughness and different building materials. Therefore, 3D-printing methods must be chosen appropriately in order to comply with the antenna's sensitivity to fabrication tolerance and resolution. The selected 3D-printing technique for the horn prototyping was Stereolithography (SLA). This laser-based 3D-printing technique uses a laser beam to scan a surface inside a tank full of photosensitive liquid resin, thereby

solidifying the resin layer by layer until the entire object is created according to the process schematic shown in Figure III.51. SLA provides a very smooth surface and a resolution as good as 20 µm along the Z axis and down to 100 µm in the XY plane depending on the 3D-printing machine performance. A descent variety of photosensitive resins can be used by this process, giving access to different mechanical or dielectric properties. A horn prototype was realized using Formlabs' SLA Form2 3D printer [III.39], which functioning is described in Figure III.51 (a). However the horn that was used for measurements was fabricated by the supplier Swissto12, specialized in SLA 3D-printing and metal coating of RF wave-guided components and antenna systems [III.40]. The copper coating provided by Swissto12 is 2 to 3 µm thick which is much thicker than the skin depth at 240 GHz (0.13 µm). The fabricated Swissto12 horn is shown in Figure III.51 (b).

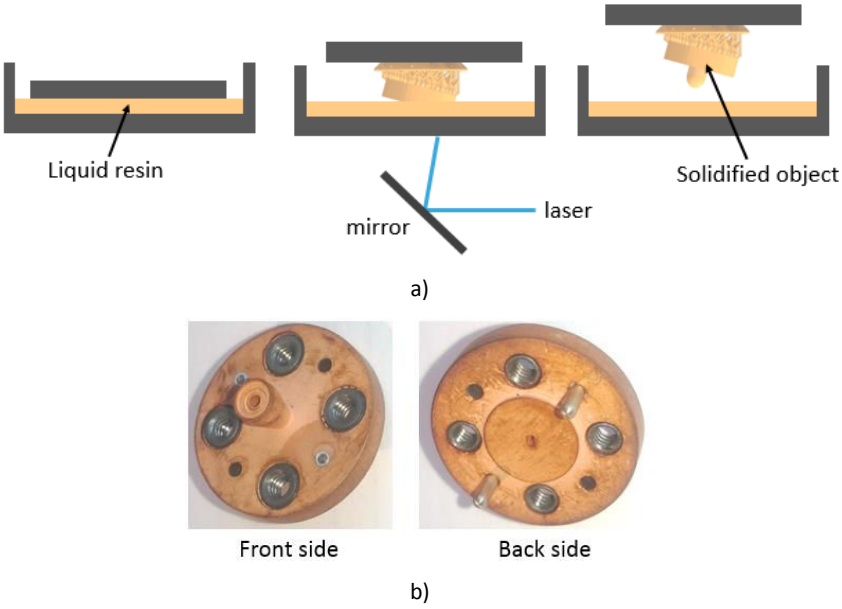

Figure III.51. (a) Schematic of the Form2 SLA 3D-printing functioning from Formlabs, and (b) photo of the 300 GHz horn prototyped by Swissto12.

3. 300 GHz 3D-printed corrugated horn measurement

a. Measurement bench description

The horn antenna (referred to as the AUT) was measured at the Institute of Smart Cities in Navarra. The antenna measurement bench uses a VNA connected to a 220-280 GHz VNA extender (VNAX) on the Tx and Rx side to generate and receive the sub-mmW signal as shown in Figure III.52 below. On the Tx side, a static commercial WR3 pyramidal horn (referred to as A_{meas}) is used as the measurement antenna. On the Rx side, the AUT connected to the second VNAX and fixated on a platform rotating around the Oz axis. This enables to measure the azimuthal radiation patterns (in the Oxy plane which will be referred to as the H plane). Measurements of plane H were realized with a distance of 30 cm between the AUT and A_{meas}.

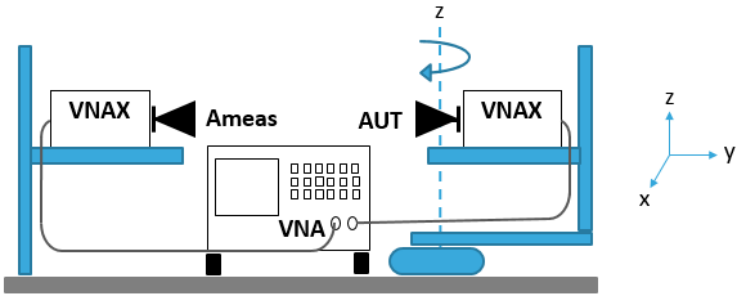

Figure III.52. Schematic of the Navarra antenna measurement bench.

b. Measurement results

As we can see in Figure III.53, the main-lobe of the radiation pattern in the H-plane *(a)* and E-plane *(b)* are stable with a Gaussian-like shape and a -10dB radiation taper between 40° and 50° as expected.

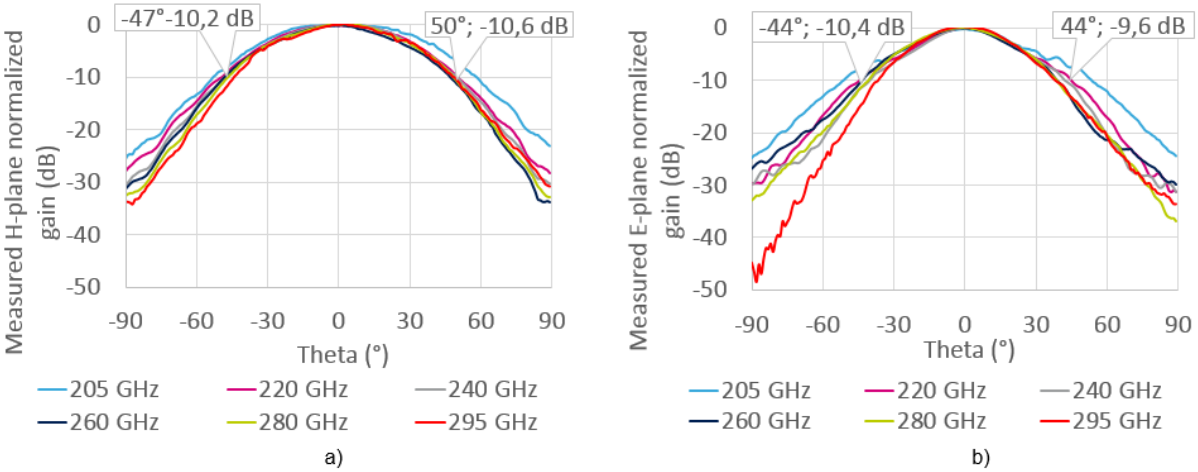

Figure III.53. (a) Measured H-plane and (b) E-plane normalized gain of the 300 GHz 3D-printed horn.

Moreover, a very good agreement between the measured and simulated normalized H-plane and E-plane gain is also achieved, as shown in Figure III.54 at 240 GHz. These promising results validate the use of SLA 3D-printing technique and metal coating for low-cost manufacturing of horn antennas up to 300 GHz.

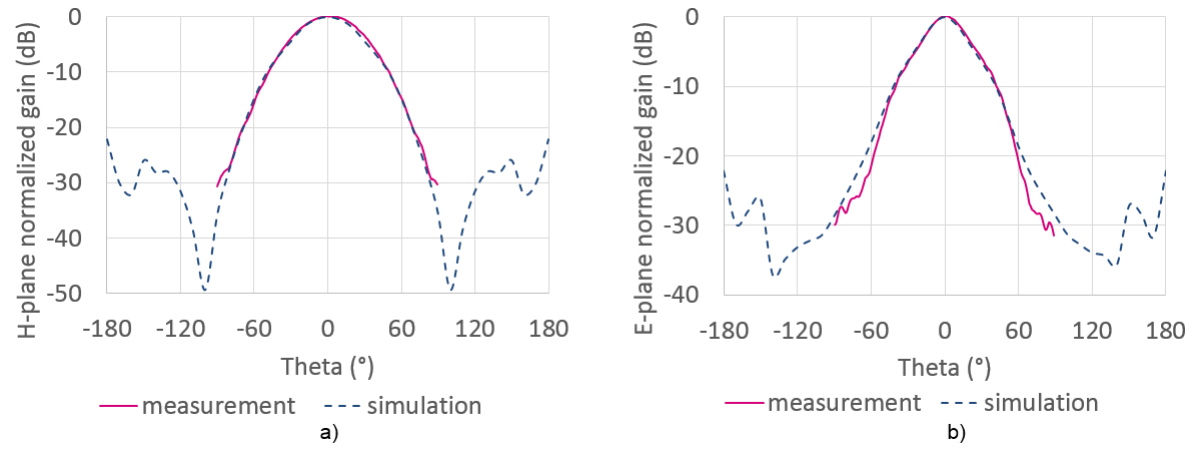

Figure III.54. Comparison between measured and simulated normalized gain in (a) the H-plane and (b) the E-plane of the 300 GHz 3D-printed horn at 240 GHz.

The measured gain in the broadside direction is shown in Figure III.55 (a) in comparison with the simulated gain as a function of the frequency. A gain from 11 dBi to 12.5 dBi is achieved between 210 GHz and 335 GHz with about ±1 dB measurement uncertainty, and a fair agreement with the simulated gain is obtained. As for the matching, a $|S_{11}|$ below -15 dB is achieved from 210 GHz up to ~315 GHz which is quite a similar BW as the one obtained in the simulation. However the overall measured $|S_{11}|$ level shown in Figure III.55 (b) is 5 dB to 10 dB higher than the simulated one between 210 GHz and 280 GHz. This is mainly due to fabrication defects of the rectangular-to-circular waveguide transition inside the horn, resulting in a slight degradation of the horn matching level. Knowing that -15 dB matching is still achieved, this discrepancy won't have a strong impact in a 50 ohm impedance environment.

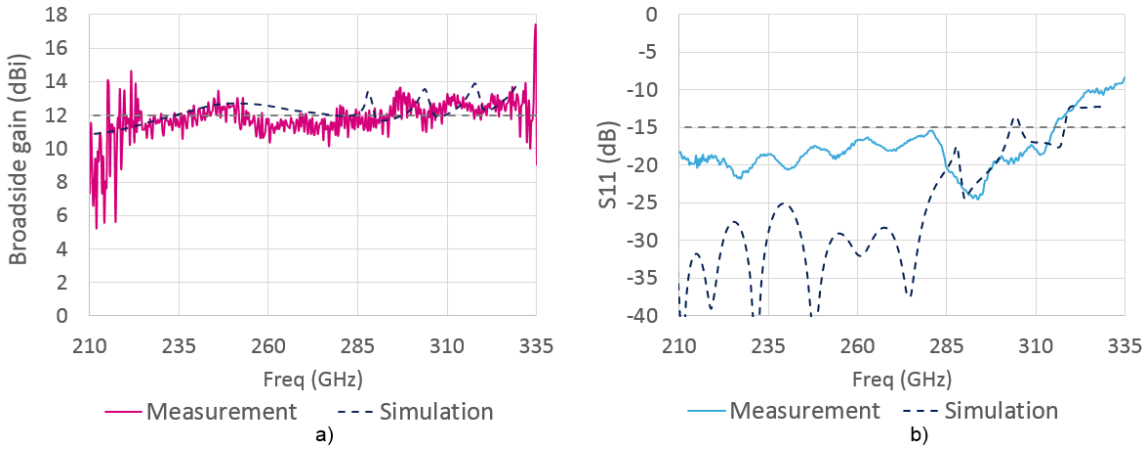

Figure III.55. Comparison between measured and simulated (a) broadside gain and (b) matching $|S_{11}|$ of the 300 GHz 3D-printed horn between 210 GHz and 335 GHz.

V. 240 GHz plastic lens using 3D printing technologies

The gain of integrated antennas is often insufficient for several meters point-to-point transmissions at mmW frequencies. To address this problem, a solution is to associate the mmW integrated antennas with quasi-optical antennas, like dielectric lenses, in order to reach medium gains around 20/25 dBi and thus higher transmitting/receiving ranges than with the AiP or the horn aalone [III.41]. In this work, an extended elliptical lens was chosen in order to properly collimate the radiation diagram of the feed source (AiP or horn) and extend the initial gain above 19 dBi. An estimation of the link budget was realized in the Introduction chapter for a wireless link based on a Silicon photonics Tx at 240 GHz. From this calculation, a gain level above 19 dBi would allow transmission distances of at least 10 cm, which would enable high-speed short distance range applications at sub-mmW/THz frequencies.

1. Elliptical extended lens operation and material proprieties

Based on geometric optics, it is possible to produce a parallel-oriented beam with an elliptical lens from a feed placed on the 1st focal point of the ellipse as shown in Figure III.56 (a). Such an elliptical lens was designed as a half ellipsoid with a small radius *a* and a big radius *b*, on top of a cylindrical extension with a height *l*. To achieve a collimated gain, the refractive index n_{lens} of the lens should be equal to the reverse eccentricity of the ellipse, $n_{lens} = 1/e = b/l$ (according to Snell-Descartes's law)

[III.21], and bigger than the reflective index of the environment (air), where *b* is calculated as followed for a specific *a* value:

$$b = \frac{a}{\sqrt{1-\varepsilon_r}} \tag{13}$$

Cost-effective lens prototyping was possible using 3D-printed techniques (cf. section III.5.c. below). Standard Acrylonitrile Butadiene Styrene (ABS) plastic was first used for the lens dielectric material, which contributes to cost effectiveness as it is used for most household-appliance packaging. With a dielectric constant of ~2.48 and tangent loss of ~0.01 measured up to 170 GHz by the European Space Agency, ABS plastic seems compatible with mmW applications. Indeed, ABS lens antennas have already been validated at 60 GHz and 120 GHz [III.41],[III.42]. Assessing its performance above 200 GHz represents an important aspect of this work. A second low-cost dielectric material consisting of a photosensitive resin was also used in order to evaluate its performance above 200 GHz as well. This resin, referred to as High Temperature (HT), exhibits a permittivity ε_r of 2.75 and a dielectric loss tanδ of 0.02 up to 140 GHz. The resulting dielectric loss inside the lens would therefore be doubled (3dB additional loss) compared to that of the ABS lens as it is noticed in Figure III.56.

To ensure maximum coupling between the feed and the lens, the lens's dimensions were optimized using ILASH software [III.43]. This software was developed by Jorge R. Costa, Carlos A. Fernandes and their team in a collaboration with the Superior Technical Institute of Lisbon associated with the University of Lisbon. This simulation software offers a relatively accurate lens design based on geometric optics + physical optics analysis method. The AiP feed and lens were co-designed to help reducing the amount of refracted rays responsible for side-lobes. This is realized by setting the AiP radiation diagram exhibiting a -10dB illumination taper at a subtended half-angle of about 50°, as requested in the AiP specifications (Figure III.56 (b)). The directivity and gain of an elliptical lens fabricated in ABS and HT are traced as a function of the diameter in the graph below. A diameter of 9 mm and a total height of 9.5 mm were chosen to achieve a gain over 20 dBi with both ABS and HT while maintaining a competitive size compared to Silicon lenses used with sub-mmW and THz sources based on III-V monolithic integrated antennas [III.44], [III.45].

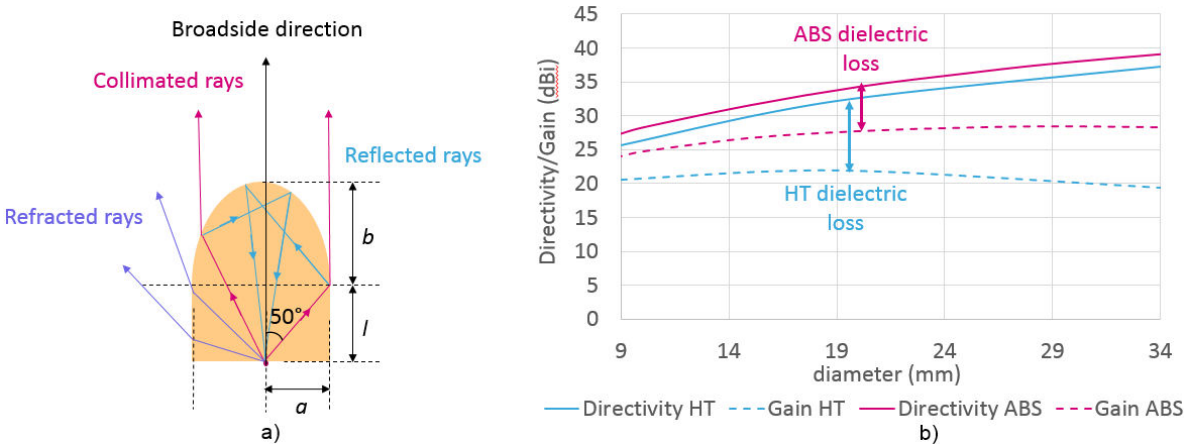

Figure III.56. (a) Elliptical lens schematic with refracted, collimated and reflected ray tracing, and (b) simulated directivity and gain of elliptical lenses in ABS plastic and HT resin fed by an ideal Gaussian feed at 240 GHz.

2. Simulation results of the AiP/lens-system

An HFSS simulation of the AiP associated to a 9 mm lens showed a broadside realized gain of ~23 dBi between 200 GHz and 280 GHz (Figure III.57 (b)). The realized gain of the AiP is increased by ~15 dB in the broadside direction. The E-field wave immersing from the focal point is collimated outside the lens as we can see in Figure III.50 (a).

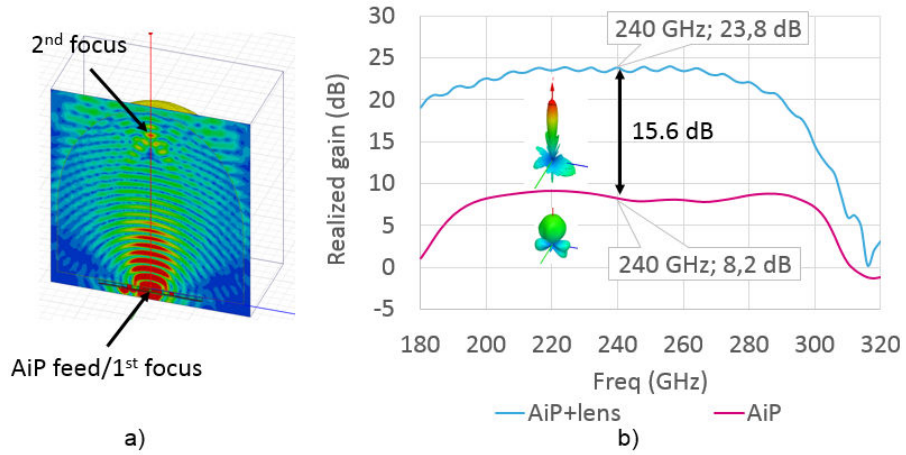

Figure III.57. (a) Simulated E-field wave propagation in and out of the lens in the E-plane cut, and (b) simulated broadside realized gain of the AiP alone and the AiP-lens system with their corresponding 3D radiation diagrams at 240 GHz.

The E-plane and H-plane of the AiP-lens radiation pattern were simulated with ILASH from 0° to 180° (Figure III.58). Assuming a quite symmetrical AiP radiation diagram, the E-plane of the AiP's radiation pattern was imported in ILASH and was rotated in a rotationally symmetry about the broadside direction axis to form the feed diagram. The simulated AiP-lens radiation patterns are shown in Figure III.58 and normalized side-lobes below -15dB were obtained with a -10dB radiation taper of about 6° on the H-plane and E-plane.

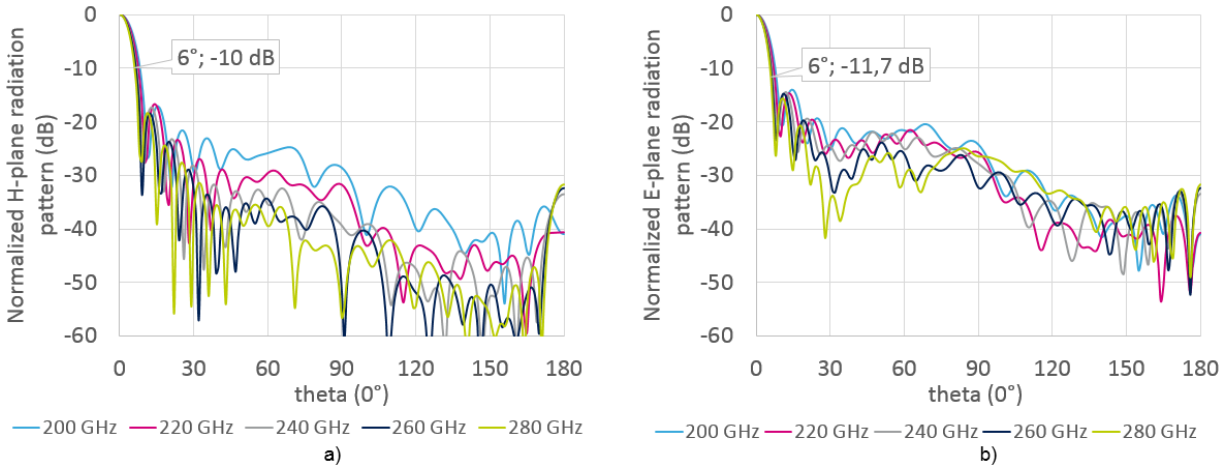

Figure III.58. Simulated radiation patterns of the AiP-lens system in the (a) H-plane and (b) E-plane.

3. 3D printed lenses prototype

Fused-Deposition-Modeling (FDM) is the most common and most affordable 3D-printing technique. It works by layering a molten plastic filament, which hardens immediately after extrusion from a hot nozzle. The process is shown in Figure III.59. This process uses thermoplastics and polymers such as

Nylon, Polycarbonate or ABS. The FDM process resolution is set by the diameter of the nozzle and can reach down to 100 µm along the Z axis and down to 200 µm in the XY plane. In this work, the HP Designjet 3D printer was used for the lens prototyping in ABS plastic and provided a resolution of ~250 µm.

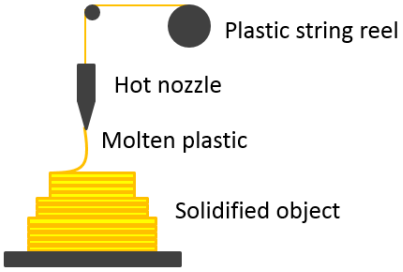

Figure III.59. Schematic view of an FDM 3D-printing process.

A first set of ABS-lenses was fabricated using FDM 3D-printing according to the design described in section III.2 allowing the AiP to be positioned at the bottom. A picture of the corresponding samples is shown in Figure III.60. However, it should be recalled that fabrication issues of the AiP prototypes with strongly disturbed E-field patterns resulted in a chaotic beam instead of the Gaussian-like beam required for optimum illumination of the lens. Lenses fabricated in HT resin (and thus using a different 3D-printing technique) will be investigated in future works in order to be able to correlate experimental performance with the simulated results.

Figure III.60. Picture of prototyped AiP-lens system.

4. Measurement results

a. Measured gain of AiP-lens system using ABS 9mm lens

As a consequence of the degraded AiP gain of the 1st prototyped batch, the AiP-lens gain is also degraded compared to the simulated gain. However, the lens seems to be working correctly by improving the gain throughout the 200-300 GHz band. Indeed, a gain improvement of 12 dB is achieved in the low frequency band (220-240 GHz) and 19 dB in the high frequency band (280-300 GHz), leading to a total broadside gain of ~16 dBi and ~13 dBi respectively.

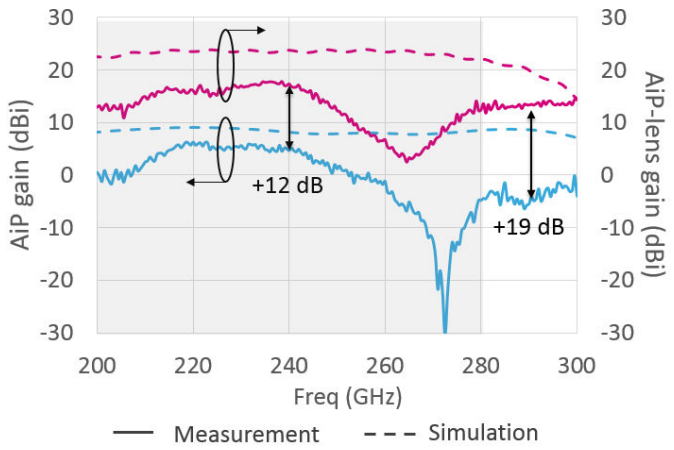

Figure III.61. Simulated and measured Broadside realized gain measurement of the AiP and AiP-lens system.

In the Figure III.62 (a), the collimating performance of the lens is clearly demonstrated with a narrow main lobe in the H-plane. Moreover, a fair enough radiation pattern can still be observed in the E-plane even though a very erratic radiation was obtained from the AiP's E-plane (Figure III.62 (b)). Indeed, the lens works by collecting the AiP's radiated energy not only from its main lobe at theta 0° but also from the side-lobes.

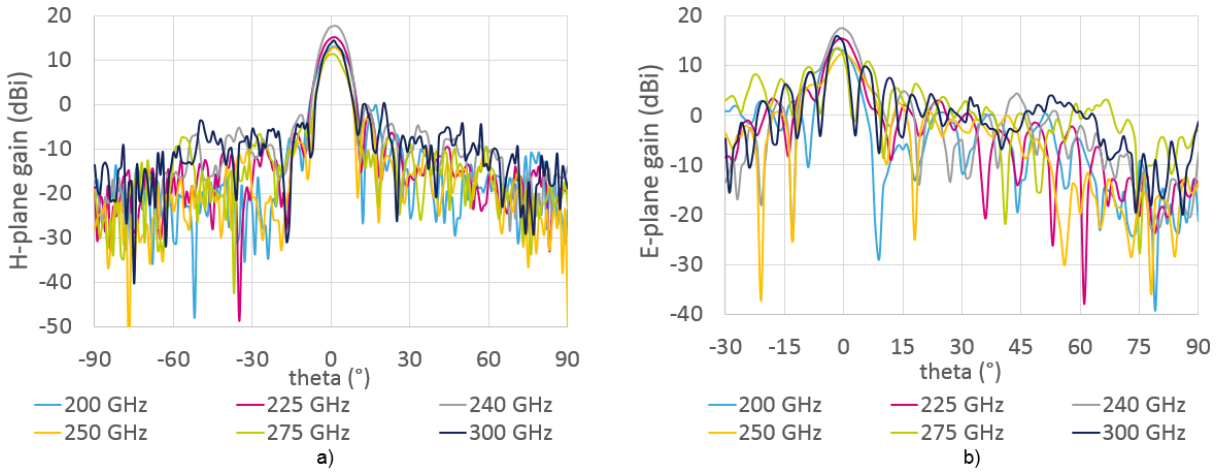

Figure III.62. Measured radiation patterns in the H-plane (left) and E-plane (right) of the AiP-lens system.

VI. 240 GHz Cassegrain antenna fabricated in metal-coated plastic 3D-printing technology

For sub-mmW and THz P2P transmissions at a couple of hundred meters like in fronthaul/backhaul links, the gain of the antenna should be high enough to overcome the high isotropic attenuation levels of free-space propagation. To illustrate this point, the FSPL of a 100 m link distance at 240 GHz would be:

$$FSPL = 10log\left[\left(\frac{4\pi d}{\lambda}\right)^2\right] = 120\ dB \quad (14)$$

Quasi-optic antennas such as reflectors are usually selected for this purpose as the signal coming from the primary feed is directly collimated by the reflector through air. Therefore, dielectric losses are much lower than those of a dielectric lens when the antenna diameter increases, thereby enabling

to achieve much higher gains. In a more complex design than a simple reflector, a Cassegrain antenna has been selected in this work. It uses a secondary reflector to re-direct the signal (originating from the feed) to the main reflector. In order to enable link distances of at least 100 m, a budget link evaluation for a 240 GHz wireless link based on realistic available Silicon photonics Tx and Silicon solid-state Rx shows a required antenna gain of at least 49 dBi. As the Cassegrain behavior can be easily predicted with geometrical-optics, it becomes extremely easy to dimension the antenna depending on the targeted gain. However, one must keep in mind that this analytical approach doesn't take into account diffraction effects that may occur at the edge of the main and sub reflectors. Figure III.63 shows an estimation of the broadside gain as a function of the antenna diameter for different antenna efficiencies. Assuming an efficiency of 50%, the main reflector's diameter D_M can be calculated as followed:

$$D_M = \sqrt{\frac{G\lambda^2}{\eta\pi^2}} = 21.35\ cm \tag{15}$$

Where, G is the linear gain of the Cassegrain antenna and η the overall Cassegrain antenna efficiency. This efficiency depends on various factors among which we can note:

- the aperture taper efficiency which denotes if the reflector is properly illuminated,
- the spillover efficiency which quantifies the amount of energy that spills over the edge of the reflector,
- the aperture blockage which quantifies the amount of energy blocked by the shade of the sub reflector superimposed on the main reflector.

For cost-effectiveness, SLA 3D-printing and final metal coating were also selected for the fabrication of this Cassegrain antenna and the 300 GHz 3D-printed horn could be used as the primary feed.

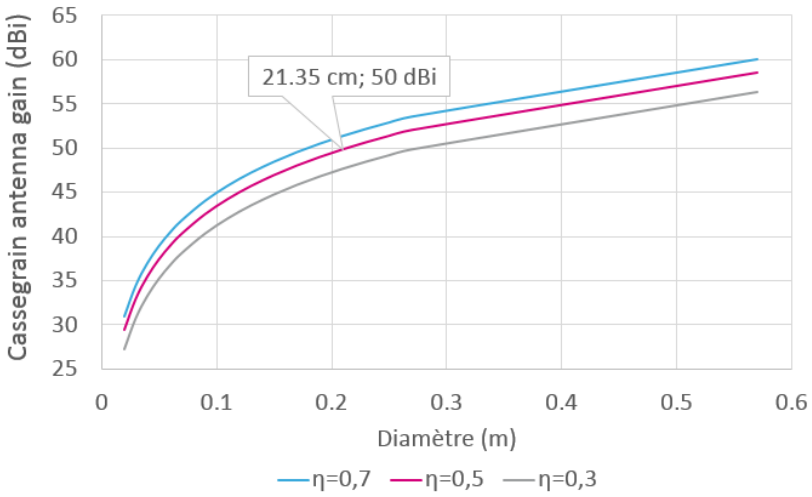

Figure III.63. Analytic broadside gain of Cassegrain antenna as a function of the main reflector's diameter for different antenna efficiencies.

1. Cassegrain design and simulation results

In a Cassegrain antenna design, the phase-center of the horn-feed is positioned at the focal point of a hyperbolic sub-reflector. The sub-reflector's 2nd focal point corresponds to the parabolic main-reflector's 1st focal point so that the signal reflected by the main-reflector is efficiently collimated. In order to avoid having to add support struts to the Cassegrain design, the feed is directly positioned at

the center of the main reflector, referred to as the apex (as shown in Figure III.64). As a result, the Cassegrain antenna is less fragile and its total height is reduced. Moreover, by placing the horn at the apex, we avoid having to use an extended WR3 waveguide to feed the horn. Thus no additional waveguide loss are encountered. This optimization aspect is particularly important when considering 3D-printing techniques for prototyping, where the surface smoothness and fabrication precisions can strongly impact on the final design dimensions and thus its frequency response above 200 GHz.

Based on equation systems given in paper [III.46], the antenna's dimensioning was defined according to several geometrical parameters among which the known parameters are the following:

- Feed horn phase center at the apex
- Main-reflector diameter D_M of 21.35 cm for a gain of 50 dBi and an efficiency of 0.5
- Horn -10dB illumination taper of ~50°
- Main-reflector focus to main diameter ratio (F/D_M) equals to 0.35 for a main-reflector that is not too deep nor too flat.

From these values, we were able to compute the following unknown parameters of the Cassegrain antenna:

- Sub-reflector diameter D_S of 9.74 cm leading to a blockage efficiency (D_S/D_M) of 84% which corresponds to 0.75 dB additional loss (negligible compared to the measurement uncertainties)
- Sub-reflector positioning L_S=4.95 cm away from the main-reflector
- Cassegrain total height L_T=5.8 cm.

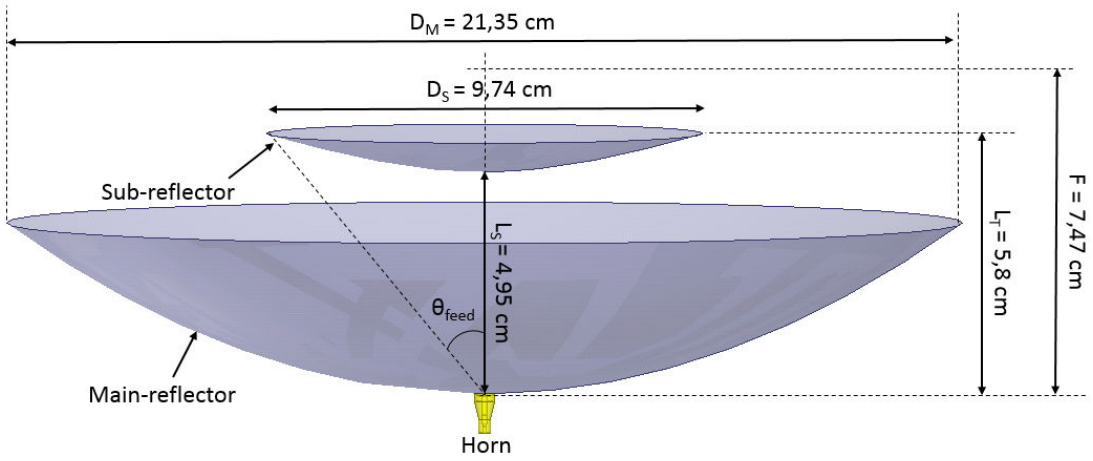

Figure III.64. HFSS schematic of the Cassegrain antenna design with the horn feed at the main reflector's apex.

Because the antenna's electrical size was bigger that 210*λ at 300 GHz, the simulation of the Cassegrain requires specific numerical methods. Altair's electromagnetic simulation from FEKO software was used in order to benefit from hybridization possibilities between different numerical methods to reduce the time and memory space needed for the simulation execution. In this approach, the horn and the sub-reflector were simulated together using the Multi-level Fast Multipole Method (MLFMM) numerical method to generate surface modes. The surface mode file was imported into the main reflector simulation to form the feed illuminating the reflector. The Large Element Physical Optics (LE-PO) numerical method was used for this second simulation in order to retrieve the gain of the complete Cassegrain antenna. A broadside realized gain of 52 dBi was finally simulated at 240 GHz,

with side-lobes in the H-plane and E-plane appearing 17 dB and 32 dB below the broadside gain respectively (Figure III.65).

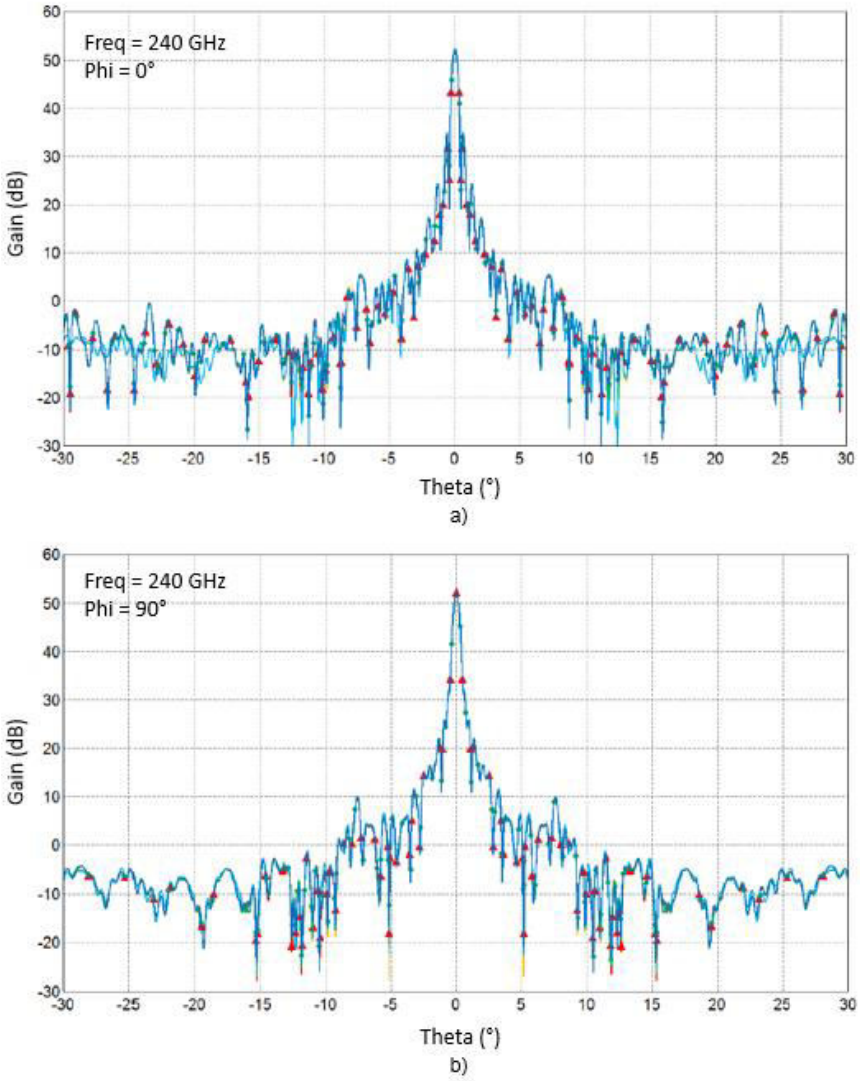

Figure III.65. Simulated gain of the Cassegrain antenna at 240 GHz in (a) the H-plane and (b) the E-plane.

2. 3D-printed plastic prototyping

This 50 dBi Cassegrain was prototyped by the supplier INITIAL using the SLA 3D-printing technique with an ABS-like material as shown in Figure III.66. This material was characterized with the Polytech'Lab antenna bench [III.47] at 140 GHz and a dielectric constant ε_r of 3.48 and tan(δ) of 0.025 were retrieved. This Cassegrain antenna will then be metal coated in order to enable its use and proceed with an experimental evaluation of its performance.

Figure III.66. Prototyped Cassegrain antenna (without metal surface coating).

VII. Conclusion

In this chapter we first laid out the state-of-the-art integrated antennas in the sub-mmW frequency band. A strong tendency to monolithically integrate the antenna with electrical and photonic components on the semiconductor substrate was noticed. Such designs have however limited performance due to electrical properties of considered semiconductor materials and integration losses. Tackling this issue, several techniques like cavity-backed antennas or dielectric lens topped antennas are often used as a way to increase the integrated antenna's performance. Despite some decent performance achievements, these techniques do not comply with industrial manufacturing constraints. To enable high-volume production, our approach was to use low-cost and low loss HDI organic substrate packaging technology to develop two different types of antenna-solution working between 200 GHz and 280 GHz: a 2x1 aperture coupled patch antenna (ACPA) and a microstrip-to-waveguide transition, the later meant to be connected to a compact THz horn.

The first antenna solution was integrated in a standard 1+2+1 dielectric build-up with a core thickness of 100 µm. The ACPA design was chosen for its wide frequency band obtained from resonance's coupling between the slot and the patch. A grounded metal cavity surrounding the patch was also added to control unwanted surface waves propagating in the substrate thereby enhancing broadside realized gain and BW. Finally a 2x1 patch array in the H-plane of the patch allows to shape up the radiation diagram for a more Gaussian-like beam. Taking into account the design constraints of the BGA HDI technology in organic substrate has proven to be challenging at such high frequency due to the very small dimensions for the ACPA and the metal cavity. A simulated final antenna gain of 8 dBi was achieved between 200 GHz and 300 GHz which corresponds to an extremely wide fractional frequency BW of 40%. Performance measurements of antenna prototypes were undertaken and revealed significant fabrication discrepancies within the antenna design due to manufacturing issues. Above 200 GHz, these fabrication inaccuracies have a great impact on the antenna's frequency behavior showing a deteriorated gain and radiation diagram.

The second antenna consists of a planar proximity coupled microstrip-to-waveguide transition connected to a THz horn. This transition was designed within a single dielectric layer in HDI organic technology. This very simple transition has the advantage of being compatible with industrial fabrication process in semi-additive technology and offers an easy assembly strategy with the horn antenna. A transmission coefficient trade-off was however noticed, partly due to inefficient coupling between the microstrip quasi-TEM mode and the waveguide TE_{01} mode. With respect to the design constraints, a simulated final transmission coefficient of about -4 dB was achieved between 200 GHz

and 280 GHz (33% fraction BW). A back-to-back configuration was prototyped in order to measure the THz performance of the transition. A dedicated measurement set-up integrating a WR3 waveguide input and output was therefore developed in 3D-printing technology and next step consists in surface metal coating in order to proceed with measurements.

The THz horn was simulated and optimized between 200 GHz and 300 GHz in order to achieve 12 dBi over the entire BW while maintaining a very compact size. To do so, corrugations were integrated inside the horn, leading to a final horn height and diameter below 7 mm and 5 mm respectively. Horn prototypes were fabricated using cost-effective means of production such as SLA 3D-printing technique and metal coating. A broadside gain of 12 dBi was measured between 200 GHz and 300 GHz, and Gaussian-like radiation patterns in the E and H planes were achieved in simulations and measurements. These good performance achievements have demonstrated that 3D-printing is becoming appropriate for high-performance and high-frequency THz antenna systems.

In order to increase the gain of the ACPA above 20 dBi between 200 GHz and 300 GHz, a dielectric elliptical extended lens was designed. A fast geometrical-optics and physical-optics analysis method was used to dimension the lens, and a co-design between the integrated ACPA and the lens was followed so as to maximize the coupling between the two elements. With a diameter of 9 mm, a compact antenna-lens system was achieved. A simulated gain enhancement of about 15 dBi was achieved throughout the band of interest. 3D-printing using FDM and SLA techniques were used to fabricate lenses with different diameters in order to evaluate the gain level and its variation depending on the diameter. Measurements have shown fair radiation patterns and 12 dB to 19 dB gain enhancement thanks to the collimating behavior of the 9 mm ABS lens from 200 GHz to 300 GHz.

Finally, for point-to-point transmissions requiring higher gain levels, a 50 dBi Cassegrain antenna was designed in order to target distances above 100 m. A very simple analytic method based on geometrical-optics was used to dimension the Cassegrain, resulting in a final antenna diameter of 21.35 cm and height of 5.8 cm. A horn feed was placed at the apex of the main reflector so as to promote a simple and less fragile overall antenna system and an easy assembly strategy. As well as for the lens and horn antenna, fast prototyping was possible using SLA 3D-printing and metal coating is still to be realized in order to proceed with measurements.

Reference

[III.1] N. T. Yardimci and M. Jarrahi, "Telecommunication compatible terahertz emitters based on plasmonic nano-antenna arrays," *IEEE Antennas and Propagation Society International Symposium, (APSURSI)*, pp. 1187–1188, Fajardo, Puerto Rico, 2016.

[III.2] D. M. Pozar, "Considerations for Millimeter Wave Printed Antennas," *IEEE Transactions on Antennas and Propagation*, vol. 31, no. 5, pp. 740–747, 1983.

[III.3] R. Han *et al.*, "A 280-GHz Schottky diode detector in 130-nm digital CMOS," *IEEE Journal of Solid-State Circuits*, vol. 46, no. 11, pp. 2602–2612, 2011.

[III.4] D. Hou, Y. Xiong, W. Hong, W. L. Goh, and J. Chen, "Silicon-based On-chip Antenna Design for Millimeter-wave / THz Applications," *IEEE Electrical Design of Advanced Packaging and Systems Symposium (EDAPS)*, pp. 130–133, Hanzhou, China, 2011.

[III.5] X. D. Deng, Y. Li, C. Liu, W. Wu, and Y. Z. Xiong, "340 GHz On-Chip 3-D Antenna with 10 dBi Gain and 80% Radiation Efficiency," *IEEE Transactions on Terahertz Science and Technology*, vol. 5, no. 4, pp. 619–627, 2015.

[III.6] W. H. Syed *et al.*, "Design, Fabrication, and Measurements of a 0.3 THz On-Chip Double Slot Antenna Enhanced by Artificial Dielectrics," *IEEE Transactions on Terahertz Science and Technology*, vol. 5, no. 2, pp. 288–298, 2015.

[III.7] D. Cavallo, W. H. Syed, and A. Neto, "Artificial dielectric enabled antennas for high frequency radiation from integrated circuits," *IEEE European Conference on Antennas and Propagation (EUCAP)*, pp. 1626–1628, Paris, France, 2017.

[III.8] J. Grzyb, P. R. Vazquez, N. Sarmah, B. Heinemann, and U. R. Pfeiffer, "High Data-Rate Communication Link at 240 GHz with On-Chip Antenna-Integrated Tx and Receiver Modules in SiGe HBT Technology," *IEEE European Conference on Antennas and Propagation (EuCAP)*, pp. 1369–1373, Paris, France, 2017.

[III.9] Y. Yan *et al.*, "Monolithically integrated 200-GHz double-slot antenna and resistive mixers in a GaAs-mHEMT MMIC process," *IEEE Transactions on Microwave Theory and Techniques*, vol. 59, no. 10 PART 1, pp. 2494–2503, 2011.

[III.10] N. Sarmah *et al.*, "A fully integrated 240-GHz direct-conversion quadrature Tx and receiver chipset in SiGe technology," *IEEE Transactions on Microwave Theory and Techniques*, vol. 64, no. 2, pp. 562–574, 2016.

[III.11] H. T. Zhu, Q. Xue, J. N. Hui, and S. W. Pang, "A 750-1000 GHz H-Plane Dielectric Horn Based on Silicon Technology," *IEEE Transactions on Antennas and Propagation*, vol. 64, no. 12, pp. 5074–5083, 2016.

[III.12] T. Tajima, H. Song, K. Ajito, M. Yaita, and N. Kukutsu, "300-GHz Step-Profiled Corrugated Horn Antennas Integrated in LTCC," *IEEE Transactions on Antennas and Propagation*, vol. 62, no. 11, pp. 5437–5444, 2014.

[III.13] T. Tajima *et al.*, "300-GHz LTCC horn antennas based on antenna-in-package technology," *IEEE European Microwave Conference (EuMC),* pp. 231–234, Nuremberg, Germany, 2013.

[III.14] W. Hong, K. H. Baek, and A. Goudelev, "Grid assembly-free 60-GHz antenna module embedded

in FR-4 transceiver carrier board," *IEEE Transactions on Antennas and Propagation*, vol. 61, no. 4, pp. 1573–1580, 2013.

[III.15] Y. P. Zhang, M. Sun, K. M. Chua, L. L. Wai, D. Liu, and B. P. Gaucher, "Antenna-in-package in LTCC for 60-GHz radio," *IEEE International workshop on Antenna Technology: Small and Smart Antennas Metamaterials and Applications (iWAT)*, pp. 279–282, Cambridge, UK, 2007.

[III.16] D. Titz, F. Ferrero, C. Luxey, and G. Jacquemod, "Antenna-in-Package Using PCB and IPD Technologies for 60 GHz Applications," *IEEE European Conference on Antennas and Propagation (EuCAP),* pp. 1–4, Prague, Czech Republic, 2012.

[III.17] S. Liao and Q. Xue, "Dual polarized planar aperture antenna on LTCC for 60-GHz antenna-in-package applications," *IEEE Transactions on Antennas and Propagation*, vol. 65, no. 1, pp. 63–70, 2017.

[III.18] J. Xu, Z. N. Chen, and X. Qing, "270-GHz LTCC-integrated strip-loaded linearly polarized radial line slot array antenna," *IEEE Transactions on Antennas and Propagation*, vol. 61, no. 4, pp. 1794–1801, 2013.

[III.19] R. Pilard *et al.*, "HDI organic technology integrating built-in antennas dedicated to 60 GHz SiP solution," *IEEE International Symposium on Antennas and Propagation Society, (APS)*, pp. 2–3, Chicago, USA, 2012.

[III.20] A. Bisognin *et al.*, "Ball Grid Array Module With Integrated Shaped Lens for 5G Backhaul/Fronthaul Communications in F-Band," *IEEE Transactions on Antennas and Propagation*, vol. 65, no. 12, pp.6380-6394, 2017.

[III.21] M. A. Matin, "Review on Millimeter Wave Antennas- Potential Candidate for 5G Enabled Applications," *Advanced Electromagnetics*, vol. 5, no. 3, 2016.

[III.22] A. S. Aishah, P. Putra, and M. Campus, "60 GHz Milimeter-Wave Antennas for Point-to-Point 5G Communication System," *MATEC Web of Conferences*, vol. 140, p. 01006, 2017.

[III.23] A. S. Thakur and G. Singh, "Rectangular Microstirp Patch Antenna Design at THz Frequency for Short Distance Wireless Communication Systems Rectangular Microstirp Patch Antenna Design at THz Frequency for Short Distance Wireless Communication Systems," *Journal of Infrared, Millimeter, and Terahertz Waves*, vol. 30, no. 1, pp. 1–8, 2009.

[III.24] I. Fitri, "A New Gridded Parasitic Patch Stacked Microstrip Antenna for Enhanced Wide Bandwidth in 60 GHz Band," *IEEE International Conference on Broadband Communication, Wireless Sensors and Powering (BCWSP)*, pp. 1–4, Jakarta, Indonesia, 2017.

[III.25] T. H. Jang, H. Y. Kim, I. S. Song, C. J. Lee, J. H. Lee, and C. S. Park, "A Wideband Aperture Efficient 60-GHz Series-Fed E-Shaped Patch Antenna Array With Copolarized Parasitic Patches," *IEEE Transactions on Antennas and Propagation*, vol. 64, no. 12, pp. 5518–5521, 2016.

[III.26] X. Zhang, L. Zhu, and Q. Sen Wu, "Sidelobe-Reduced and Gain-Enhanced Square Patch Antennas with Adjustable Beamwidth under TM03 Mode Operation," *IEEE Transactions on Antennas and Propagation*, vol. 66, no. 4, pp. 1704–1713, 2018.

[III.27] A. Bisognin, "Evaluation de technologies organiques faibles pertes et d'impression plastique 3D afin de contribuer au développement de solutions antennaires innovantes dans la bande 60 GHz – 140GHz," *PhD dissertation*, University of Nice Sophia Antipolis, 2015.

[III.28] A. Bisognin *et al.*, "Broadband Circularly Polarized Aperture-Coupled Microstrip Antenna in HDI technology for WiGig applications," *IEEE European Conference on Antennas and Propagation (EuCAP)*, Lisbon, Portugal, 2015.

[III.29] H. Lu *et al.*, “Design, Modeling, Fabrication and Characterization of 2-5-µm Redistribution Layer Traces by Advanced Semiadditive Processes on Low-Cost Panel-Based Glass Interposers,” *IEEE Transactions on Components, Packaging and Manufacturing Technology*, vol. 6, no. 6, pp. 959–967, 2016.

[III.30] H. Gulan *et al.*, “Probe based antenna measurements up to 325 GHz for upcoming millimeter-wave applications,” *International Workshop on Antenna Technology, iWAT 2013*, no. 1, pp. 228–231, Karlsruhe, Germany, 2013.

[III.31] C. a. Balanis, “Antenna Theory Analysis and Design Third Edition,” *MICROSTRIP ANTENNAS, third edition, John wiley & sons*, 2005.

[III.32] A. Mozharovskiy, et al. "Wideband tapered antipodal fin-line waveguide-to-microstrip transition for E-band applications." *IEEE European Microwave Conference (EuMC),* pp. 1187-1190, Nuremberg, Germany, 2013.

[III.33] T. Ta, H. Song, and M. Yaita, “300-GHz Microstrip-to-Waveguide Transition Integrated in LTCC,” *IEEE MTT-S International Microwave Symposium (IMS),* pp. 8–11, Tampa, USA, 2014.

[III.34] A. A. Brazález, E. Rajo-iglesias, and P. Kildal, “Design of Millimeter-Wave Wideband Gap Waveguide Transitions Considering Integration into the Antenna System,” *IEEE European Conference on Antennas and Propagation (EuCAP),* pp. 13–17, Lisbon, Portugal, 2015.

[III.35] H. Iizuka, T. Watanabe, K. Sato, and K. Nishikawa, “Millimeter-wave microstrip line to waveguide transition fabricated on a single layer dielectric substrate,” *IEICE Transactions on Communications*, vol. 85, no. 6, pp. 1169–1177, 2002.

[III.36] K. Seo, “Planar Microstrip-To-Waveguide Transition in Millimeter-Wave Band,” *Advancement in Microstrip Antennas with Recent Applications*, InTech, 2013.

[III.37] M. Liang, J. Wu, X. Yu, and H. Xin, “3D printing technology for RF and THz antennas,” *IEEE International Symposium on Antennas and Propagation (ISAP)*, pp. 536–537, Okinawa, Japan, 2016.

[III.38] A. Bisognin *et al.*, “Comparizon of 3D printed Plastic and micromachined Teflon Lenses for WiGig modules,” *IEEE Antennas and Propagation Society International Symposium (APSURSI)*, pp. 109–110, Memphis, USA, 2014.

[III.39] “Formlabs.” [Online]. Available: https://formlabs.com/fr/3d-printers/form-2/.

[III.40] A. Von Bieren, E. De Rijk, J. P. Ansermet, and A. Macor, “Monolithic metal-coated plastic components for mm-wave applications,” *IEEE International Conference on Infrared, Millimeter, and Terahertz Waves (IRMMW-THz)*, pp. 1-2, Tucson, USA, 2014.

[III.41] A. Bisognin *et al.*, “3D printed plastic 60 GHz lens: Enabling innovative millimeter wave antenna solution and system,” *IEEE MTT-S International Microwave Symposium (IMS)*, pp. 6–9, Tampa, USA, 2014.

[III.42] A. Bisognin *et al.*, “A 120 GHz 3D-printed plastic elliptical lens antenna with an IPD patch antenna source,” *IEEE International Conference on Ultra-Wideband, (ICUWB)*, pp. 171–174, Paris, France, 2014.

[III.43] E. Lima, J. R. Costa, M. G. Silveirinha, and C. A. Fernandes, “ILASH – Software Tool for the Design of Integrated Lens Antennas,” *IEEE International Symposium on Antennas and Propagation Society (APS),* pp. 3–6, San Diego, USA, 2008.

[III.44] T. Tajima, H. J. Song, and M. Yaita, “Compact THz LTCC Receiver Module for 300 GHz Wireless Communications,” *IEEE Microwave and Wireless Components Letters*, vol. 26, no. 4, pp. 291–

293, 2016.

[III.45] A. Wakatsuki, Y. Muramoto, and T. Ishibashi, “Development of terahertz-wave photomixer module using a uni-traveling-carrier photodiode,” *NTT Technical Review*, vol. 10, no. 2, 2012.

[III.46] T. Milligan and C. Granet, “Designing axially symmetric Cassegrain or Gregorian dual-reflector antennas from combinations of prescribed geometric parameters, part 2: minimum blockage condition while taking into account the Phas-center of the feed,” *IEEE Antennas and Propagation Magazine*, vol. 40, no. 3, pp. 82–87, 1998.

[III.47] H. Gulan, C. Luxey, and D. Titz, “Mm-Wave Sub-mm-Wave Antenna Measurement,” 2015.

Chapter 4: 300 GHz wireless link demonstration using a transmitter integrated in Silicon Photonics technology

Table of Contents

Chapter 4: 300 GHz wireless link demonstration using a transmitter integrated in Silicon Photonics technology

Towards the development of low-cost wireless systems exceeding 10 Gb/s, a wireless communication demonstration is an important step in order to assess the achievable maximum data-rate (and frequency bandwidth) of industrial Silicon Photonics blocks. To do so, a THz wireless link based on a Silicon Photonics Tx using the PIC25G chips presented in chapter 2 was tested with 1550-nm telecom-based optical sources and a Schottky diode direct detection Rx. The BER was measured over data-rates ranging from 10 Gb/s up to 25 Gb/ using OOK modulation scheme. This digital signal based on amplitude modulations is particularly attractive for low-cost Silicon Photonics-based transceivers, as they are cheaper to implement and requiring less complex Rx equipment for direct detection. The measurements have been conducted at the IEMN laboratory of the University of Lille. This chapter presents a detailed description of this THz wireless demonstration and associated BER measurement results using Silicon Photonics photodiodes for the Tx photomixer. We will also demonstrate how the BW of the Tx measurement system can be a limiting factor in the evaluation of the maximum achievable data-rate of the Silicon Photonics chip. Finally, we will discuss possible perspectives from a benchmark of today's state-of-the-art wireless THz links.

I. Experimental set-up description for single carrier data transmission

1. Description of the global THz link set-up

The experimental setup used to evaluate the indoor 300 GHz wireless link based on a photonics Tx is shown above, in Figure IV.1. The setup can be divided into two parts: the optical subsystem that handles the optical signal through optical fibers (in blue) and the electrical subsystem that handles the baseband electrical signal through 40 GHz coaxial cables (in pink).

In the optical subsystem, two external cavity lasers (ECL) create a frequency beat note at a carrier frequency of 300 GHz by heterodyning two wavelengths λ_1 and λ_2 set around 1550 nm with a resolution of 12.5 MHz. To enable the generation of this beat note, a polarization controller fiber is used at the output of each ECL to align their polarization. The carrier frequency of the beat note can be tuned by changing one or both laser wavelengths and a feedback loop is used between the two ECLs to ensure the stability of the carrier frequency. Then, an external NRZ optical MZM driven by a baseband Pseudo-Random Bit Sequence (PRBS) signal generator modulates the optical frequency-beat. Two modulation techniques can be considered: the double sub-carrier modulation technique where both sub-carriers λ_1 and λ_2 are modulated as opposed to the single sub-carrier modulation technique. In this demonstration, the double sub-carrier modulation technique was preferred because it offers a higher SNR. The optical modulated signal is then further amplified by an Erbium Doped Fiber Amplifier (EDFA) and injected into the photodiode with a cleaved SMF illuminating the integrated GC designed inside the IC chip. In order to maximize the optical coupling of the incident optical signal with the GC, an additional polarization controller was added within the optical path. The incoming optical power level

can be adjusted thanks to a manually-controlled attenuator also connected to the optical path. Therefore, the photo-generated current amplitude at the photodiode's output can be controlled as well.

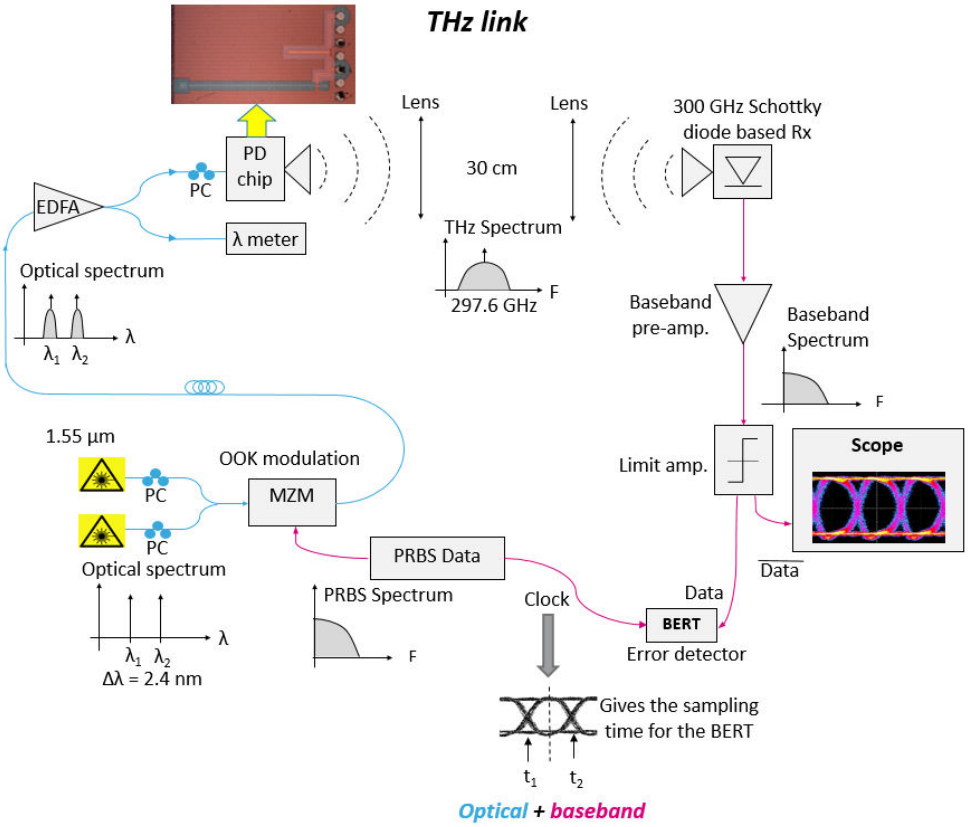

Figure IV.1. Schematic of the measurement setup of the THz link used for data communication. PD = Photodiode.

After photomixing, the electrical THz signal is collected by a GSG probe waveguide-connected (WR3) to the Tx radiating antenna-system. This antenna-system consists of a 300 GHz horn and a 50-mm diameter Teflon lens to collimate the radiation of the horn. An identical antenna-system (lens + horn) was used at the Rx's side. The free-space propagation distance (lens to lens) was limited to 0.3 m by the configuration of the experimental setup and the available space in the lab.

A 25 GHz baseband BW Schottky diode operating at 300 GHz was used at the Rx for direct detection. In this approach, the baseband signal is recovered by selecting the signal's envelop and filtering out the THz carrier frequency. The RF output of the Rx is further amplified by a pre-amplifier, which is an effective way to increase the Rx sensitivity. A pre-amplifier with a BW of 14 GHz or 38 GHz was used depending on the targeted data-rate. A 40 GHz BW limiting amplifier was then used to reshape the baseband signal and drive the detection circuits for the BER Tester (BERT). The limiting amplifier actually works by smoothening the different digital states of the received eye diagram due to its very low saturation power level that tends to clip the signal. The real-time BER is finally retrieved with the BERT. To enable good synchronization between the transmitted signal and the BERT, the digital clock used for the PRBS generation is also sent to the BERT to set the sampling time.

Pictures of the wireless link setup are shown in Figure IV.2 such as the fiber illuminating the photodiode with an optical PRBS signal, the THz wireless link with the horn/lens antenna-system and the eye diagram and BERT display.

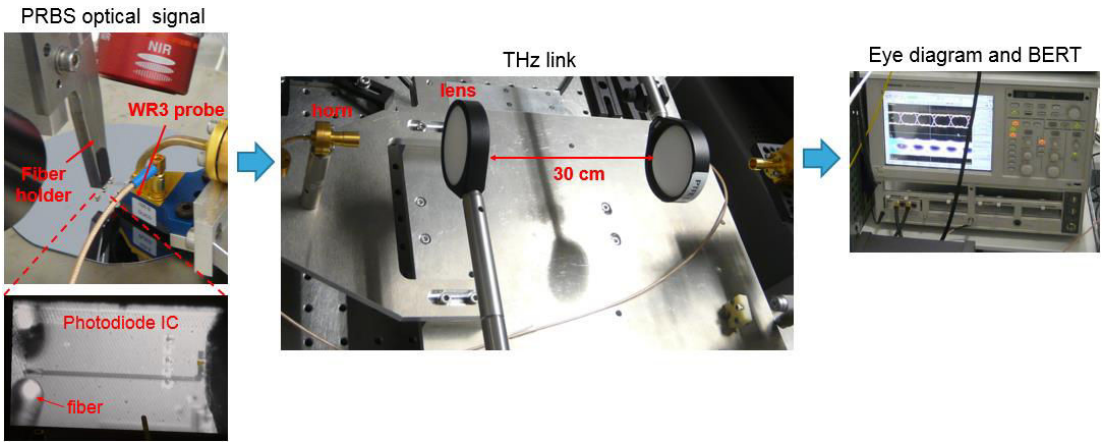

Figure IV.2. Pictures of the main blocks of the Tx and Rx sides of the measurement set-up.

In order to estimate the gain of the horn/lens system and then the THz wireless link budget, a CW signal measurement of the THz link was first realized after calibrating the setup. In this configuration, the MZM and BERT were removed and replaced by a VNA and a mmW extender. The horns were positioned at the focal distance of the lenses (7.5 cm). The gain of the antennas used in the Tx and Rx sides of the measurement bench was calculated according to the decibel version of the Friis transmission equation:

$$P_R - P_T = S_{21} = G_T + G_R + FSPL \quad (16)$$

With G_T and G_R the transmitted and received gains (as the Tx and Rx antennas are identical, $G_T = G_R = G$) and *FSPL* the free space path loss at 300 GHz (reaching 71.5 dB at a distance of 30 cm). Therefore, a $|S_{21}|$ of -71.5 dB is calculated at 300 GHz in a scenario where isotropic antennas are used (G = 0 dBi). As the horns were added to the THz link, the $|S_{21}|$ was actually measured and improved to -23 dB as shown in Figure IV.3, which corresponds to a far-field gain G of about 24 dBi. The measured $|S_{21}|$ was finally improved to -4 dB with the horn/lens systems, which corresponds to an antenna "gain" G of about 34 dBi. However, let's note that with a lens diameter of 50 mm, the far-field zone would be 5 m away from the antenna at 300 GHz. Therefore, the actual setup configuration corresponds to a near-field experimentation. Consequently, the measured "gain" is not in fact the real far-field gain which would be certainly higher than 34 dBi.

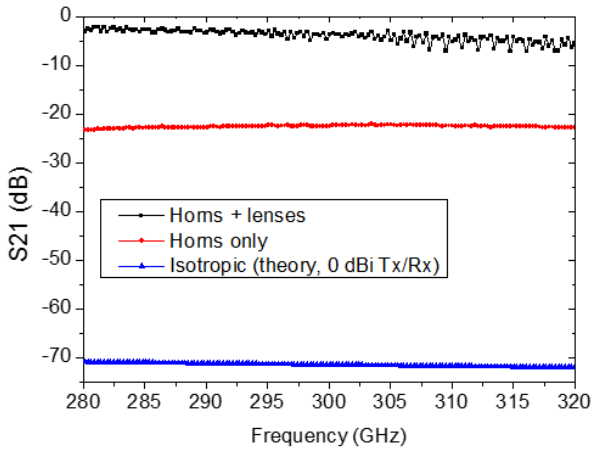

Figure IV.3.| S_{21}| measurement of the THz antenna characterization setup between 280 GHz and 320 GHz, for isotropic link (0 dBi gain) in blue, with a horn antenna (measured gain of ~24 dBi at 300 GHz) in red, and for a horn/lens antenna (near-field measured "gain" of ~34 dBi at 300 GHz) in black.

2. THz link system's $|S_{21}|$ measurement for bandwidth estimation

Then a measurement of the whole wireless system's S parameters was realized with the aim of evaluating the maximum available modulation BW of the THz link and thus the achievable data-rate. In this configuration, port 1 of the VNA was connected to the MZM's input instead of the PRBS generator (Figure IV.1), while port 2 was connected to the Rx output right after the pre-amplifier. The obtained overall $|S_{21}|$ response shown in Figure IV.4 is quite flat over a 10 GHz BW. Ripples are observed on the grey curve with a periodicity of ~0.5 GHz. We believe that this is due to the high directivity of the horn/lens coupled antennas creating a Fabry-Perot cavity in the THz path between Tx and Rx. With a free-space distance of *L = 30 cm*, the Free Spectral Range is :

$$FSR = \frac{2}{c * n * L} = 0.5\ GHz \tag{17}$$

with c= 3.10-8 m/s and n = 1 (in the air), which indeed corresponds to the ripple periodicity. Furthermore, when adding the 14 GHz (-1 dB cut-off) pre-amplifier, an additional ripple is created in the baseband path (shown in pink in Figure IV.1) as seen on the black curve. This effect comes from the impedance mismatch between the Schottky diode output and the pre-amplifier. A total ripple < 5 dB is obtained on a > 10 GHz BW, which is suitable for up to 10 Gbps transmission. For higher data-rate transmission, the pre-amplifier featuring a wider BW of 38 GHz was used. In order to avoid higher signal distortion when increasing the data-rate, RF cables were removed and the pre-amplifier was directly connected to the BERT.

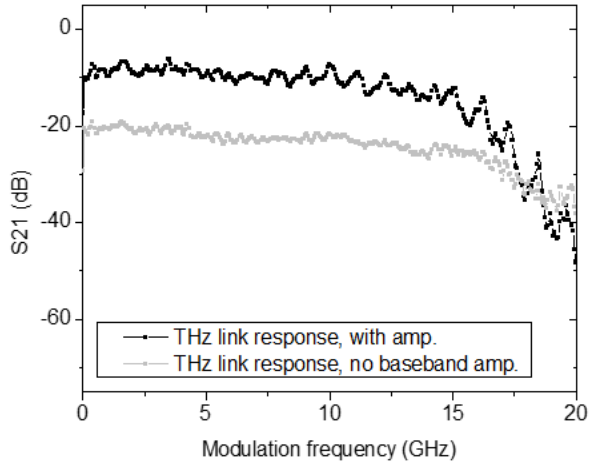

Figure IV.4. Baseband evolution of the $|S_{21}|$ of the whole THz link using the matched PIN-PD (2 mA and 2V bias), with (black curve) and without (grey) pre-amplifier, at 297.6 GHz carrier frequency.

Finally, the sensitivity of the Rx was evaluated to be around -40 dBm at 10 Gbps, which corresponds to the minimal required power at which the BER value is < 10^{-10}. At 20 Gb/s and 25 Gb/s, Rx sensitivities of -36 dBm and -32 dBm were estimated respectively which of course has an impact on the minimum achievable BER during testing.

3. Equipment reference and main characteristics

A brief listing of the equipment used for this wireless link data communication setup is given below with their main characteristics:

- External modulator: ModBox-1550nm-NRZ-44 Gb/s chirp-free Lithium Niobate Mach-Zehnder intensity modulator

  - Controlled linear polarization
  - Input AC voltage of 0.45 V (Vpp)
  - Bias controller to lock the operating point of the modulator at the quadrature point
  - Spectrum linewidth of 1 MHz
  - Return loss of -10 dB
  - Output power of ~6 dBm
- External Cavity Lasers: Agilent 81642A Tunable Laser Module
  - Wavelength range from 1510 nm to 1640 nm
  - Wavelength accuracy of ± 0.015 nm
  - -3 dB spectrum linewidth : 100 KHz
  - Continuous output power during tuning ≥ 4 dBm
  - Power stability of ± 0.03 dB over 24 hours
  - Polarization maintenance fiber
- PRBS signal generator and BERT: Half-clock ASNT_PRBS45 0.1-45Gbps PRBS Generator form ADSANTEC
  - Data-rate from 0.1 Gb/s to 45 Gb/s
  - Differential data output with an amplitude up to 1.4 V
  - Sine wave half-rate clock with a frequency of n GHz to generate a 2n Gb/s PRBS signal
- Digital oscilloscope: Tektronix DSA8200
  - Provides digital signal path testing up to 43 Gb/s and bandwidth performance testing from 12 GHz up to > 70 GHz.

II. Single-channel wireless link measurement using an external modulator

OOK modulated signal transmissions were first evaluated as they represent the simplest modulation scheme. In this case, the NRZ external modulator was used and was driven by a 2^7-1 PRBS sequence. BERs were evaluated as a function of the photocurrent which is proportional to the input optical power. The BER measurement time was set to 1 second by default. Moreover, if we consider zero errors detected and a BER calculation confidence level *CL* of 95%, the minimum number of bit *N* to test for a given BER is:

$$N = \frac{-\ln(1 - CL)}{BER} \tag{18}$$

Therefore, for a BER threshold of 10^{-9}, a stream of at least 3 Gbits is required. The test time that is required to measure *N* bits depends on the targeted data rate as follow:

$$t = \frac{N}{data\ rate} \tag{19}$$

Therefore, at 10 Gb/s and 25 Gb/s, the acquisition time should be at least 0.3 seconds and 0.12 seconds respectively. This means that the sampling time of 1 second set at the BERT is definitely long enough.

1. Unmatched and matched SiGe PIN photodiode BER performance at 10 Gb/s OOK

At a fixed data-rate of 10 Gb/s, BER measurements at 301 GHz were realized using the four PICs integrating the SiGe PIN-PD and with matching circuits (PD1, PD2, PD3, and PD4 shown in Figure IV.5).

This set of measurements enables to analyze the impact of different matching networks on the data transmission performance of the PIC. At the Rx side, two pre-amplifiers of 14 GHz BW delivering a total gain of 28 dB were connected in series with the 40 GHz BW limiting amplifier. This enables for the limiting amplifier to receive enough power to operate above its sensitivity threshold.

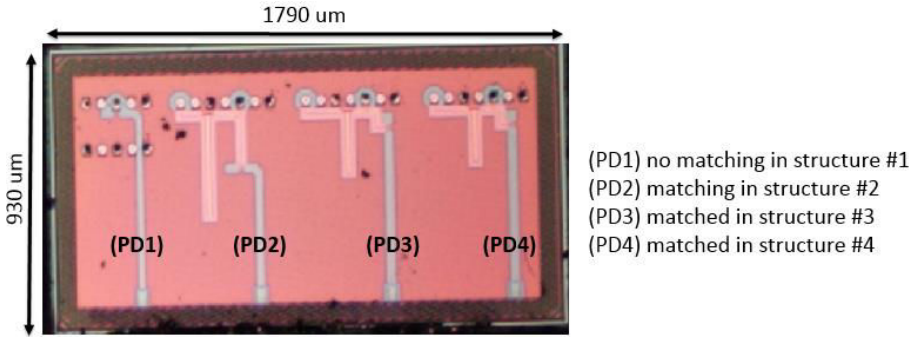

Figure IV.5. Microscope picture of the four PICs integrating the SiGe PIN-PD1 and with three different matching circuits.

The BER results for each PICs are presented in Figure IV.6 (a). A BER below 10^{-9} was achieved for a current higher than 1.75 mA with the PD4, and the BER strongly deteriorates as the matching of the photodiode moves away from the 301 GHz carrier frequency (as shown in Figure IV.6 (b)) which is in line with the expected IC frequency behavior. Indeed, a strong shift of the photocurrent can be seen if we compare the PD4 to the PD1 curves, (from 1.25 mA to 2.75 mA respectively for a BER of 10^{-6}). However, when we look at the output power in Figure IV.6 (c), less than 2 dB difference is obtained at 300 GHz between PD4 and PD1, which seems small in comparison to the free space path loss value at 30 cm (71 dB at 300 GHz) but is in fact significant in comparison to the measurement system's dynamic range *of* about 4 to 6 dB calculated as follows:

$$Dyn = P_{out} + 2 * Ga + FSPL - Rx.sens \quad (20)$$

with P_{out} being the photodiode's output power (-33 dBm to -31 dBm), *Ga* the antenna gain (34 dBi), *FSPL* the free space path loss (-71 dB) and *Rx.sens* the Rx sensitivity (-40 dBm). Indeed, this BER shift is partially due to the fact that the Rx's sensitivity is almost reached. Therefore, a higher system gain (amplifier or Tx and Rx antennas) would be required to increase the system's dynamic range and thus lower down the impact of the measurement system's performance on the achieved BER.

In addition, the BER of PD2 (in red) and PD3 (in blue) are very similar. This can be explained by the achieved output power shown in Figure IV.6 (c). Indeed, we notice that PD2 delivers more power, but is more dispersive around 300 GHz whereas PD3 delivers less power (with a relative measurement incertitude below 1 dB) but is less dispersive and hence more stable around 300 GHz. Those 2 facts tend to compensate one another, resulting in an almost equivalent BER for a photocurrent above 1.75 mA.

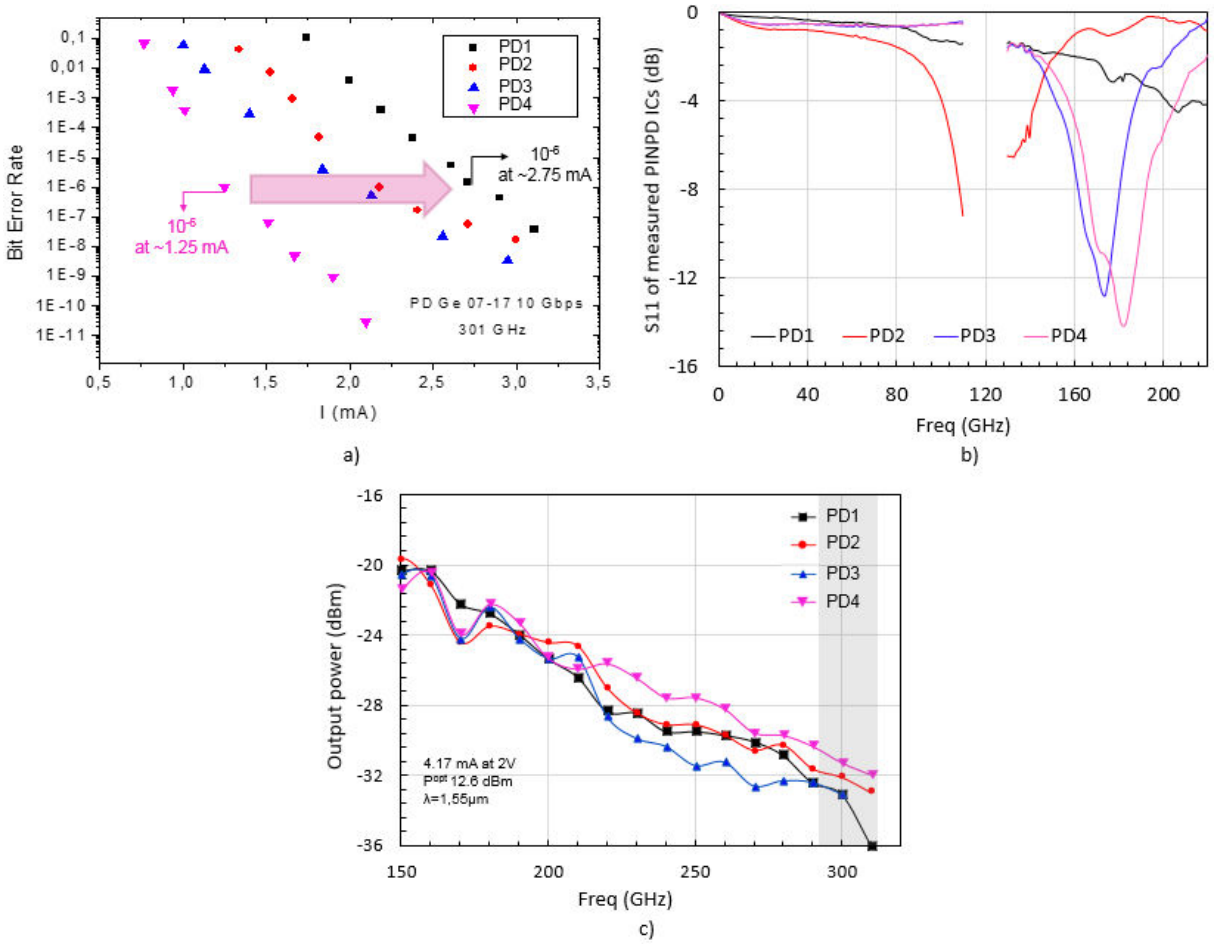

Figure IV.6. BER measurement at 10 Gb/s and 301 GHz for a Tx using the PD1 (black), and with an integrated matching network with PD2, PD3, PD4 (red, blue and pink) (a), and corresponding measured $|S_{11}|$ (b) and output power (c) as a function of the frequency.

2. BER measurement of OOK data signals from 10 Gb/s to 25 Gb/s using the SiGe PD3

To evaluate the BER at 10 Gb/s, 16 Gb/s, 20 Gb/s and 25 Gb/s at the carrier frequency of 301 GHz, two different Rx setups were used so as to be optimized to the BW of the measurement set-up. At 10 Gb/s and 16 Gb/s, the 14GHz-BW 24dB-gain cascaded-pre-amplifiers were used. At 20 Gb/s and 25 Gb/s, a pre-amplifier with a 38 GHz bandwidth and a gain of 28 dB was used in order to support higher data-rates. Indeed, this amplifier should be sufficient for up to 32 Gb/s data-rate. However, by widening the gain of the amplifier, the noise is also increased. In this case, if two wide-band pre-amplifiers were to be used, random saturation of the limiting amplifier would be inevitable which would considerable deteriorate the BER. For this reason, only one pre-amplifier was used at 20 Gb/s and 25 Gb/s.

In Figure IV.7, we notice that three abnormalities emerge from the measured BERs. First, the BER curves are not linear as a function of the photocurrent but rather have a decreasing slope as the photocurrent increases. Also, the BER curves associated to the different data-rates are shifted towards higher photocurrent as the data-rate increases. Finally, as the data-rate increases, the global slope of each BER curve gets lower than the previous BER curve. Several phenomena occurring during the data transmission can explain these behaviors.

At 10 Gb/s for instance, the BER rises quickly for photocurrents decreasing below 1.3 mA due to a stronger inability of the limiting amplifier to correct the signal's shape. For photocurrents above 1.3 mA however, the limiting amplifier receives more power thereby restoring its performance. Therefore, this part of the BER curve is more representative of the system's real data transmission quality, with a minimum BER of almost 10^{-11} achieved at 2.1 mA at 10 Gb/s. Another effect impacting on the BER slope decrease at each data-rate is the photodiode's behavior transitioning to its nonlinear regime when reaching photocurrents above 2 mA. This is particularly noticeable at 16 Gb/s around the minimum BER of $6.3*10^{-9}$ at 3.57 mA. Around this point, a relative BER flatness can be noticed inside the red circle which is linked to the lack of transmitted power due to the photodiode's saturation level around 4 mA.

Furthermore, as the data-rate increases, a BER shift to the right side of the graph is noticed, which is explained by a data transmission that undergoes statistically more bit errors per sampling time due to the higher data-rate.

Two last effects are manifested by a lower global BER slope above 10 Gb/s compared to the BER slope at 10 Gb/s. The first effect is the limited BW of the global system (BW of the Rx amplifier at 16 Gb/s and BW of the photodiode combined with the GSG probe at higher data-rates). The second effect would be the photodiode's output power variation as a function of the frequency. This frequency response plays a part in the BER slope degradation when the data-rates increases due to a wider required frequency BW.

At a data-rate of 20 Gb/s, we successfully measured a BER performance < 10^{-9} for a photocurrent of 3.75 mA. The DC reverse bias of the photodiode was set to 1.6 Volts. Moreover, a BER below the FEC threshold (around 10^{-3}) was achieved at 25 Gb/s for a slightly increased photocurrent of 4 mA and a bias of 1.8 Volts. From a BER comparison between 20 Gb/s and 25 Gb/s, as the data-rate increases, the BER slope decreases. This behavior correlates once more with the BW of the whole system which is limited due to the overall combined effects of the photodiode frequency response, the THz link and the Rx frequency dependence around 300 GHz (and particularly the Schottky diode's limited BW of 25 GHz). This last aspect has a direct impact on the linear response of the detector and thus on the maximum achievable error-free data-rate.

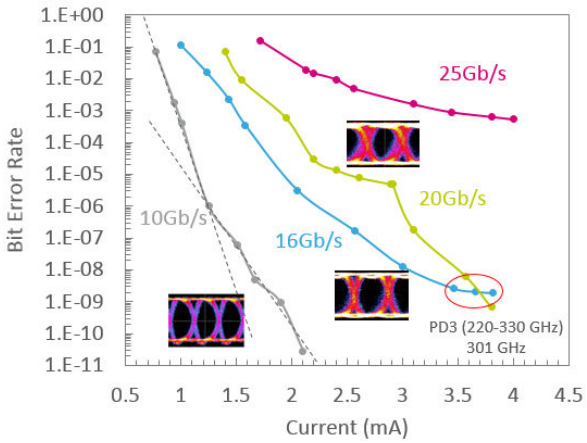

Figure IV.7. BER measurement at 300 GHz for OOK modulation at 10 Gb/s in grey, 16 Gb/s in blue (14 GHz BW pre-amplifier), and 20 Gb/s in green, 25 Gb/s in pink (38 GHz BW pre-amplifier) using the SiGe PIN-PD matched at 220-330 GHz.

3. Impact of the measurement system's bandwidth on the BER for OOK modulation at 20 Gb/s and 25 Gb/s

In order to clearly point out the BW impact of the measurement system on the data transmission quality, BER measurements at identical data-rates were measured for Rx setups operating at two different BWs. Data-rates of 20 Gb/s and 25 Gb/s were firstly measured using two pre-amplifiers of 14 GHz BW and finally using one pre-amplifier of 38 GHz BW. The BER graphs are shown in Figure IV.8 and clearly demonstrate a strong influence of the pre-amplifier's characteristics on the BER slopes. Indeed, they are steeper when the 38 GHz BW amplifier is used, compared to a more moderate slope when using the 14 GHz BW amplifier (for the same data-rate). However, for a photocurrent below 1.96 mA at 20 Gb/s and 2.13 mA at 25 Gb/s, the BER associated to the highest BW becomes higher than the BER associated to the lower BW, which doesn't seem coherent. This behavior is in fact linked to the limiting-amplifier's low saturation power level. Indeed, only one pre-amplifier was used in the 38 GHz BW setup, resulting in an under-driven limiting amplifier and therefore a lower quality of the measured data stream compared to the 14 GHz BW setup using two pre-amplifiers. This analysis shows how important it is to consider the performance of every component of the measurement system.

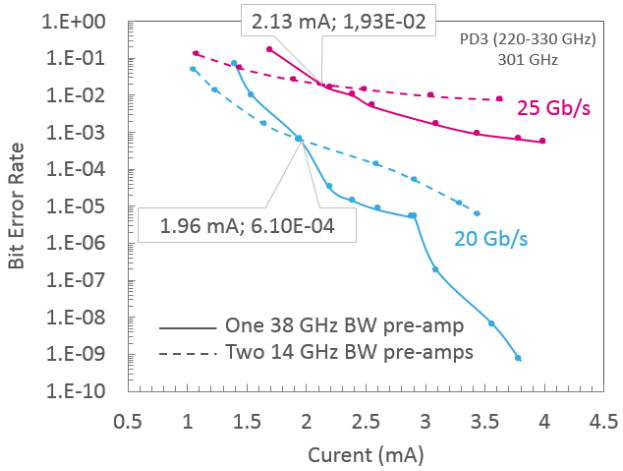

Figure IV.8. Rx bandwidth impact on the measured BER at 20 Gb/s and 25 Gb/s a Rx setup using a 14 GHz pre-amplifier and another setup using a 38 GHz pre-amplifier.

4. Benchmarking of achieved data-rates with OOK modulation scheme using different solid-state and photonics technologies

The 40 Gb/s OOK goal presented in the Introduction seems very challenging to be reached with a single channel transmission because it would involve an input power higher than the photodiode's saturation point. Nevertheless, the measured error-free PRBS signal at 20 Gb/s is still considered as a good and fair achievement. Indeed, in the context of low-cost multi-Gb/s mmW and THz wireless links, the potentiality of industrial Si-photonics operating at THz frequency bands to enable simple modulations and high data-rates is clearly demonstrated. Taking WiGig Si-based 60 GHz communication systems as a first comparison point, almost 7 Gb/s are delivered on a 2.16 GHz licensed-channel width corresponding to a 3.3% relative BW with higher-order modulation schemes like 64-QAM (which requires power-consuming hardware processing) when at 300 GHz, the proposed THz link based on a Silicon Photonics Tx achieves a data-rate almost 3 times higher while only using OOK modulation on a 13% relative BW.

Several state-of-the-art cases (shown in Table IV.1) were taken from the literature to help positioning our work amongst today's existing wireless THz links operating on OOK modulation scheme and using different microelectronics processes. In [IV.1], CMOS-based links have achieved up to 12.5 Gb/s over 5 m at 240 GHz using OOK modulation schemes. In [IV.2], a mHEMT-based Tx has already enabled up to 25 Gb/s OOK data transmission at 220 GHz over 50 cm. However, due to the limited achievable BW of solid-state transistor's in the THz regime (mostly around 25 GHz BW), photonics-based technologies represent a good alternative around 300 GHz due to their intrinsically large BWs and therefore have a strong potential to thrive in the THz communication applications. Wireless links based on III-V photonics using UTC-PDs have indeed demonstrated up to 40 Gb/s OOK data transmissions at a distance of 50 cm at 300 GHz [IV.3], and increasing the modulation complexity has enabled to achieve up to 32 Gb/s at up to 25 m [IV.4].

Therefore, with an achieved 20 Gb/s data-rates at 300 GHz with OOK modulation scheme over 30 cm, it appears that Si-Photonics transmitters could soon surpass state-of-the-art CMOS-based transmitters both in terms of BW and data-rate. It should also be possible for Silicon Photonics Tx to achieve up to 25 Gb/s in OOK modulation and 50 Gb/s in PAM4 modulation, thereby competing with III-V UTC-PD solutions using signal amplitude modulation (while achievable powers remain ~20 dB below what is feasible using UTC-PD).

Ref	Technology	Carrier frequency	Data-rate	Modulation	Distance	Tx power consumption (mW)
[IV.1]	55 nm BiCMOS	130 GHz	12.5 Gb/s	OOK	5 m	59
[IV.2]	mHEMT	220 GHz	25 Gb/s	OOK	0,5 m	
[IV.5]	65 nm CMOS	260 GHz	10 Gb/s	OOK	0,04 m	688
[IV.3]	III-V photonics	300 GHz	40 Gb/s	OOK	0,5 m	
[IV.4]	III-V photonics	385 GHz	32 Gb/s	16QAM	25 m	
This work	Silicon Photonics	300 GHz	20 Gb/s	OOK	0,3 m	

Table IV.1. Benchmarking of state-of-the-art achieved data-rates with OOK modulation scheme using different technologies.

III. Dual-channel wireless link setup for up to 100 Gb/s data-rate

To reach up to 50 Gb/s data-rate in OOK modulation and 100 Gb/s in PAM4 modulation, a solution consists in achieving double channel transmission. In this configuration, two sub-carrier frequencies are used to transmit the information over 25 Gbaud/s each (25 Gb/s for OOK and 50 Gb/s for PAM4). Therefore, the measurement setup should be modified to enable BER measurement of the two different channels. Figure IV.9 shows a schematic of the envisioned double channel THz link measurement setup. On the Tx side, three laser sources are used instead of two to generate three different wavelengths (λ_1, λ_2, λ_3) around 1.55 µm. An additional external modulator would be needed to modulate λ_2 and λ_3 with two different data sequences while λ_1 remains untouched. That being said, dedicated PAM4 modulators would have to be used in PAM4 transmission to maximize the 4 data states level during the signal modulation. After this, the three optical signals are coupled into a single

optical fiber to create two frequency beats at frequencies $f_1 = c/(\lambda_2 - \lambda_1)$ and $f_2 = c/(\lambda_3 - \lambda_1)$. Those two modulated optical signals are then converted into electrical signals by photomixing through the PIN-PD IC. On the Rx side, the two signals need to be separated in order to evaluate the signal integrity of each transmitted data. For this reason, a WR3 diplexer is required and needs to be designed and prototyped since no commercial WR3 diplexers are available. Complex waveguide structures are often achieved to reach the desired filtering function at THz frequencies, like the THz diplexer presented in [IV.6]. However, a much simpler design is proposed in the perspectives of this research work along with a project on the development of an industrial manufacturing technique that would allow the fabrication of THz waveguide components in a more general way. Following the diplexer, a second Rx chain would be required to double the number of channels. This implies the use of two Schottky diodes operating around the frequency f_1 and the frequency f_2, two pre-amplifiers and two limiting amplifiers. A BERT and an oscilloscope capable of receiving on two different ports would be used to measure and evaluate the two sub-carrier frequency signals.

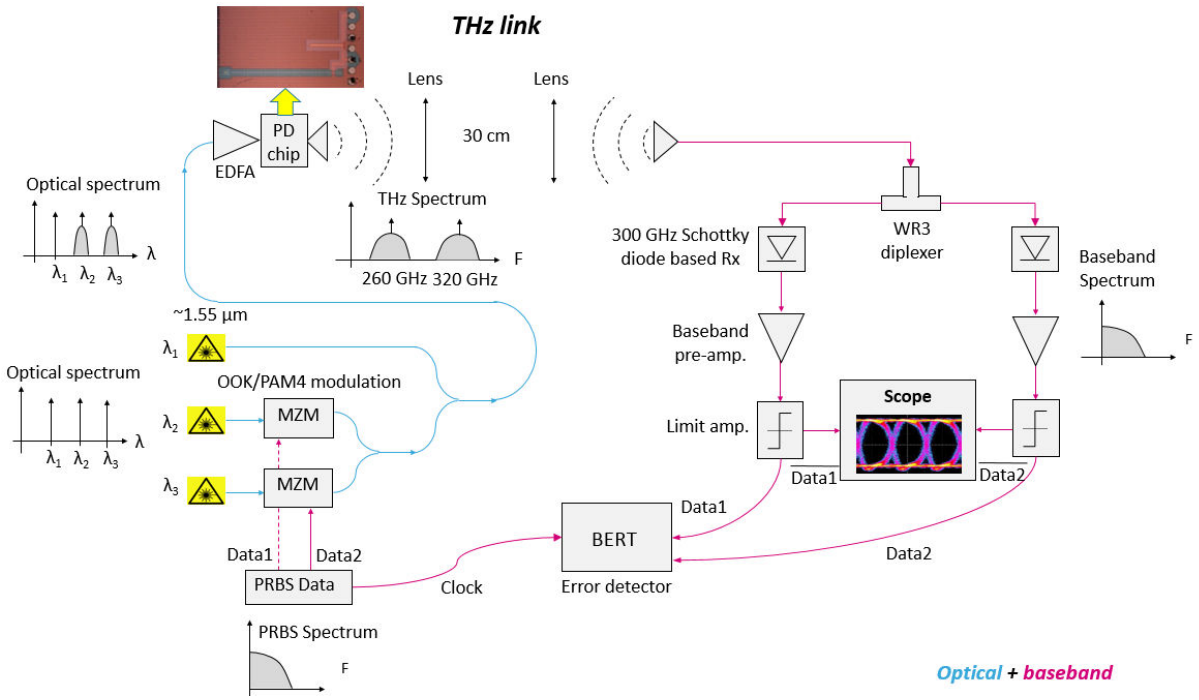

Figure IV.9. Schematic of the measurement setup of the THz link used for data communication. PD = photodiode.

IV. Conclusion

OOK modulated signals were successfully transmitted up to 25 Gb/s with a BER performance $<10^{-9}$ at 20 Gb/s. These data communication demonstrations are, from our best knowledge, the first wireless THz transmissions using Silicon Photonics technology developed within an industrial platform process. With the results of this data-communication demonstration, we have shown that Silicon Photonics technology is seriously competing with transistor-based solid-state technologies. Moreover, it is important to recall that the maximum achievable data-rate was here limited by the Rx BW and overall experimental setup performance which had a significant impact on the measured BER. Therefore, the obtained results should be looked at carefully. By increasing the BW of the experimental setup, the photodiode's impact on the BER could be more thoroughly analyzed and it would be possible to

improved BER at 25 Gb/s. Reaching 50 Gb/s seems also possible using PAM4 amplitude modulation scheme. This demonstration will be realized shortly by replacing the OOK external modulator by a PAM4 external modulator. Moving to double-channel transmission, up to 100 Gb/s is also feasible with PAM4 modulation.

Reference

[IV.1] N. Dolatsha et al., “A compact 130GHz fully packaged point-to-point wireless system with 3D-printed 26dBi lens antenna achieving 12.5Gb/s at 1.55pJ/b/m,” *IEEE International Solid-State Circuits Conference (ISSCC)*, San Francisco, USA, 2017.

[IV.2] I. Kallfass et al., “All Active MMIC-Based Wireless Communication at 220 GHz,” *IEEE Transactions on Terahertz Science and Technology*, vol. 1, no. 2, pp. 477–487, 2011.

[IV.3] T. Nagatsuma et al., “Terahertz wireless communications based on photonics technologies,” Optics Express, vol. 21, no. 20, p. 23736, 2013.

[IV.4] P. Latzel et al., “THz transmission using QAM-16 and 32 Gbit/s on 25m,” *IEEE International Conference on Infrared, Millimeter, and Terahertz waves (IRMMW-THz)*, Copenhagen, Denmark, 2016.

[IV.5] J. D. Park, S. Kang, S. V. Thyagarajan, E. Alon, and A. M. Niknejad, “A 260 GHz fully integrated CMOS transceiver for wireless chip-to-chip communication,” *IEEE Symposium on VLSI Circuits, VLSIC*, vol. 2, pp. 48–49, 2012.

[IV.6] A. Gonzalez, T. Kojima, K. Kaneko, and S. Asayama, “275-500 GHz Waveguide Diplexer to Combine Local Oscillators for Different Frequency Bands,” *IEEE Transactions on Terahertz Science and Technology*, vol. 7, no. 6, pp. 669–676, 2017.

Chapter 5: Conclusion & Perspectives

Chapter 5: Conclusion & Perspectives

Through chapters 2 to 4, the main blocks of a THz wireless transceiver based on Silicon Photonics technology targeting the 200-280 GHz band were developed and evaluated to enable very short range high-speed applications as well as medium range P2P transmissions. Through this study, interesting insights on the technologies used up to 300 GHz were obtained as well as design performance limitations with respect to the frequency. This last chapter sums up the main conclusions drawn from those results and brings a critical point-of-view in order to put those analysis into perspective. This leads us to envision several research topics in order to further develop the Silicon Photonics based wireless link and contribute to the development of innovative THz packaging technologies capable of delivering high THz performance at low cost.

I. Conclusion

A preliminary THz signal generation design was developed in Silicon Photonics technology with an integrated SiGe photodiode and simple matching circuits to enable sub-mmW/THz optical-to-electrical conversion. On-wafer measurements were realized in DC and RF regimes. DC characterization has shown a photodiode darkness current of 10 nA at a reverse bias of 1 V which is low compared to the reported darkness currents found in the literature for PIN SiGe photodiodes (up to 62 nA at 1 V reverse bias in [V.1]). RF characteristics have shown a saturation power of about 11.3 mW at a reverse DC bias of 1 V which should be pushed to a higher level by increasing the DC bias up to 2 V. Measurements between 130 GHz and 310 GHz have shown similar achieved output power levels compared to state-of-the-art output power levels of III-V UTC photodiodes (about 20 dB above). Indeed, at 300 GHz a power level of -31 dBm was achieved with the developed Silicon Photonics IC when about -7 dBm was achieved in III-V Photonics [V.2]. These results enable to validate the functioning of the photodiode model developed by STMicroelectronics at frequencies up to 310 GHz. Even though 50Ω matching circuits were design to match the photodiode in specific bandwidths, the measured matching bandwidths were globally shifted to about 17% towards lower frequencies, which enabled us to re-estimate the equivalent circuit of the SiGe photodiode for the future design of matched THz photomixers. From our best knowledge, this is the first time that a PIN photodiode developed in industrial Silicon Photonics is evaluated up to 310 GHz for THz transmissions, and the overall output power levels that were obtained enable us to seriously consider this device for THz photomixing.

Data-communication demonstrations were successfully achieved at 300 GHz using the photodiode IC as a photomixer on the Tx side and a Schottky diode direct detector at the Rx side. Up to 25 Gb/s error-free data-rate was successfully achieved using OOK modulation on a single channel over 30 cm with an output power of about -30 dBm and a photocurrent of about 4 mA. When looking at the reported wireless communication demonstrations using OOK modulation over short distances (4 cm to 5 m), it can be noticed that Silicon Photonics is seriously competing with solid-state technologies (as shown in Figure V.1). Moreover, maximum achievable data-rates could actually be increased to 50 Gb/s through PAM4 modulation, which would allow Silicon Photonics technology to compete with III-V Photonics technology in direct detection configuration. Thus, PAM4 data-communication

measurements will soon be realized to validate 50 Gb/s single channel transmission in real time detection. Furthermore, the addition of a second channel to the measurement setup will enable to achieve up to 100 Gb/s in PAM4 modulation. Overall, such industrial Silicon Photonics wireless demonstrations are unprecedented with regards to the reported demonstrations in the literature, and these promising results are paving the way towards low-cost Silicon Photonics SoC transmitters operating at THz frequencies.

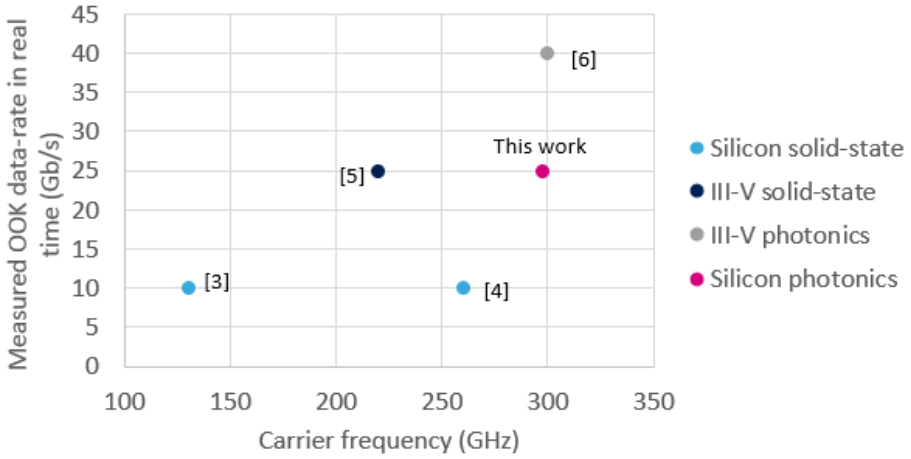

Figure V.1. Achieved wireless communication data-rate using developed Silicon Photonics IC compared to data-rate achieved with different technologies using OOK modulation over distances below 5m ([V.3]–[V.6]*).*

In order to move to a THz Silicon Photonics SoC in which optical modulation functions are implemented, OOK and PAM4 electro-optical modulators have been designed and integrated with the previous IC. Simulated eye diagrams were evaluated for different data-rates and promising results were obtained: eye diagram wide open at 50 Gb/s using PRBS modulation. To support the obtained simulations, these ICs are soon going to be measured in data-communication scenarios in order to achieve a first Silicon Photonics THz SoC.

From the antenna side, after having ascertained that on-chip integrated microstrip antennas in silicon wafers are not the appropriate approach to achieve wideband cost-effective antennas, the Antenna-in-Package solution was considered due to its compatibility with industrial processes. Hence, the first 300 GHz Antennas-in-Package have been achieved using industrial packaging technology during this PhD. In order to enable at least 40 Gb/s data-rate operations using OOK modulation, a RF bandwidth of 80 GHz was required. Therefore, an Aperture-Coupled Patch microstrip antenna was implemented for a design working between 200 GHz and 280 GHz. This enabled to assess the performance of organic substrate technology in this frequency range. The resulting 2x1 antenna array reached a simulated broadside gain of about 8 dBi throughout almost 40% relative bandwidth around 250 GHz even though respecting industrial design rule constrains was challenging. This is a very good simulated achievement with regards to the gain bandwidth performance of the reported THz microstrip integrated antennas (below 15 %) as shown in Figure V.2. Gain measurements have shown a fair agreement with post-simulations (after adjusting the dimensions of the simulated antenna to the actual manufactured-antenna dimensions), thereby validating the manufacturing process associated to HDI organic substrate technology from 200 GHz to 300 GHz. However those measurements have also revealed the high fabrication sensitivity of this technology to process control and copper balance, resulting in a much smaller BW (9%) and gain (5 dBi) at 230 GHz. Therefore, the fabrication control process and copper balance should be optimized in order to enable proper design fabrication for this

type of antennas. Moreover, the fabrication tolerance becomes high relatively to the operating frequency of the antenna, thereby increasing the impact on the antenna's frequency response as the carrier frequency increases. Therefore at 300 GHz, we seem to be at the limit of this technology in order to comply with current design rules and industrial packaging process variability. Consequently, for frequencies above 300 GHz, it would be desirable to move to a substrate packaging technology capable of delivering more aggressive design rule constraints.

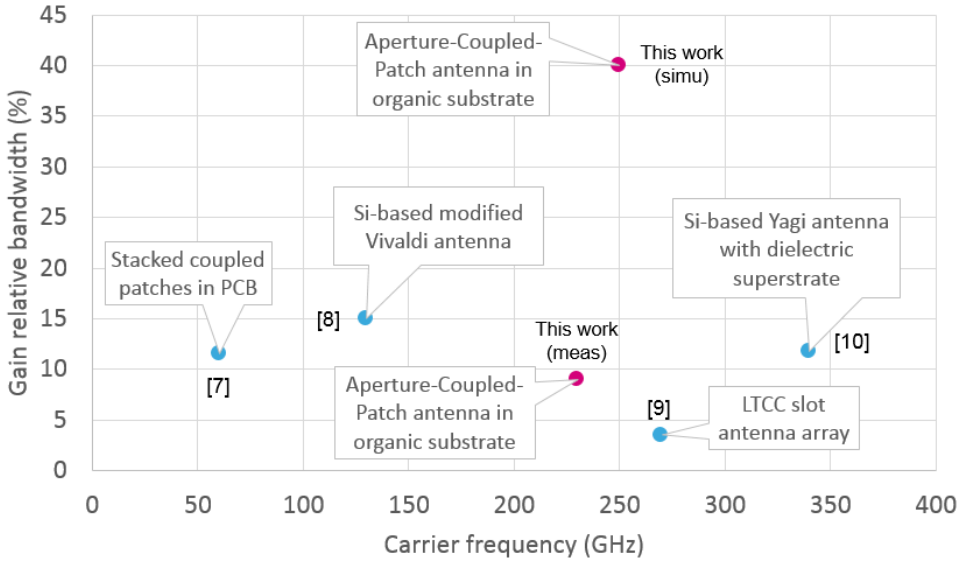

Figure V.2. Achieved simulated and measured gain relative bandwidth of developed Aperture-Coupled-Patch antenna compared to reported state-of-the-art gain relative bandwidth for different integrated antenna technologies from [V.7]–[V.10].

In addition, 3D-printed dielectric lenses and waveguide-fed horn antenna have been achieved above 200 GHz exhibiting promising results, thereby validating the use of fast 3D-printing prototyping techniques in order to pave the way for low-cost development of higher performance wireless systems. Indeed, gains higher than 20 dBi can be reached with the use of quasi-optical antennas and full duplex transmissions can be enabled by leveraging the developed conical horn's polarization diversity.

II. Perspectives

As described in Chapter 2, the complete THz transceiver consists of an optical signal frequency beat generator, an optical modulator and a photomixer. Therefore, in order to push the SoC integration further, an integrated frequency comb and an arrayed wavelength generator still need to be implemented as shown in the complete wireless link schematic in Figure V.3, in order to generate the 240 GHz optical signal. On this matter, a future PhD thesis focusing on the design of these optical functions in PIC25G technology will be undertaken in the near future.

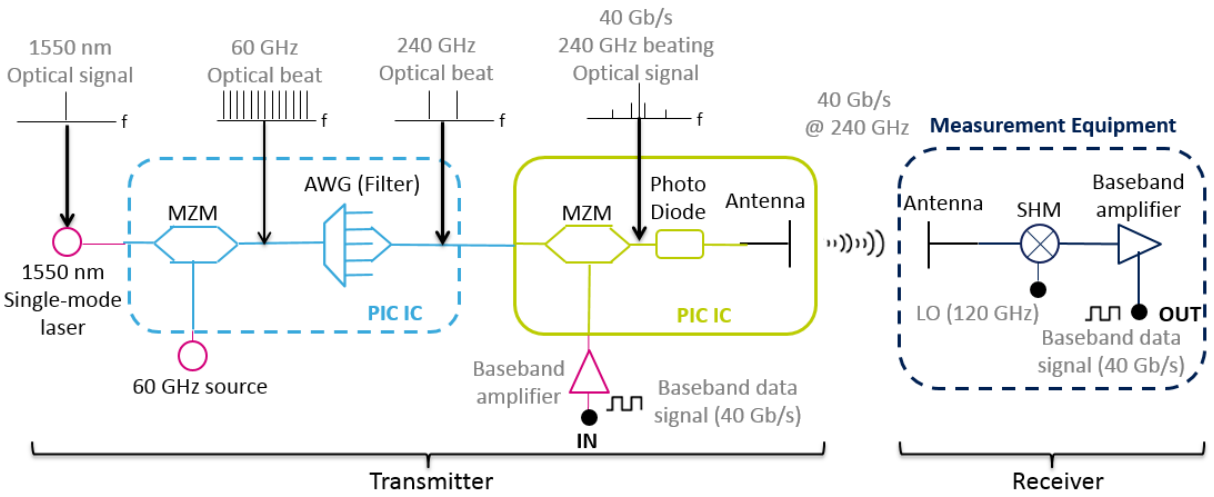

Figure V.3. Complete THz wireless link based on integrated Silicon Photonics Tx and integrated Si BiCMOS Rx.

From the optical source side, it will also be necessary to investigate the integration of long wavelength III-V VCSEL [V.11] in flip-chip mount configuration using a packaging interposer to enable 1550 µm optical source generation within the transmitter module. Clearly, the current packaging solutions used by high speed optical links which generally calls upon active alignment procedures of optical fibers cannot be considered for low-cost THz module. Therefore, the main challenge concerns the availability of an electro-optical packaging technology in order to move from an IC demonstrator to a module demonstrator. On this topic, preliminary investigations dealing with the development of a thin glass interposer used as an optical and electrical connection with the flip-chipped PICs have already shown promising results. In papers [V.12] and [V.13], a new fabrication process based on femtosecond laser lithography, wet etching and polymer lamination is indeed proposed for the fabrication of step index polymer optical waveguides on top of a glass carrier. A schematic of the complete foreseen module architecture is shown in Figure V.4 (a) and first single-mode waveguide topology and E-field distribution results are shown in Figure V.4 (b, c). In order to redirect the optical beam propagating from the glass carrier towards the PICs, the development of a slanted mirror located across the waveguide is also investigated. These ongoing experimental studies are part of Jean-Marc Boucaud's on-going PhD thesis on the development of a fully functional electro-optical glass interposer, within a collaboration between STMicroelectronics and the IEMN laboratory.

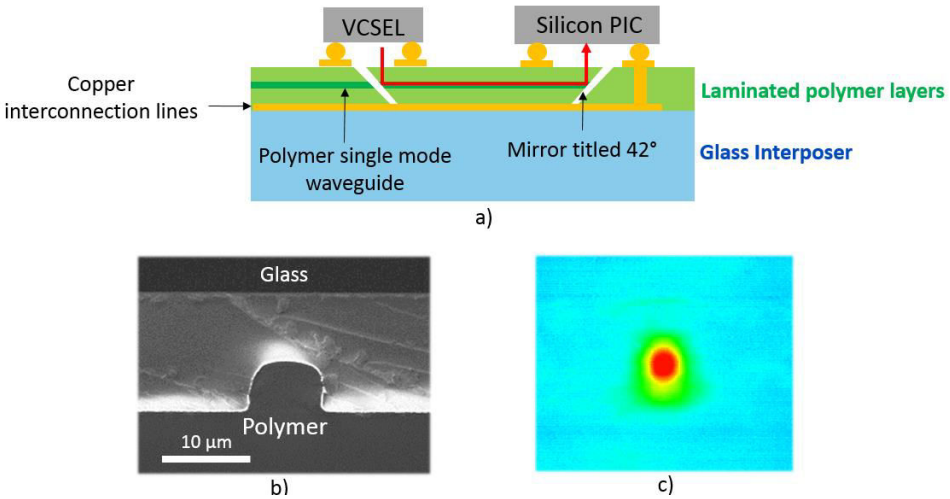

Figure V.4. (a) Glass interposer solution for cost-effective large-scale production, (b) scanning electron microscope (SEM) micrograph of a waveguide cross-section, (c) mode profiles from IR camera of a straight waveguide from [V.13].

Focusing on the design of the receiver, multiple detection configurations can be considered. Amongst the conventional direct detection THz receivers (advised for low-power links), the diode detector and sub-harmonic mixer (SHM) are the most commonly developed. However, each configuration delivers different characteristics and should therefore be used according to an appropriate estimation of the THz application specifications. Attributes related to commercial Schottky diode direct detectors are simple and inexpensive systems. However, their sensitivity tends to be quite limiting (~-15 dBm) due to a high noise figure. On the other hand, commercial SHMs require more power consumption (partly due to the LO power requirement) but feature much better sensitivity (~-53 dBm). As shown in Figure V.5 (a), this sensitivity difference between the two detector types translates into an achievable transmission range 50 times higher using a SHM at 240 GHz. Therefore, the envisioned integrated direct detection receiver will be realized using a SHM associated with a 120 GHz LO. The main challenge of this solution concerns the assessment of achievable SHM performance leveraging STMicroelectronics' Schottky diode available in 55nm BiCMOS technology (called B55 [V.14]). A Frequency Division Duplexing (FDD) approach seems to be the most suitable solution to enable 40 Gb/s data-rates due to available Schottky diodes bandwidth. Therefore, a double-channel SHM receiver targeting the bandwidths of 200-240 GHz and 240-280 GHz is considered and its schematic is shown in Figure V.5 (b). To this end, optimizations on the current Schottky diode model are undertaken in order to minimize intrinsic parasitics and a preliminary solution has started to demonstrate a cut-off frequency > 1 THz which is compliant with the integration of Si-based Rx in the 200 GHz – 300 GHz band. This project is part of an ongoing PhD project realized by Vincent Gidel within a collaboration between STMicroelectronics and Polytech'Lab at the University of Nice Sophia-Antipolis.

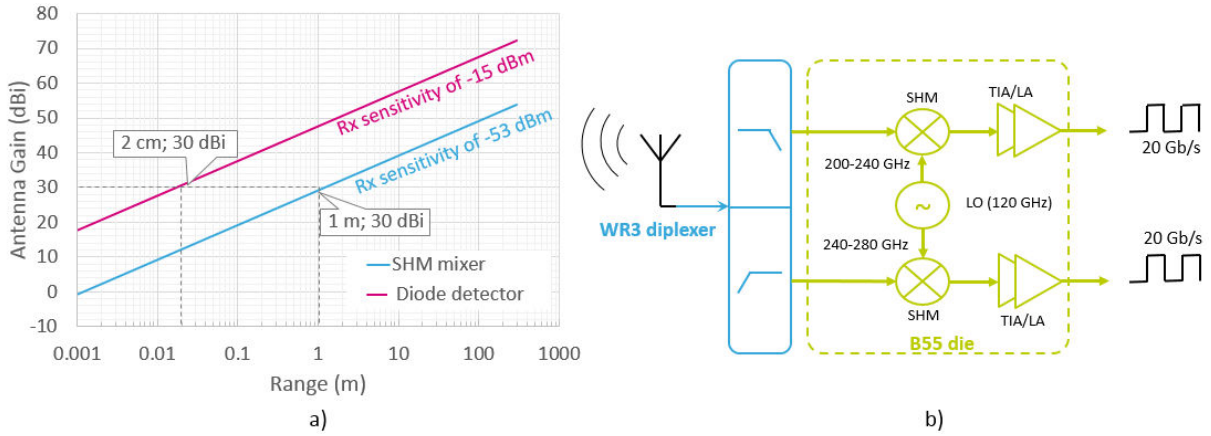

Figure V.5. (a) Antenna gain requirement as a function of the transmission range for Schottky diode detection and Sub-harmonic detection at 240 GHz, (b) Double-channel sub-harmonic mixer receiver schematic.

Finally, in order to leverage the promising 3D-printed horn antenna achieved during the PhD for the development of an antenna system supporting FDD, it is also necessary to define a new assembly strategy. Indeed, the microstrip-to-waveguide vertical transition described in Chapter 3 has shown serious shortcomings in terms of transmission bandwidth, due to poor microstrip-to-waveguide coupling. As an alternative, E-plane microstrip-to-waveguide transition designs, such as the one proposed in [V.15] up to 750 GHz, seems to be the most appealing solution. For this reason, a preliminary design demonstration was realized on HFSS based on this transition architecture targeting the G band (140-220 GHz). In this design, the microstrip is inserted inside a rectangular channel connected to the WR5 waveguide through an opening as shown in Figure V.6 (a). Inside the WR5, a radial stub is exiting the TE_{01} mode, thereby achieving a simulated transmission coefficient higher than -1 dB as shown in Figure V.6 (b). Therefore, this transition design shows promising potential for operations between 200 GHz and 300 GHz. However, manufacturing this type of transition cannot yet be achieved due to the lack of a dedicated planar THz packaging technology.

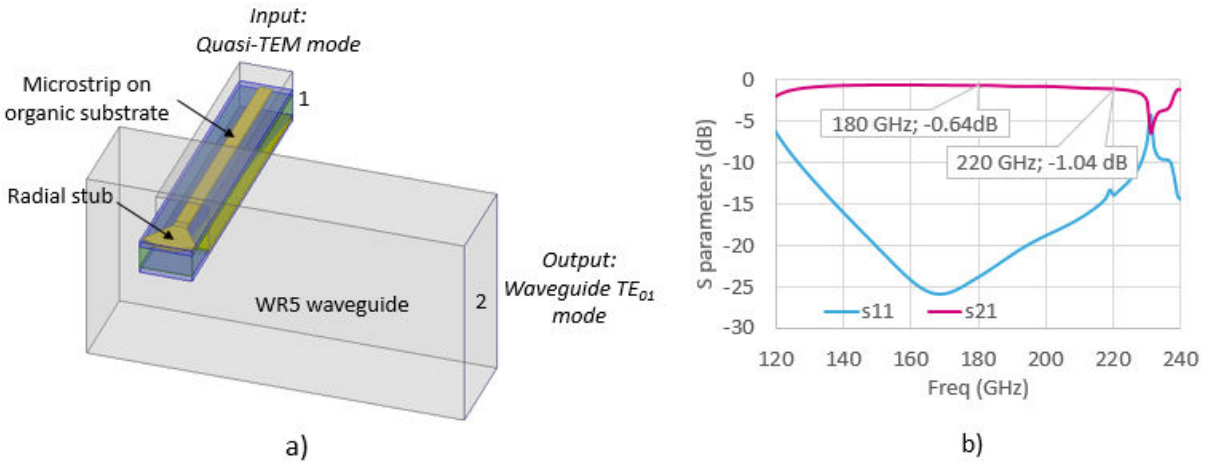

Figure V.6. (a) E-plane horizontal microstrip-to-waveguide transition design in HFSS, (b) corresponding S parameters simulated with HFSS.

On this topic, diverse micromachining techniques have already proven to reach extremely high resolutions for waveguide-based components working at up to 1 THz [V.16]. As of now, the pending challenge consists in developing an industrial manufacturing process and tooling that would deliver very small 3D features (<100 µm). A process based on femtosecond laser ablation seems to be a

promising micromachining technique in micro-electronics [V.16] as it enables 3D micrometric structuration with 1-µm precision and fast prototyping. The laser ablation technique can also apply to various materials such as thin glass substrate, glass fiber reinforced polymer PCBs or LTCC substrates (depending on the cost/quality and function of the final product) for the development of advanced THz electronics packaging [V.17]. Finally, this technology requires no dedicated masks nor clean-room process environment, which make it accessible at lower costs compared to UV photolithography micromachining or Dry Reactive Ion Etching. This laser micromachining technique is actually under evaluation in the context of Cybelle Belem-Goncalves's on-going PhD thesis within a collaboration between STMicroelectronics, the IEMN laboratory, and Polytech'Lab.

Furthermore, it is likely that this new technology could provide access to more aggressive design rules and consequently pave the way of innovative antenna designs operating above 300 GHz. Therefore, a fully automated probe-based antenna measurement setup targeting frequencies from 200 GHz to 700 GHz is being developed as part of Cybelle Belem-Concalves's PhD research work [V.18] (Figure V.7). This measurement bench is built on the architectural basis of the existing 60-140 GHz bench at Polytech'Lab [V.19] featuring motorized rotary arms for 3D radiation pattern and gain measurement. As retrieving the phase information above 100 GHz has proven to be very challenging, amplitude detection has been chosen using a Schottky diode direct detector and a lock-in amplifier to improve the sensitivity of the setup (instead of a traditional mixer-based solution). The dynamic of such a receiver enables to measure actual antenna gain ranging from 3 dBi to 24 dBi.

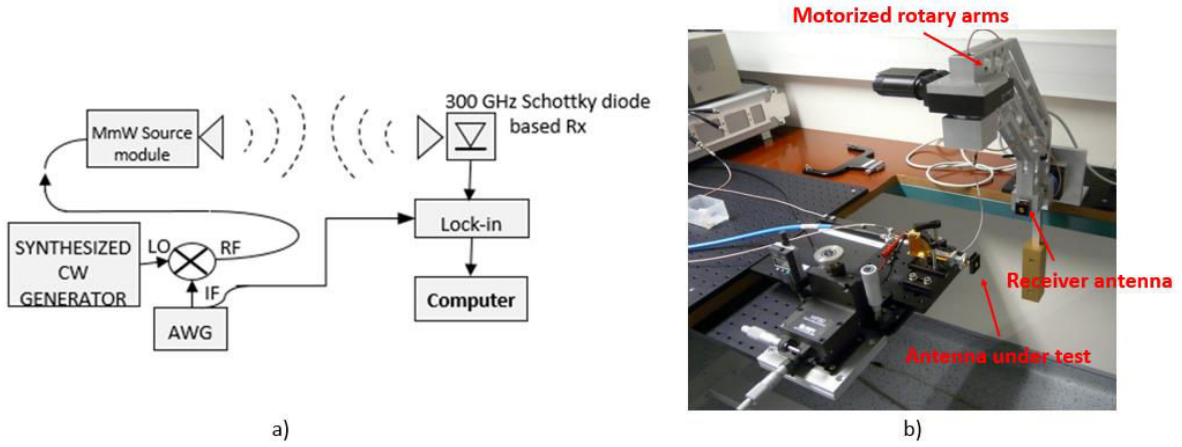

Figure V.7. (a) THz measurement bench schematic, and (b) picture of the 3D radiation pattern measurement system.

In views of further consolidating the realization of THz Silicon-based transmitter systems above 300 GHz, the wireless data communication measurement setup would also need to be upgraded. For instance, in order to evaluate a double-channel THz data transmission, a second channel needs to be added to the actual measurement setup, as presented in Chapter 4. In the context of my PhD thesis, a double-channel data-communication demonstration targeting a BW of 40 GHz around the carrier frequencies 260 GHz and 320 GHz was considered. This preliminary study highlighted the need for a THz diplexer at the receiver side of the setup to enable the evaluation of each channel. Therefore, a first WR3 diplexer was simulated with HFSS using a design featuring a low-pass filter with a cut-off frequency of 280 GHz and a high-pass filter with a cut-off frequency of 300 GHz (Figure V.8 (a)). A simulated transmission coefficients higher than -2.7 dB and -1.7 dB was achieved in the low band and high band respectively with a rejection at 280 GHz an at 300 GHz below -50 dB as shown in Figure V.8 (b). Adjusting this design to micromachining process constraints would allow to consider the

prototyping of this complex waveguide structure as soon as the femtosecond laser micromachining technology mentioned above is developed.

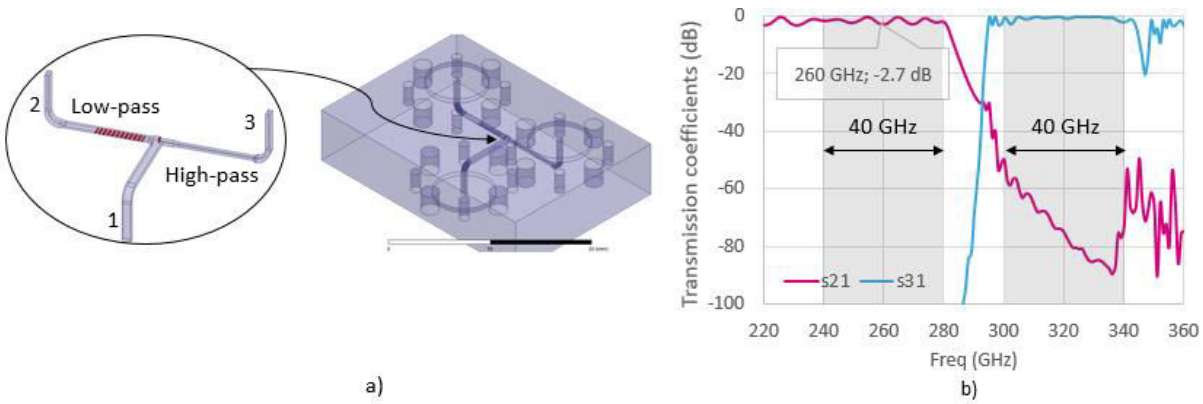

Figure V.8. (a) WR3 diplexer preliminary design on HFSS, (b) low-band and high-band transmission coefficients $|S_{21}|$ and $|S_{31}|$ with HFSS simulation.

Reference

[V.1] J. M. Fedeli *et al.*, "High Performance Waveguide Integrated Germanium Pin Photodiodes for Optical Communication Applications," *IEEE International Silicon-Germanium Technology and Device Meeting (ISTDM)*, pp. 131–132, Singapore, Singapore, 2014.

[V.2] H.-J. Song, K. Ajito, Y. Muramoto, A. Wakatsuki, T. Nagatsuma, and N. Kukutsu, "24 Gbit/s data transmission in 300 GHz band for future terahertz communications," *IEEE Electronics Letters*, vol. 48, no. 15, p. 953-954, 2012.

[V.3] N. Dolatsha *et al.*, "A compact 130GHz fully packaged point-to-point wireless system with 3D-printed 26dBi lens antenna achieving 12.5Gb/s at 1.55pJ/b/m," *IEEE International Solid-State Circuits Conference (ISSCC)*, pp. 306–307, San Francisco, USA, 2017.

[V.4] J. D. Park, S. Kang, S. V. Thyagarajan, E. Alon, and A. M. Niknejad, "A 260 GHz fully integrated CMOS transceiver for wireless chip-to-chip communication," *IEEE Symposium on VLSI Circuits (VLSIC)*, pp. 48–49, Honolulu, USA, 2012.

[V.5] I. Kallfass *et al.*, "All active MMIC-based wireless communication at 220 GHz," *IEEE Transactions on Terahertz Science and Technology*, vol. 1, no. 2, pp. 477–487, 2011.

[V.6] T. Nagatsuma *et al.*, "Terahertz wireless communications based on Photonics technologies," *Optics Express*, vol. 21, no. 20, pp. 23736-23747, 2013.

[V.7] S. Liao and Q. Xue, "Dual polarized planar aperture antenna on LTCC for 60-GHz antenna-in-package applications," *IEEE Transactions on Antennas and Propagation*, vol. 65, no. 1, pp. 63–70, 2017.

[V.8] D. Hou, Y. Xiong, W. Hong, W. L. Goh, and J. Chen, "Silicon-based On-chip Antenna Design for Millimeter-wave / THz Applications," *IEEE Electrical Design of Advanced Packaging and Systems Symposium (EDAPS)*, pp. 1-4, Hanzhou, China, 2012.

[V.9] J. Xu, Z. N. Chen, and X. Qing, "270-GHz LTCC-integrated strip-loaded linearly polarized radial line slot array antenna," *IEEE Transactions on Antennas and Propagation*, vol. 61, no. 4, pp. 1794–1801, 2013.

[V.10] X. D. Deng, Y. Li, C. Liu, W. Wu, and Y. Z. Xiong, "340 GHz On-Chip 3-D Antenna with 10 dBi Gain and 80% Radiation Efficiency," *IEEE Transactions on Terahertz Science and Technology*, vol. 5, no. 4, pp. 619–627, 2015.

[V.11] Y. Rao, "InP-based Long Wavelength VCSEL using High Contrast Grating,", *PhD dissertation,* University of California at Berkeley, 2012.

[V.12] J. M. Boucaud *et al.*, "Cost effective laser structuration of optical waveguides on thin glass interposer," *IEEE Journal of Lightwave Technology*, vol. 35, no. 20, pp. 4445–4450, 2017.

[V.13] J. M. Boucaud *et al.*, "Single Mode Polymer Optical Waveguides and Out-of- plane Coupling Structure on a Glass Substrate," *Electronic System-Integration Technology Conference (ESTC)*, Dresden, Germany, 2018, [Accepted for publication].

[V.14] "BiCMOS055 Technology Offer", *STMicroelectonics*, [V.Online]. Available: https://mycmp.fr/IMG/pdf/04_kt_bicmos055_overview2016-3.pdf.

[V.15] T. J. Reck *et al.*, "Micromachined Probes for Submillimeter-Wave On-Wafer Measurements — Part II : RF Design and Characterization," *IEEE Transactions on Terahertz Science and*

Technology, vol. 1, no. 2, pp. 357–363, 2011.

[V.16] G. Chattopadhyay, T. Reck, C. Lee, and C. Jung-Kubiak, "Micromachined packaging for terahertz systems," *Proceedings of the IEEE*, vol. 105, no. 6, pp. 1139–1150, 2017.

[V.17] R. Farkouh, "Femtosecond Laser Micromachining of Low- Temperature Co-Fired Ceramic and Glass Fiber Reinforced Polymer Printed Circuit Boards Materials," *PhD dissertation,* University of Nebraska - Lincoln, 2017.

[V.18] C. Belem-Goncalves, E. Lacombe, C. Del Rio, F. Gianesello, C. Luxey, and G. Ducournau, "Compact measurement setup for antennas operating in the 220-325 GHz band," in *IEEE International Symposium on Antennas and Propagation (ISAP)*, Busan, Korea, 2018, [Accecpted for publication].

[V.19] H. Gulan, C. Luxey, and D. Titz, "Mm-Wave Sub-mm-Wave Antenna Measurement," 2015.

Publications

Publication list

[1] **Elsa Lacombe**, Cybelle Belem-Goncalves, Cyril Luxey, Frederic Gianesello, Cedric Durand, Daniel Gloria, Guillaume Ducournau, ***"300 GHz OOK Transmitter Integrated in Advanced Silicon Photonics Technology and Achieving 20 Gb/s",*** IEEE Radio Frequency Integrated Circuits Symposium (RFIC), Philadelphia, USA, 10-12 June 2018.

[2] **Elsa Lacombe**, Cybelle Belem-Goncalves, Cyril Luxey, Frederic Gianesello, Cedric Durand, Daniel Gloria, Guillaume Ducournau, ***"10-Gb/s Indoor THz Communications Using Industrial Si Photonics Technology"***, IEEE Microwave and Wireless Components Letters (MWCL), Vol 28, Issue 4, p. 362 – 364, April 2018.

[3] **Elsa Lacombe**, Frederic Gianesello, Cyril Luxey, Cedric Durand, Diane Titz, Jorge R. Costa, Carlos Fernandez, Carlos del Río Bocio, Guillaume Ducournau, Heiko Gulan, Thomas Zwick, ***"THz Packaging Solution for Low Cost Si-based 40 Gb/s Wireless Link System"***, European Conference on Antennas and Propagation (EuCAP), London, UK, 8-13 April 2018.

[4] **Elsa Lacombe**, Frederic Gianesello, Aimeric Bisognin, Cyril Luxey, Diane Titz, Heiko Gulan, Thomas Zwick***, "240 GHz Antenna Integrated on Low-Cost Organic Substrate Packaging Technology Targeting High-Data Rate sub-THz Telecommunication"***, IEEE European Microwave Week (EuMW), Nuremberg, Germany, 8-13 October 2017.

[5] **Elsa Lacombe**, Frederic Gianesello, Aimeric Bisognin, Cyril Luxey, Diane Titz, Heiko Gulan, Thomas Zwick, Jorge Costa, Carlos A. Fernandes, ***"Low-Cost Plastic Lens Fabricated in FDM 3D-Printing Technology Targeting High Data Rate Wireless Links Above 200 GHz"***, International Conference on Electromagnetics and Advance Applications – Antenna and Propagation in Wireless Communications (ICEAA), Verona, Italy, 11-15 September 2017.

[6] **Elsa Lacombe**, Frederic Gianesello, Aimeric Bisognin, Cyril Luxey, Diane Titz, Heiko Gulan, Thomas Zwick, Jorge Costa, Carlos A. Fernandes, ***"Low-Cost 3D-Printed 240 GHz Plastic Lens fed by Integrated Antenna in Organic Substrate Targeting Sub-THz High Data Rate Wireless Links",*** IEEE Antenna and Propagation Symposium (APS), San Diego, USA, 9-14 July 2017.

[7] **Elsa Lacombe**, Frederic Gianesello, Cedric Durand, Guillaume Ducournau, Cyril Luxey, Daniel Gloria, ***"Sub-THz Source Integrated in Low-Cost Silicon Photonic Technology targeting 40 Gb/s Wireless Links",*** IEEE Radio-Frequency Integrated Circuits (RFIC), Honolulu, Hawaii, 4-6 June 2017.

[8] **Elsa Lacombe**, Frederic Gianesello, Cyril Luxey, Guillaume Ducournau, Cedric Durand, Daniel Gloria, Aimeric Bisognin, Diane Titz, Jorge R. Costa, Carlos A. Fernandes, ***"Emetteur sub-THz faible coût intégré en technologie Photonique sur Silicium et utilisant un boîtier organique avec antenne intégrée",*** Journée Nationale Micro-Ondes, Saint Malo (JNM), France, 16-19 May 2017.

[9] **Elsa Lacombe**, Frederic Gianesello, Cyril Luxey, Cedric Durand, Daniel Gloria, Aimeric Bisognin, Diane Titz, Jorge R. Costa, Carlos A. Fernandes, ***"Enabling Low Cost THz Radiating Source Leveraging Si Photonics, IC Packaging Substrate & 3D Printing Technologies",*** European Conference on Antennas and Propagation (EuCAP), Paris, France, 19-24 March 2017.

[10] **Elsa Lacombe**, Frederic Gianesello, Cedric Durand, Guillaume Ducournau, Cyril Luxey, Daniel Gloria, ***"Sub-THz Source Integrated in Industrial Silicon Photonic Technology targeting High***

Data Rate Wireless Applications", IEEE Silicon Monolithic Integrated Circuits in RF Systems (SiFR), Phoenix, USA, 15-18 January 2017.

[11] **Elsa Lacombe**, Frederic Gianesello, Cyril Luxey, Daniel Gloria, Cedric Durand, Guillaume Ducournau, ***"Source de puissance sub-THz intégrée en technologie photonique sur silicium pour communications haut débit"***, Journées Nano, Micro et Optoélectronique (JNMO), Les Issambres, France, 30 May – 1 June 2016.

Acronym list

3GPP	3rd Generation Partnership Project
ABS	Acrylonitrile Butadiene Styrene
ACPA	Aperture Coupled Patch Antenna
ADL	Artificial Dielectric Layer
AiP	Antenna-in-Package
AM	Additive Manufacturing
ASK	Amplitude Shift Keying
AUT	Antenna Under Test
AWG	Arrayed Waveguide Grating
B2B	Back-to-Back
BBU	Baseband Unit
BEOL	Back End Of Line
BER	Bit Error Rate
BGA	Ball Grid Array
BOX	Buried Oxide
BPSK	Binary Phase Shift Keying
BS	Base Station
BW	Bandwidth
CAD	Computer-Aided-Design
CO	Central Office
CPRI	Common Public Radio Interface
C-RAN	Centralized Radio Access Network
CW	Continuous Wave
DAC	Digital-to-Analog Converter
DOCSIS	Data Over Cable Service Interface Specification
D-RAN	Distributed Radio Access Network
DRC	Design Rule Constraints
ECL	External Cavity Laser
EDFA	Erbium Doped Fiber Amplifier
EIRP	Equivalent Isotropic Radiated Power
EM	Electromagnetic
eMBB	Enhanced Mobile Broadband
FDD	Frequency Division Duplexing
FDM	Fused Deposition Modeling
FEC	Forward Error Correction
FEOL	Front End Of Line
FSPL	Free Space Path Loss
GaAs	Gallium Arsenide
GbE	Gigabit Ethernet
GC	Grating Coupler
HDI	High Density Interconnect
HetNet	Heterogeneous Network
HSPM	High Speed Phase Modulator

HTCC	High Temperature Co-Fired Ceramic
IC	Integrated Circuit
IF	Intermediate Frequency
InP	Indium Phosphide
IoT	Internet of Things
ITU	International Telecommunication Union
LGA	Land Grid Array
LoRa	Long Range
LPD	Longitudinal Photodiode
LTCC	Low Temperature Co-Fired Ceramic
LTE	Long Term Evolution
M2M	Machine-to-Machine
MIMO	Multiple-Input Multiple-Output
mmW	Millimeter Wave
MZM	Mach Zehnder Modulator
NR	New Radio
NRZ	Non-Return-to-Zero
O-E	Opto-electronic
OOK	On-Off Keying
P2P	Point-to-Point
PA	Power Amplifier
PAM	Pulse Amplitude Modulation
PCB	Printed Circuit Board
PIC	Photonic Integrated Circuit
PIC25G	Photonic Integrated Circuit at 25 Gb/s
PIN	P-doped/Intrinsic/N-doped
PIN-PD	PIN Photodiode
PINPM	PIN Phase Modulator
PRBS	Pseudo-Random Bit Sequence
QAM16	16state-Quadrature-Amplitude-Modulation
QPSK	Quadrature Phase Shift Keying
RAN	Radio Access Network
RF	Radio Frequency
RFIC	Radio Frequency Integrated Circuit
RoF	Radio-over-Fiber
RRH	Remote Radio Head
Rx	Receiver
SiGe	Silicon Germanium
SIW	Substrate Integrated Waveguide
SLA	Stereolithography
SMF	Single Mode Fiber
SNR	Signal-to-Noise Ratio
SoC	System-in-Package
SOI	Semiconductor-On-Insulator
TDD	Time Division Duplexing
Tx	Transmitter
UTC-PD	Uni-travelling-Carrier Photodiode
vBBU	Virtualized Baseband Unit

VCO	Voltage Controlled Oscillator
VCSEL	Vertical-Cavity Surface-Emitting Laser
VM	Virtual machine
VNA	Vectorial Network Analyzer
VNAx	Vectorial Network Analyzer extender
VPD	Vertical Photodiode
WAN	Wide Area Network
WG PIN-PD	Waveguide integrated PIN-PD
WRC	World Radio-communication Conferences